博 士 学 位 論 文

氏名（本籍）	Daniel Shipwiisho Likius（Namibia）
学位の種類	博　士（工学）
学位記番号	博甲第　128号
学位授与年月日	平成　26年　　3月　　31日
学位授与の要件	学位規則第4条第　1項
学位論文題目	ELECTRICAL CONDUCTIVITIES, PLASMONIC PROPERTIES AND VIS-RESPONSIVE ACTIVITIES OF Ag-NANOPARTICLES /TITANIA COMPOSITE THIN FILMS FABRICATED USING MOLECULAR PRECURSOR METHOD (MPM)

論文審査委員	主査	佐藤　光史
	副査	大倉　利典
	副査	小野　幸子
	副査	鷹野　一朗
	副査	大石　知司（芝浦工業大学）
	副査	
	副査	

工学院大学大学院

ELECTRICAL CONDUCTIVITIES, PLASMONIC PROPERTIES AND VIS-RESPONSIVE ACTIVITIES OF Ag-NANOPARTICLES/TITANIA COMPOSITE THIN FILMS FABRICATED USING MOLECULAR PRECURSOR METHOD (MPM).

By

Daniel Shipwiisho Likius

B.Sc. (Chemistry and Cell and Molecular Biology); University of Namibia, 2006

M.Sc. (Inorganic Chemistry); University of Namibia, 2008

A THESIS SUBMITTED IN PARTIAL FULFILLMENT OF

THE REQUIREMENTS FOR THE DEGREE OF

DOCTOR OF PHILOSOPHY

in

THE GRADUATE SCHOOL

(Applied Chemistry and Chemical Engineering)

Supervisor: Prof. Mitsunobu SATO

KOGAKUIN UNIVERSITY

(TOKYO, JAPAN), MARCH 2014

TABLE OF CONTENTS

LIST OF ABBREVIATION AND SYBOLS

Abbreviation	Definition
ADD	Average Dark-current Density
Ag-NP/TiO_2	Silver-nanoparticles/Titania composite
Ag/ZrO_2	Silver-nanoparticles/zirconia composite
Ag-NPs	Silver nanoparticles
APD	Average Photocurrent Density
CB	Conduction band
COMP-Agn	Ag-NP/TiO_2 composite; n is the Ag mol% in titania
COMP-AgnZirconia	Ag-NP/ZrO_2 composite; n is the Ag mol% in zirconia
CVD	Chemical Vapour deposition
DI	Deionised water
DRS	Diffused Reflectance spectrum
DSSC	Dye Sensitized Solar Cell
e^-	electrons
Eg	Band gab
eV	Band gab energy
Fe-SEM	Field Emission-Scanning Electron Microscope
H^+	holes
HOMO	Highest Occupied Molecular Orbitals
IPCE	Incident Photo-to-Current Convension Efficiency

K-M	Kubelka-Munk equation
LSPR	Localized Surface Plasmon Resonance
LUMO	Lower Unoccupied Molecular Orbitals
MB	Methylene Blue
MPM	Molecular Precursor Method
nm	Nanometer
PVD	Physical Vapour Deposition
P25 TiO_2	Degussa`s Commercial titania
QD	Quantum Dots
S_{Ag}	Silver precursor solution
$S_{composite}$	Silver:Titania composite precursor soulution
SPR	Surface Plasmon Resonance
$S_{titania}$	Titania precursor solution
UV	Ultraviolet
TEM	Transmission Electron Microscopic
TG/DTA	Thermal Gravimetric/Differential Thermal Analysis
VB	Valence band
Vis	Visible light
XRD	X-Ray Diffraction
λ	wavelength
φ_{Ag}	Silver volumetric fraction

ACKNOWLEGMENTS

The last few years in Coordination Engineering Laboratory have been tumultuous but exciting. Now, the academic atmosphere that provided a valuable anchor, too, must be hauled up for journeys beyond. The end of this most enjoyable academic challenge has arrived, but I cannot look back without a sense of loss – loss of continuous joys of discovery and academic enrichment. I wish to express my deepest gratitude to my supervisor, **Prof. Mitsunobu SATO**, for his innovative ideas given to me throughout the entire course of my Ph.D. candidature, his patient guidance in the experiments, and his painstaking modification of the publications and this thesis. I also feel thankful to his high integrity and dedication in the scientific research, which have greatly inspired me. I would like to thank, **Dr. Hiroki Nagai**, for his incredible support. Nagai helped me endure this long journey with his sustained encouragement. He has an uncanny ability to visualize the final outcome of research effort. I also greatly appreciate **Hiroki Hara**'s support and for giving me a lifetime worth of precious memories. Many others at the Kogakuin University helped me crystallize my research approach. I would particularly like to mention **Prof. Akisato Mizumo, Prof. Tohru Hoda, Dr. Norio Baba, Dr. Naoya Yoshida, Dr. Shakur Haidel, Roy Kadokura and Junko Usuki** for their support. I would like also to thanks the internal examiners; **Prof. Okura Toshinori, Prof. Ono Sachiko, Prof. Ichiro Takano** as well as the external examiner; **Prof. Ohishi Tomoji** (Shibaura Institute of Technology) for their constructive comments and time they took to go through this thesis.

I would sincerely like to thank our group members **Chihiro Mochizuki, Sohei Aoyama, Tatsuya Suzuki, Taishi Segawa and Soichiro Takano** for many useful discussions and

their help in carrying out my research work in the lab. I thank Namibian Embassy in Japan for genuine critiques that consistently helped me remain rooted in the reality of Africa without suppressing the dreams of greatness for Namibia. I also thank **His Excellency, Dr. Hifikepunye Pohamba, Prof. Lazarus Hangula, Prof. Osmund Mwandemele, Prof. Enos Kiremire (my mentor) and Dr. Erold Naomab**, all of the University of Namibia (**UNAM**), for provided constant encouragement.

I would like to thank the most important people in my life, my all family members. Thank you **Grandma Letisia** for giving me eternal hope and for being a constant source of strength. You gave me roots and wings. I regret that you died before I was fully able to spread my wings.

Above all, thank you Ministry of Education, Culture, Sports, Science and Technology of Japan (**MEXT**) for the scholarship with the recommendation from Embassy of Japan in Pretoria, South Africa. Thanks **Oltilie Taukeni, Dhiginina-Omuwa Hilma Andreas, Thomas and Karina Mwahafa, Patrick Nghuulondo, Peter Ndeilenga, Petrus Kashinduka, Johanna and Andreas Namene, Elise Shilongo, Kosmas Sylvia, Hersmith Sebestian, Beverly Uazengisa, Sanio Mutilifa, Dudley Delie** and **Kunikatsu Shimamoto-san for your support during my 4 years in Japan**!!

DECLARATIONS

I, **Daniel Shipwiisho Likius**, declare hereby that this study is a true reflection of my own research, and that this work, or part thereof has not been submitted for a degree in any other institution of higher education.

…… Date:……..

Daniel Shipwiisho Likius

*To my later grandmother, Mukwamalanga Letisia Andreas Kashinduka (**1943-2008**)*

And to

Tommy, Enos, Johanna and Junior

CHAPTER 1 INTRODUCTION

1−1 INTRODUCTION

1-1.1 Motivation for the development of visible-light harvesters.

Prehistoric man discovered fire. Ever since that momentous occasion, there has existed an ideology of utilizing the planet's natural resources for proliferation, sustenance, and personal comfort. The trouble being we seem to have, in large part, viewed this luxury as an infinite resource, especially starting from the end of the nineteenth century. The industrial revolution that spread over the world by the end of nineteenth century marked a new era in the history of human kind. These results in high consumption of fossil fuels, causing three primary global problems: depletion of fossil fuels, pollution, and climate change. Figure 1.1 shows world power consumption in the past, its current status and two future forecasts based on different approaches: 1. "use what's cheapest, no environmental concern", 2. "save the planet, invest in the future now".

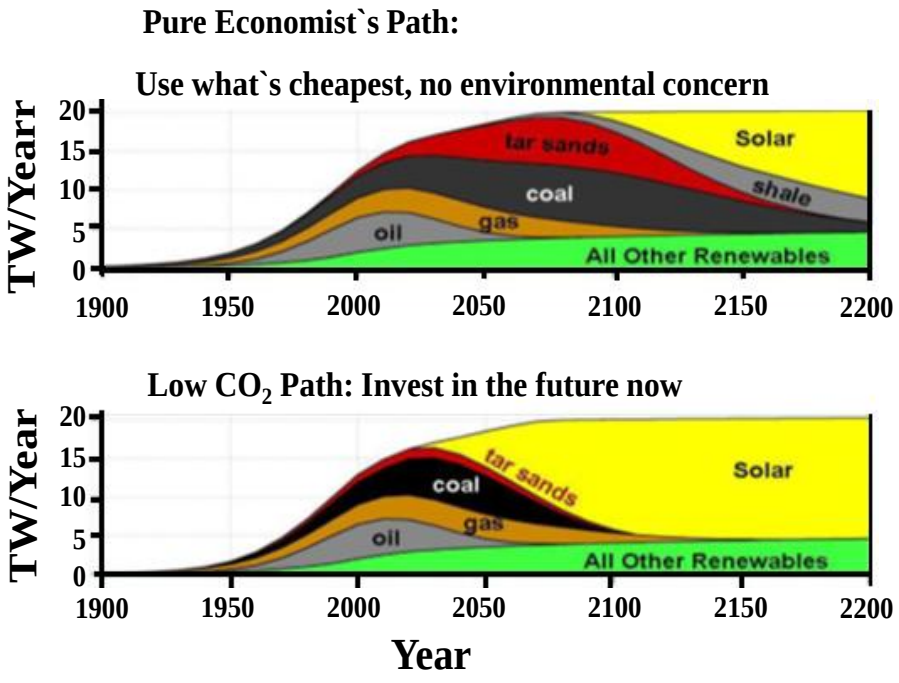

Fig. 1.1 World power consumption **[1]**.

In both future forecasts shown in figure 1.1, the world is forced to make another worldwide revolutionary technological transition due to depletion of resources. However, the largest challenge for our global society is to find ways to replace slowly but inevitably vanishing fossil fuel supplies by renewable resources and, at the same time, avoid negative effects from the current energy system on climate, environment, and health **[2]**.

In view of the severe future ecological impacts of energy production by combustion of fossil fuels, solar energy is seriously considered as an alternative. Therefore, direct utilization of solar radiation to produce electricity is close to an ideal way to utilize the nature's renewable energy flow. This is because solar energy converters such as solar panels themselves operate without noise, toxic and greenhouse gas emissions, and require very little maintenance. With all that said, the concept of solar energy converters is accepted by most regulators, engineers, and those in the general public who acknowledge that gas emissions affect the environment. It is everyone's responsibility on this planet to not only reduces the impact that gas emissions make, but to also ameliorate the damage that industrialization has caused thus far. Moreover, not all energy generation need to produce effluent. The solar energy is a very potential leading renewable energy source since it does not produce effluent and it is readily available.

1-1.2 Availability of light on mother planet earth

Citing data from recent observations, Stephen Hawking **[3]** noted that "normal matter (mainly the sun) is only 5 percent of the energy density of the known universe; 27 percent is dark matter, 68 percent is dark energy." Never the rest, it is everyone`s responsibility to find the way of how to utilize the 5 percentage of the energy available.

The sun is the nature's renewable energy flow since it is about half way through its evolution to its next stage, so theoretically, it will shine for the next six billion years **[4]**. Based on its long life and accessibility, solar energy is indeed a very potential leading renewable energy source. From these, there is no doubt that solar energy is a renewable resource and it will be always available. For practical purposes, it is an infinite energy source. Peippo **[5]** demonstrated that the sunlight is accessible forever and nearly everywhere. Near the earth surface, the sun produces 0.2−0.3 mol photons $m^{-2}h^{-1}$ in the range of 300−400nm with a typical UV flux of 20−30 Wm^{-2} **[4]**. This suggest the use of the sunlight as an economically and ecologically sensible light source. Figure 1.2 shows the standard AM1.5 global solar spectrum.

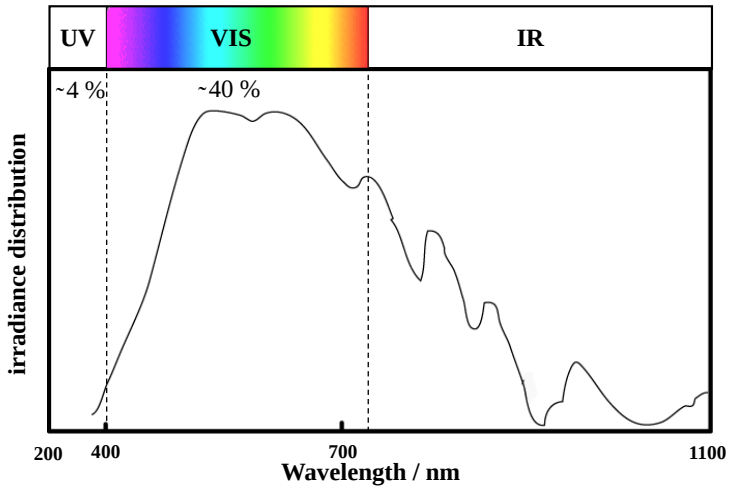

Fig. 1.2 The standard solar spectra irradiance (AM1.5 global = one sun). Shown data are from http://www.pv.unsw.edu.au/am1.5.html.

Solar energy converters with high reactivity under VIS-light may allow utilizing the main part of the solar spectrum or interior lighting. Based on global standard solar spectrum in figure 1.2, ultraviolet light makes up 3 – 5 % of the solar spectrum, whereas

the spectrum consists of ~ 40 % visible light **[6]**. Therefore many researchers have been and are still trying to shift the solar energy converters` threshold to use visible light in high efficiency under sunlight irradiation and widen the spectrum wavelength greater than 400 nm **[8−11]**. The use of heat-treatment is essential in the manufacturing processes of many highly functional materials and solar energy converters **[8]**.

1-1.3 Electronic structure of a semiconductor

Most of the highly functional industrial materials and solar energy converters are made up of semiconductor materials. A suitable semiconductor must be identified based on its: stability, reactivity, toxicity, availability and capability to move photo-generated electrons proceed under mild conditions at room temperature, normal atmospheric pressure and under light irradiation. In order one to be able to identify a suitable semiconductor, it is always important to understand the electronic structure of a semiconductor.

To start with, atoms and molecules are the essential building blocks of all things. The manner in which things are "constructed" with these building blocks is vitally important to their properties and how they interact. When molecular orbitals are formed from two atoms, each type of atomic orbital gives rise to two molecular orbitals **[12]**. When *N* atoms are used, *N* molecular orbitals are formed. In solids, *N* is very large, resulting in a large number of orbitals. The overlap of a large number of orbitals leads to molecular orbitals that are closely spaced in energy and so form a virtually continuous band **[13, 14]**. Figure 1.3 shows the change in the electronic structure of a semiconductor compound with increasing number of monomeric units *N*. The overlap of the lowest unoccupied molecular orbitals (LUMO) results in the formation of a conduction band

and a valence band is formed from overlapping the highest occupied molecular orbitals (HOMO). The band separation is known as the band gap (E_g), a region devoid of energy levels. From the illustration shown in figure 1.4, the reduction in the band gap size with the formation of bands can clearly be seen.

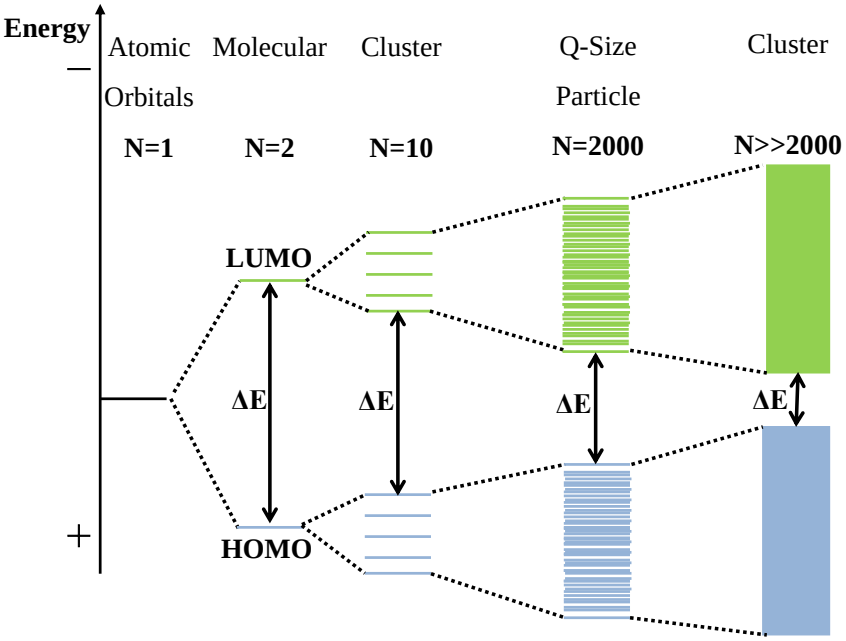

Fig. 1.3 Change in the electronic structure of a semiconductor compound with increasing number of monomeric units *N* **[13, 14]**.

1-1.4 How is semiconductor differing from insulator and the metal?

Figure 1.4 can helps one to differentiate between a semiconductor from metal and insulator. In metal such as in silver, the conduction band and valence band lie very close to each other in which electrons move freely **[13]**. Metals are good conductors because at their Fermi level, there is a large density of energetically available states that each electron can occupy. Electrons can move quite freely between energy levels without a high energy cost. Insulators, by contrast, are very poor conductors of electricity because

there is a large band gap between electron-occupied energy levels and empty energy levels that allow for electron motion.

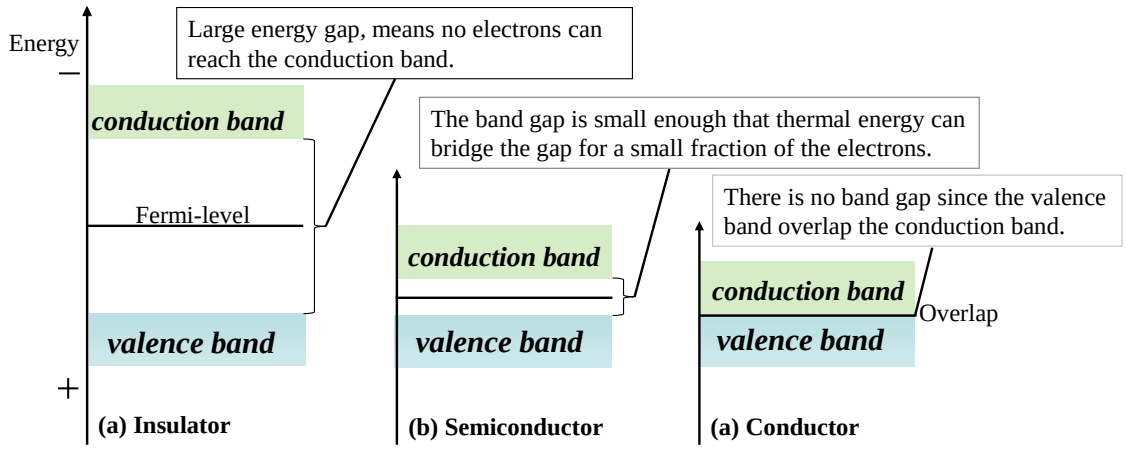

Fig. 1.4 The different between insulator, semiconductor and conductor.

Semiconductors are defined by their unique electric conductive behavior. Semiconductors absorb light radiation with the threshold wavelength that provides sufficient photon energy to overcome the band gap between the valence and conduction bands **[15]**. This threshold wavelength, required to promote the excited state, corresponds to the minimal photon energy and depends on the band-gap energy. Figure 1.5 show how a general semiconductor can be excited when received minimum photon energy.

Due to this behavior, metal oxide semiconductor materials such as TiO_2, ZnO, MoO_3, SnO_2, CuO, CoO, Co_3O_4 etc have been extensively studied due to their unusual catalytic and optoelectronic properties **[11, 16, 17]**. Figure 1.6 shows the various band positions of different semiconductors.

Although many semiconductors have smaller band gaps and absorb in the visible range

(e.g. CdS and Fe_2O_3 with band-gap values of 2.5 and 2.3 eV, respectively), just a few of them are catalytically active because the energy levels of either the conduction or valence bands are unsuitable to construct light-harvesting assemblies and facilitate photo-induced charge separation processes (e^- and h^+), a necessity for the follow of the electrons or reduction-oxidation (redox) reaction. This limitation, together with poor photo-corrosion stability of many semiconductors, limits significantly the number of potential light-harvesting materials.

Figure 1.7 shows the primary processes that occur when a semiconductor is excited upon received minimum photon energy in the presence of O_2 and H_2O, which corresponds to an aqueous phase or atmospheric environment. The photo-formed electrons and holes generate active oxygen species such as O_2 and OH radicals, respectively. This process is known as a photocatalytic reaction and semiconductor is act as photocatalyst **[9, 18]**.

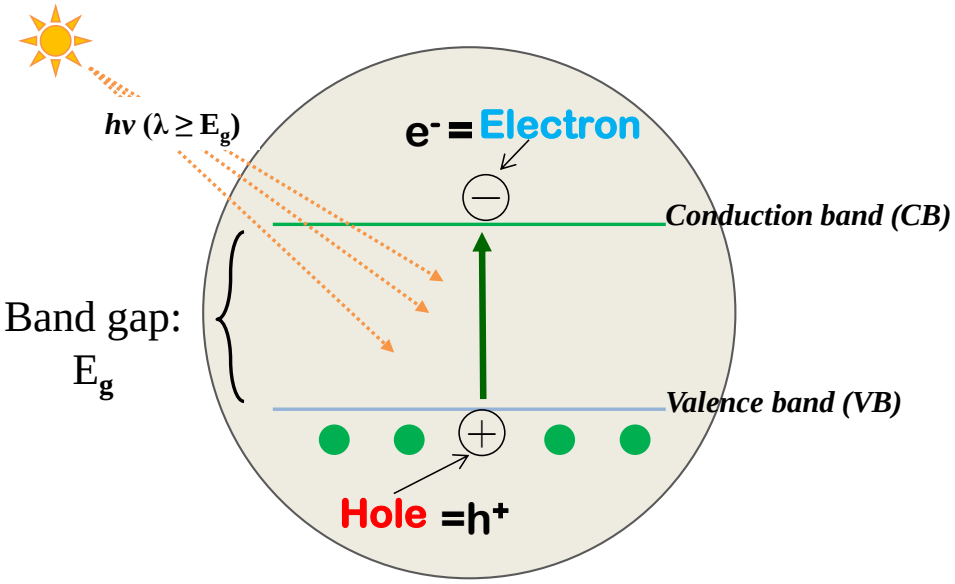

Fig. 1.5 Excitation of semiconductor: e−–h+ pair formation by illuminated a metal oxide semiconductor particle.

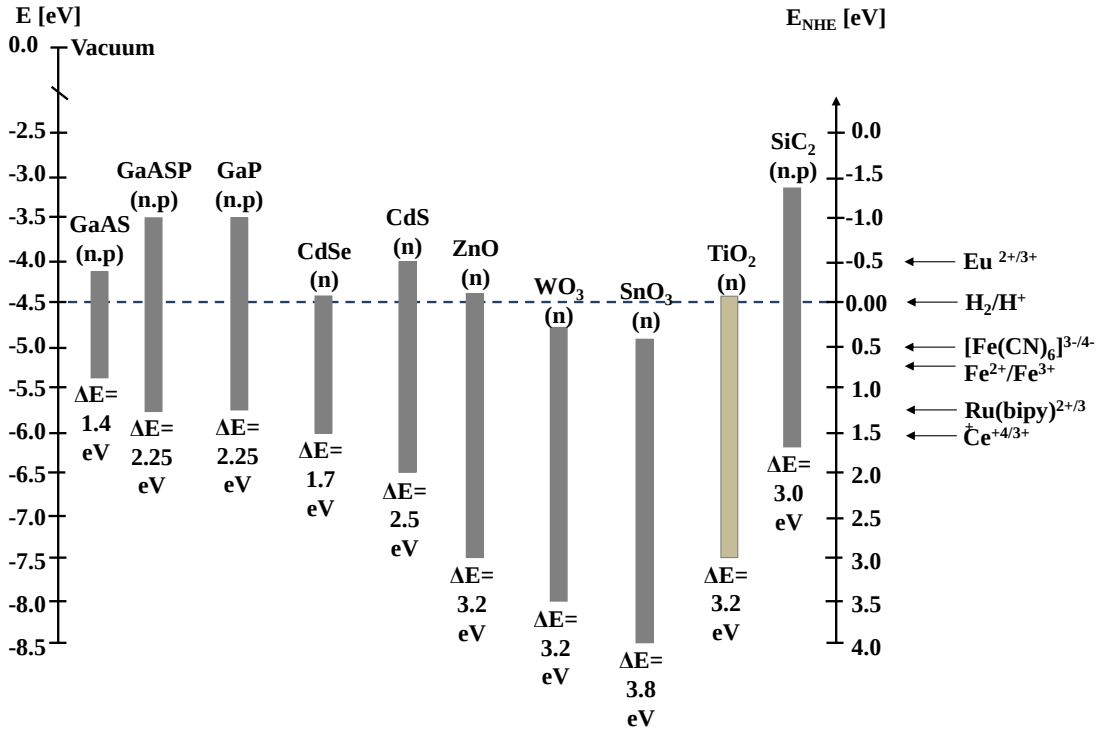

Fig. 1.6 Band gap energies of various semiconductors in an aqueous electrolyte at pH = 1. **[12]**.

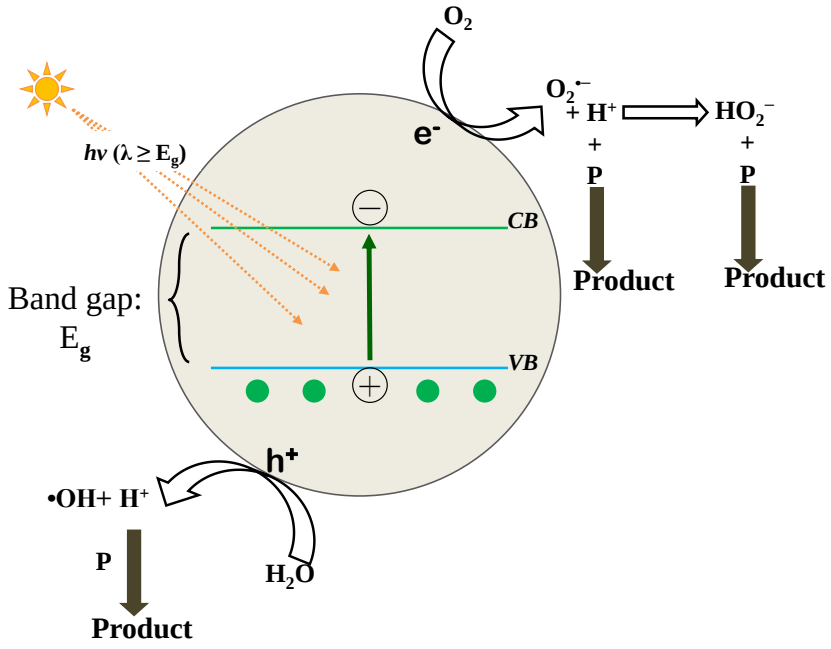

Fig. 1.7. How semiconductor act as a photocatalyst.

Flowcharts of Equations 1.1-1.5 illustrate the primary processes that happen when the titania as semiconductor is excited in the presence of H_2O and O_2:

$$TiO_2 + hv \Longrightarrow e^-_{cb} + h^+_{vb} \quad \ldots\ldots\ldots\ldots\ldots\ldots\ldots\ldots\ldots\ldots\ldots\ldots\ldots\ldots \quad (1.1)$$

$$h^+_{vb} + H_2O_{(ads)}\rho \Longrightarrow HO^{\bullet} + H^+ \quad \ldots\ldots\ldots\ldots\ldots\ldots\ldots\ldots\ldots\ldots\ldots\ldots\ldots \quad (1.2)$$

$$h^+_{vb} + OH^-_{(ads)} \Longrightarrow HO^{\bullet} \quad \ldots\ldots\ldots\ldots\ldots\ldots\ldots\ldots\ldots\ldots\ldots\ldots\ldots\ldots \quad (1.3)$$

$$e^-_{cb} + O_{2(ads)} \Longrightarrow O^{\bullet -}_2 \quad \ldots\ldots\ldots\ldots\ldots\ldots\ldots\ldots\ldots\ldots\ldots\ldots\ldots\ldots \quad (1.4)$$

$$2O^{\bullet -}_2 + H_2O \Longrightarrow 2HO^{\bullet} + 2OH^- + O_2 \ldots\ldots\ldots\ldots\ldots\ldots\ldots\ldots\ldots\ldots \quad (1.5)$$

For a semiconductor to be capable of producing hydroxyl radicals, the potential of the valence band must be greater than the potential of OH•. From figure 1.6, it can be seen that ZnO, TiO_2, WO_3 and SnO_2 have the potential to produce hydroxyl radicals. Large-band-gap semiconductors are therefore the most suitable for photo-induced charge separation processes, because they provide sufficient negative and positive redox potentials in conductance bands and valence bands, respectively. The disadvantage of using wide band-gap semiconductors is the requirement for high energy input. Hence, the photoresponse of these semiconductor is low under the sunlight because the part of the solar spectrum in the UV region is small (≲4%), e.g. the band gap of TiO_2 anatase is 3.2 eV and rutile is 3.0 eV corresponding to an absorbance threshold, λ = 388 and 415 nm respectively **[19, 20]**.

1-1.5 TiO_2 as promising and industrially functional semiconductor material

Among the oxides, materials scientists are overwhelmingly interested in the fundamental aspects and applications of semiconducting wide band-gap oxide materials. These types of materials show a wide range of electrical and optical properties. They can be transparent in the visible and infrared (IR) range. Most of the wide band-gap semiconductors illustrated in figure 1.6 especially metal oxides and sulfides such as TiO_2, ZnO, ZnS, WO_3, CdS, Fe_2O_3 etc., are commercially available and investigated in the literature in photocatalytic processes **[6, 21]**. However, only few of them are appropriate for efficient photocatalytic reaction of a wide range of organic and metal compounds. Of all the semiconductors tested in laboratory, TiO_2 has been proven to be the most suitable for widespread applications **[9]**: from paint to sunscreen to food coloring to photocatalyst, hydrogen production, storage medium, sensors, solar cells, and various biological and health-related applications.

ZnO is unstable due to inappropriate dissolution to yield $Zn(OH)_2$ on the ZnO particle surfaces and thus leading to catalyst inactivation over time **[22]**. Although WO_3 can be activated in the visible light up to 500 nm, it is generally less photocatalytically active than TiO_2 **[23]**. Hematite (α-Fe_2O_3) is also absorptive in the visible range (absorption onset = 560 nm) but shows much lower photocatalytic activity than TiO_2 **[24]**. CdS does not show photocatalytic activity like TiO_2 but it has been extensively studied because of its spectral response to wavelengths of the solar spectrum. Its usage is however, limited due to photo-corrosion property **[25, 26]**. The photocatalytic activity of ZnS has not received as much attention as TiO_2 because of its generally poorer catalytic efficiency and photo instability **[27]**.

In this thesis, titanium dioxide (TiO_2), also known as titanium (IV) oxide or titania, which is a naturally occurring oxide of titanium will be studied. TiO_2 is a wide-band-gap semiconducting, highly reactive, non-toxic, and cost-efficient material and the movements of photo-generated electrons proceed under mild conditions at room temperature, normal atmospheric pressure and under light irradiation, making light-harvesting a much desired ecologically environmentally-harmonious. It is also an extremely stable material even in the presence of aqueous electrolyte solutions, much more so than other types of semiconductor that has been tried. In fact, TiO_2 semiconductor is presently the most actively and widely investigated for applications that can effectively address environmental pollution **[28]**. However, extensive research continues to further optimize this technology in order to develop a new visible-light-driven TiO_2 nano-based thin film that can use visible light in high efficiency under sunlight irradiation and widen the spectrum of potential applications. Development of material engineering in the nanometer scale has generated new photonic materials and systems that could potentially lead to realization of high efficiency and low-cost light harvesting material.

1-1.6 Why nanoparticles are interesting?

It has been said that a nanometer (nm) is "magic point on the length scale, for this is the point where the smallest man-made devices meet the atoms and molecules of the natural world" **[29]**. Indeed, the public is becoming aware the quote of the chemist and Nobel Laureate, Richard Smalley: "Just wait-the next centrury is going to be incredible. We are about to be build things that work on smallest possible length scales, atom by atom. These little nanothings will revolutionize out industries and our lives" **[30]**. So what are

these “nanothings” that are going to change our lives? Perhaps the best way to begin is to compare nanothings with small things in our world.

Figure 1.8 compares the size of bacteria, virus, nanocrystals and the Buckminster fullerence molecule. We can note that bacteria are huge in comparison and it is helpful to realize that the volume of one *Bacillus cereus bacterium* could hold a million 5 nm nanoparticles. These illustrations help make the point that nanocrystals, particularly in the 1-10 nm range (100 to 70 000 atoms) serve as bridges from the molecules to condensed matter.

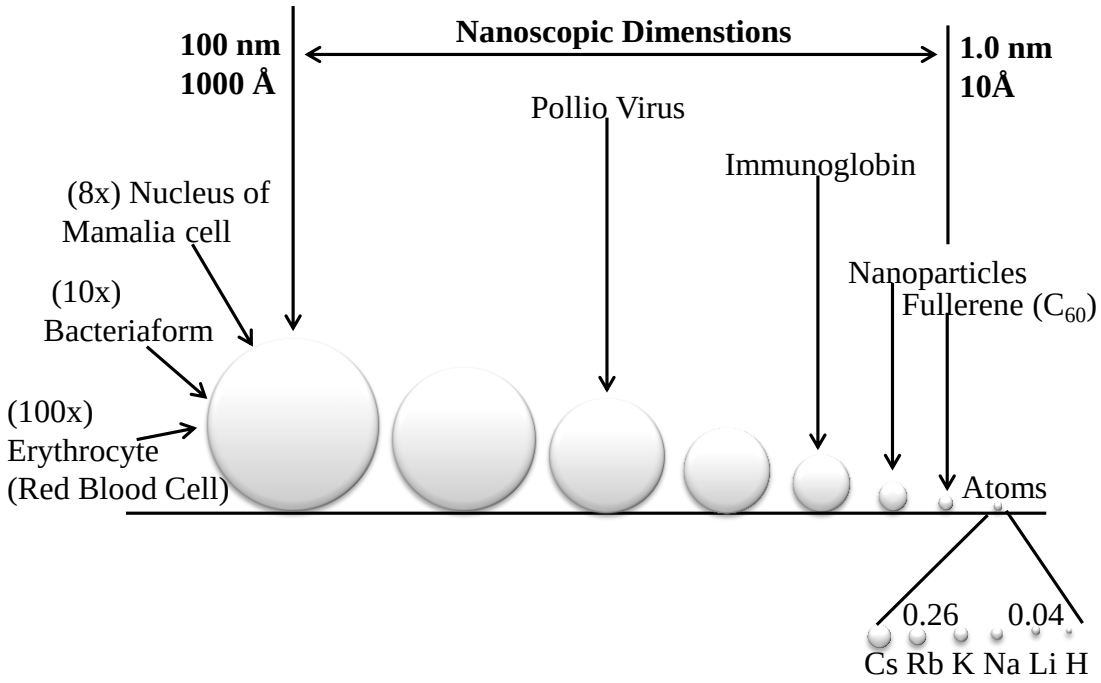

Fig. 1.8 Size comparisons of nanocrystals with bacteria, viruses, molecules and atoms.

After the understanding of what are nanoparticles, one of the first and most natural a question to ask when starting to deal with nanoparticles is: “why are nanoparticles so interesting”? Why even bother to work with these extremely small structures when

handling and synthesis is much more complicated than that of their macroscopic counterparts. The answer lies in the nature of and unique properties possessed by nanostructures. As technology advances and devices enter nanodimensions, it is imperative for us to understand the science and properties of materials at this scale. Moreover, literature survey reveals that about 18,000 publications, including papers and patents, have been published on nanocomposites in the last two decades **[31]**.

It has been reported that at the nanoscale (below about 100 nm), a material's property can change dramatically. In this size range intrinsic, properties change due to size alone. For semiconductors such as TiO_2, ZnO, CdS and Si, band gaps change. In some cases, for band gaps in the visible spectrum, this means that colors can change with size change in the 1-10 nm range. The special properties of nanomaterials tabulated in Table 1 are the mainly due to quantum size confinement in nanoclusters and an extremely large surface-to-volume ratio relative to bulk materials **[32]**.

With only a reduction in size and no change in the substance itself, materials can exhibit new properties such as electrical conductivity, insulating behavior, elasticity, greater strength, different color, and greater reactivity-characteristics that the very same substances do not exhibit at the micro- or macro scale. For example,

1. By the time gold crystals are just 4 nm across, the melting point drops to 700 K from its "encyclopedia value" of 1337 K **[34]**.
2. White crystals such as those of ZnO and TiO_2 are used as paint pigments or whitening agents, but they become increasingly colorless as the crystals shrink in size, and ZnO and TiO_2 colloids become invisible to the human eye below about 15 nm **[31]**.

3. Aluminum-can spontaneously combust at the nanoscale and has been used as rocket fuel.
4. Nano-scale copper becomes a highly elastic metal at room temperature. It can be stretched up to 50 times its original length without breaking.

Table 1 Adjustable properties of nanomaterials **[33]**.

Properties	Examples
Catalytic	Better catalytic efficiency through higher surface-to-volume ratio.
Electrical	Increased electrical conductivity in ceramics and magnetic nanocomposites, increased electric resistance in metals.
Magnetic	Increased magnetic coercivity up to a critical grain size, super paramagnetic behaviour.
Mechanical	Improved hardness and toughness of metals and alloys, ductility and super plasticity of ceramics.
Optical	Spectral shift of optical absorption and fluorescence properties, increased quantum efficiency of semiconductor crystals.
Sterical	Increased selectivity, hollow spheres for specific drug transportation and controlled release.
Biological	Increased permeability through biological barriers (membranes, blood-brain barrier, etc.), improved biocompatibility.

Moreover, figure 1.9 shows another good example on how the building blocks of gold particles, from atomic to the mesoscopic, can result in changing colors **[34]**. Collections of gold particles can appear orange, purple, red or greenish, depending upon the specific size of the particles making up the sample. Color changes can be largely explained by classical electromagnetic scattering theory, Mie theory. In 1908, Mie explained the colors of colloidal metals, and in particular those of gold, "quantitatively" by solving the fundamental problems of absorption and scattering of light by small spheres **[35]**.

The solution to this generic problem now bearing his name unofficially, though Debye carried out a similar independent investigation for completely different reasons at about the same time **[36]**. Since Mie's work, numerous researchers have investigated the properties of metals because of their unusual optical properties. Like gold nanoparticles, silver nanoparticles possess plasmon resonance in the visible spectrum, which gives rise to colors. This is due to the surface plasmon-oscillation mode of the conduction electrons that are coupled through the surface to the external electromagnetic field **[37]**. As we will see in literature review chapter (Chapter 2 of this thesis), gold, silver and copper are very attractive subjects for these investigations, while the d-band metals such as platinum, iridium and rhodium are optical less exciting.

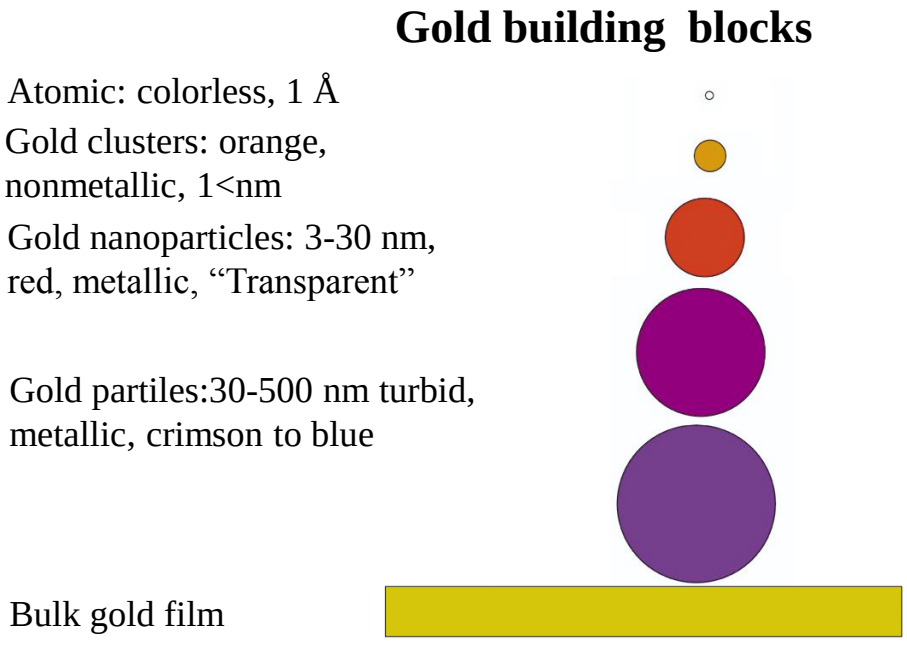

Fig. 1.**9**. Gold building blocks from atomic to the mesoscopic, and their changing colors **[34]**.

1-1.7 Evolution of nanomaterials and the definition of nanotechnology

After the pioneering works of Efros and Efros, 1982 **[38]** and Brus, 1984 **[39]** on the size quantization effect in semiconductor nanoparticles, research on nanostructured materials has generated great interest in the scientific community. Tremendous opportunities in science and technology are now possible because of the new properties exhibited by these materials and the challenging problems in theoretical physics associated with the new properties **[40, 41]**. In general, 'nanotechnology' is the engineering of functional systems at the molecular scale. In its original sense, nanotechnology refers to the projected ability to construct items from the bottom up, using techniques and tools being developed today to make complete, high-performance products **[42]**. As nanotechnology became an accepted concept, the meaning of the word shifted to encompass the simpler kinds of nanometer-scale technology, which come along with fabrication of nanostructured material. It is well understood that exploiting quantum property changes at the nanoscale as we illustrated in the previous section, is the key to nanotechnology`s novelty, power and potential **[43]**.

Through nanoscale manipulation, scientists have been dramatically transforming existing bulks materials and designing new nanoscale one. Nano-size has the potential for revolutionizing the ways in which materials and products are created and the range and nature of functionalities that can be accessed. Figure 1.10 shows the part, present and the way forward regarding nanotechnology **[42]**. Today, companies are now manufacturing nanoparticles for use in hundreds of commercial products−from crack-resistance paints **[44]** and resistant clothing to odor-eating socks, self-cleaning windows, and anti-graffiti coating for walls. For instead, exploiting the antibacterial properties of Ag NP, Smith and Nephew developed wound dressing (bandages) coating with silver nanocrystals designed to prevent infection **[45]**. This is already having a

significant commercial impact, which will assuredly increase in the future.

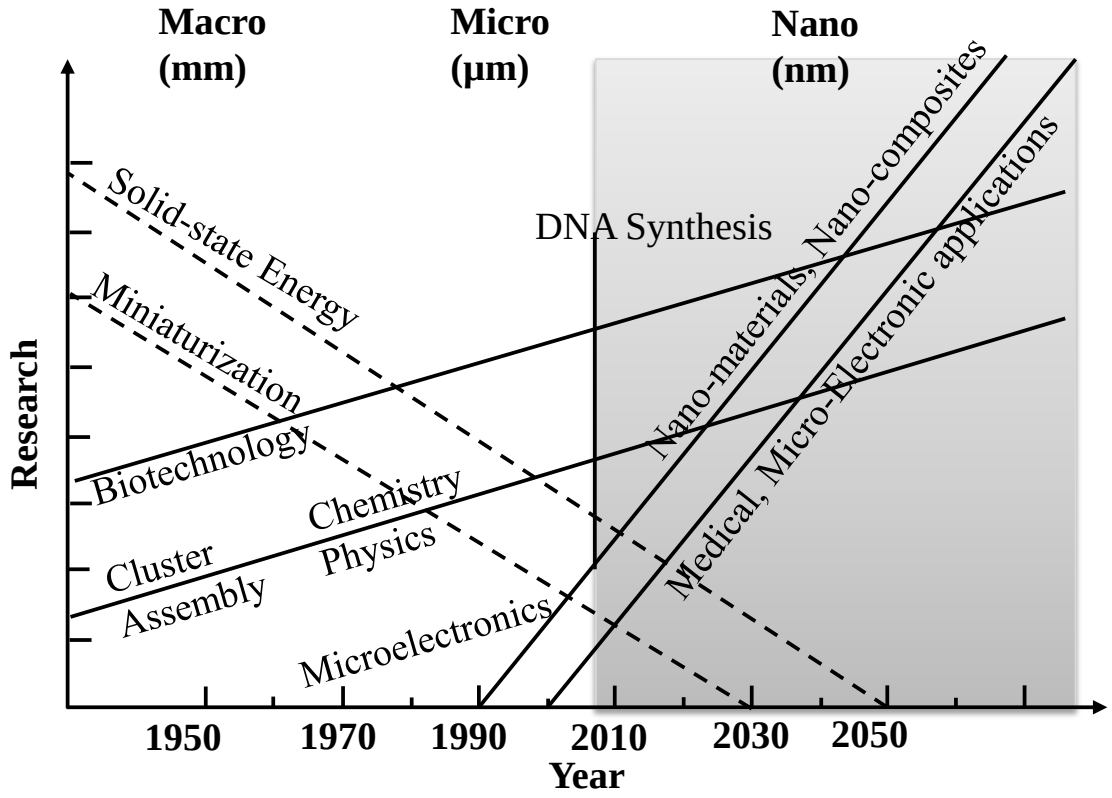

Fig. 1.10. Evolution of science and technology and the future.

1-1.8 Synthetic methods of nanomaterials

There are two general ways available to produce nanomaterials **[46−48]** as shown in figure 1.11. One is to start with a bulk materials, involve use of energy to break it into smaller pieces using mechanical, chemical or other form of energy (top-down). Examples of top-down are milling, mechano-chemical processing, etching, electroexplosion, sonication, sputtering, and laser-ablation.

An opposite approach involve atoms **[50]**, molecules **[51]**, clusters and nanoparticles **[52, 53]** can be used as functional building blocks for fabricating advanced and totally

new phases of condensed matter on the nanometre length scale mainly via chemical reaction (bottom-up). The example for bottom-up include methods such as sol-gel, aerosol, MPM, CVD, electrospinning, template synthesis, self-assemble, and atomic condensation. Both approaches can be done in either in gas, liquid, supercritical fluids, solid states or in a vacuum **[54]**.

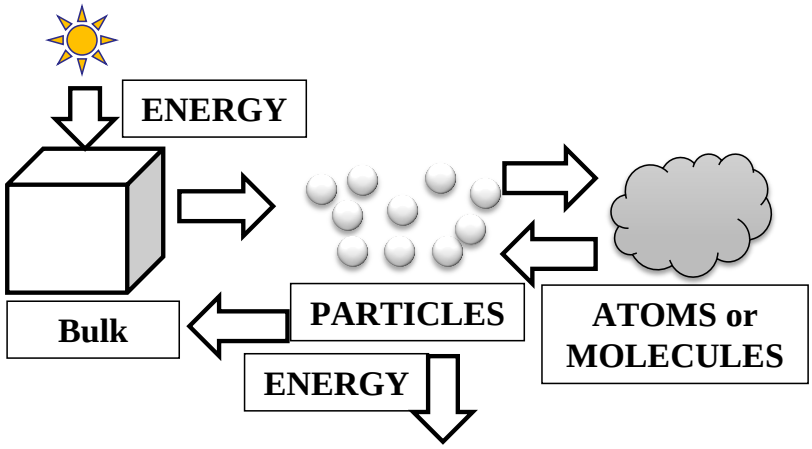

Fig. 1.11. Two basic approaches to nanomaterial fabrication: Top-down approach (from left to the right). Bottom-up approach (from right to the left) **[46, 49]**.

Using a bottom-up approach gives the opportunity to produce nanoparticles between 1 and 100 nm **[46, 49]**. Bottom-up also gives the advantage of producing stable nanoparticles compared to nanoparticles produced with a top-down approach, because the nanoparticles are placed in defined crystalline structures **[55]**.

1-1.9 Plasmonic properties of silver in visible light energy conversion

It is also well known that using silver nanoparticles (Ag NP), light can excite the collective oscillations of the free electron density, also known as plasmon resonances **[56, 57]**. The excitation of plasmon resonances is a unique property of Ag NP and

represents the most efficient mechanism by which light interacts with matter. Theoretically, the excitation of plasmon resonances on a NP can be named either as surface plasmon resonance (SPR) or localized surface plasmon resonance (LSPR) **[58]**. When particles are small as compared to the wavelength of incident radiation, the entire particle experiences the same phase of the incident radiation. For Ag NP, this mainly occurs around the 400 nm wavelength, a phenomenon known as SPR. The excitation of plasmon resonances in NPs produces a local electromagnetic field that extends from the particle surface and into the surrounding environment **[59, 60]**. This field is 'enhanced' as compared to the incident field and is a concentration of the incident field between the particles. The condition is that, NP must be large enough (c.a. 10 or more atoms) to have free electron density, but be small enough (less than the wavelength of visible light) that the optical properties change with particle size, shape, and local environment **[60, 61]**. Figure 1.12 shows how size and shape influence the position of Ag NP plasmon band.

As the particle dimensions become larger, the different areas experience different phases resulting in the formation of multiple plasmon modes. The increase in bandwidth is also a result of radiative damping of the plasmon oscillations in the NP. The efficient emission (scattering) of photons reduces the lifetime of the plasmon oscillations and broadens the plasmon band, a phenomenon known as LSPR **[60]**. However, the overall plasmon coupled peak depends on the particle size and shape, distance between, nature of the supporting substrate, and local dielectric environment **[61, 63]**.

Titanium dioxide displays photocatalytic behavior under near-ultraviolet (UV) illumination. In another scientific field as shown above, it is well understood that the excitation of localized plasmon resonance on the surface of silver (Ag) nanoparticles

(NPs) causes a tremendous increase of the near-field amplitude at well-defined wavelengths in the visible region **[64]**. The exact resonance wavelength depends on the shape and the dielectric environment of the NPs. These optical properties of Ag NP, make Ag NPs attractive to be incorporated into TiO_2 as composite. The fabrication of Ag/TiO_2 composite structure is therefore the main part of this research.

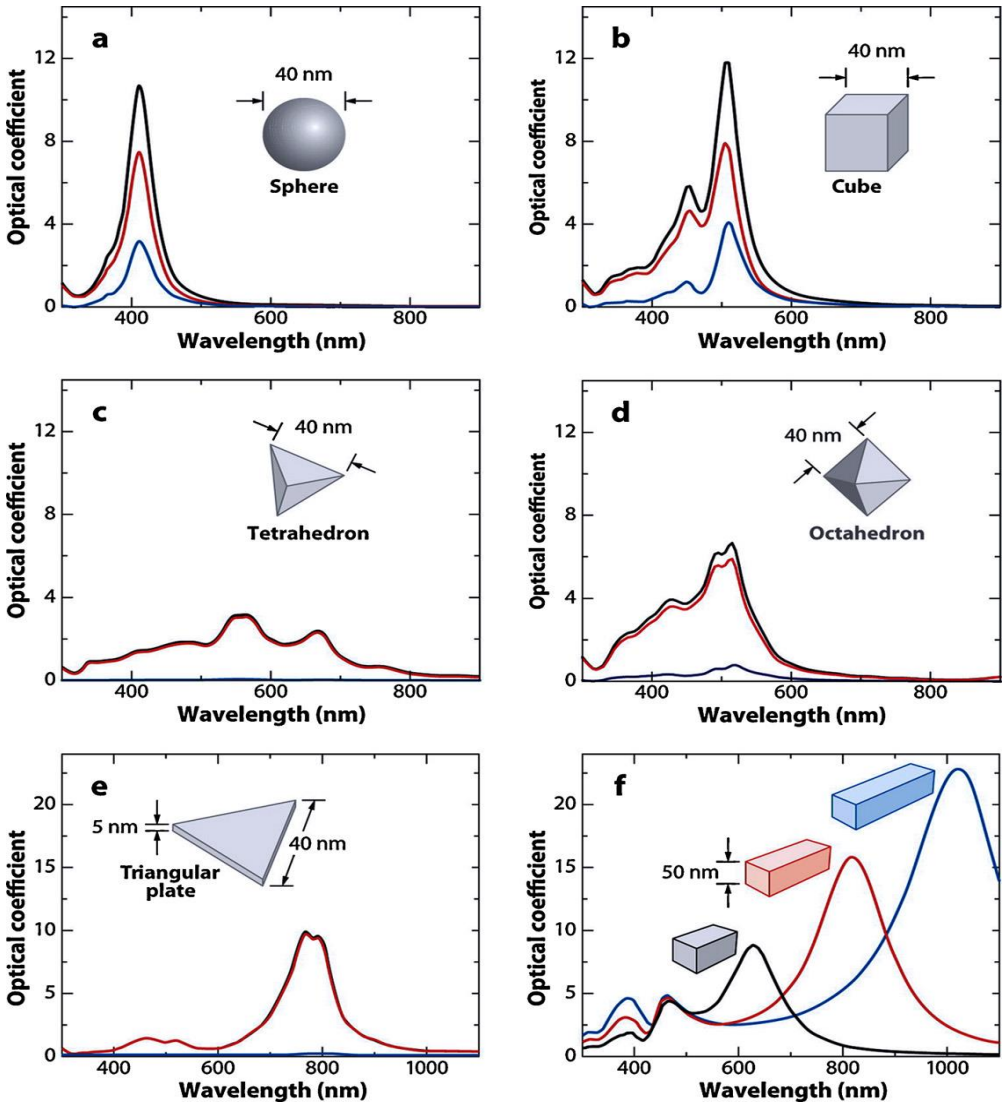

Fig. 1.12. Extinction (black), absorption (red), and scattering (blue) spectra calculated for Ag nanoparticles of different shapes. Reprinted from Ref. **[62]**.

1-1.10. The significance of composite structures

Composite materials (also called composition materials or shortened to composites) are materials made from two or more constituent materials with significantly different physical or chemical properties, that when combined, produce a material with characteristics different from the individual components. The individual components remain separate and distinct within the finished structure. The new material may be preferred for many reasons: common examples include materials which are stronger, lighter or less expensive when compared to traditional materials. The earliest man-made composite materials were straw and mud combined to form bricks for building construction. This ancient brick-making process was documented by Egyptian tomb paintings. Wattle and daub is one of the oldest man-made composite materials, at over 6000 years old **[65]**. Concrete is also a composite with inorganic material, and is used more than any other man-made material in the world. The use of composite makes it possible to provide: an increase by a factor of 2–3 in engineering life, an increase in operating reliability under severe manufacturing conditions, a reduction in loss due to corrosion, and a reduction in transport and operating expenditure **[66]**. The ergonomic nature and design of a final object in the case of using composites may lead to improvements.

1-1.11. Fundamental aspects of metal oxides as composites

Within the class of inorganic materials, oxide-based compounds show the most diverse range of properties. Because of their fundamental properties and obvious utility in applications, significant efforts have been invested in the growth of oxides as composite

and as thin films. Various classes of metal oxides are schematically represented in flowchart below.

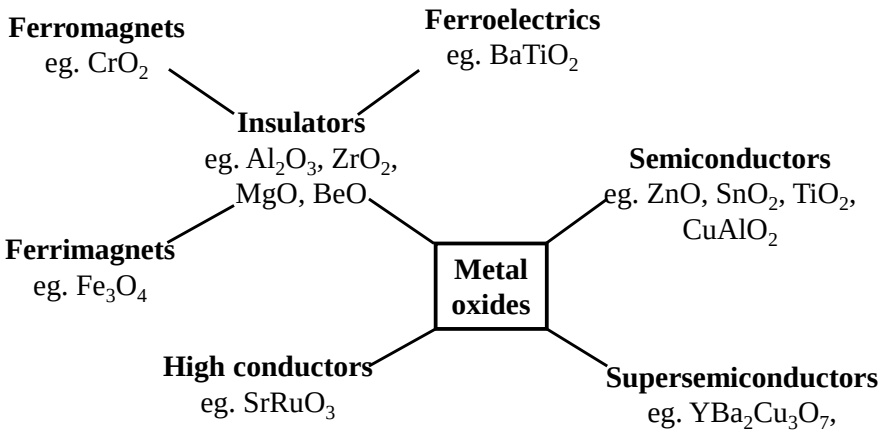

Flowchart 1.1. Classifications of metal oxides **[21]**

The electronic properties of these materials mainly depend on the nature of cation–oxygen bonding, which is explained either by solid-state band theory or by ionic bonding concepts from solid-state chemistry or by combining aspects of both approaches **[67]**. For example, a closed-shell compound such as Al_2O_3 is an insulator displaying large band gaps. In many cases, these insulators can serve as effective host materials for efficient luminescence when doped with rare earth or transition metal cations.

Moreover, metal oxides containing transition metal cations can yield high conductivity materials, such as $SrRuO_3$ **[68]** or even superconductors, as with $YBa_2Cu_3O_7$ **[69]**. Collective phenomenon involving electric dipole interactions in insulators yields ferroelectrics such as $BaTiO_3$ **[70]**. Unpaired electron spin in some oxides results in ferromagnetism, as in CrO_2 **[71]** or ferrimagnetism, as in Fe_3O_4 **[72]**. In addition, many oxides display interesting metal–insulator transitions that are dependent on temperature

(eg, V_2O_3), pressure (eg, NiO), or magnetic fields (eg, (La,Sr)MnO_3) **[73]**. Among these oxides, materials scientists are overwhelmingly interested in the fundamental aspects and applications of semiconducting wide band-gap oxide materials such as titanium dioxide (TiO_2).

2-1.12. Modification of TiO_2 to be active under visible light

Today it is well known that titanium dioxide is an n-type semiconductor that has a band gap of 3.2 eV for anatase, 3.0 eV for rutile, and ~3.2 eV for brookite **[74]**. This obviously illustrate that all polymorphs of titanium dioxide have wide band gap that cannot respond to visible light. Fortunately, in addition to the metal oxide semiconductor properties of TiO_2, whose primary function is to absorb light energy, several other components can be added to modify the TiO_2 semiconductor system based on their application and improve overall efficiency. However, a major drawback of TiO_2 is the large band gap. Titanium dioxide can only be activated upon irradiation with a photon of light <400 nm, limiting its use under solar irradiation **[8, 10]**. Therefore, in order to utilize TiO_2 to its full potential it is necessary to decrease the band gap size to facilitating visible light absorption. Therefore many researchers are concentrating on how to improve the material available in order to harvest this vast amount of light by shift the threshold of the photo-response of TiO_2 into the visible region through doping TiO_2 with a foreign substance **[11]**.

All the efforts to improve the activity of TiO_2 can be categorized into three approaches. First, many researchers attempted to improve the quantum yield. It was found that, among other factors, the crystal structure **[75]**, the presence of hydroxyl groups on the surface **[76]**, and the presence of oxygen deficiencies affect the photocatalytic activity

[78]. Second, attempts have been made to enhance the photocatalytic activity by extending light absorption from the UV region into the visible region: a considerable increase in the photocatalytic activity in the visible region has been observed in nitrogen-doped titanium oxide (TiO_xN_y) **[79]**. The photo absorption of TiO_2 can be extended to the visible region by doping with nitrogen, carbon, and a few other elements **[80]**. However, the doped materials suffer from lower absorbance than undoped TiO_2 and fast e^-/h^+ recombination rates, which ultimately limits their photochemical activity.

Third, successful attempts have been made to suppress the recombination of electron-hole pairs in TiO_2. There the deposited particles act as electron traps aiding electron-hole separation **[16]**. A question that arises is why not using a thicker TiO_2 film to observe a much higher photocatalytic activity? It has been reported that the absorption coefficient and refractive index are 90 cm^{-1} and 2.19 at a wavelength of 380 nm, respectively **[81]**. The values indicate that thick TiO_2 is opaque like a mirror. Thus an appropriate thickness for the TiO_2 layer in order to have an overall high transmission is estimated to be less than 100 nm. In other words, it is impossible to enhance photoresponsive activity with thick TiO_2.

This thesis forms part of a fourth approach, namely; synthesising a plasmonic visible-light responsive thin film. Yes the doping of TiO_2 with other substances is a very promising method to achieve visible light response TiO_2. Noble metals deposited or doped on TiO_2 (Pt, Au, Pd, Rh, Ni, Cu, Sn and Ag) show various effects on the photocatalytic activity of TiO_2 by different mechanisms **[82, 83]**. Recently, Christopher *et al.,* 2010 **[84]** report that composite materials composed of optically active Ag

nanostructures and TiO_2 photocatalysts show enhanced photoactivity compared to the pure TiO_2 in the decomposition of methylene blue. Wu and his colleague, 2010; prepared montmorillonite (MMT)-supported Ag/TiO_2 composite (Ag/TiO_2/MMT) through a one-step, low temperature solvothermal technique. This Ag/TiO_2/MMT composite exhibits high photocatalytic activity and good recycling performance in the degradation of *E. coli* under visible light. The high visible-light photocatalytic activity of the Ag/TiO_2/MMT composite is ascribed to the increase in surface active centers and the localized surface plasmon effect of the Ag nanoparticles. Therefore, the Ag/TiO_2 composite materials with excellent stability, recyclability, and bactericidal activities are promising photocatalysts for application in decontamination.

Moreover, the electrical conductivity of titania is around 10^{12} ohm cm at 25 ºC and the electrical conductivity of silver is around 10^{-6} ohm cm. Doping Ag into the TiO_2 matrix to fabricate a Ag/TiO_2 composite thin film does enhance the composite`s electrical conductivity **[85]**. In fact, it is well reported that the reduction in electrical resistivity of TiO_2 causes an increase in photo-response activity and decreased the recombining probability of the photogenerated electrons and holes in titania **[86, 87]**. Therefore, the fabrication of Ag/TiO_2 composite structure is necessary for the improvement the functional structure of TiO_2. However, competing factors which can negatively affect photoresponsive activity include; (1) reduced access of TiO_2 to light, given high Ag surface coverage, (2) Ag blockage of active TiO_2 sites, (3) poor Ag dispersion, (4) increased recombination rates when doped to higher than optimal levels, and (5) inhibition of the role of O_2 due to scavenging of electrons by Ag deposits need a further investigations **[88, 89]**.

1-1.13 Techniques for synthesis Ag/TiO_2 nanostructures

Fabrication of Ag/TiO_2 composite thin films is performed using various techniques, each of which offers a unique set of advantages and disadvantages; currently, it remains unclear which of these will eventually prove to be the most effective. Physical techniques such as thermal evaporation and sputtering involve atom by atom, molecule by molecule growth, or ion deposition on various materials in a vacuum system **[21]**. $Ag\text{-}TiO_2$ films from sputtering or vapor deposition are expensive and require sophisticated equipment. In fact, the major problems for the physical techniques are often a wide size distribution, lack of particle crystallinity, and the cost and scalability of the production.

The reported chemical processes for the preparation of nanostructured Ag/TiO_2 electrodes include the sol-gel technique **[90, 91]** and molecular precursor method **[92]**. Certainly one of the most technologically important aspects of sol-gel and MPM processing is that their fluid solution is ideal for preparing thin films by such common processes as dipping, spinning, spraying, screen printing, etc **[8, 93]**. More than 80% of the most important commercial products are optical coatings such as antireflection coatings, Schott-type coatings for architectural glass, hydrophilic and hydrophobic coatings, antiscratch and hybrid hard coating for plastics, UV shielding coatings, coatings for heads-up display, colored Ormosil coatings for containers, etc. **[94]**. Compared to traditional coatings or film forming processes such as thermal spray, CVD and PVD, the sol-gel and MPM films formation require considerably less equipment, is potentially less expensive and has the ability to allow a precise control of the microstructure of the deposited film.

The above paragraph is by no means a complete listing of the available synthetic methods, but rather a broad sampling of what has been reported. Unfortunately, all of the methods listed have some inherent problems, and while each method has certain advantages and disadvantages, the selection of a proper synthetic procedure depends on the nature of the nanoparticle application. For instead, metal ion-implantation with V, Cr, Mn, Fe, and Ni was possible to shift the absorption band toward visible light regions. However, Ag, Mg, or Ti ion - implanted TiO_2 showed no shift **[21, 95]**. Figure 1.13 shows another example how the band gap of TiO_2 can be shifted into visible light region, depending on the techniques employed, which would enhance its potential for chemical solar energy conversion and open possibilities for further applications.

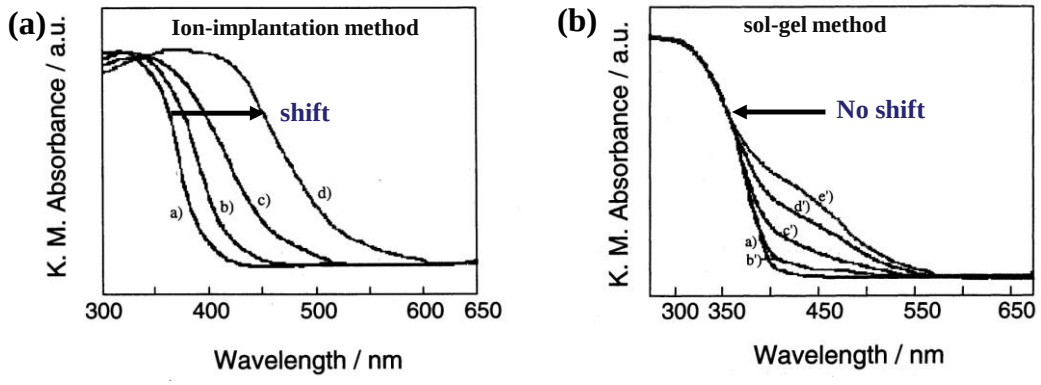

Fig.1.13 The UV-Vis absorption spectra of Cr-ion doped TiO_2 fabricated by ion-implantation method **(a)** and sol-gel method **(b).** These absorption spectra shift smoothly towards visible light regions, the extent strongly depending on the amount of ions implanted and the method and the method used **[96]**.

With the chemical technique, the major problem is often a limited flexibility in the size of particles that can be produced and such methods are usually sold on their ability to make <10 nm particles. Certainly, small particles are desirable in catalysis, where the

main emphasis is on surface-to-volume ratio, but for optical applications, larger particles are often necessary. Small Ag nanoparticles do not interact with light nearly as efficiently as particles that are in the 50–100 nm range and do so strictly through energy absorption **[97]**. On the other hand, the plasmon resonances in larger Ag nanoparticles have a significant light-scattering component that can be advantageously used in applications that require efficient optical labels, such as in chemical assays **[84]**.

Akpan and Hameed **[98]**, give a critical review on the advancements in sol–gel method of doping TiO_2 photocatalysts. Various sol–gel and related systems of doping were considered, ranging from co-doping, transition metal ions doping, rare earth metal ions doping to other metals and non-metals ions doping of TiO_2. The results available showed that doping TiO_2 with transition metal ions usually resulted in a hampered efficiency of the TiO_2 photocatalyst, though in some few cases, enhancements of the photocatalytic activity of TiO_2 were recorded by doping it with some transition metal ions. In most cases, co-doping of TiO_2 increases the efficiency of its photocatalytic activity. The review reveals that there are some elemental ions that cannot be used to dope TiO_2 because of their negative effects on the photocatalytic activity of the catalyst, while others must be used with caution as their doping will create minimal or no impacts on the TiO_2 photocatalytic efficiency.

My work is therefore, focused on the synthesis of Ag nanoparticles and their incorporation into matrices of TiO_2. Since TiO_2 is environmental friendly, Ag coated TiO_2 (Ag-TiO_2) has been widely studied **[84, 86−89, 99−102]**. It is well-known that the incorporation of noble metal nanoparticles into various matrices will extend their utility in material and device applications. Such nanocomposites could exhibit novel optical properties as the plasmon resonances are strongly affected by the surrounding matrix as

well as because closely spaced particles in matrices can exhibit cooperative phenomena when interacting with light.

The choice of synthesis technique can be a key factor in determining the effectiveness of the photoresponse as studies have shown that TiO_2 production and physical form are among the most important factors in determining the overall photocatalytic efficiency **[83]**. The optimum synthetic method should address all of the above problems and additionally yield particles with no extraneous chemicals that can potentially alter the particle's optical properties and surface chemistry. According to a recent review by Minami, 2013 **[103]** and Nagai and Sato, 2012 **[8]**, a synthetic method seem to fulfills all of the above requirements seem to be sol-gel and MPM, respectively.

1−2 SOL-GEL METHOD

Sol–gel processing of TiO_2 thin films has been studied in detail over the past 20 years. A common method used to make dense, nanocrystalline TiO_2 thin films is through mixing a titanium alkoxide precursor with a solvent followed by addition of a small amount of catalyst (typically in water). Sol-gel comprises of many chemical methods, starting from a liquid solution of molecular precursors, among which the most widely adopted is certainly the alkoxides method **[93]**. Given the relatively high hydrolysis reactivity of titanium alkoxides, a chelating agent is typically added prior to the catalyst. The coating is then deposited on a substrate either through dip- or spin-coating. The coated substrate is then cured for varying lengths of time at temperatures between 400 and 600ºC. Flowcharts of Equation 1.6-1.7 show the typical method of synthesis metal oxide using sol-gel method. Alkoxides are molecules with general formula $M(OR)_n$, where R represents an alkyl or aryl group and M the metal whose oxide will form the final

matrix inorganic structure. Typically a starting alcoholic solution of the alkoxide is prepared, using the alkoxide corresponding alcohol as solvent. In other words, if R is an ethyl or a methyl group ethanol or methanol will be used, respectively. This is the so called solution stage, and is followed by the gelation stage, which is initiated by the addition of a certain amount of water. At this stage the precursors undergo hydrolysis and condensation reactions according to the general equestion 1.6 and 1.7 respectively **[93, 104]**:

1. Hydrolysis: $M(OR)_n + H_2O \rightarrow M(OR)_{n-1}(OH) + ROH$……(1.6)

2. Condensation: $M(OR)_n + M(OR)_{n-1}(OH) \rightarrow (RO)_{n-1}M\text{-}O\text{-}M(OR)_{n-1} + ROH$

$M(OR)_{n-1}(OH) + M(OR)_{n-1}(OH) \rightarrow (RO)_{n-1}M\text{-}O\text{-}M(OR)_{n-1} + H_2O$…….(1.7)

The interest in this synthesis method arises due to the possibility of synthesizing nonmetallic inorganic materials like glasses, glass ceramics or ceramic materials at very low temperatures compared to the high temperature process required by melting glass or firing ceramics. The heat-treatment of thin films in this method is generally important for the formation of crystallized metal oxides **[8]**. However sol-gel process is slow and complicated due to additional reactants include water as the hydrolysis agent, alcohols as the solvent, and an acid or base as a catalyst. The major difficulties to overcome in developing a successful bottom-up approach is controlling the growth of the particles and then stopping the newly formed particles from agglomerating **[104]**. Therefore one of the aims of my research is to avoid agglomeration which is associated with sol-gel method.

Despite these draw backs, various works incorporated Ag in TiO_2 films via sol-gel

process **[102]**. Using sol–gel chemistry, Ag can be introduced into both the bulk and surface of the TiO_2 film through addition of a silver salt into the initial coating solution. It is worth noting Ag has been suggested to promote the anatase to rutile transformation, while suppressing anatase grain growth. It is well known that photocatalytic and antibacterial properties of Ag-TiO_2 thin films depend upon crystal phase **[88, 105]**, lattice defects, surface area **[106, 107]**, particle size of Ag **[108]** as well as chemical state of Ag and its distribution within the TiO_2 matrix. Therefore, controlling of these performance-related material properties and establishment of a better synthetic method that allowing the modification of these parameters is essential.

Moreover, the sol-gel techniques are most effective and popular on preparation of metal−oxide nanocomposites **[109−111]**. However it is well reported that incorporating more amount nanoparticles was limited by the sol-gel dip-coating method due to nanoparticles coalesce with each other into huge particles during sintering **[85]**. Hence, Tseng *et al.*, **[111]** started this research, gave a commendations for the preparation of effective stable photocatalyst based on titania films and modified with small amount of noble metal nanoparticles (NPs). Therefore, a new method must be proposed.

1−3 MOLECULAR PRECURSOR METHOD (MPM)

In this thesis, I proposed the molecular precursor method which is one of the wet processes for thin film formation of crystallized metal oxides heat-treatment thin films **[8, 92]**. The method is based on the formation of excellent precursor films involving anionic metal complexes and alkylammonium cation. Like sol-gel method, MPM also requires heat-treatment to eliminate organic ligands from metal complexes involved in spin-coated precursor films and to fabricate thin films of crystallized metal oxides or

phosphates **[112, 113]**. Higher larger surface area along with crystallinity and decreased impurities are some of the main factors influence the enhancement of photoreactivity of TiO_2 **[8]**.

Moreover, the crystallite size is an indicator of crystallinity **[114, 115]**. Nagai and his group **[116]**, compared the crystallite sizes of the TiO_2 thin films fabricated by MPM and those fabricated my sol-gel method. The crystallite size of the oxide particles in the resultant thin films fabricated by the MPM is generally smaller than those prepared by the conventional sol–gel method. From this point of view, MPM opens up a completely new perspective for materials design that benefits from the introduction of the synthesis of smaller crystallite size.

Titania usually exists in three different polymorphs; anatase (tetragonal, a=b=3.78Å; c=9.50Å), rutile (tetragonal,a=b=4.58Å; c=2.95Å) and brookite (rhombohedral, a=5.43Å; b=9.16Å; c=5.13Å). Among these phases of titania, anatase shows a better photocatalytic activity and antibacterial performance **[117, 118]**. The production of high photoactivity material with high temperature anatase phase stability is one of the key challenges in smart coating technology. The temperature difference between the phase transformation from anatase to rutile in the sol–gel method and the MPM is reported by Nagai *et al.,* **[8, 116]**. Using both MPM and conventional sol-gel method, the anatase phase appears during the heat-treatment of both precursor films at a temperature between 400 and 500°C. By using MPM, anatase can be transformed to the rutile one between 500 and 700°C while a conventional sol–gel process showed that anatase could not transformed to the rutile one, even when heat-treated at 900°C **[119−121]**. In the absence of a dopant or precursor modification, anatase to rutile transformation in synthetic TiO_2

usually occurs at a temperature of 600 ºC to 700 ºC. Any improvement in the anatase phase transformation at lowest temperatures observed in MPM is expected to reduce the cost of the thin film and to show a higher photocatalytic activity. On the basis of these, compared to a sol–gel solution, the molecular precursor solution for titania thin film fabrication is extremely has practical advantages.

1−4 OVERVIEW OF THE THESIS

There is significant research being carried out on titanium dioxide semiconductors because of the wide amount of applications associated with the materials. In 1972 Fujishima and Honda published an article in Nature **[122]** that drove titanium dioxide (TiO_2) into the world of research. They demonstrated that TiO_2 as semiconductor has the capability to splitting water in a photoelectrochemical cell. Their work initiate a revolution in the world of semiconductor research with Frank and Bard (1977) going on to demonstrate titanium dioxide's unique properties for environmental remediation through the reduction of CN^- in water **[123]**, and Ollis *et al.,* (1989) using TiO_2 for the pulification of pollutant water **[124]**. In the 1990's, after O'Regan and Gratzel's paper on the dye sensitised solar cell **[125]**, TiO_2 became one of the most internationally researched semiconductor materials. The increase in TiO_2 publications per year demonstrates the growth in the area. In 1995 there were 700 TiO_2 publications, 2002 later that number increased to over 2000 publications **[126]**.

So why does TiO_2 attract such interest? There are many reasons why and they are addressed throughout the literature review (Chapter 2) of this thesis but for the purpose of this body of work the important question is why has it attracted my interest? As shown in the introduction above, several techniques have been employed to synthesize

TiO_2 nanomaterials. The MPM as mentioned in section 1−3 seem to be the most suitable chemical process for the synthesis of semiconductor nanomaterials using chemical process. The crystallite size of the oxide particles in the resultant thin films fabricated by the MPM is generally smaller than those prepared by the conventional sol–gel method, thus it attracted my interest.

In this thesis, the MPM will be used to fabricating silver nanoparticles/titania composite thin films. The synthesis and studies of Ag/TiO_2 heterostructures are intensively reported in large quantities, however, there are few reports about Ag/TiO_2 thin films with high Ag content >20 mol% prepared by chemical methods such as sol-gel so far in the literatures. It is well reported that incorporating more amount Ag particles was limited by the sol-gel dip-coating method up to 18 mol% due to Ag particles coalesce with each other into huge particles during sintering **[85]**. Compared to a conventional sol–gel solution, the stability of the molecular precursor solution for Ti complex of EDTA and a SrO precursor solution containing a Sr complex of EDTA is extremely high, and therefore, the molecular precursor method has practical advantages **[127]**. Simple as this process appears the ability of incorporate unprecedented high amounts of Ag, greater than or equal to 20 mol % into TiO_2 system using MPM is investigated throughout this thesis. This PhD thesis pass through the synthesis of silver nanoparticles-titania ($Ag\text{-}NP/TiO_2$) composite thin films, with the final aim of finding the percolation threshold for the electrical conductivity and studying their visible-light-driven plasmonic properties. Crystal structural, surface morphology and nanostructures of the fabricated thin films will be performed using XRD, XPS, FE-SEM and TEM, respectively. The XRD and XPS measurements will be used to reveal whether silver particles obtained are in metallic or oxidize form. Homogeneous

distribution and growth of Ag-NP in the composite thin films will be clarified by the FE-SEM and TEM observations. The absorption spectra of Ag-NP/TiO_2 composite thin films will be analyzed by using Kubelk-Munk equation for diffuse reflectance spectra (DRS), in order to study the plasmonic effect of Ag NP in dielectric TiO_2 matrix.

1−5 AIMS AND OBJECTIVES

The main focus of my research will mainly base therefore on two topics; one being reduce TiO_2 film`s relatively high electrical resistivity by incorporating Ag NP, which is currently stand at 10^{12} Ω cm^2 for pure TiO_2 thin film and at 10^3 Ω cm^2 for Ag/TiO_2 composite thin film prepared by sol-gel method.

Because of TiO_2`s high band gap of 3.2 eV (anatase), only UV light source has been found to be effective in the excitation of the electrons in TiO_2. My second area of interest regarding TiO_2 involves shifting the threshold of TiO_2's photo response to Vis-region. In Ag/TiO_2 systems, Ag increases the photo responsive activity through two separate mechanisms; serving as an e- trap, hence aiding in (e^-/h^+) separation and enhancing e^- excitation through creation of a local electric field. In addition, Ag doping results in visible light response, presumably due to the surface plasmon resonance of the Ag particles and not through TiO_2 band gap shifting.

With the main emphasis on lower electrical resistivity and plasmonic properties associated with Ag-NP/TiO_2 composite thin films, shifting the threshold of TiO_2's photo response to Vis-region will be finally investigated by study the photoelectrochemical (photocurrent), and photocatalytic properties of the fabricated composite thin films. The optical study such as photocurrent and photocatalytic may open up a variety of optical

and photonic applications such as photovoltaic for the fabrication of new electrochemical-TiO_2 based solar cells and further investigation of other possible applications such as; antibacterial, hydrogen production, biosensors, optical filters, plasmonic waveguides, and substrates for surface-enhanced Raman spectroscopy.

1−6 REFERENCES

1. Alleman J, Robbins S. (2009). *National Renewable Energy laboratory* (NREL). http://www.nrel.gov/.

2. Grätzel M. (2009). *Acc. Chem. Res.*, **42:11**, 1788–1798.

3. Smith B. (2013). Stephen Hawking Touches On God And Dark Matter At Caltech Speech. *Pasadena, California.* 2013−04−18 11:09:45.

4. Goslich R., Dillert R., Bahnemann D. (1997). *Wat. Sci. and Techno.* **35:4**, 137−148.

5. Peippo K. (1992), *NEMO-raportti* **23**, 1342−7.

6. Ermolli I., Matthes K., Dudok de Wit T., Krivova NA., Tourpali K., Weber M., Unruh YC., Gray L., Langematz U., Pilewskie P., Rozanov E., Schmutz W., Shapiro A., Solanki SK., Woods TN. (2013). *Atmos. Chem. Phys.*, **13**, 3945–3977.

7. Wang Y, Liu L., Xu L., Meng C., Zhu W. (2013). *J. Appl. Phys.* **113**, 174311.

8. Nagai H., Sato M. (2012). *InTech*, Chapter **5**, 103−128.

9. Herrmann J-M., (2012). *Environ. Sci. and Pol. Res.Int.* 19:**9**, 3655–3665.

10. Nwanya A., Ezema F., Ejikeme P. (2011). *Int. J. Phys. Sci* 6:**22**, 5190−5201.

11. Kumar S., Devi L., (2011). *J Phys Chem.* A, 115:**46**, 13211–13241.

12. Mills A., Hunte L. (1997). *J. Photochem. Photobiol. A*, **108**, 1−35.

13. Shriver DF., Atkins PW. (1999). *Oxford University Press*: Oxford.

14. Hoffmann MR., Martin ST., Choi W., Bahnemann DW. (1995). *Chem. Rev.* **95** 69−76.

15. Hosono H., Facchetti A., Marks T. (2010). *Transp. Electron*., 31–59.

16. Bloh J., Dillert R., Bahnemann D. (2012). *Environ. Sci. and pollu. Res. Inter*., 19:**9**, 3688–3695.

17. Baratto C., Comini E., Faglia G., Ferroni M., Ponzoni A., Vomiero A., Sberveglieri G. (2010). *Tran. Electro.: From Synthesis to Applications*, 417–442.

18. Kupreev OV., Lazarouk SK, Borisenko VE, Kun L., Kang TB. (2013). *J. Appl. Spectro*, 79, 6−12.

19. Kočí K., Obalová L., Lacný Z. (2008). *Chem. Papers*, **62**, 1–9.

20. Korsunovskii GA. (1978). *Russ J Phys Chem* **52**, 2276–2279

21. Banerjee AN. (2011). *Nano, Sci. and Appl.* 2011:**4**. DOI: 10.2147/NSA.S9040

22. Litter MI. (1999). *Appl. Cat. B: Environ.* **23**, 89–114.

23. Georgieva J. (2011). *J. Sol. Stat. Electrochem*., **16**, 1504−7.

24. Sharma P., Kumar P., Solanki, A., Shrivastav R., Dass S., Satsangi VR. (2011). *J. Soli State Electrochem*., **16**. doi:10.1007/s10008-011-1552-z

25. Ahmed R., Will G., Bell J., Wang H. (2012). *J. Nanopart. Res*., **14**. doi:10.1007/s11051-012-1140-x

26. Wang, B., Kerr, LL. (2011). *J. Solid State Electrochem*, **16**, 1496-3.

27. Chen H., Hu Y., Zeng X. (2010). *J. Mater. Sci.*, 46:**8**, 2715–2719.

28. Bhawana P., Fulekar MH (2012). *Res.J.Chem.Sci.* 2:**2**, 90-96.

29. Wong E. (1999), quoted by R.S. Boyd, Knight Rider Newspaper, Kansas City Star, Monday, November 8, 1999.

30. Smallay R., (1999). *Congressional Hearings*, Summer, 1999.

31. Anandhan S., Bandyopadhyay S. (2011). John Cuppoletti (Ed.), *InTech.* ISBN: 978-953-307-352-1.

32. Burda C., Chen X, Narayanan R., El-Sayed M.A. (2005). *Chem. Rev.*, 105:**4**, 1025–

1102.

33. Luther W. (2004). *Fut. Techno*., **54**,1436−5928.

34. Mulvaney P. (2001). *MRS Bulletin.* 26:**12**, 1009−1014.

35. Mie G. (1908). *Transl. into English from Ann. Phys.* (Leipzig), **25**, 377−445.

36. Debye P. (1909) .*Ann, Phys.,* **30**, 57−136.

37. Jacob JA., Biswas N., Kapoor S., Mukherjee T. (2007). *Collo. and surf. A: Physicochem. Eng. Aspects.* **301**, 329−334.

38. Efros AlL, Efros AL. (1982). *Sov Phys Semicond.,* **16**:772–775.

39. Brus LE. (1984). *J Chem Phys.,* 80, 4403–4409.

40. Cox AJ., Louderback JG., Bloomfield LA. (1993). *Phys Rev Lett.,*71:**6**, 923–926.

41. Alivisatos AP. (1996). *Science.,* 271:**5251**, 933–937).

42. Alagarasi A. (2011). *Introduction to Nanomaterials*. Unpublished. http://www.nccr.iitm.ac.in/2011.pdf.

43. Starke L. (2006). *Worldwatch Institute*, 4-34. ISBN-10:1-84407-275-4.

44. Lin B. (2012). *Patent Family Members* **1**, CN: 202209007 U.

45. Smith and Nephew Together at last (2004). *Smith and Nephew Pty. Ltd*. Product information; 2004.

46. Moriarty P., (2001). *Rep. Prog. Phys.*, **64**, 297−381.

47. Zhang Z., Wei, Z., Wan MX. (2002). *Macromol.*, **35**, 5937−5942.

48. Gao J., Bender CM., Murphy CJ. (2003). *Langmuir*, **19**, 9065−9070.

49. Schmid G., Bäumle M., Geerkens M., Heim I., Osemann C., Sawitowski T. (1999). *Chem. Soc. Rev.* 28:**3**, 179−185.

50. Eigler DM., Schweizer EK. (1990). *Nature* **344**, 524–526.

51. Heinrich AJ., Lutz CP., Gupta JA., Eigler DM. (2002). *Mol. Casc. Sci*. **298**, 1381-1387.

52. Kiely CJ., Fink J., Brust M., Bethell D., Schiffrin DJ. (1998). *Nature* **396**, 444−453.

53. Brust M., Walker M., Bethell D., Schiffrin DJ., Whyman R. (1994). *J. Chem. Soc. Chem. Commun.* 801−812.

54. Rosei F. (2004). *J. Phys.: Condens. Matter* **16**, S1373–S1436.

55. Cao G. (2004). *Imperial College,* London, 78-79.

56. Farcau C., Giloan M., Vinteler E., Astilean S. (2012). *Appl. Physc.* B,106.

57. Zhu J., Ren Y. (2012). *J. Nanopart. Res.,* **14**. doi:10.1007/s11051-012-1326-2

58. Felicia AM., Shauna G-C., Andy Y., Hai T., James WM. (2013). *J Nanopart Res* **15**:1442−1447.

59. Sepúlveda B., Angelomé PC., Lechuga LM., Liz-Marzán LM. (2009). *Nano Today*, **4**, 2009.

60. Awazu K., Fujimaki M., Rockstuhl C., Tominaga J., Murakami H., Ohki Y., Yoshida N., Watanabe T. (2008). *J. Amer. Chem. Soc.,*130:**5**,1676–80.

61. Haes, AJ., Van Duyne RP. (2002). *J. Amer. Chem. Soc.,* 124:**35**, 10596−10604.

62. Lu XM., Rycenga M., Skrabalak SE., Wiley B., Xia YN. (2009). *Rev. Phys. Chem*. **60**, 167−192.

63. Sung J., Hicks ME., Van Duyne RP., Spears GK. (2007). *J. Phys. Chem. C*, 111:**28**, 10368−10376.

64. Kawawaki T., Takahashi Y., and Tatsuma T. (2013). *J. Phys. Chem. C*, **117**, 5901−5907.

65. Shaffer GD. (1993). *J. Field Archaeology*, 20:**1**, 59−75.

66. Kholoud MM., El-Noura A., Eftaihab A., Al-Warthanb A., Reda AA., Ammarb R. AA. (2010). *Arabian J. Chem.* **3**, 135–140.

67. Fukuyama H, Nagaosa N, (1999). *Physics and Chemistry of Transition Metal Oxides.* Berlin, Germany: Springer; 1999.

68. Han JH., Lee W., Jeon W., Lee SW., Hwang SC. (2012). *Chem. Mater.* **24**, 4686−4692.

69. Araki T., Izumi Hirabayashi (2003). *Supercond. Sci. Technol.* 16:**11**, R71.

70. Zhang Q., Cagin T., Goddard AW. (2006). *Curr. Iss.* 103:**40**, 14695-14700.

71. Coey JMD. (2002). *J. of Appl. Phys.*, 91:**10**, 123−134.

72. Rajkumar N., Umamahaeswari D., Ramachandran K. (2010). *Int. J. Nanosci.* **9**, 243−257.

73. Noguera C. (1996). Cambridge, UK: *Cambridge University Press*; 1996.

74. Cui Y., Du H., Wen TL. (2008). *J. Mater. Sci. Technol.*, 24:5, 134−234.

75. Diebold U. (2003). *Sur. Sci. Rep.* **48**, 53−229.

76. Lee J., Mubeen S., Ji X., Stucky G., Moskovits M.(2012). *Nano let.*, 12:**9**, 5014–5019.

78. Nagai H., Aoyama S., Hara H., Mochizuki C., Takano I., Honda T., Sato M. (2010). *J. Mater. Sci.*, 45:**20**, 5704–5710.

79. Xiong B., Li J-L., Yang B., Yu Y.(2012). *J. Nanomater.*, **2012**, 1–13.

80. Chibber S., Ansari S.A., Satar R. (2013). *Nanopart Res.*, **15**,1492.

81. Tang H., Prasad K., Sanjines R., Schmid PE., Levy F. (1994). *J. Appl. Phys*., **75**, 2042−2047.

82. Sobana N., Muruganadham M., Swaminathan M. (2006). *J. Mol. Catal. A: Chem*, 258:**1-2**,124−132.

83. Loganathan K., Bommusamy P., Muthaiahpillai P., Velayutham M. (2011). *Environ. Eng. Res.*, 16:**2**, 81−90.

84. Christopher P., Xin H., Linic S. (2011). *Nat Chem* **3**,1–6.

85. Li H., Zhao G., Song B., Han G. (2008). *J. Cluster Science*, 667-673.

86. Velmurugan R., Sreedhar B. Swaminathan M. (2011). *Chem. Centr. J.*, 5:**46**, 232−241.

87. Wang D., Shi L., Luo Q., Li X., An J. (2012). *J Mater Sci* **47**, 2136–2145.

88. Akgun BA., Wren AW, Durucan C, Towler MR, Mellott NP. (2011). *J Sol-Gel Sci Technol*. **59**:228–238

89. Akgun BA., Durucan, C. Mellott NP. (2011). *J. Sol-Gel Sci. and Techno.*, **58**, 2011.

90. Zhao G., Kozuka H., Yoko T. (1996). *Thin Solid Films*, 277:**1-2**, 147−154.

91. Nasr-Esfahani M., Habibi M. H. (2008). *Int. J. Photoener.*, **2008**, 1–11.

92. Sato M., Hara H., Nishide T., Sawada Y. (1996). *J. Mater. Chem.*, **6**, 1767−1770.

93. Brinker CJ., Scherer GW. (1990). *Academic Press*, New York, (1990).

94. Uhlmann DR. (1998). *J. Sol-Gel Sci. Technol.* **13**, 153-162.

95. Anpo M. (2000). *Synthesis*, 72: **9**. 1787–1792.

96. Anpo M. (2004). *Bull. Chem. Soc. Jpn.*, **77**, 1427–1442.

97. Kaneko M., Okura I. (2002). *Sci. and Techno*., Springer, Tokyo, 33.

98. Akpan UG., Hameed BH. (2010). *Appl. Catal. A: Gen.* **375**, 1–11.

99. Wu T-S., Wang K-X, Li G-D, Sun S-Y, Sun J., Chen J-S. (2010). *Mater. Appl. Mater. and Interface*, 2:**2**, 544–550.

100. Zhang F-J., Oh W-C (2010). *Bull. Korean Chem. Soc.*, 31:**7**, 1981−1987.

101. Koch M., Kiefer S., Cavelius C., Kraegeloh A. (2012). *J. Nanopar. Res.*, **14**:2.

102. Lin Y-C. (2013). *Clean Techn Environ Policy* **15**:359–366 .

103. Minami T. (2013). *J Sol-Gel Sci Technol*, **65**:4–11.

104. Buso D., (2008). *Universita degli Studi di Padova, Italy. PhD dissertation*,

123-125

105. Tanaka K., Capule MFV., Hisanaga T. (1991).*Chem, Phys. Lett.* 1**87**, 73-76.

106. Xagas AP., Androulaki E., Hiskia A., Falaras P. (1999). *Thin Solid Films* **357**:173−178.

107. Heintz O., Robert D., Weber JV. (2000). *J Photoch Photobio A*, **135**:77–80

108. Anpo M., Takeuchi M. (2003). *J Catal* **216**, 505–516.

109. Kedziora A., Strek W., Kepinski L., Bugla-Ploskonska G., Doroszkiewicz W. (2012). *J. Sol-Gel Sci. and Techno*., **62**, 132-145

110. Huanga C-H., Chang C-C., Tsaia J-H. (2013). *Semicond.*, 47:**6**, 835–837..

111. Tseng TK., Lin YS., Chen YJ., Chu H. (2010). *Int. J. Mol. Sci.* **11**, 2336−2361.

112. Mochizuki C, Sasaki Y, Hara H, Sato M, Hayakawa T, Yang F, Hu X, Shen H, Wang S (2009). *J. Biomed. Mater. Res. Part B* **90**: 290−301.

113. Sato M, Hara H, Kuritani M, Nishide T (1997). *Sol. Energy Mater. Sol. Cells* **45**: 43−49.

114. Yu JC, Yu J, Zhang L, Ho W (2002). *J. Photochem. Photobiol. A* **148**: 263−271.

115. Kominami H, Kato J, Murakami S, Kera Y, Inoue M, Inui T, Ohtani B (1999). *J. Mol. Catal. A. Chem.* **144**: 165−171.

116. Nagai H., C. Mochizuki, H. Hara, I. Takano, M. Sato (2008). S*ol. Ener. Mater. Sol. Cells*, 92:**9**, 1136–1144.

117. Sofianou M-V., Trapalis C., Psycharis V., Boukos N., Vaimakis T., Yu J., Wang W. (2012). *Environ Sci. and Pol. Res. Int.*, 19:**9**, 3719–3726.

118. Damodar RA., You S-J., Chou H-H. (2009). *J. Hazard. Mater.* **172**, 1321–1328.

119. Czanderna AW., Rao CNR., Honig JM. (1958). *Trans. Faraday Soc.*, **54**, 1069.

120. Yoganarasimhan SR., Rao CNR. (1962). *Trans. Faraday Soc.* **58**, 1579.

121. Kumar, SR., Pillai SC., Hareesh US., Mukundan P., Warrier KGK. (2000). *Mater*

Lett 43:**5–6**, 286–290.

122. Fujishima A., Honda K. (1972). *Nature* **238**, 37–38.

123. Frank SN., Bard AJ. (1977). *J Am Chem Soc.,* **99**, 303–304.

124. Ollis DF., Pelizzetti E., Serpone N., (1989). *Wiley/Interscience*, New York, 603–637.

125. O'Regan, B., Gratzel, M. (1991). *Nature* **353**, 737–740.

126. Goetzberger A., C. Hebling (2000). *Sol. Ener. Mater. & Sol. Cel.*, **62**, 1−19.

127. Sato M, Tanji T, Hara H, Nishide T, Sakashita Y (1999). *J. Mater. Chem.* **9**, 1539−1542.

CHAPTER 2 LITERATURE REVIEW

2−1 LITERITURE REVIEW

2-1.1 Historical background of TiO_2

The understanding of the background of TiO_2 will make one appreciate the progress of studying TiO_2 as a promising semiconductor so far in literatures. Titanium is the world's fourth most abundant metal and ninth most abundant element. It was discovered in 1791 in England by Reverend William Gregor, who recognised the presence of a new element in ilmenite **[1]**. It was then rediscovered in rutile ore several years later by a German chemist, Heinrich Klaporth who named it after Titans, mythological first sons of the goddess Ge (earth in Greek mythology) **[2]**. Titanium is not found in its elemental state, it occurs mainly in minerals like rutile, ilmenite, leucoxene, anatase, brookite, perovskite and spene. It is also found in titanates and many iron ores. The metal has been detected in meteorites and stars. In fact, samples brought back from the moon by Apollo 17 contained 12.1 % TiO_2 **[3]**.

Titanium dioxide (TiO_2) was discovered in 1821 but it was not until 1916 that modern technology had progressed to the point where it could be massively produced **[4]**. The primary source and the most stable form of titanium dioxide is rutile ore. It was discovered in Spain by Werner in 1803. Its name is derived from the Latin rutilus, red because of the deep colour observed in some specimens when the transmitted light is viewed **[1]**. Rutile is one of three main polymorphs of titanium dioxide (TiO_2), the other polymorphs being; anatase and brookite **[5]**. Brookite was discovered in 1825 by A. Levy and was named after an English mineralogist, H. J. Brooke **[1]**. In 1801 anatase was named by R. J. Hauy from the Greek word 'anatasis' meaning extension, due to its longer vertical axis compared to that of rutile. Figure 2.1 shows the crystal structures of

three main polymorphs of titanium dioxide.

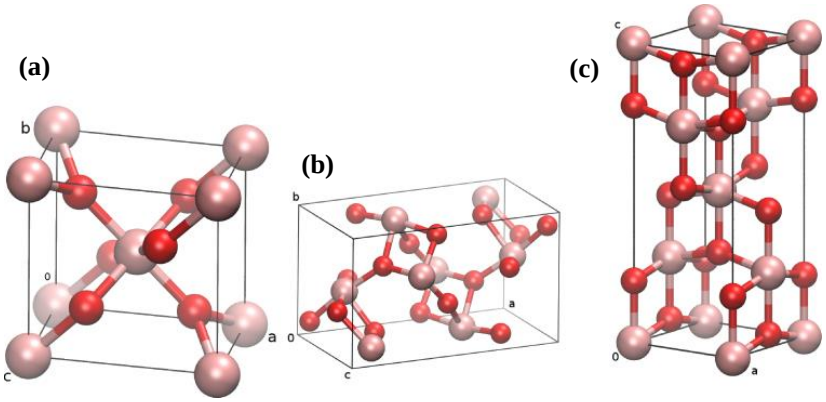

Fig. 2.1. Crystalline structures of titanium dioxide (a) rutile, (b) brookite, (c) anatase **[6]**.

In all three forms, titanium (Ti^{4+}) atoms are co-ordinated to six oxygen (O^{2-}) atoms, forming TiO_6 octahedra **[7, 8]**. All three forms differ only in the arrangement of these octahedra. The anatase structure, is made up of corner (vertice) sharing octahedra (figure 2.1b) resulting in a tetragonal structure. In rutile, the octahedra share edges to give a tetragonal structure (figure 2.1a) and in brookite both edges and corners are shared to give an orthorhombic structure (figure 2.1c).

TiO_2 powders have been commonly used as white pigments from ancient times. They are inexpensive, chemically stable and harmless, and have no absorption in the visible region **[2]**. Therefore, they have a white color. However, the chemical stability of TiO_2 holds only in the dark. Instead, it is active under UV light irradiation, inducing some chemical reactions. Such activity under sunlight was known from the flaking of paints and the degradation of fabrics incorporated with TiO_2 **[9]**. Scientific studies on photoreactive of TiO_2 have been reported since the early part of the 20^{th} century. For

example, there was a report on the photobleaching of dyes by TiO_2 both in vacuo and in oxygen in 1938 **[10]**. It was reported that UV absorption produces active oxygen species on the TiO_2 surface, causing the photobleaching of dyes. It was also known that TiO_2 itself does not change through the photoreaction, although the ‘‘photocatalyst’’ terminology was not used for TiO_2 in the report, but called a photosensitizer **[11]**.

In the late 1960s, one of the present authors **[12]** began to investigate the photoelectrolysis of water, using a single crystal n-type TiO_2 (rutile) semiconductor electrode, because it has a sufficiently positive valence band edge to oxidize water to oxygen. The possibility of solar photoelectrolysis was demonstrated for the first time in 1969 with the system shown in figure 2.2, which was exposed to near-UV light, and was connected to a platinum black counter electrode through an electrical load **[12]**.

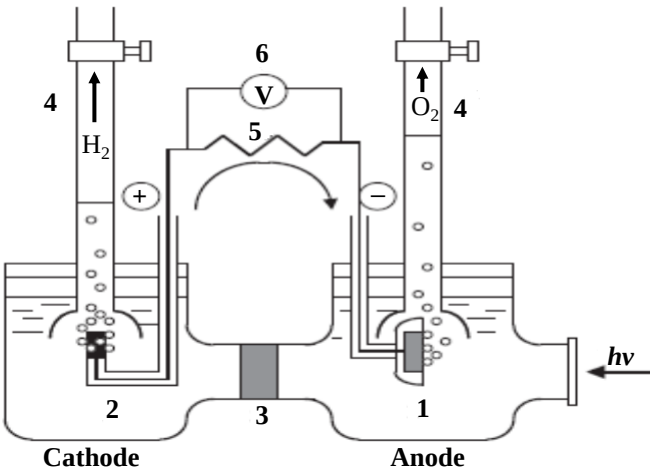

Fig. 2.2 Schematic diagram of electrochemical photocell. (1) n-type TiO_2 electrode; (2) platinum black counter electrode; (3) ionically conducting separator; (4) gas buret; (5) load resistance; and (6) voltmeter **[11]**.

Since the photo splitting of water into H_2 and O_2 using an electrochemical cell illustrated in figure 2.2, a large number of applications using TiO_2 as a semiconductor materials in photocatalytic technology have been investigated for their potential in the conversion of light energy into useful chemical energy **[13, 14]**. The problem of light-assisted water splitting has also been focused in the late 1970s with the photocatalytic approach, i.e., in 1977 when Frank and Bard investigated the reduction of cyanide (CN^-) in water **[15]**. This led into an increasingly well researched area of TiO_2 because of the potential implications for environmental water and air purification utilising solar energy **[16, 17]**. In the 80s, there have been several exciting breakthroughs with respect to titanium dioxide **[18, 19]**.

Based on the basic research results, real industrial applications have been achieved since the end of the 1990s. Nano sized titanium dioxide was employed to excellent use in an efficient solar cell, the dye sensitised solar cell (DSSC) as reported by O'Regan and Graetzel in 1991 **[20]**. In 1995 TiO_2 was used as a coating on ceramic surface by TOTO Company in Japan **[13]** while its application for inactivation of pathogenic micro-organisms in air and water was found in 1996. In 1997, Wang *et al.* **[21]** reported TiO_2 surfaces with excellent anti-fogging and self-cleaning abilities which were attributed to the super hydrophilic attributes of the TiO_2 surfaces. In addition, this field is still being developed further in the 21st century. It seem that TiO_2 photocatalysis is one of the best examples how, on the time scale of tens of years, basic scientific knowledge can be developed into a technological field and can produce a new industry, whereby photocatalyst will be the key to a clean and better future.

2-1.2 Doping TiO_2 systems based on semiconductors

Technically, incorporates, dopes or impregnates are some of the terminologies used in material science describe the introduction of foreign elements into the parent photocatalyst without giving rise to a new crystallographic forms, phases or structures and the aim is to enhance the net separation of photogenerated charges and thereby efficiently harness the wide visible-light component of about 43% in the solar spectrum as opposed to the narrow ultraviolet component of ~4%. It is thus an area of increasing research activity in light-harvesting study. Although discovered as a modification technique in the early 1980s, doping has become a standard and routine method in the design of visible-light-driven TiO_2 based structures **[18, 19]**. Researches into TiO_2 doping have spanned several decades and are reviewed **[8, 22−24]**. In fact, similar photocatalysts sensitive to visible light have already been reported in 1984 **[18]**.

2-1.2.1 Doping TiO_2 systems based on semiconductors and nonmetals; the creation of oxygen vacancy

Since Asahi *et al.*, **[25]** reported that non-metallic ions such as a substitutional nitride ion at the oxygen sites of TiO_2 are effective at enabling the thin film to be responsive to Vis light, doping involving the use of nonmetals has been extremely investigated. They claimed that the presence of nitrogen narrows the band gap of TiO_2 thus making it capable of performing visible light driven photocatalysis. The nitrogen substitutional doping of TiO_2 was early claimed as a method for narrowing the band gap by exclusively changing the valence band structure. Today it is well known that the introduction of non-metal such as N **[26, 27]**, C **[28]** and S **[29]** impurity in TiO_2 do shift the energy levels above the parent TiO_2 valence enabling the thin film to be responsive to Vis light **[22]**. Scheme 2.I shows the change in band gap of TiO_2 doped

with nonmetals. Asahi *et al*. **[25]** claimed that the presence of nitrogen narrows the band gap of TiO_2 thus making it capable of performing visible light driven photocatalysis. However, Ihara *et al.* **[30]** suggested that it is the oxygen vacancies that contributed to the visible light activity, and the doped nitrogen only enhanced the stabilisation of these oxygen vacancies. They also confirmed this role of oxygen vacancies in plasma-treated TiO_2 photocatalysts.

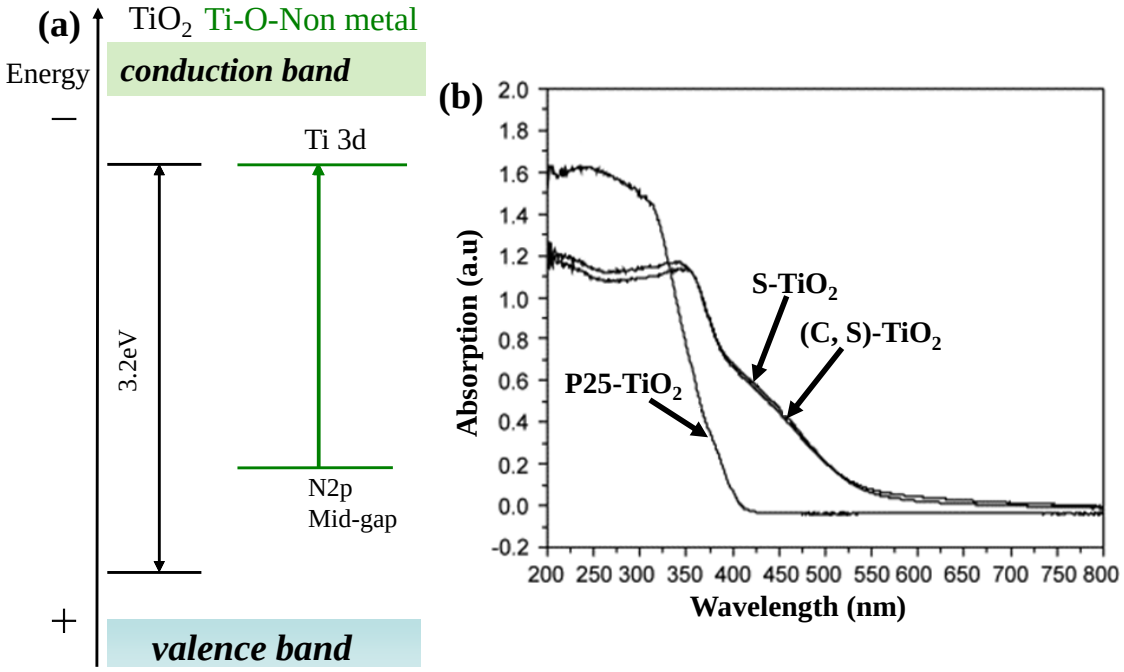

Scheme 2.I The change in band-gap and (a) UV–vis absorption profiles of TiO_2 (b) after doped with nonmetal (C and/or S) [**29**].

In addition the structural oxygen vacancy caused visible light photocatalytic activity was also reported by Irie *et al.,* **[31]**. Currently there appears to be some agreement on the mechanism of nitrogen doped visible light absorption explained by Martyanov *et al.*, **[32]** and seconded by Nagai *et al.*, **[33]**. All the three articles explained that TiO_2 oxygen lattice sites substituted by nitrogen atoms form an occupied midgap (N−2p)

level above the (O−2p) valence band as shown in scheme 2. Irradiation with UV light excites electrons in both the valence band and the narrow (N−2p) band, but irradiating with visible light only excites electrons in the narrow (N−2p) band.

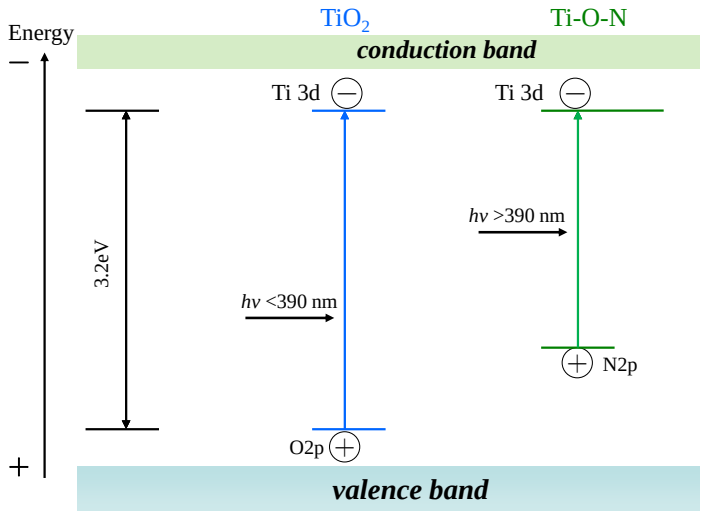

Scheme 2.II Schematic of N−doped TiO_2 photocatalysis.

2-1.2.2 Doping TiO_2 systems based on semiconductors and sensitizers

One method of extending TiO_2's light sensitivity to the visible region of the spectrum is the use of colored substances or sensitizers **[34, 35]**. In systems with sensitizers, the dye absorbs visible light and in the excited state injects electrons into the semiconductor. Scheme 2.III show the how colored substances facilitate photoexcitation of electrons in TiO_2. Physical adsorption of dyes occurs through the weak Van der Waals interaction between the dye molecule and the surface of semiconductor. In systems with sensitizers the dye absorbs visible light and in the excited state injects electrons into the semiconductor **[36]**. Various dyes (catechol, porphyrins, phthalocyanines, etc.) have been employed as sensitizers, but most of them are toxic and, more important, easily

undergo a self-degradation process, that makes them unsuitable for durable applications in photocatalysis **[37]**.

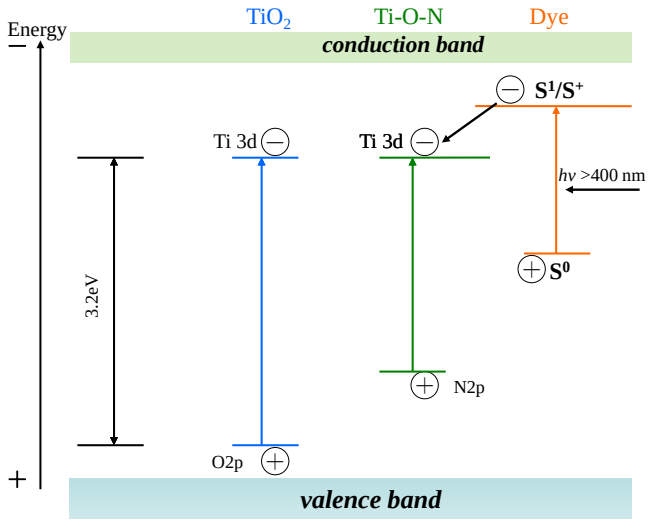

Scheme 2.III Schematic diagram of the operation of the non-metal–semiconductor structures and a dye– sensitizer system during the action of visible light. Legend: S^0, S^1, and S^+ are the sensitizer in the ground, excited, and one- electron oxidized states respectively .

2-1.2.3 Doping TiO_2 system based on semiconductors and transition metals

The implantation of various transition-metal ions such as V^{5+}, Cr^{3+} , and Cu^{2+} into the lattice of Ti^{4+} in anatase thin films was investigated by Anpo`s group, **[38, 39]**. The photoreactivities of chemically modified TiO_2 thin films decreased under UV irradiation, although those TiO_2 thin films modified with transition-metal ions can now response to Vis-light irradiation. The doping of wide-band semiconductors with transition metals may result in the formation of new energy levels between VB and CB, inducing a shift of light absorption towards the visible light region. Scheme 2.IV shows the change in

band gap of TiO_2 upon doped with transition metals.

However, transition metals may also act as recombination sites for the photo induced charge carriers thus, lowering the quantum efficiency **[40]**. Transition metals have also been found to cause thermal instability to the TiO_2 nanomaterials. Irie *et al.*, **[41]** argues that despite the fact that a decrease in band gap energy has been achieved by many groups through metal doping, photocatalytic activity has not been remarkably enhanced because the metals introduced were not incorporated into the TiO_2 framework. In addition, metals remaining on the TiO_2 surface cover photo reaction sites.

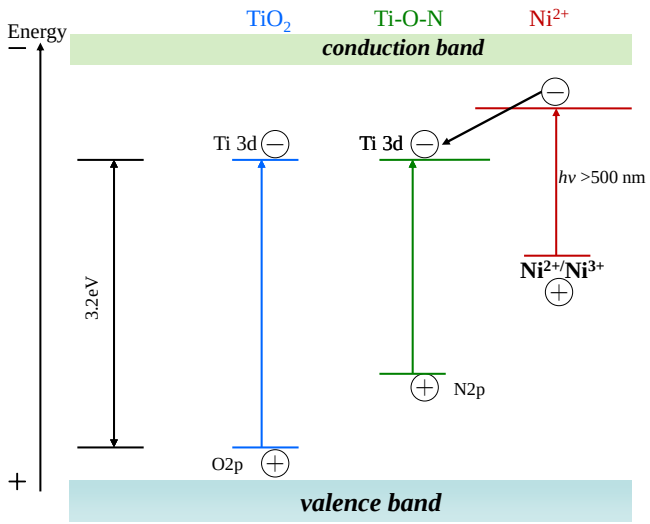

Scheme 2.IV Schematic diagram of the operation of the TiO_2 band- gap after doped with transition metal (Ni^{2+}) **[42]**.

2-1.2.4 Doping TiO_2 systems based on semiconductor heterostructures

In binary systems based on narrow-band and wide-band semiconductors the absorption of visible light by the narrow-band component also leads to the injection of an electron into the wide-band semiconductor. Scheme 2.V show the change in band gap of TiO_2

whereby the hole remains spatially separated from the electron and interacts with the electron donor **[34, 35]**.

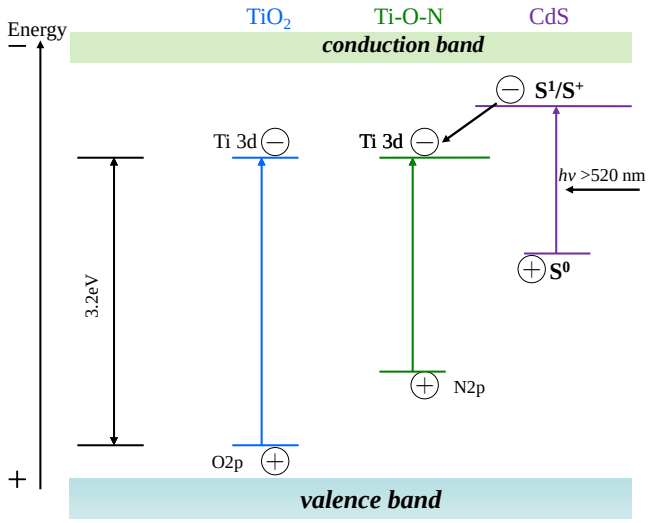

Scheme 2.V Schematic diagram of the spatial separation of the photo generated charges in the CdS/TiO_2 heterostructure during the action of visible light **[23]**.

2-1.2.5 Doping TiO_2 system based on semiconductors and noble metals

Another approach way to increase the efficiency of TiO_2's light sensitivity to the visible region is to couple semiconductor nanoparticles to noble metal co-catalysts to enhance the quantum yield of the electron transfer processes through improvement in charge separation in the semiconductor, discharging photogenerated electrons across the interface and providing a redox pathway with low over-potential **[43−46]**. On the basis of photocatalytic activity and band structure analysis, a plasmonic Z-scheme photocatalytic mechanism is proposed (Scheme 2.VI); namely, two-step visible-light absorption is caused by the localized surface plasmon resonance of metallic Ag nanoparticles and the band gap photoexcitation of TiO_2. The present results suggest that

metallic Ag nanoparticles can act as an effective active component for the construction of a Z-scheme visible-light photocatalyst **[47, 48]**.

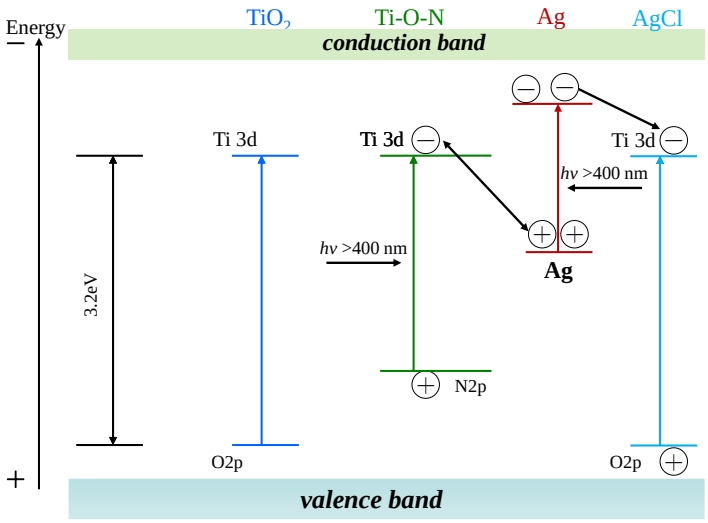

Scheme 2.VI A plasmonic Z-scheme mechanism of TiO_2/Ag/AgCl composite.

2-1.3 Historical background of noble metal nanoparticles

Solutions of liquid (colloidal) gold and silver have been used since Ancient Roman times to colour glass of intense shades of yellow, red, or mauve, depending on the concentrations of the two metals. A fine example is the famous Lycurgus Cup in the British Museum, dated 4th century AD **[49]**. For all the middle ages Au and Ag colloids have also been used in medicine believing in their curative properties for various diseases **[50]**. In 15th century Italian artisans in Gubbio and Deruta were able to prepare brightly coloured porcelain, called luster, containing silver and silver - copper alloy nanoparticles **[49]**. The technique was developed in the Islamic world during the 9th century and exploited the reducing atmosphere obtained heating dried genista up to 600°C to obtain nanoparticles by reducing metal oxides or metal salts previously

deposed on the ceramic piece from a vinegar solution **[51]**. In the 17th century the glass-colouring process was further refined by Andreus Cassius and Johann Kunchel by contriving "Purple of Cassius", a precipitate of colloidal Au and stannic hydroxide they added to the base glass **[49]**.

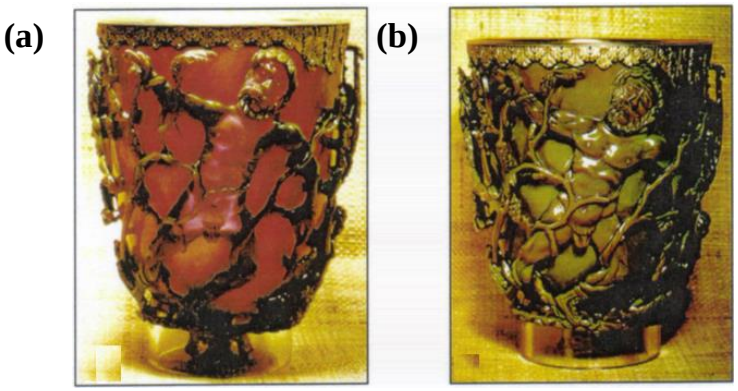

Fig. 2.3: The Lycurgus Cup, dating from the 4th century A.D., is made from glass impregnated with gold nanoparticles; seen in (a) transmitted and (b) reflecting light.

Never the less, the first "scientific" study of metal nanoparticles is dated back to the seminal work of Michael Faraday around 1850 **[52]**. Other synthetic methods for colloidal metal particles have been developed in the early 20th century, both physical or chemical, until the fundamental work of Turkevitch in 1951 **[53]**. He started a systematic study of AuNP synthesis with various methods by using transmission electron microscopy (TEM) analysis to optimise the preparative conditions until obtaining what is commonly known as the Turkevitch method. For Ag nanoparticle suspensions, a common method is the Lee–Meisel method, which is a variation of the Turkevich method in that $AgNO_3$ is used as the metal source **[54]**. Today, silver nanoparticles are mainly produced in a liquid ("liquid chemical methods") by reduction of $AgNO_3$. This causes Ag^+ ions to be reduced to neutral silver atoms. Microwave

irradiation can facilitates the thermal decomposition of citrate ions, as shown in Scheme 2.VII, to afford aqueous electrons and citrate^{3-} oxidation products, acetone-1, 3-dicarboxylate, and carbon dioxide **[55]**. Scheme 2.VII with equations 2.1-2.3 illustrates a flowchart whereby citrate^{3-} oxidation mechanism to facilitate the nucleation of Ag^{+} by irradiation, proposed by Park *et al.*, **[56]**.

Citrate acts both as reducing and stabilizing agents. Electron donation from citrate^{3-} leads to AgNP seeds that act as catalysts for further Ag^{+} reduction, and citrate^{3-} decomposition. These electrons are the driving force for the rapid reduction of Ag^{+}, Scheme 2.VII, to nanoparticle clusters **[57]**.

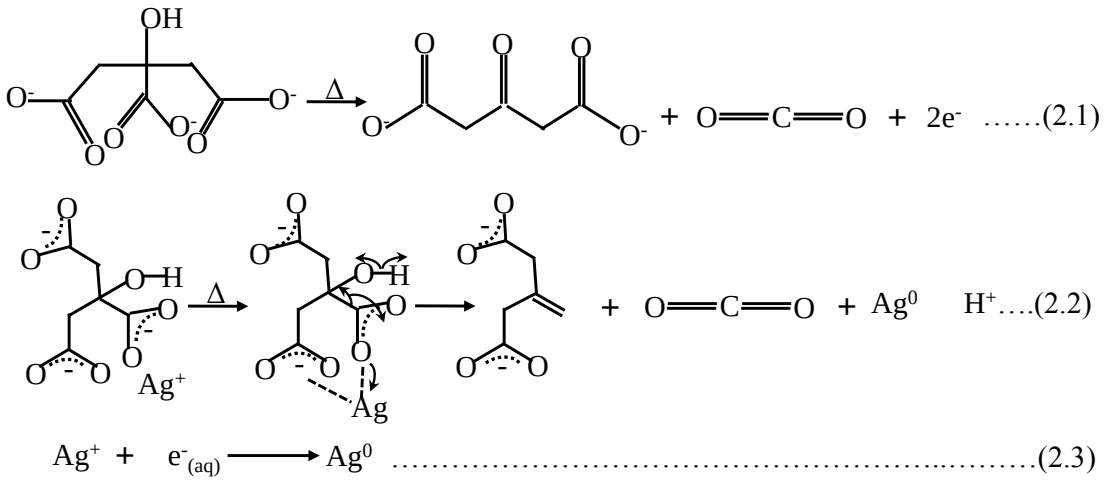

Scheme 2.VII Flowchart of **Eq.2.1** citrate^{3-} oxidation, **Eq.2.2** silver ion reduction and **Eq. 2.3** nucleation of an Ag^{+} precursor by aqueous electrons.

As more and more of these silver atoms form, the solution becomes supersaturated, and silver gradually starts to precipitate in the form of sub-nanometer particles. The rest of the silver atoms that form stick to the existing particles, and, if the solution is stirred vigorously enough, the particles will be fairly uniform in size. To prevent the particles

from aggregating, some sort of stabilizing agent that sticks to the nanoparticle surface is usually added. They can be functionalized with various organic ligands to create organic-inorganic hybrids with advanced functionality. Following propagation, by small cluster aggregation, termination is facilitated by the introduction of a stabilizing agent, Scheme 2.VIII below:

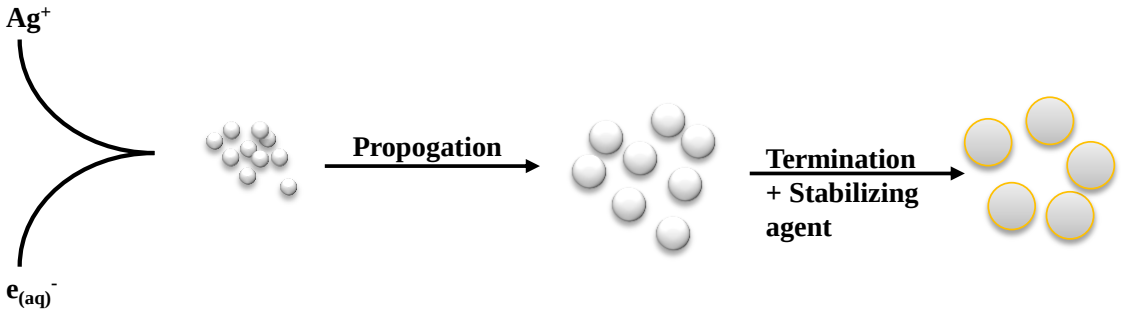

Scheme 2.VIII The stages of Ag NP fabrication.

2-1.4 Ag nanoparticles synthetic Methods

Nanoparticles of noble metals can be prepared via different techniques, such as wet chemical synthesis, solvent exchange, chemical reduction with or without a stabilizing agent, thermal decomposition, in various polymers and sol–gel glasses **[58]**. Physical methods, such as ion implantation, pulse laser ablation and all the sputtering techniques, are used to obtain Ag nanoparticles supported on substrates or embedded in solid matrices. One problem with all these conventional physical methods is the observation that the deposited material, in addition to containing nanoparticles, also containing large, µm-sized particles.

The most widely used methods are based on chemical reduction in solution (wet chemistry) to yield nanoparticles colloids **[58]**. The early methods **[53, 54]**, to produce

suspensions of very small noble-metal particles are still used today **[59]** and continue to be the standard by which other synthesis methods are compared. For Ag nanoparticle suspensions, a common method is the Lee–Meisel method **[54]**. The same procedure can be used to reduce whatever Ag salt, but particle size control is very limited in this case **[60]**.

Brust and Schiffrin, **[61]** developed the two phases method, that is the most widely used for thiols stabilized Ag nanoparticles in organic solvents. Basically $AgNO_3$ is dissolved in water and subsequently transported in toluene by tetraoctylammonium bromide (TOAB), that act as a phase transfer agent. The toluene solution is then mixed and thoroughly stirred together with an aqueous solution of $NaBH_4$ in presence of thioalkanes or aminoalkanes. In this case, particles size can be tuned in the 1–30 nm range. Referred to as the Creighton method **[60]**, the synthesis procedure routinely yields <10 nm particles of narrow size distribution. This method can also be adapted to produce particles of other metals such as Pt, Pd, Cu, Ni, etc., although the specific protocols depend on the reduction potential of the source ion. Cu and Ni suspensions, for example, are not very stable as the metal particles are easily oxidized requiring strong capping ligands to prevent the oxidation **[62, 63]**.

All these wet chemical approaches require the reduction of Ag^+ and the chemisorptions or physisorption of ligands on the surface of metal nanoparticles to avoid their coagulation and precipitation. To understand the synthesis of silver nanoparticles the following sections will describe how silver nanoparticles are formed, through reduction and how the growth can be controlled, through stabilization process.

2-1.4.1 Reduction of Ag ions

The synthesis of silver nanoparticles in this thesis will be based on a wet chemical method. It is therefore better to understand the mechanism involved for the synthesis of metallic silver. The most starting point of the synthesis reported in literature is the production of a silver nitrate ($AgNO_3$) solution. When silver nitrate is dissolved it splits into a positive silver ion (Ag^+) and a negative nitrate ion (NO^-). To turn the silver ions into solid silver, the ions have to be reduced by receiving an electron from a donator. Pastoriza-Santos and Liz-Marz´an **[64]** proposed that the reduction of silver ions to silver nanoparticles by *N*,*N*,dimethylformamide (DMF) in water takes place as follows:

$$HCONMe_2 + 2Ag^+ + H_2O \rightarrow 2Ag^0 + Me_2NCOOH + 2H^+ \quad \text{.....(2.4)}$$

The equation 2.4 is illustrating the reduction of the silver ions by addition of an electron. Colloidal silver particles in the nanometer size range were synthesized by reduction with DMF, using the silane coupling agent as a stabilizer. The figure 2.4 below illustrates the reduction of (Ag^+) in a solution of ethanol. After the "silver seed" has been formed it starts to grow and continue the growth until the equilibrium between the final nanoparticles and the $Ag^+$of the solution is reached.

There are a number of parameters that can be adjusted in order to control the growth of particle. For example, small particles can be achieved by using a fast reduction agent **[60]**. A fast reduction agent results in the formation of many "silver seeds" in the beginning of the synthesis process. This high amount of "silver seeds" will abbreviate the time in which the seeds can grow and prevent the formation of large nanoparticles. If the solution is homogenous the particles end up within a narrow size distribution. Further control of the synthesis of silver nanoparticles can be obtained with the use of a stabilizer, which will be the topic of the next subsection.

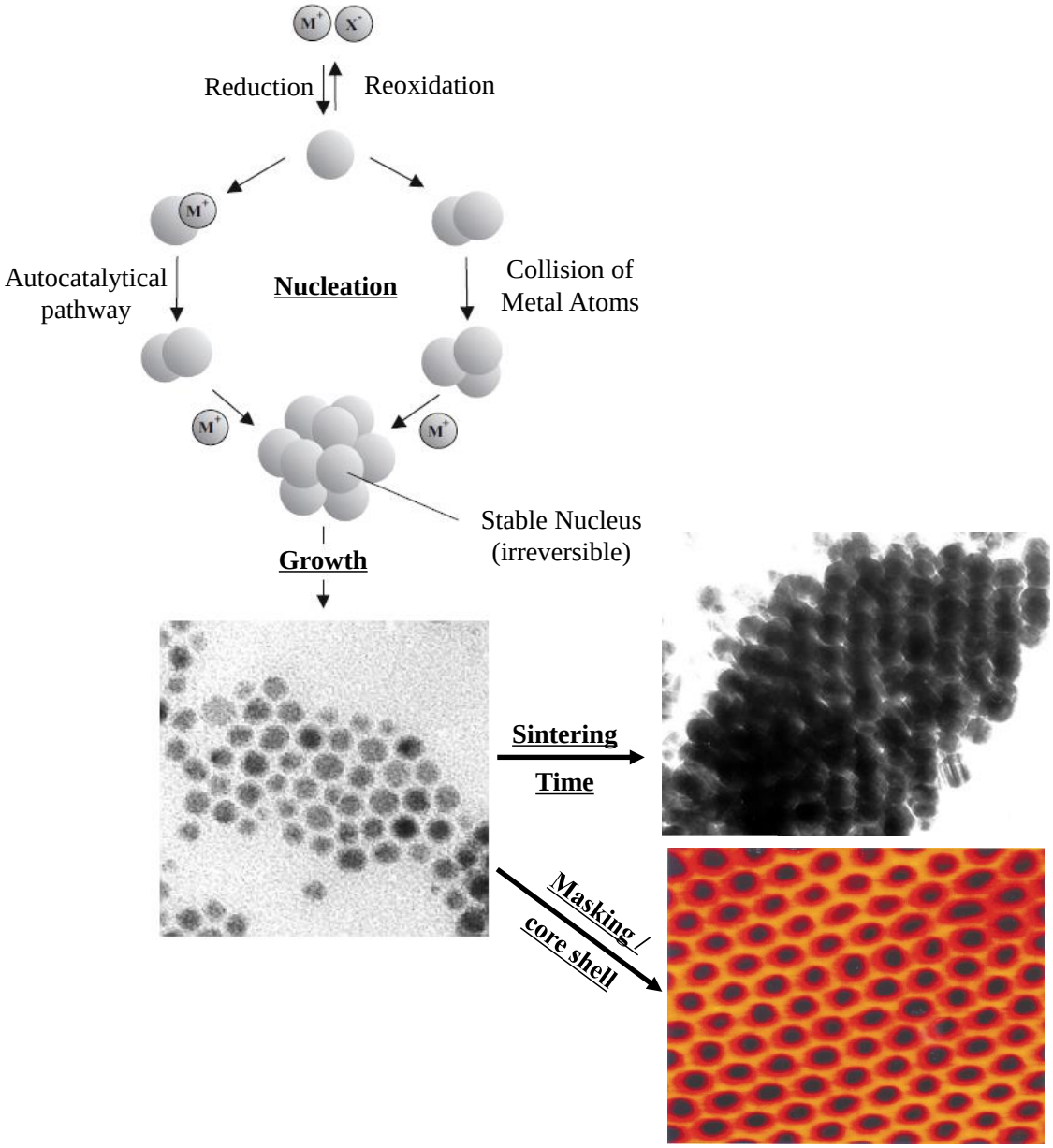

Fig. 2.4 Formation of masked nanostructured metal via the salt reduction method **[65]**.

2-1.4.2 Stabilizers in reduction of Ag ions

It is important to use protective agents to stabilize dispersive nanoparticles during the course of metal nanoparticle preparation, and protect the nanoparticles that can be absorbed on or bind onto nanoparticle surfaces, avoiding their agglomeration **[66]**. The

presence of surfactants comprising functionalities (*e.g.*, thiols, amines, acids, and alcohols) for interactions with particle surfaces can stabilize particle growth, and protect particles from sedimentation, agglomeration, or losing their surface properties **[67]**. A stabilizer is therefore, a substrate, often a donor ligand, surfactant or a polymer, with the purpose of preventing particles from agglomerating. This is done by producing a protective shell around the forming particle. The efficiency of a certain stabilizer is connected with the properties of the solvent. If the solvent permits the stabilizer to stretch away from the particle the solvent is good. On the other hand if the solvent makes the stabilizer collapse on the surface of the particle the solvent is poor. This is only a problem if the particle is not covered 100% by stabilizer **[68]**. If the particle is not covered 100% and two particles move towards each other the result will be a decrease in Gibbs energy **[69]**. This means that the polymers on the surface of one particle will interpenetrate with the polymers of the other and promote a further coiling. This in turn results in the two particles bundling together.

Nanostructured colloidal silver requires protective agents for stabilization and to prevent agglomeration. The two basic modes of stabilization which have been distinguished are electrostatic and steric **[70]**. Electrostatic stabilization [see Fig. 2.5 (a)] involves the coulombic repulsion between the particles caused by the electrical double layer formed by ions adsorbed at the particle surface (e.g., sodium citrate) and the corresponding counter ions. As an example, silver sols are prepared by the reduction of [$AuCl4^-$] with sodium citrate **[57]**. By coordinating sterically demanding organic molecules that act as protective shields on the metallic surface, steric stabilization [Fig. 2.5(b)] is achieved. In this waynanometallic cores are separated from each other, and agglomeration is prevented.

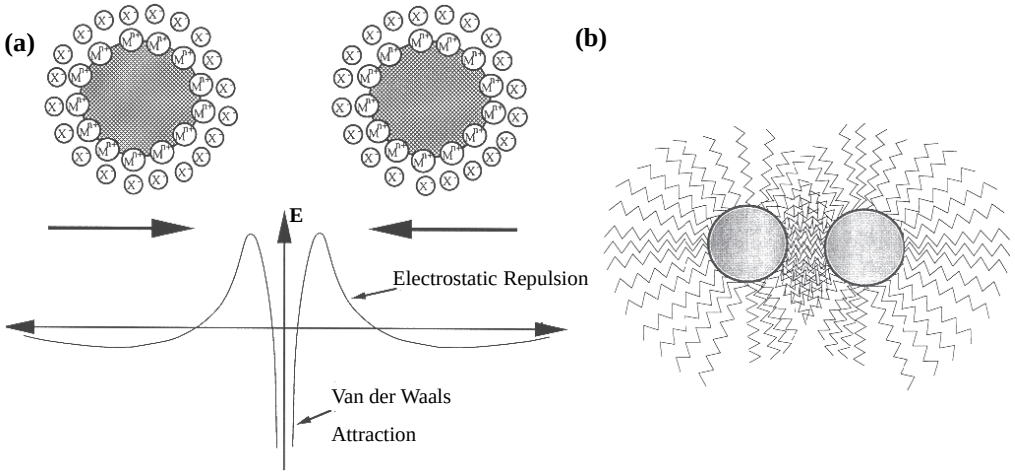

Fig. 2.5 (a) Electrostatic stabilization of nanostructured metal colloids. **(b)** Steric stabilization of nanostructured metal colloids. (Scheme adapted from Ref. **[70]**)

2-1.4.3 Solvent in reduction of Ag ions

When one is discussing good and poor solvents the important property to look at is the polar or nonpolar properties of the solvent **[71]**. If particles covered with these polymers are placed in a polar solvent such as water, the polymers will pack together on the surface in order to minimize the contact surface where polymer meets water. To make the polymer expand away from the particle a nonpolar environment is needed. This could for example be methanol, ethanol or ethylenglycol. The solvent can also be categorized by its protic or aprotic properties. Protic solvents have the ability to exchange protons. The three solvents mentioned before are protic solvents. Benzene is an example of an aprotic solvent.

The use of a good solvent and an effective stabilizer does not only prevent the silver nanoparticles from agglomerating, it also shields the silver nanoparticles from the solution. This shielding stops the growth of the silver nanoparticles, which is a disadvantage when larger nanoparticles are wanted. Heating the solution is one way to

solve this problem **[72]** and an appropriate way to do this will be described in the next section. A successful production of nanoparticles is determined by the ability to produce particles with uniform distributions and long stability, given their tendency to rapidly agglomerate in aqueous solution. The main classes of protective groups I selected from the literature are: polymers and block copolymers; P, N, S donors (e.g., phosphines, amines, thioethers); solvents such as THF, THF/MeOH, or propylene carbonate; long chain alcohols; surfactants; and organometallics **[73−76]**. In general, lipophilic protective agents give metal colloids that are soluble in organic media (organosols) while hydrophilic agents yield water-soluble colloids (hydrosols) **[77]**.

2-1.4.4 Green chemistry for synthesis of Ag nanoparticles

Green chemistry is defined as the "design of chemical products and processes to reduce or eliminate the use and generation of hazardous substances" **[78]**. In the global efforts to reduce generated hazardous waste, "green"chemistry and chemical processes are progressively integrating with modern developments in science and industry. Implementation of these sustainable processes should adopt the 12 fundamental principles of green chemistry **[79]**. These principles are geared to guide in minimizing the use of unsafe products and maximizing the efficiency of chemical processes. Hence, any synthetic route or chemical process should address these principles by using environmentally benign solvents and nontoxic chemical.

The green synthesis of Ag NPs involves three main steps, which must be evaluated based on green chemistry perspectives, including (1) selection of solvent medium, (2) selection of environmentally benign reducing agent, and (3) selection of nontoxic substances for the Ag NPs stability **[80]**. Based on this approach, Sharma *et al.*, **[76]** and

Kaler *et al.*, **[81]**, wrote an overview of Ag NP preparation by green synthesis approaches that have advantages over conventional methods involving chemical agents associated with environmental toxicity. In their review, the mentioned that green synthetic methods include mixed-valence polysaccharide, tollens, irradiation, biological and polyoxometallates.

Solutions of $AgNO_3$ containing glucose and starch in water gave starch protected Ag NPs, which could be integrated into medical applications. The starch in the solution mixture avoids use of relatively toxic organic solvents **[81]**. Additionally, the binding interactions between starch and Ag NPs are weak and can be reversible at higher temperatures, allowing separation of the synthesized particles.

Tollens process involves the reduction of $Ag(NH_3)_2^+$ by saccharides forming Ag NP films with particle sizes from 50–200 nm, Ag hydrosols with particles in the order of 20–50 nm, and Ag colloid particles of different shapes **[82]**. The basic tollens reaction involves the reduction of $Ag(NH_3)_2^+{}_{(aq)}$, a tollens reagent, by an aldehyde, Eq. (2.5).

$$Ag\ (NH_3)_2^+{}_{(aq)} + RCHO_{(aq)} \rightarrow Ag_{(s)} + RCOOH_{(aq)} \quad \ldots\ldots\ldots\ldots\ldots\ldots\ldots\ldots (2.5)$$

The reduction of $Ag(NH_3)_2^+$ by HTAB (n-hexadecyltrimethylammonium bromide) gave Ag NPs of different morphologies: cubes, triangles, wires, and aligned wires.

Ag NPs can be successfully synthesized by using a variety of irradiation methods. For example, laser irradiation of an aqueous solution of Ag salt and surfactant can fabricate Ag NPs with a well-defined shape and size distribution **[83]**. Ag NPs synthesis by irradiation of Ag^+ ions does not involve a reducing agent and is an appealing procedure.

Eco-friendly bio-organisms in plant extracts contain proteins, which act as both reducing and capping agents forming stable and shape-controlled Ag NPs. For example, the extract of unicellular green algae *Chlorella vulgaris* was used to synthesize single-crystalline Ag nanoplates at room temperature **[84]**.

Polyoxometalates, POMs, have the potential of synthesizing Ag NPs because they are soluble in water and have the capability of undergoing stepwise, multielectron redox reactions without disturbing their structure **[77]**. For example, Ag NPs were synthesized by illuminating a deaerated solution of POM/S/Ag^{+} (POM: $[PW_{12}O_{40}]^{3-}$, $[SiW_{12}O_{40}]^{4-}$; S:propan-2-ol or 2,4-dichlorophenol). In this method POMs serve both as a photocatalyst, a reducing agent, and as a stabilizer. In another study, one-step synthesis and stabilization of Ag nanostructures with Mo^{V}–Mo^{VI} mixed-valence POMs in water at room temperature has been demonstrated **[85]**. This method did not use a catalyst or a selective etching agent. Recently, Sakai and Tatsuma, **[86]** also developed a one-step synthesis method of glutathione-protected Au, Ag, Cu, Pd and Pt cluster powders. Average cluster sizes can be controlled by tuning the molar ratio of glutathione to metal salts as starting materials.

2-1.5 Synthesis of Ag/TiO_2 system and their applications in literatures

The unique properties of Ag NPs have been extended into a broader range of applications. Incorporation of Ag NPs with other materials is an attractive method of increasing compatibility for specific applications.

2-1.5.1 Synthetic techniques of Ag/TiO_2 system

There are hundreds publications devoted to the fabrication techniques of noble

metal/titania heterostructures and the properties description of obtained materials. The methods of synthesis including sol-gel process with thermoinduced **[87]**, photo- or chemical reduction of metal ions deposited on the TiO_2 surface **[88]**, as well as combination of ion-exchange and reduction process were proposed for preparation of films containing small particles of noble metals and semiconductor **[89]**. Most of these methods are still in the development stages and the problems experienced involve the stability and aggregation of nanoparticles, control of crystal growth, morphology, size and size distribution, and occasional difficulty in the management of the synthesis.

2-1.5.2 Plasmonic property of Ag/TiO_2 system

Titanium dioxide (TiO_2) displays photoresponsive behavior under near-ultraviolet (UV) illumination. In another scientific field, it is well understood that the excitation of localized plasmon polaritons on the surface of noble metal nanoparticles (NPs) causes a tremendous increase of the near-field amplitude at well-defined wavelengths in visible-light region. Metallic NPs, usually silver or gold, interact with visible light to create a collective oscillation of the conduction electrons called a plasmon **[90, 91]**. This phenomenon gives rise to two characteristic properties: an intense absorption feature at wavelengths resonant with the electron oscillation, surface plasmon resonance (SPR), and a greatly enhanced electromagnetic field near the particle, localized surface plasmon (LSPR). LSPR is an optical phenomena generated by light when it interacts with conductive nanoparticles (NPs) that are smaller than the incident wavelength **[57]**. As in surface plasmon resonance, the electric field of incident light can be deposited to collectively excite electrons of a conduction band, with the result being coherent localized plasmon oscillations with a resonant frequency that strongly depends on the

composition, size, geometry, dielectric environment and separation distance of NPs **[92, 93]**. The theory on the plamon resonance of noble metals especial gold and silver are reported by Romeo *et al* **[94]** and also by Felicia *et al.,* **[57]** respectively. Notably, the maximum absorption wavelength of plasmonic particles has been found to be greatly dependent on factors such as size, shape, and dielectric environment **[95]**. Plasmon offers a platform for biological and chemical sensing that typically relies on one or more of the following mechanisms: (1) resonant Rayleigh scattering, (2) charge-transfer interactions at the surface of the NP, (3) NP aggregation, and (4) changes in local refractive index **[96]**. These metal-doping also have an influence on the titania crystal structure leading to distinct improving in the application fields **[97]**. Thus, enormous efforts have been devoted to the research of TiO_2 material, which has led to many promising applications in areas ranging from photovoltaic and photocatalysis to photo-/electrochromics and sensors **[98]**. Recently, metal-doping strategy has been invoked to improve the photosensitivity of TiO_2 into visible region **[99]**. Noble metal incorporation into the titania dielectric provides an absorption feature due to the plasmon that occurring over the visible range of the spectrum **[100]**. In fact, silver as a noble metal have attracted considerable attention, as a result of its remarkable role on the improvement of photoactivity of semiconductors. Therefore, many researchers have been recently focused on modifying TiO_2 with Ag by synthesis Ag/TiO_2 composites **[101−111]**. However, the separation of produced Ag nanoparticles that can be embedded into titania for further applications is still an important issue. Most of the previous work demonstrated that NPs are easily aggregated during sintering **[112]** and oxidized **[93]** and lose their plasmon resonance gradually under ambient conditions **[113]**. By using different reducing agents and stabilizers, masking with alumina and silica, the particle

size and morphology of silver nanoparticles have been controlled. Moreover, selection of solvent medium and selection of ecofriendly nontoxic reducing and stabilizing agents are the most important issues which must be considered in green synthesis of silver nanoparticles.

2-1.6 Mechanism of photo-responsive Ag NP/TiO_2 system

2-1.6.1 Mechanism of UV-responsive Ag NP/TiO_2 system.

Scheme 2.IX illustrates how silver enhance the electron-hole separation by acting as electron traps and enhance photo-responsive under UV-light irradiation. Electron transfer between photoexcited semiconductor and metal is an important phenomenon in study of the enhancement of photoresponsive of TiO_2 under UV-light irradiation **[114]**.

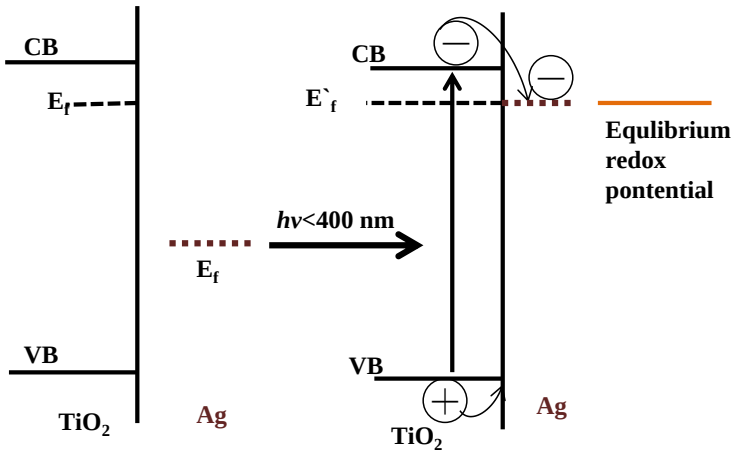

Scheme 2.IX Mechanism for charge separation at a UV light–irradiated Ag nanoparticle–TiO_2 system.

TiO_2 nanoparticles modified with precious metals have been extensively employed in photocatalytic water-splitting reactions. A direct correlation between the work function of the metal and the photocatalytic activity for the generation of NH_3 from azide ions

has been made for metallized TiO_2 systems **[115]**. Recent studies have shown that silver or silver ion doped TiO_2 composites exhibit shift in the Fermi level to more negative potentials **[103, 116]**. Such a shift in the Fermi level improves the energetics of the composite system and enhances the efficiency of interfacial charge-transfer process. The unusual property of Ag nanoparticles to undergo quantized charging makes them a unique candidate to achieve Fermi-level equilibration **[117, 118]**. Platinum metal, on the other hand, introduces ohmic contact facilitating a quick transfer of electrons to the electrolyte **[119]**. Silver has a Fermi-level or electron accepting region at an energy level just below the conduction band **[120]**. Therefore, after light absorption and charge separation, the electron in the conduction band can be effectively trapped by silver, while the hole oxidizes water and forms hydroxyl radicals, without the threat of recombination. However, Liu *et al.,* **[121]** reported that higher amount of silver would cover more TiO_2 surface and hinder the contact between TiO_2 and organics, which would increase diffuse distance and decrease the amount of received photons. This observation was supported by Li *et al.,* **[122]**.

2-1.6.2 Mechanism of vis-responsive Ag NP/TiO_2 system.

The current effort is the use of surface plasmon resonance of silver-based nanoparticles as a method for converting visible sunlight into energy for activating titanium dioxide. Surface plasmon resonance (SPR) phenomena have been identified as means for absorbing visible light for silver and gold particles **[123, 124]**. On the other hand, the silver doped TiO_2 catalysts shows an absorption threshold extended into the visible region. It is obvious that the Ag clusters give rise to localized energy levels in the band gap of TiO_2 into which the valence band electrons of TiO_2 are excited at wavelength

longer than 400 nm. This is mainly because of the excitation of plasmon resonances in Ag NPs produces a local electromagnetic field that extends from the particle surface and into the surrounding environment and conduction band of TiO_2.

The enhanced photochemical activity is attributed to radiative transfer of energy, mediated by surface plasmons, from Ag particles to the semiconductor leading to higher concentrations of charge carriers (e-/h+ pairs) in the semiconductor and therefore to higher photochemical activity **[104, 122]**. Scheme 2.X illustrates how Ag plasmon can be shift the photoresponse of TiO_2 from UV region to Visible-light region **[104]**.

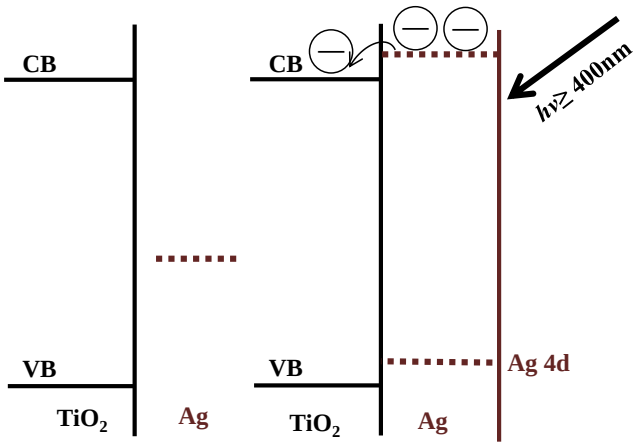

Scheme 2.X Mechanism for charge separation at a visible light–irradiated Ag nanoparticle–TiO_2 system.

While most relate this improvement to electronic effects, it has been pointed out that the addition of Ag can modify the grain sizes of the TiO_2, so increasing the surface area and hence also the photoactivity **[126]**. However, the photo response of the Ag-doped TiO_2 composite significantly depends on the Ag nature (ion or metallic) and concentration, preparation method and operating conditions **[122]**. Both positive and negative results have been reported from doping with metal.

While some authors have reported an increased photo-responsive of TiO_2 under visible light due to certain Ag doping, others have reported a decreased activity **[127]**. But generally the photo-responsive property of Ag doped TiO_2 has been reported to be quite higher than the undoped TiO_2 and therefore is seen to be of very high research value. Doping TiO_2 with Ag resultant in the following observation: Anatase size (at 600^oC) decreased from 37 nm to 19 nm; specific surface area increased from 45 to 63 m^2/g, and photocatalytic activity increased by 18% **[128]**. Phase transfer appeared from anatase to rutile at 700^oC and phase transformation was completed at 800^oC [**33**]. In the absence of a dopant or precursor modification, anatase to rutile transformation in synthetic TiO_2 usually occurs at a temperature of 600 ºC to 700 ºC **[128, 129]**. All these observations will depend on the fabrication techniques employed for the synthesis of Ag/TiO_2 system.

2-1.7 Electrical conductivity of Ag/TiO_2 system

Nanoparticles and nanostructured materials comprising metals (Ag, Pt, *etc*.) and semiconductors (SiO_2, In_2O_3:SnO_2) that exhibit size-dependent catalytic properties have recently been used as advanced materials for designing next generations of electronic devices **[130]**. During the last decade indium tin oxide nanoparticles (ITO-NPs) have attracted considerable interest due to their unique optical and electrical properties such as high transmittance in Vis, high resistance in infrared (IR), and very good electrical conductivity. Similar to other semiconductors ITO conductivity is owed to the formation of an oxygen vacancy due to the band gap (3.6 eV) **[131]**. Recently, some researchers have found that TiO_2-based film could become an indium-free alternative to tin doped indium oxide, due to advantages of TiO_2 low cost and non- toxicity. TiO_2

films are applied in many optical devices, for example in solar cells as antireflective (AR) coating **[132]**. However, the insulating properties of pure TiO_2 limit its application in electronics as film. In order to overcome this disadvantage, TiO_2 is usually doped with different metals, for example Nb **[133]**, Pd **[134]**, or V **[135]**. However, some elements like, for example, Pd **[136]**, when introduced into a TiO_2 matrix, simultaneously cause a reduction of transmission coefficient. On the other hand, is well established that the relatively high resistivity of titania films (10^{12} Ω·cm at 25°C) can be reduced by incorporating metal nanoparticles into the titania matrix based on the fact that the electrically conducting particles can be randomly distributed within the semiconductor matrix to form a composite **[112, 137]**. Doping TiO_2 with Ag should provide realization of conductive and semiconducting films based on a TiO_2 matrix. It is known that, electrical properties of TiO_2 were influenced by changes of annealing temperature **[138]**. Resistivity of thin films was found to decrease as the annealing temperatures increase.

Another way of enhance electrical conductivity of a semiconductor is through the investigation of quantum dot (QD) using a metal particle connected by tunnel contacts to metal electrodes. In such systems, when studying their conductivity, the Coulomb−blockade phenomenon and resonance−tunneling effects are observed for electrons **[139]**. The methods of fabricating electrical contacts to QDs from semiconductor materials are not developed **[140]**.

2-1.8 Application of Ag/TiO_2 system

2-1.8.1 Photoelectrochemical properties of Ag/TiO_2 system

A pioneering proposal to adopt a localized plasmon for the enhancement of photochemical reactions was first made by Nitzan and Brus, **[141]** in 1981 based on their theoretical calculations of highly localized electromagnetic fields on rough metal surfaces. Soon thereafter, the first experimental evidence confirming the enhancement of a photochemical reaction by surface plasmons was reported by Chen and Osgood, **[142]** in 1983. Since then, numerous studies have been carried out on the control of photochemical reactions by localized plasmons, mainly in systems comprising chemically synthesized metal/semiconductor nanoparticles, as described in review articles by Watanabe *et al.*, **[143]**. One interesting example was reported by Fedurco *et al*, **[144]** who found that increments in the photocurrent caused a reduction of carbon dioxide in solution at a roughened Ag electrode. The quantum yield of the photocurrent exhibited a sharp maximum at the peak wavelength of Ag surface plasmons **[145]**. These studies have shown that the utilization of localized plasmons is a promising means of improving the efficiency of photochemical reactions, especially in the visible-near-infrared wavelength region.

Today, the plasmon-induced charge separation can be recognized as one of the sensitization effects of TiO_2 **[146]**. The maximum value of incident photon-to-current conversion efficiency (IPCE) of a two-dimensional gold nanorod array on a single crystalline TiO_2 exceeds 10% **[147]**. However, wet type cells such as ITO/TiO_2/AuNPs/electrolyte/Au (ITO.indium tin oxide; electrolyte contains a redox species) have been employed so far **[86]**. Although a solid state cell was developed by using hole-transport materials (HTMs) instead of an electrolyte solution containing a redox couple (ITO/TiO2/AuNPs/ HTM/Au), their IPCE values were four orders of magnitude lower than those of the wet type cells. The fabrication of a easily without

undue loss of the efficiency solar cell would be a first step to develop solar cells without unstable factors like organic compounds or a liquid electrolyte at lower cost of materials and fabrication than the conventional cells.

2-1.8.2 Photocatalyst properties of Ag/TiO_2 system

Titanium oxide is of special interest because of its photochemical activity, allowing us to use TiO_2 to make devices for photolysis of water and also to carry out oxidation of toxic organic compounds down to carbon dioxide and water on its surface. The electronic and optical properties of titanium dioxide as a semiconductor are considerably affected by atoms of impurity elements within its composition. However, this effect has been poorly studied, especially for nanostructures **[148]**. Titanium oxide, also being a nontoxic and relatively cheap material, today is considered as one of the most promising photocatalysts and can be used for purification of water and air to remove organic compounds which are harmful to human health and to make self-cleaning and antibacterial coatings **[149]**.

Considering that most solar radiation passing through the Earth's atmosphere is radiation in the visible rangeas I demonstrated it in Chapter 1, I can say that nanostructured titanium oxide, doped with noble metal, is a promising material for use in systems for purification. Many researchers have demonstrated that the addition of Ag NP to titania, can effectively enhance the degradation efficiency of photocatalytic reactions **[110]**. This is because they act as an electron trap promoting interfacial charge transfer processes in the composite systems. As a result, more photoinduced holes will have opportunity to participate in the oxidation reactions on the surface. Indeed, Ag nanoparticles act as electron scavengers, decreasing the charge carrier recombination.

Time Resolved Microwave Conductivity (TRMC) measurements done by Grabowska *et al.*, **[116]**, show also that more electrons are produced in the conduction band of P25 under UV illumination of Ag−modified P25. Surface modification by silver nanoparticles induces also a modification of the absorption properties of the photocatalyst creating an activity under visible light. However, Zhou *et al*., **[150]** reported that with further loadings of Ag NP, the chance of recombination of photoinduced electrons and holes will increase leading to reduction in the rate of a decomposition reaction.

Sangpour *et al*., **[151]** fabricated titania thin film system containing noble metallic nanoparticles such as Au, Ag, and Cu prepared by utilizing radio frequency reactive magnetron cosputtering method. The photocatalytic activity of all synthesized samples annealed at 600ºC in an Ar + H_2 (80 + 20%) environment was evaluated by measuring the rate of photodegradation reaction of methylene blue (MB) under similar conditions in the presence of UV and visible light irradiation. The photoenhancement of the studied was determined in the following order: Cu:TiO_2 > Au:TiO_2 > Ag:TiO_2 > TiO_2. Surface plasmon resonance of the metals and the presence of the Ti^{3+} oxygen vacancy in the photoirradiated thin films were found responsible for the enhancement of the MB photodegradation reaction.

Moreover, silver-doped TiO_2 nanofibers having different silver contents were prepared by calcination of electrospun nanofiber mats consisting of silver nitrate, titanium isopropoxide and poly(vinyl acetate) at 600˚C **[152]**. The results affirmed formation of silver-doped TiO_2 nanofibers composed of anatase and rutile when the silver nitrate content in the original electrospun solution was more than 3 wt%. Study of the

photocatalytic degradation of methylene blue dye clarified that increase the silver content strongly enhances the dye oxidation process. The Ag/TiO_2/MMT materials with excellent stability, large amount of Ag in TiO_2 and bactericidal activities are promising photocatalysts for application in decontamination **[105]**. Pant *et al.*, **[153]**, also prepared Ag–TiO_2/nylon-6 fiber nanocomposites. The antibacterial property of a TiO_2/nylon-6 composite mat loaded with Ag NPs was tested against Escherichia coli, and the photoactive property was tested against methylene blue. They found that they have good photocatalytic and antimicrobial properties (even in absence of UV light), excellent recyclability and stability for potential applications in environmental remediation.

Akhavan **[154]** study the photodegradation of Escherichia coli bacteria in presence of Ag/anatase-TiO_2 nanocomposite film with an effective storage of silver nanoparticles was investigated in the visible and the solar light irradiations. Antibacterial activity of the nanocomposite film against *E. coli* bacteria was 5.1 times stronger than activity of the anatase-TiO_2. They also study the durability of the nanocomposite film. They found out that Ag–TiO_2/Ag/a−TiO_2 was at least 11 times higher than the anatase−TiO_2 film. Therefore, the Ag/TiO_2 system can be nominated as one of the effective and long-lasting antibacterial nanocomposite materials.

Recently, TiO_2 and TiO_2−Ag composites films were prepared by sol–gel method and coated on glass fibre roving **[155]**. The antibacterial activity studies of TiO_2 and TiO_2 composite films were evaluated by photocatalytic reaction against *P.aeruginosa* bacteria. The results shown that pure TiO_2 and TiO_2 porous (TiO_2-PEG) films have disinfection efficiency 57% and 93% within 15 min under UV irradiation, respectively. TiO_2−Ag film has highest antibacterial effect under UV irradiation and that disinfection efficiency

is 100% within 10 min. It has been found that Ag doped TiO_2 films have the higher disinfection efficiency than that of pure TiO_2 due to the effect of silver species. This shows us that there is still a big potential for using Ag/TiO_2 against bacteria.

2-1.8.3 Other potential applications application

Some of the odorous problems from industries are caused by the volatile organic compounds (VOCs), acetic acid, and dimethyl sulfide (DMS). VOCs and acetic acid are necessary materials in the manufacturing processes. DMS can be transferred from the dimethyl sulfoxide (DMSO), which is one of main compounds in the stripper. These odorous exhausts would persecute residents' health and lower the environmental quality in the neighborhood. Recently, Lin (2013) in Taiwan, reported that $Ag–TiO_2$/functional filter can be applied to removal these odorous compounds **[114]**. Comparing the TiO_2 type, P25 TiO_2 (Degussa, Germany)/functional filter showed the more superior photodegradation efficiency than ST01 TiO_2 (Ishihra Sangyo, Japan)/functional filter. In addition, Ag-modifying TiO_2/functional filter enhanced the photocatalysis via postponing the recombination between electrons and holes. Dastjerdi and Montazer, **[125]** wrote a review on the application of inorganic nano-structured materials in the modification of textiles. They discussed nano-structured anti-microbial agents include TiO_2 nano-particles, silver TiO_2 nano-composites. Silver doped in TiO_2 can lead to denaturing of protein and cell death because of their reaction with nucleophilic amino acid residues in proteins, and attach to sulfhydryl, amino, imidazole, phosphate and carboxyl groups of membrane or enzyme proteins.

Many researchers **[156−157]** reported that Ag−doped titania coatings were found to be significantly more photocatalytically, photoelectrochemically and antimicrobially active

than a titania coating. No antimicrobial activity was observed in the dark—indicating that silver ion diffusion was not the mechanism for antimicrobial action. The mode of action was explained in terms of a charge separation model. The coatings also demonstrated significantly higher activity against the Gram-positive organisms than against the Gram-negative. Therefore, the Ag–TiO_2 nanosized coating can be a potentially useful coating for hard surfaces in a hospital environment due to its robustness, stability to cleaning and reuse, and its excellent antimicrobial response. Interestingly, recently Bae *et al.*, **[158]**, the agglomeration of AgNPs (loss of nanosized characteristics) played an important role in the environmental toxicity. Their study demonstrated that when the AgNPs were exposed in the ecosystem and then formed agglomerates, nanotoxicity was reduced. Shrivastava *et al.,* **[159]** in their review, they proposed a mechanism of antimicrobial action, as illustrated in figure 2.6. It is however necessary, according to Prabhu and Poulose **[160]** to understand that further research is required on the topic to thoroughly establish the claims.

Akgun and his group, **[108, 109]** prepared TiO_2 and silver-containing TiO_2 (Ag-TiO_2) thin films on silica precoated float glass substrates by a sol–gel spin coating method. The bactericidal activity of the films was determined against Staphylococcus epidermidis under natural and ultraviolet (UV) illumination and hence the bactericidal and photocatalytic activity, is controlled by post-coating calcination treatment (100–650 ºC). Ag-incorporated films were found to have superior bactericidal and photocataltyic activity performance compared to TiO_2 thin films. It is shown that with optimized thin film processing parameters, both TiO_2 and Ag-TiO_2 thin films calcined at 450 ºC were bactericidal and photocatalytically active. Therefore the calcination treatment temperature is important and will be also consider in this thesis.

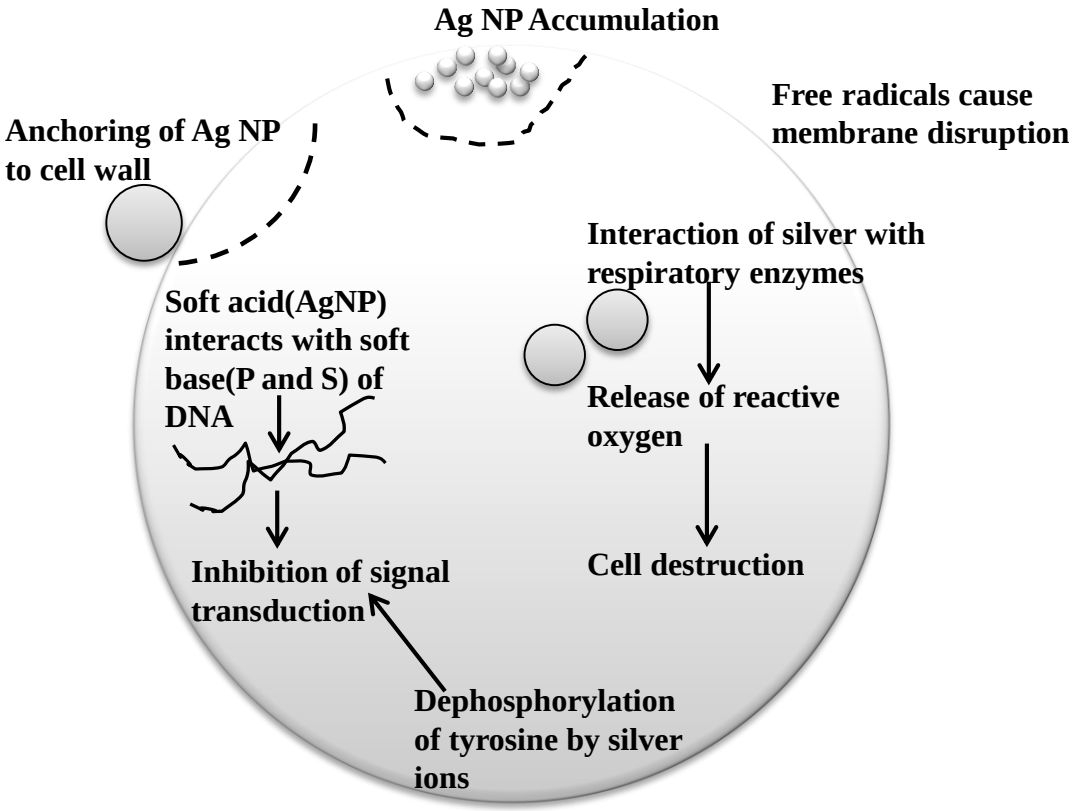

Figure 2.6 Various modes of action of silver nanoparticles on bacteria.

2-2 REFERENCES

1. Habashi F. (2001). *An Inter. J.*, 22:**1**, 25−53.

2. Yousef, P., Shon, H., Phuntsho, S., Okour, Y., Cho, D., Kim, K. S., Li, H., (2008). *J. Korean Ind. Eng. Chem.*,19:**1**, 1−16

3. Carp O., Huisman CL., Reller A. (2004). *Prog. Solid. State. Chem.*, **32**, 33-177.

4. Jelks B. (1966). Titanium: its occurrence, chemistry and technology, *New York*, Ronald Press.

5. Addamo M., Bellardita M., Di Paola A., Palmisano L. (2006). *Chem. Commun.*, **47**, 4943–4945.

6. Moellmann J., Ehrlich E., Ralf Tonner R., Grimme S. (2012). *J. Phys.: Condens. Matter,* **24**, 424206.

7. Nicholls D. (1974). *MacMillan Education*: Hong Kong.

8. Cui Y., Du H., WEN LT. (2008). *J. Mater. Sci. Technol.,* **24**, 2008

9. Keidel E. (1929). *Farben-Zeitung.* **34**, 1242.

10. Doodeve CF., Kitchener JA. (1938). *Trans. Faraday Soc.* **34**, 902.

11. Hashimoto K., Irie H., Fujishima A. (2005). *Japanese J. of Appl. Phys*., 44:**12**, 8269–8285.

12. Fujishima A., Honda K., S. Kikuchi S. (1969). *Kogyo Kagaku Zasshi* **72**,108

13. Fujishima A., Rao TN., Tryk DA. (2000). *Photochem. Photobiol*, **1**, 1–21.

14. Sato M., Hara H., Nishide T., Sawada Y. (1996). *J. Mater. Chem.*, **6**, 1767−1770.

15. Frank SN., Bard AJ. (1977). *J. Am. Chem. Soc.* **99**, 303–304.

16. Anpo M., Yamashita H. (1997), In: M. Schiavello (Ed.), Heterogeneous Photocatalysis, *Wiley*, London.

17. Banerjeel S., Gopal J., Muraleedharan P., Tyagi A, Raj1 B. (2006). *Curr. Sci.*, 90:**10**, 12−18.

18. Anpo M., Aikawa N., Kubokaw Y. (1984). *J. Phys. Chem.*, **88**, 3998.

19. Anpo M, Alkawan N, Kubokaway Y (1985). *J Phys Chem* **89**, 5017.

20. O'Regan B., Gratzel M. (1991). *Nature* **353**, 737–740.

21. Wang R., Hashimoto K., Fujishima A., Chikuni M., Kojima E., Kitamura A. (1997). *Nature* **1997**, 388.

22. Zaleska A. (2008). *Science,* **1**, 157–164.

23. Kumar S., L. Devi (2011). *The J. Phys Chem. A*, 115:**46**, 13211–13241, 2011.

23. Long M., W. Cai, (2011). *Frontiers of Chem. in China*, 6:**3**, 190–199.

24. Morales-Torres S., Pastrana-Martínez LM., Figueiredo JL., Faria JL., Silva AMT. (2012). *Environ Sci Pollut Res* **19**, 3676–3687

25. Asahi R, Morikawa T, Ohwaki T, Aoki K, Taga Y (2001). *Sci.* **293**, 269-271.

26. Asahi R., Morikawa T. (2007). *Chem. Phys.*, 339:**1–3**, 57–63.

27. Yates HM., Nolan MG., Sheel DW., Pemble ME., (2006). *J. Photochem. Photobiol. A: Chem.*, 179:**1–2**, 213–223.

28. Jung D., Kim G., Kim M-S., Kim B-W. (2012). *Korean J. Chem. Eng*., **29**.

29. Hamal DB., Klabunde K J.(2007), *J. Coll. Interface Sci.*, 311: **2**, 514–22.

30. Ihara T., Miyoshi M., Iriama Y., Matumoto O., Sugihara, S. (2003). *Appl. Catalysis B: Environ.*, **42**, 403-409.

31. Irie H., Washizuka S., Yoshino N., Hashimoto K. (2003). *Chem. Commun.* (Cambridge, England), **11**, 1298.

32. Martyanov IN., Sitharaman U., Rodrigues S., Klabunde KJ. (2004). *Commun*. 2476–2477.

33. Nagai H, Hasegawa M, Hara H, Mochizuki C, Takano I, Sato M (2008). *J. Mater. Sci.* **43**, 6902-6911.

34. Xiong B., Wang C., Luo J., Chen B., Zhou B., Zhu Z. (2013). *Sci. China Chem*., **56**.

35. Ouyang J., Chang M., Li X. (2012). *J. Mater. Sci.*, 47:**9**, 4187–4193.

36. Ahmed R., Will G., Bell J., Wang H. (2012). *J. Nanopart. Res.*, **14**, 1140-1153.

37. Chatterjee D., Dasgupta S. (2005). *J. Photochem. and Photobiol. C*, 6:**2-*3***,186– 205.

38. Anpo M, Kishiguchi S, Ichihashi Y, Takeuchi M, Yamashita H, Ikeue K, Morin B, Davidson A, Che M (2001). *Res. Chem. Intermed.* **27**, 459-467.

39. Anpo M, Ichihashi Y, Takeuchi M, Yamashita H (1998). *Chem. Intermed.* **24**, 143-149.

40. Choi W., Termin A., and Hoffmann MR. (1994). *J. Phys. Chem.*, 98:**51**, 13669–13679.

41. Irie H., Watanabe Y., Hashimoto K. (2008). *Chem. Phys. Lett.* **457**, 202–205.

42. Li-Hua G., Song-Hua G. (2010). E-Product E-Service and E-Entertainment 2010 (ICEEE), *International Conference*. **7-9**, 1-3.

43. Zhao G., Kozuka H., Yoko T. (1996). *Thin Solid Films*, 277:**1-2**, 147-154.

44. Fedurco M., Shklover V., Augustynski J. (1997). *J. Phys. Chem.*, 101:**26**, 5158–5165.

44. Loganathan K., Bommusamy P., Muthaiahpillai P., Velayutham M. (2011). *Environ. Eng. Res.*,16:**2**, 81-90.

45. Wang YX., Li S., Ma Y., Yu H., Yu J. (2011). *J. Phys. Chem. C*, **115**, 14648–14655.

46. Barakat MA., Al-Hutailah RI., Hashim MH., Qayyum E., Kuhn JN. (2013). *Environ Sci Pollut Res* **20**, 3751–3759.

47. Maeda K., Higashi M., Lu DL., Abe R., Domen K. (2013). *ACS Catal.* **3**, 1026−1033.

48. Liu R, Wang P., Wang X., Yu H., Yu J. (2012). *J. Phys. Chem. C*, **116**, 17721−17728.

49. Cao, G. (2004). Nanostructures and Nanomaterials, Synthesis, Properties and Applications, *Imperial College, London*, 2004.

50. Daniel, M.C., Astruc D., (2004). *Chem. Rev.*, **104**, 293 - 346.

51. Padeletti G., Fermo P. (2003). *Appl. Phys. A*, **76**, 515 – 525.

52. Faraday M. (1857). *Trans. Roy. Soc.*, **147**, 145 - 181.

53. Turkevich J., Stevenson PC., Hillier J. (1951). *Faraday Soc.* **11**, 55.

54. Lee PC., Meisel DJ., (1982). *Phys. Chem.* **86**, 3391–3395.

55. Mpourmpakis G., Vlachos DG. (2009). *Phys Rev Lett* 102:**4**, 126−132.

56. Park H-H., Zhang X., Choi Y-J., Kim H., Park H-H., Hill RH. (2010). *J Ceram Soc Jpn* **118**,1002–1005.

57. Felicia AM., Gaye-Campbell S., Ting AYH., Mitchell WJ. (2013). *J Nanopart Res* **15**,1442−1447.

58. Kuntyi O., Okhremchuk Y., Bilan' O., Hapke J., Saldan I. (2013). *Cent. Eur. J. Chem.* 11:**4**, 514−518.

59. Kumar KP., Paul W., Sharma CP. (2012). *BioNanoSci.*, **2**,144–152.

60. Creighton JA., Blatchford CG., Albrecht MG. (1979). *J Chem. Soc. Farad. Trans. II* **75**, 790–798.

61. Brust M., Walker M., Bethell D., Schiffrin DJ., Whyman R. (1994). *J. Chem. Soc. Chem. Commun.* **801**, 1743−1754.

62. Sinha A., Kumar DS., Kumar TVV., Rao V., Ramachandrarao P. (1999). *J. Mater. Synth. Proces.* **7**, 373–377.

63. Sastry M., Patil V., Mayya KS., Paranjape DV., Singh P., Sainkar SR. (1998). *Thin Solid Films*, **324**, 239–244.

64. Pastoriza-Santos I., Liz-Marz´an LM., (1999). *Langmuir* **15**, 948.

65. BVnnemann H., Richards R. (2001). *Eur. J. Inorg. Chem.* **2001**, 2455–2480.

66. Darroudi M., Ahmad MB., Zamiric R., Abdullah AH., Ibrahim NA., Shameli K., Husin MS. (2011). *J. Alloys Comp.*, **509**, 1301–1304.

67. Almeida E., Moreira ACL., Brito-Silva AM., Galembeck A., Melo CP., Menezes LS., Araújo CB. (2012). *Appl. Phys. B*, **108**, 9−16.

68. Korbekandi H., Iravani S. (2012). Silver Nanoparticles. *InTech.* **2012** DOI: 10.5772/34157.

69. Hu W., Xiao S., Deng H.,Luo W., Deng L. (2010). *InTech.* **2010.** DOI: 10.5772/8512.

70. Bradley JS. (2007). Chapter 6. The Chemistry of Transition Metal Colloids. ed.G. Schmid, *VCH, Weinheim*, 469–473.

71. Dinh C-T., Nguyen T-D., Kleitz F., Do T-O. (2011). *ACS Appl. Mater. Interfaces* **3**, 2228–2234.

72. Rifai S., Breen CA., Solis DJ., Swager TM (2006). *Chem. Mater.*, 18:**1**, 21–25.

73. Schmid G., Maihack V., Lantermann F., Peschel S. (1996). *J. Chem. Soc. Dalton Trans.* 589–595.

74. BVnnemann H., Brijoux W., Brinkmann R. (1999). *Rev. Roum. Chim*., **44**, 1003–1010.

75. Riess G. (2003). *Prog. Polym. Sci*. **28**, 1107–1170.

76. Sharma VK, Yngard RA., Lin Y. (2009). *Adv. Colloid and Interface Sci.* 145: **1–2**, 83–96.

77. Liu R., Li S., Yu X., Zhang G., Ma Y., Yao J. (2011). *J. Mater. Chem.*, **21**, 14917−14924.

78. Horvath P., Anastas P, (2007). *Chem. Rev.* **107**, 2169−2173.

79. Anastas P., Eghbali N. (2010). *Chem. Soc. Rev.*, **39**, 301−312.

80. El-Shishtawya RM., Asiri AM, Al-Otaibi MM. (2011). *Spectrochimica Acta Part A*, **79**,1505– 1510.

81. Kaler A., Patel N., Banerjee UC. (2010). *Crips*, 11:**4**, 68-71.

82. Sato Y, Wang JJ., Batchelder DN., Smith DA. (2002). *Langmuir* **18**, 2959–2961.

83. Shameli K., Ahmad MB., Yunus WMZW., Rustaiyan A., Ibrahim N. A., Zargar M., Abdollahi Y. (2010). *Int J Nanomedicine* **5**, 875–887.

84. Narayanan K. B., Sakthivel N. (2010). *Adv. Colloid and Interface Sci.* **156**,1–13.

85. Zhang G., Keita B., Dolbecq A., Mialane P., Sécheresse F., Miserque F., Nadjo L. (2007). *Chem. Mater.* **19**, 5821–5823.

86. Sakai N., Fujiwara Y., Takahashi Y., Tatsuma T. (2009). *ChemPhysChem* **10**, 766.

87. Gnatyuk Y., Manuilov E., Smirnova N., Huang W., Eremenko A. (2006). *Nato Sci. Series*, **223**, 485-490.

88. Banerjee A., (2011). *Nanotec. Sci. and Appli.*, **4**, 35–65.

89. Chilibon I., Marat-Mendes JN. (2012). *J Sol-Gel Sci Technol*, **64**, 20−26.

90. Farcau C., Giloan M., Vinteler E., Astilean S. (2012). *Appl. Phys. B*, **106**, 123−132.

91. Zhu J., Ren Y. (2012). *J. Nanopar. Res.,* **14**. doi:10.1007/s11051-012-1326-2.

92. Sepúlveda B., Angelomé PC., Lechuga LM., Liz-Marzán LM., (2009). *Nano Today*, **4**, 123-129.

93. Awazu K., Fujimaki M., Rockstuhl C., Tominaga J., Murakami H., Ohki Y., Yoshida N., Watanabe T. (2008). *J. Am. Chem. Soc.*, 130:**5**, 1676–80.

94. Romeo N., Bosio A., Canevari V., Zanotti L. (1986). *7th EC PV Solar Energy Conference*, 656–661.

95. Standridge SD., Schatz GC., Hupp JT. (2009). *Langmuir :The ACS J. surfaces and colloids*, 25:**5**, 2596–600.

96. Petryayeva E., Krull U. (2011). *Analytica chimica acta*, 706: **1**, 8–24.

97. Ko KH., Lee YC. Jung YJ. (2005). *J. Coll. and Interface Sci*., 283:**2**, 482-487.

98. Chen X., Mao SD. (2007). *Chem. Rev.*, 107:**7**, 2891- 2959.

99. Kanjwal M. A., Barakat NAM., Sheikh FA., Khil MS., Kim HY. (2010). *Inter. J. Appl. Cer. Techno.,* 7, Suppl. **1**, E54-E63.

100. Barakat NAM., Woo KD., Kanjwal MA., Choi KE., Khil MS. Kim HY. (2008). *Langmuir,* **24**, 11982–11987.

101. Sobana N., Muruganadham M., Swaminathan M., (2006). *J. Mol. Catal. A: Chem*., 258:**1-2**, 124–132.

102. Tryba B., Piszcz M., Morawski AW. (2010). *Mater. Sci.,* 5-8..

103. Nasr-Esfahani M., Habibi MH. (2008). *Inter. J. Photoenergy,* **2008**, 1–11.

104. Christopher P., Ingram DB., Linic S. (2010). *J. Phys. Chem. C* **114**, 9173–9177.

105. Wu T-S., Wang K-X., Li G-D., Sun S-Y., Sun J., Chen J-S. (2010). *ACS Appl. Mater. Interfaces*, 2:**2**, 544–550.

106. Zhang F-J., Oh W-C. (2010), *Bull. Korean Chem. Soc.,* 31: **7**, 1981-1987.

107. Velmurugan R., Sreedhar B., Swaminathan M. (2011). *Chem. Cent. J.*, 5:**46**.

108. Akgun B. A., Wren WA., Durucan C., Towler MR., Mellott NP. (2011). *J Sol-Gel Sci Technol*, **59**, 228–238.

109. Akgun BA., Durucan C., Mellott NP. (2011). *J Sol-Gel Sci Technol*, **58**:277–289.

110. Wang Y., Liu L., Xu L., Meng C., Zhu W. (2013). *J. Appl. Phys. 113*, 174311.

111. Koch M., Kiefer S., Cavelius C., Kraegeloh A. (2012). *J. Nanopart. Res*. **14**, 646−657.

112. Li H., Zhao G., Song B., Han G. (2008). *J. Cluster Science*, 667−673.

113. Takahashi Y., Tatsuma T. (2010). *Nanoscale*, **2**, 1494−1499.

114. Lin Y-C. (2013). *Clean Techn Environ Policy* **15**, 359–366 .

115. Nosaka Y., Norimatsu K., Miyama H. (1984). *Phys. Lett.* **106**, 128.

116. Grabowska E., Zaleska A., Sorgues S., Kunst M., Etcheberry A., Colbeau-Justin C., Remita H. (2013). *J. Phys. Chem. C*, **117**, 1955−1962.

117. Subramanian V., Wolf E., Kamat P. (2004). *J. Amer. Chem. Soc.*, 126:**15**, 4943–4950.

118. Jakob M., Levanon H., Dame N. (2003). *Nano*, 3:**3**, 353-358.

119. Rosseler O., Shankar MV., Du Maithaa K-L., Schmidlin L., Keller N., Keller V. (2010). *J. Catal*. **269**, 179–190.

120. Takai A., Kamat PV. (2011). *ACS Nano*, 5:**9**, 7369–7376.

121. Liu SX., Qu ZP., Han XW., Sun CL. (2004). *Catalysis Today*, **93–95**, 877–884.

122. Li J., Xu J., Dai W-L., Fan K. (2009). *J. Phys. Chem. C*, **113**, 8343–8349.

123. Hou W., Liu Z., Pavaskar P., Hung WH., Cronin SB. (2011). *J Catal* **277**,149–153.

124. Christopher P., Xin H., Linic S. (2011). *Nat Chem* **3**,1–6.

125. Dastjerdi R., Montazer M. (2010). *Coll. and Surf. B: Biointerfaces* **79**, 5–18.

126. Wu X., Tatsuma T. (2011). *Commun.* **10**, 2011.

127. Kumar SR., Pillai SC., Hareesh US., Mukundan P., Warrier KGK. (2000). *Mater. Lett*, 43:**5–6**, 286–290

128. Shon H., Phuntsho S., Okour Y., Cho D-L., Kim K. S., Li H-J., Na S., Kim J. B., Kim J-H. (2008). *J. Korean Ind. Eng. Chem.*, 19:**1**, 1-16.

129. Yoganarasimhan SR., Rao CNR. (1962). *Trans. Faraday Soc.*, **58**, 1579-1589

130. Feng X., Li R., Ma Y., Fan Q., Huang W., (2011). *Synthetic Met.* **161**, 1940.

131. Senthilkumar V., Senthil K., Vickraman P. (2012). *Mater. Res. Bull.* **47**, 1051.

132. Fujibayashi T., Matsui T., Kondo M. (2006). *Appl. Phys. Lett*. **88**, 183508.

133. Sato Y., Akizuki H., Shigesato Y. (2008). *Thin Solid Films* **516**, 5758.

134. Sieradzka K., Mazur M., Wojcieszak D., Domaradzki J., Kaczmarek D., Prociow E. (2012). *Thin Solid Films* **520**, 3472.

135. Sieradzka K., Kaczmarek D., Morgiel J., Domaradzki J., Prociow E., Adamiak B. (2013). *Cent. Eur. J. Phys.* 11:**2**, 251–257.

136. Sieradzka K., Kaczmarek D., Domaradzki J., Prociów E., Mazur M., Górnicka B. (2011). *Cent. Eur. J. Phys.* **9**, 313.

137. Sharma P., Kanchan DK., Gondaliya N., Pant M., Jayswal MS. (2013). *Ionics* **19**, 301–307.

138. Sarah MSP., Musa MZ., Asiah MN., Rusop M. (2010). 2010 *International Conference on Electronic Devices, Systems and Applications*, 361–364.

139. Pool ChP., Owens FJ. Jr., (2009). *Tekhnosfera, Moscow, Rus*. 189-216.

140. Kharlamov VF., Korostelev DA., Bogoraz IG., Milovidova OA., Sergeyev VO. (2013). *Semiconductors*, 47:**4**, 494–500.

141. Nitzan A., Brus LE. (1981). *J. Chem. Phys.*, **74**, 5321–5322.

142. Chen CJ., Osgood RM.Jr (1983), *Phys. Rev. Lett.* **50**, 1705.

143. Watanabe K., Menzel D., Nilius N., Freund H-J. (2006). *Chem. Rev.* **106**, 4301–4320.

145. Murakoshi K., Tanaka H., Sawai Y., Nakato Y. (2002*). J. Phys. Chem. B* **106**, 3041–3045.

146. Takahashi Y., Tatsuma T. (2011). *Appl. Phys. Lett.*, 99:**18**, 182110−182113.

147. Nishijima Y., Ueno K., Yokota Y., Murakoshi K., Misawa H., (2010). *J. Phys. Chem. Lett.* **1**, 2031.

148. Kupreev OV., Lazarouk SK., Borisenko VE., Kun L., Tay Beng Kang TB. (2013). *J. Appl. Spectroscopy*, 79:**6**.125−129.

149. Wu Z., Dong F., Zhao W., Wang H., Liu Y., Guan B. (2009). *Nanotech*., **20**, 235701.

150. Zhou W., Liu H., Wang J., Liu D., Du G., Cui J. (2010). ACS Appl. *Mater. Interfaces*, 2:**8**, 2385–2392.

151. Sangpour P., Hashemi F., Moshfegh AZ. (2010). *J. Phys. Chem. C*, **114**, 13955–13961.

152. Nasser AMB, Kanjwal MA., Al-Deyab SS., Chronakis IS., Yong KH. (2011). *Mater. Sci. and Appl*., **2**, 1188-1193.

153. Pant HR., Pandeya DR., Nam KT., Baek W., Hong ST., Kim HY. (2011). *J. Hazardous Mater.* **189**; 465–471.

154. Akhavan O. (2009). *J. Coll. and Inter. Sci.*, **336**, 117–124.

155. Ubonchonlakate K., Sikong L., Saito F. (2012). *Procedia Engineer.* **32**, 656− 662.

156. Nakada T., Yang F., Yoshida A., Tatsuma T., Tamada K. (2011). *Hyomen Kagaku*, **32**, 727-732 (in Jpn).

157. Kazuma E., Tatsuma T. (2013). *Nanorods. J. Phys. Chem. C*, **117**, 2435−2441.

158. Bae E., Lee B-C., Kim Y., Choi K., Yi J. (2013). *Korean J. Chem. Eng.*, 30:**2**, 364-368..

159. Shrivastava S., Bera T., Roy A., Singh G., Ramachandrarao P., Dash D. (2007). *Nanotechnology* **18**, 1–9.

160. Prabhu S., Poulosev EK. (2012). *Inter. Nano Lett.* 2:**32**. 1-8.

CHAPTER 3 EXPERIMENTAL PROCEDURES

3−1 MATERIAL AND METHODS

The materials and methods used in this thesis are described in this chapter. The breakdown of the chapter starts with the tabulation of the sourcing of chemicals used to build-up of the thin films. Thin film supportive substrate cleaning procedures, preparation of precursor solutions and thin films, characterization techniques and the equipment used follows, and highlights, difficulties, or variability in the measurements. Finally, measurement of TG-DTA and preparation for the potassium chloride salt bridge will be outlined at the end of this chapter. With exceptions, the measurements of UV-Vis spectra of the thin films, setup of the photocurrent and decoloration of methylene blue (MB) are described in Chapters 8, 9 and 10 respectively.

3-1.1 Materials

Table 3.1 shows the chemicals used in this thesis. All chemicals were used without further purification with exception to ethanol that was dehydrated using molecular sieve A4. Polished quartz glass substrates with dimensions of 250 × 250 × 1.5 mm^3 were purchased from Akishima Glass Co., Ltd., Japan. NaCl single crystals were purchased from MANAC Incorporated, Japan. Cu grid plates used for the preparation of ultra-thin film for TEM measurements were purchased from NISSHIN EM Co., Japan. A Ag plate (20 × 20 × 0.2 mm^3) used as a counter electrode for photocurrent measurements was purchased from Soekawa Chemical Co., Ltd, Tokyo, Japan. Ag/AgCl electrode used as reference electrodes was purchased from Cypress System Inc, California, USA.

3-1.2 Fabrication procedures of a thin film

3-1.2.1 Substrate Cleaning Process

Table 3.1 Chemicals used in this thesis.

Chemical	Abbreviation[1)]	Fw	Supplier[3)]
2-propanol	IPA	60.10	TC
30% hydrogen peroxide	H_2O_2	34.01	SCI
ethanol [2)]	EtOH	46.07	UCI
Methanol	MeOH	32.04	TC
methylene blue	MB	373.90	WPCI
ethylenediamine-N,N,N',N'- tetra acetic acid	EDTA	292.25	KC
dibutylamine	Bu_2NH	129.25	WPCI
titanium tetraisopropoxide	TTIP ($Ti(O^iPr)_4$)	273.14	KC
silver acetate	AgAc	166.91	WPCI
potassium chloride	KCl	74.55	WPCI
agar, powder	-	-	TC
sodium sulfate	Na_2SO_4	142.04	WPCI
nitrilotriacetic acid	NTA	191.14	TC
zirconium tetra-butylamine	$Zr(o\text{-}Bu)_4$	383.68	WPCI

1) Abbreviation that are used in this thesis and recognised in chemical industry.

2) The purchased solvent was dried over 4A molecular sieves before use. Other materials were used without further purification.

3) Supplier codes are as follows: TC; Taisei Chemical Co., Ltd., SCI; Santoku Chemical Industry Co., Ltd., UCI; Ueno Chemical Industries, Ltd., WPCI; Wako Pure Chemical Industry, Ltd., KC; Kanto Chemical Co., TCI; Tokyo Chemical Industry. Co. Ltd.

High quality thin films require ultra clean glass substrate surface without particle contamination, metal contamination, organic contamination, ionic contamination, water absorption, native oxide and atomic scale roughness. It's considered that this substrate cleaning process is very important to realize the fabrication of a desirable thin film that can undergo reproducibility. Mostly people use water as the cleaning substance. Water is called the universal solvent because more substances dissolve in water than in any other chemical. This has to do with the polarity of each water molecule. The hydrogen side of each water (H_2O) molecule carries a slight positive electric charge, while the oxygen side carries a slight negative electric charge. This helps water dissociate many ionic compounds into their positive and negative ions. The positive part of an ionic compound is attracted to the oxygen side of water while the negative portion of the compound is attracted to the hydrogen side of water. However, water is not truly pure. Pure water has less than 1 colony of bacteria per milliliter and less than 1 particle per milliliter. Instead, water contains minerals and other substances dissolved from the surrounding rocks and environment. Never the rest, deionized (DI) water is the most available cleaning substance available in any laboratory that can be used to clean glass substrates. Commercial DI water is known to be highly purified and filtered to remove all traces of ionic, particulate, and bacterial contamination. The theoretical resistivity of pure water is 18.25 MΩcm at 25ºC **[1]**.

In this thesis, the quartz glass substrates that are used as supportive surfaces for the thin films were cleaned on a basis of cleaning process, which was proposed in our laboratory. The first step, which use a solution of surfactant/alkaline as detergent/water (H_2O) (detergent : H_2O = 5 : 95, called by Clean-Aec), was performed to remove any organic material and metallic impurities. This was followed by rinsing several times with DI

water. After that, these glass substrates were cleaned with 2-propanol (IPA) in an ultrasonic bath to remove physisorbed organic molecules, natives and chemical oxides from the surfaces. Then the wafers were dried in a drying oven at 70°C.

3-1.2.2 Preparation of Precursor Solutions

As shown in Scheme 3.I(a), the precursor solution $\boldsymbol{S_{Ti}}$ contains a Ti^{4+} complex of EDTA was prepared in accordance with the molecular precursor method (MPM) reported in our laboratory **[2]**.

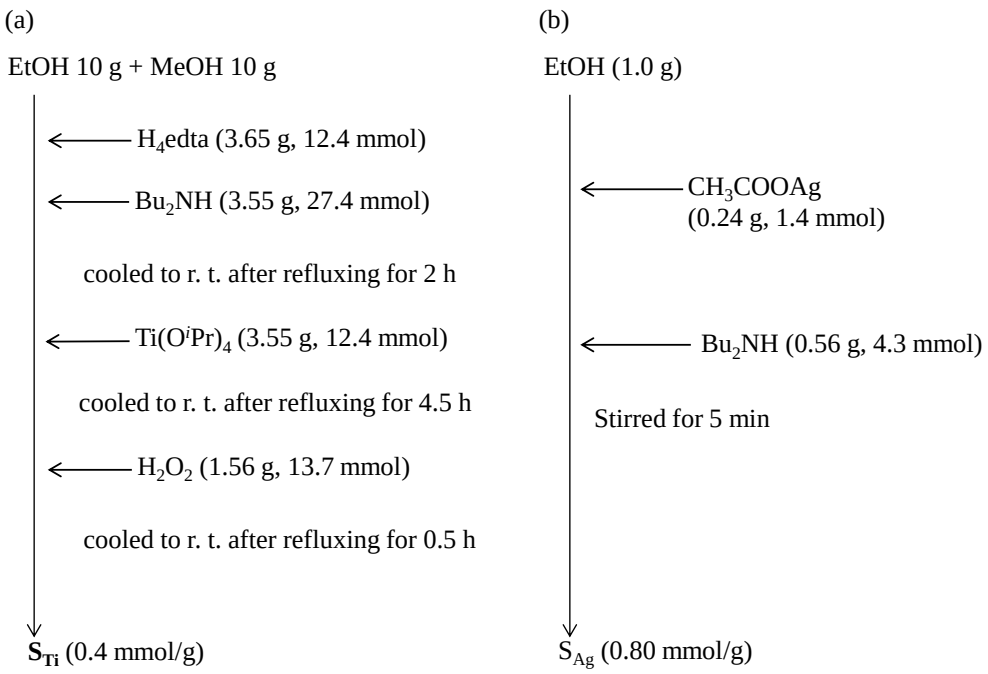

Scheme 3.I. Preparation procedures of the (a) precursor solution $\boldsymbol{S_{Ti}}$ contains a Ti^{4+} complex of EDTA and (b) precursor solution, $\mathbf{S_{Ag}}$ containing silver acetate.

A stable precursor solution for the spin-coating process can be facilely prepared by reacting an isolated Ti(IV) complex of EDTA with dibutylamine in ethanol, where EDTA (H_4edta) represents ethylenediamine-N,N,N′,N′-tetraacetic acid. Upon the

addition of hydrogen peroxide, the solution of an orange-red color was obtained. The red color of the coating solution is characteristic of Ti^{4+} complexes coordinated with the H_2edta^{2-} and peroxo ligand. Based on the structural study reported by Nagai and Sato **[3]**, it was indicated that the central Ti^{4+} ion is linked by two nitrogen atoms of EDTA ligand in a Ti complex $[Ti(O_2)(Hedta)]^-$. The peroxo complex of Ti^{4+} can be formed in ethanol under the presence of butylamine. Figure 3.1 shows an ORTEP view of the precursor complex having the EDTA and peroxo ligands linked to the central Ti^{4+} ion. These coordinations of both EDTA and peroxo ligand with central Ti^{4+} ions enhanced the stability of the coating solution. Furthermore, the coordination number of EDTA ligand in the complex ion is 5, make the percursor complex having excelent stability, homogeneity, miscibility and coatability.

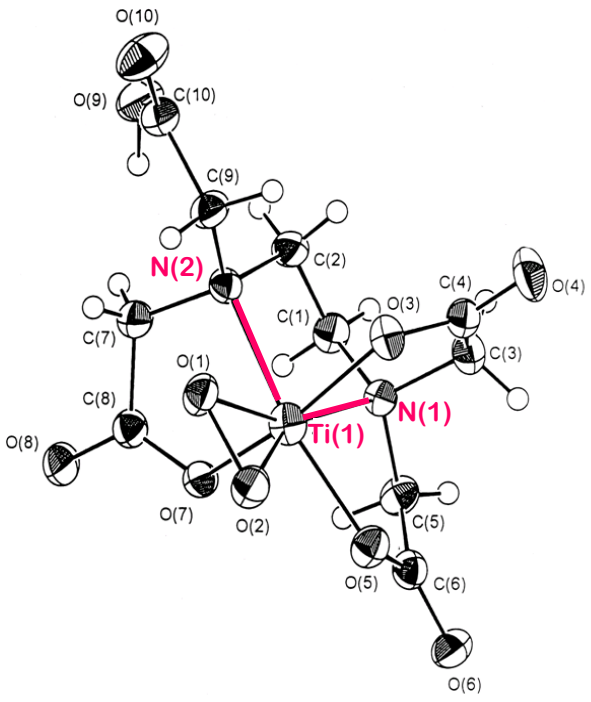

Fig.3.1 The structure of the EDTA complex formed in the solution was examined in order to determine the X-ray crystal structure of its diethylammonium salt **[3]**.The

single crystal was $\{(C_2H_5)_2NH_2\}[Ti(O_2)(Hedta)]\cdot 1.5H_2O$; in a monoclinic crystal system, $P_{21/c}$ with a = 8.583(1), b = 6.886(1), c = 36.117(2) Å, and β = 92.780(3)°.

The ethanol solution of Ag-nanoparticle, $\boldsymbol{S_{Ag}}$ for fabrication of Ag-nanoparticles titania (Ag NP/TiO_2) composite thin film was also prepared separately, based on the new method developed in this thesis. Scheme 3.I(b) shows how the silver precursor solution, $\mathbf{S_{Ag}}$ was synthesized. Usually, for Ag nanoparticle suspensions, a common method is the Lee–Meisel method **[4]**, which is a variation of the Turkevich method **[5]** in that Ag nitrate is used as the metal source. The application of acetate adapted in this thesis in the reaction allowed synthesizing metallic nanoparticles without any additional reducer. It makes that kind of synthesis simple, fast, and relatively cheap, and makes it possible to obtain pure composites without any impurities, which is a big advantage when compared to the reduction of silver nitrate **[6, 7]**.

3-1.2.3 Spin coating the precursor solutions and heat treatment furnace

Spin coating is one of the thin film fabricating processes used to deposit ultra-thin films on substrates. It is performed by deposition a precursor solution with enough amounts to be evenly spread on the substrate surface. The precursor solutions employed in this thesis can easily washed away with water from substrate surface and the substrate can be recycled. Recycling of such a substrate in an industrial application would constitute a large improvement in the loading process, and will be suggested in the Recommendations section of this thesis. Figure 3.2 illustrates the steps involved in spin coating system employed in this thesis. A spin coating system is used for thin film formations and for creating new materials at high temperature. Figure 3.3 shows two

thin films of titania (TiO_2) and Ag nanoparticles (Ag NP) were formed by heat treating the spin-coated precursor films and applying the solutions S_{Ti} and S_{Ag}, respectively.

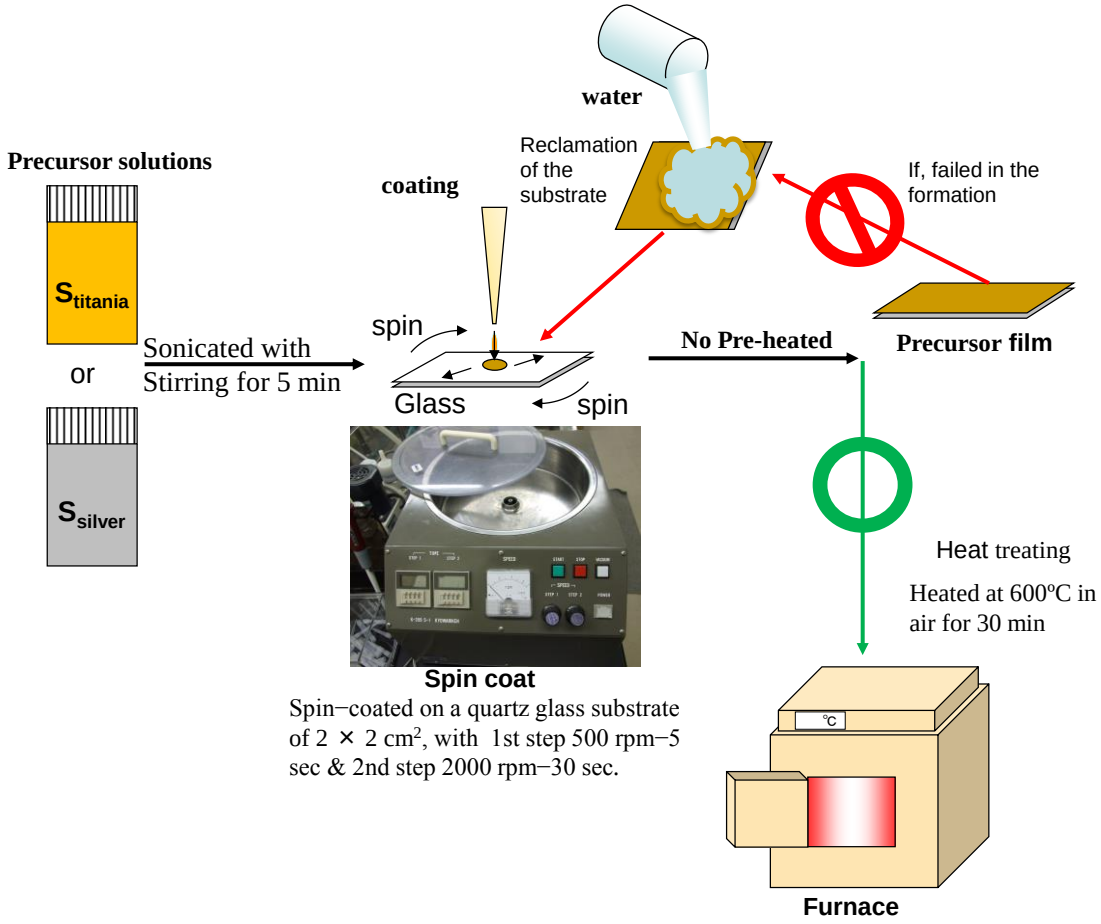

Fig. 3.2 Fabrication of thin films on quartz glass using spin coating system

3-1.2.4 Preparation of Ag/ Titania composite Precursor Solutions and Thin films

The $S_{composite}$, with different compositions were achieved by mixing a certain amount of S_{Ag} with S_{Ti}. Then, the $S_{composite}$ were sonicated with stirring for 5 min to increase the homogeneity. Figure 3.4a–h shows the photographs of the ten resultant composite thin films. Thin films were fabricated by heat-treatment at 600°C for 0.5h to remove residual organic compounds.

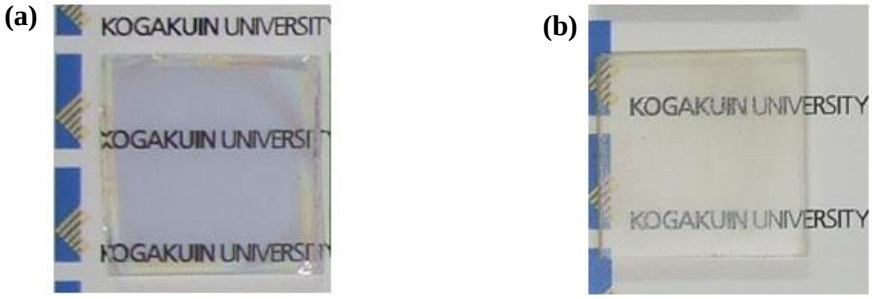

Fig. 3.3 Photographs of (a) TiO_2 thin film and (b) Ag NP fabricated at 600ºC for 30 mins.

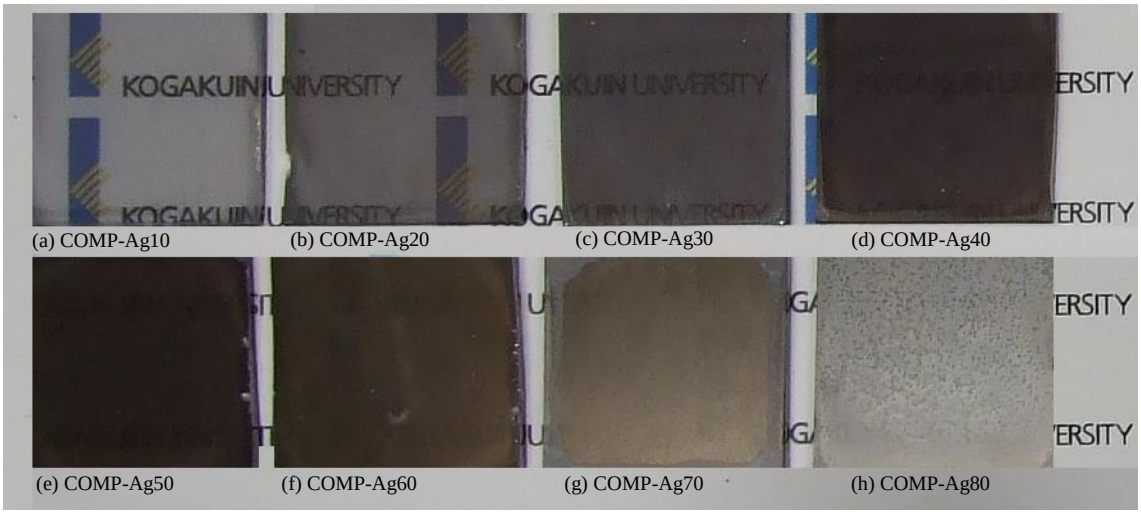

Fig. 3.4 Photographs a–h, of the Ag-NP/TiO_2 composite thin films at various amounts of Ag molar concentrations: a 10, b 20, c 30, d 40, e 50, f 60, g 70, and h 80, respectively.

The Ag-nanoparticle/titania composite (COMP-Ag*n*) films were fabricated by heat treating the spin-coated precursor films, while applying the solution $\boldsymbol{S_{composite}}$, at *x* ºC for *y* min in air. The number *n* in the notation of the composite films indicates the silver molar percentage (Ag mol%) to TiO_2; for example, the name COMP-Ag40 indicates

that the silver molar percentage in the $\mathbf{S}_{\boldsymbol{composite}}$ solution was 40 mol%. The Ag-NP/TiO_2 composite thin films were deposited by spin coating of the $\boldsymbol{S}_{\boldsymbol{composite}}$ onto the substrates with a double step mode: first at 500 rpm—5 s and then at 2000 rpm—30 s in all the cases. The furnace for heat treatment used in this investigation was QHC-P610CP (ULVAC RIKO Co. Ltd).

3−2 MATERIALS CHARACTERIZATIONS

One essential prerequisite for the fabrication, characterization and development of nanomaterial based thin films is the availability of techniques, which allow the characterization of the physical and chemical properties of a nanoscale level. Meanwhile there is a considerable arsenal detection and characterization of methods for nanostructures. Here, I am presenting only the methods that were employed in this thesis for the study of nanomaterial properties. In the following sections the specifications and limitations of the main methods used for characterization of composite thin films employed in this thesis will be briefly summarized.

3-2.1 Atomic structure and chemical composition

3-2.1.1 X-ray diffraction (XRD)

To characterize a thin film atomic structure at large scale, XRD technique appears as the most powerful methods. It is based on the diffraction of an X-ray incident beam by reticular planes of crystalline phases in a thin film sample. The bean is diffracted at specific angular positions with respect to the incident beam depending on the phases of the sample. When the crystal size is reduced toward nanometric scale, then a broadening of diffraction peaks is observed and the width of the peak is directly correlated to the

size of the nanocrystalline domains, which based on Debye-Scherrer relationship **[8]**. Neutron beam can be also used to replace the X-ray incident beam, whoever, the diffracted intensities are modulated by weighting factors, which differ between X-ray and neutron due to the difference in the nature of interaction. Moreover, neutron diffraction requires also neutron facilities, however all techniques can be performed on dry powder, thin films or on a liquid suspensions.

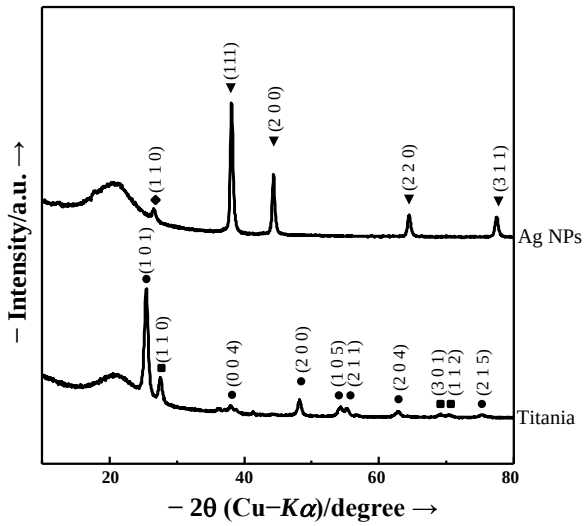

Fig. 3.5 XRD patterns of the silver and titania thin films. The peaks of each phase are denoted as follows: filled inverted triangle silver, filled circle anatase, and filled square rutile (MXP-18 AHF22, Bruker AXS).

In this thesis, the X-ray diffraction (XRD) patterns of Ag particles, titania, and COMP-Agn films were measured using an X-ray diffractometer (MXP-18 AHF22, Bruker AXS) with Cu–Ka rays generated at 45 kV and 300 mA. Parallel beam optic was employed with an incident angle of 0.3º. Figure 3.5 shows XRD patterns of the films fabricated at 600ºC applying the solutions $\boldsymbol{S_{Ti}}$ and $\boldsymbol{S_{Ag}}$, respectively, from which it was elucidated that the resultant silver and titania films contain Ag crystallized in the

cubic system [JCPDS card 4-783, 1978] and titania crystallized in the tetragonal system [JCPDS card 21-1272, 1978; JCPDS card 21-1276, 1978], respectively.

3-2.1.2 X-ray Photoemission Spectroscopy (XPS)

XPS or Electron Spectroscopy for Chemical Analysis (ESCA) refers to the photoemission of electrons produced by a monochromatic X-Ray or UV beam. XPS spectrometers measure the kinetic energies of the electrons. Due to the limited means of free path of the electrons in a thin film, only few nanometric layers are investigated. Since binding energies (eV) are highly sensitive to chemical bonding, a map of the bonding configuration is obtained for surface layers. Another method used to investigate the conduction band of the material is X-ray Absorption Spectroscopy (XAS). However, XAS methods are selective and well adapted for samples with lower crystallinity (amorphous).

In this thesis, a Phi Quantum 2000 Scanning ESCA Microprobe (Shimadzu) with a focused monochromatic Al-Kα X-ray (1486.6 eV) source was employed in order to evaluate the elemental states and quantities—Ti, O, C and Ag— in the thin films. Figure 3.6 shows the XPS high resolution wide scans for COMP-Ag50.

No critical surface charging during the XPS measurements was observed; thereby, no correction of binding energy was performed. The depth profiles were obtained with the identical instrument. The stepwise etching was performed by bombarding the Ar^+ ions with 2 kV for 3 min before measuring each layer. The major XPS peaks include Ag 3d, Ti 2p, and O 1s. The XPS peak for C1s (284.8 eV) is due to the adventitious hydrocarbon from the XPS instrument itself.

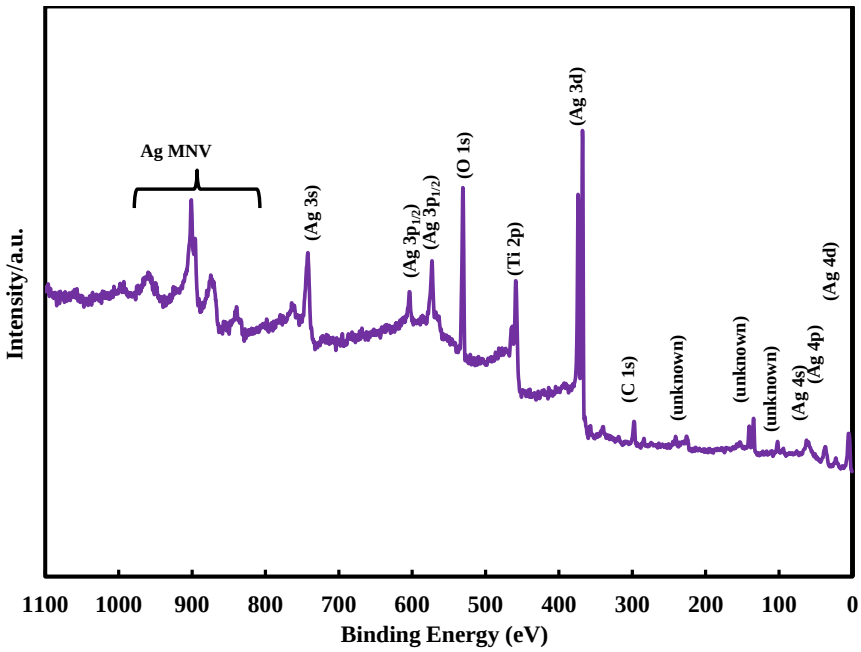

Fig. 3.6 Representative wide-scan XPS survey spectrum taken from the surface of COMP-Ag70 composite thin films. (Phi Quantum 2000 Scanning ESCA Microprobe).

3-2.2 Determination of size, shape and surface area of the thin films

Electron microscopies are methods of choice used to investigate particles size, shape and structures and also agglomerates. They regroup two techniques, namely: Field Emission Scanning Electron microscopy (FE-SEM) or Transmission Electron Microscopy and both techniques will be employed in this thesis. STEM microscopes are field emission gun scanning/transmission electron microscopes. The STEM combines the features of both TEM and SEM. Apart from electrons microscopic methods, other methods include Brunauer Emmet Teller (BET), helium pycnometry, epiphaniometer, laser granulometries, Zeta potential, elliptically polarized light scattering.

3-2.2.1 Field Emission Scanning Electron microscopy (FE-SEM)

FE-SEM is a microscope that uses a stream of electrons rather than beam of light to form an image (electrons are emitted from a field-emission gun). The SEM was used in this study rather than a light microscope, because SEM has a large depth of field, which allows a large amount of the substrate surface to be focused and observed at one time. FE microscopes could reach resolutions of the order of 1 nm using a cold cathode. If they are equipped with an Energy Dispersive Spectrometer (EDS), chemical composition can be obtained. Preparation of the samples is relatively easy, although some most SEMs may require the sample to be conductive. In our laboratory, the nonconductive thin films are usually coated with gold particles through sputtering technique. The photograph of FE-SEM in our laboratory is shown in figure 3.7. The surface morphology of the resultant films was observed using a FE-SEM (S-4200, Hitachi) at an accelerating voltage of 5.0 kV. The elemental mapping of COMP-Ag70 films was observed with an EDS equipment which is equipped on FE-SEM (S-4200, Hitachi).

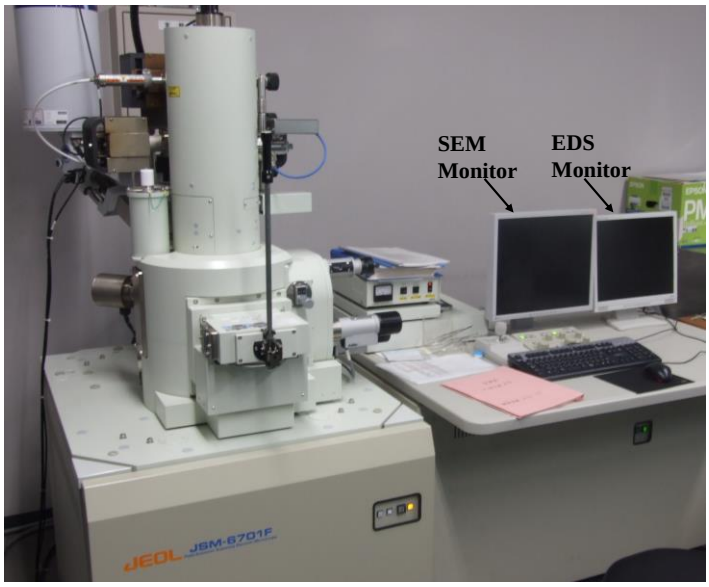

Fig. 3.7 Photo for FE-SEM (Field Emission Scanning Electron microscopy.

Figure 3.8 shows the surface morphology of the silver and titania films obtained. Then size distribution and shape of nanoparticles can be investigated by FE-SEM.

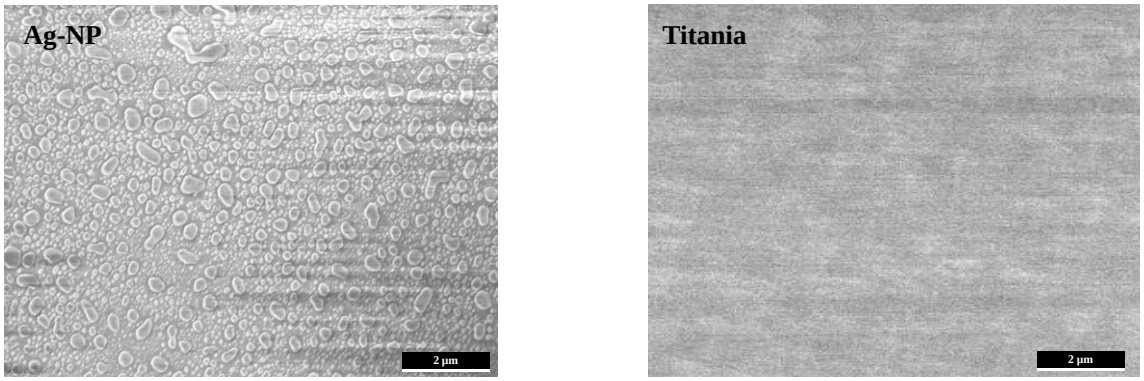

Fig. 3.8 Surface morphology of silver and titania thin films obtained by SEM at an accelerating voltage of 1 kV. (S-4200, Hitachi).

3-2.2.2 Transmission Electron Microscopy (TEM)

Unlike the observation of the surface of the thin film using SEM, the study of internal morphology of the thin film is important and TEM image is the most important analysis method to characterize physical film quality and interface condition. Size distribution (with low statistic) can be obtained by counting the number of particles. At lower magnifications, the way in which nanoparticles are connected can be observed. Then, qualitative information about the agglomerates structures is deduced from observations. The TEM resolution is below 1 nm for the High Resolution Microscopes (HRTEM). High resolution is performed to look at crystal quality and interfaces. Figure 3.9 shows TEM system. First, focus lenses change convergent angle and beam size. The electron beam transmitted through the thin fragment sample passes objective lens and projective lens, and finally projected on fluorescent screen. Recording of the image is performed

by direct exposure on exclusive film for electron microscope set lower part of the fluorescent screen.

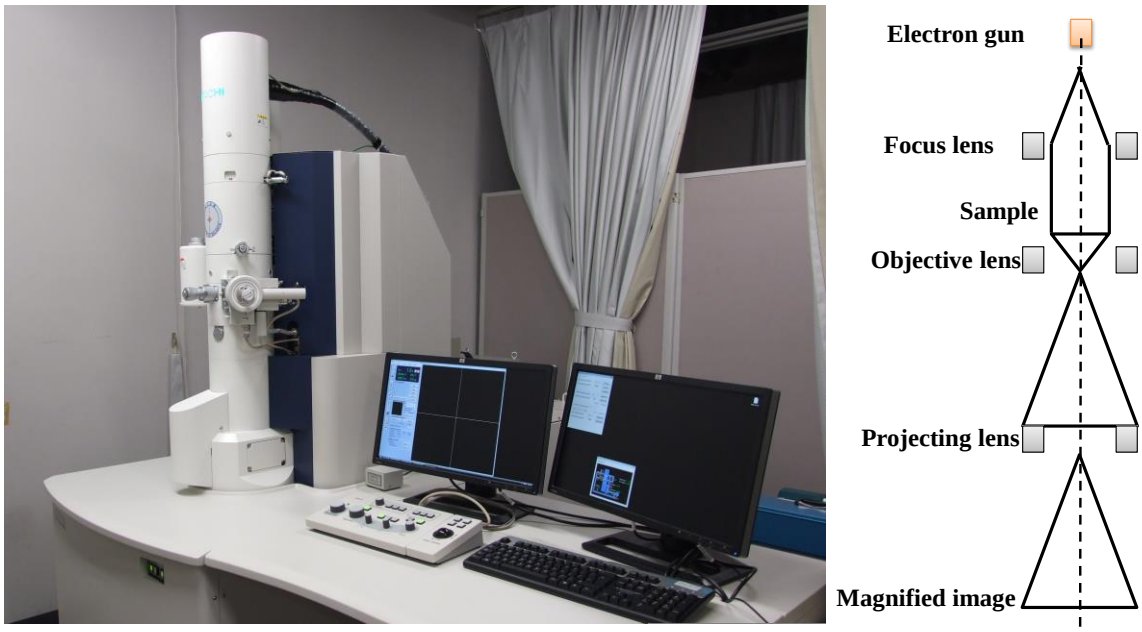

Fig. 3.9 Photo and schematic diagram for TEM (Transmission Electron Microscopy) observation. Several magnetic lenses are used to magnify the object image.

Electron interacts strongly with lattice by scattering. Thus, sample has to be very thin fragment. Required thickness of the sample is 5 to 500 nm at 100 kV. TEM images are obtained in very high resolution such as 0.2 to 0.3 nm at 200 kV. In this thesis, the nanostructure images were observed with a transmission electron microscope (TEM H8100, Hitachi) at an accelerating voltage of 120 kV.

3-2.2.3 Thickness Analysis – Profilometry

The film thicknesses of titania and COMP-Agn films were measured using a stylus profilometer (DEKTAK3, Sloan) with the travel length set to 30 mm in order to traverse the breadth of the 10 mm x 30 mm deposited film. This was done to ensure that the

height of the film was measured at both sides in order to correct for any unevenness or tilt of the underlying substrate. The scan traverse is shown below in figure 3.10.

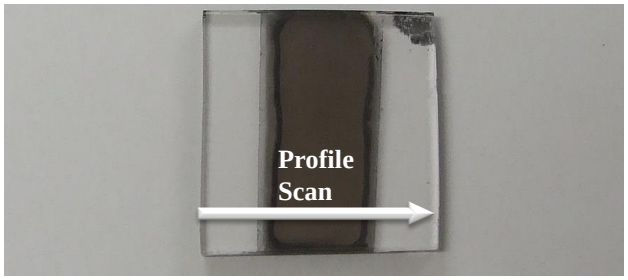

Fig. 3.10 Profile scan of a 10 x 30 mm Ag/TiO_2 composite thin film on a 30 mm x 30 mm glass slide.

The samples were measured at three points across the film and repeated at the first point three times, and at the second point two times to give a total of six perspectives as to the distribution of scan data. One such scan is shown in figure 3.11, below.

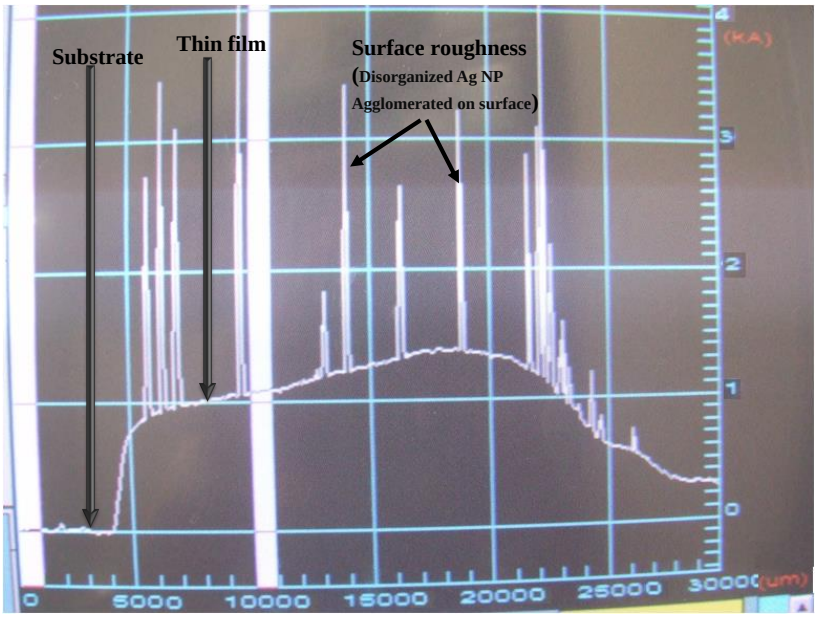

Fig. 3.11 Sample profilometric scan covering a 30 mm travel span.

The data was corrected for any underlying sample tilt and curvature by the software produced by Veeco Inc. Surface roughness is a product of disorganized film growth, and may be a result of Ag NPs agglomerated on surface of the thin film. Moreover, any moisture present while loading will lead to the decomposition of the film as described by Schopf and Koßmehl, [8] and the resultant film will be rough and porous, while dissolved gasses may result in bubbles on the surface producing porosity.

3.2.3 Four probe technique

The four probe technique shown in figure 3.12 was employed in this thesis to determine the electrical resistance of the synthesized thin films.

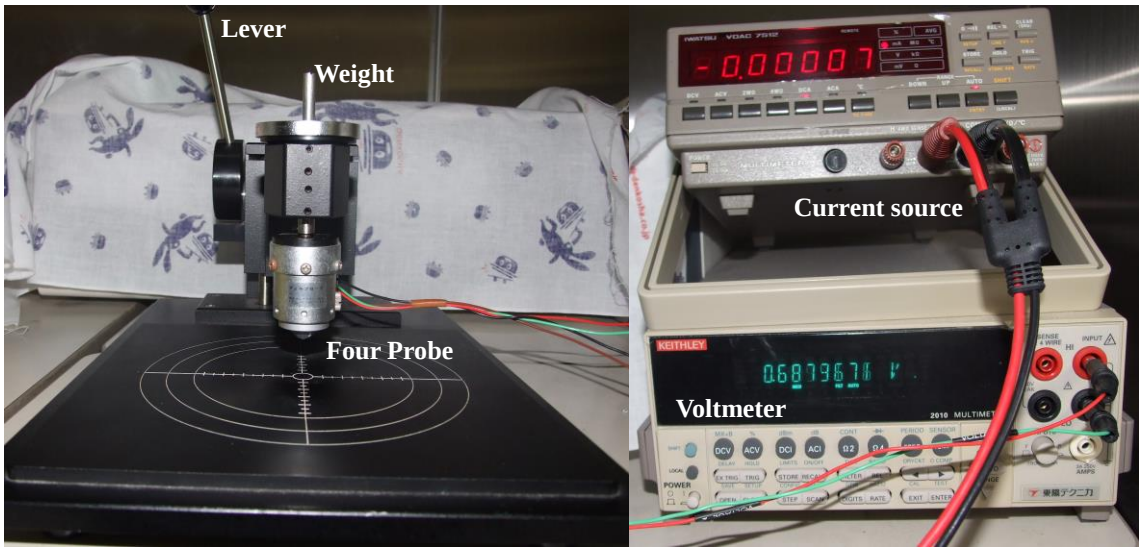

Fig. 3.12 Photo of four probe system

The film thicknesses of titania and COMP-Ag*n* films were measured using a stylus profilometer (DEKTAK3, Sloan). The electrical resistance at 25°C was measured using the four probe method involving two multimeters (VOAC7512, Iwatsu and Model 2010 Multimeter, Keithley) and a regulated DC power supply (Model PAB 32-1.2, Kikusui

Electronics Corp.). Four gold-plated tungsten probes (FELL type, K&S) were placed at intervals of 1 mm, and an added load of 0.2 kg was applied.

Using data obtained from four probe measurement, resistance of the thin film can be calculated from potential difference (voltage (v)) between inside 2 terminals (Between B and C probes) after applying the current (I) between outside 2 terminals (between A and D probes) as illustrated in figure 3.13.

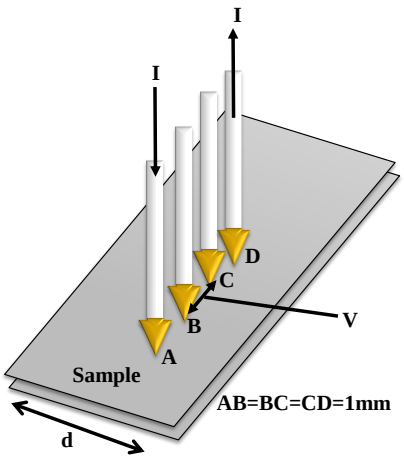

Fig. 3.13 Illustration of four point probe system

For an arbitrarily shaped sample the electrical resistance (ρ) is given by:

$$\rho = \frac{V}{I} \cdot CF \ldots\ldots\ldots\ldots\ldots\ldots\ldots\ldots\ldots\ldots\ldots\ldots\ldots\ldots\ldots\ldots (3.1)$$

where CF is correction factor that depends on the sample geometry. For instead, if the distance among probes (s; in this study, s= 1 mm) is greatly shorter than the width of samples (d), CF equals to:

$$\frac{\pi}{In \cdot 2} = 4.53 \ldots\ldots\ldots\ldots\ldots\ldots\ldots\ldots\ldots\ldots\ldots\ldots\ldots\ldots\ldots\ldots\ldots (3.2)$$

The electrical resistivity, ρ, of the films was calculated using equation (3.3):

$\rho = cRt$ ... ...(3.3)

where c, R, and t represent the correction value (4.53), electrical resistance, and film thickness, respectively.

3-2.4 Mechanical strength of the thin films

The mechanical properties of samples are often determined by means of indentation methods **[10]**. Young`s modulus can be investigated using a indenter for a load from 0 N to 200 N, by the depth sensing indentation (DSI) method for an indentation load from 0 mN to 2000 mN and by the impulse excitation technique (IET) at room temperature and high temperatures. Marshall *et al.*, **[11]** developed a method for determining the Young`s modulus based on the measurement of elastic recovery of the in-surface dimensions of Knoop indentations. The extent of recovery depends on the elasticity index, or H/E ratio. The DSI method is the most frequently used indentation test for determination the Young`s modulus, knoop hardness and stress. It was developed by Oliver and Pharr, 1992 **[12]** and it is based on recording the load – penetration curves during the loading and unloading process and takes into account the large elastic recovery during unloading. Young`s modulus can be determined from the slope of the unloading curve using a modified form of Sneddon`s flat punch equation **[13]**. According to the ASTM standard **[14]** in the case of isotropic samples of rectangular shape with appropriate dimensions, the Young's modulus E can be calculated as:

$$E = 0.9465 \times \left[\frac{m \times {f_r}^2}{b}\right] \times \left[\frac{L^3}{t^3}\right] \text{ ... ... } (3.4)$$

where f_r represents the resonance frequency and m the mass of the sample. L, b, and t are the dimensional units (length, width, and thickness).

The instrumented scratch tests included sliding-scratching over 5 mm length at a speed of 0.2 mm/s under a constant load, using a Rockwell diamond indenter, on test specimens. The scratch hardness (HS) can be calculated using equestion 3.5 **[15]**.

$$HS = \mathrm{H}_R \times \left[\frac{{f_S}^2}{f_R}\right] \times \left[\frac{W_R^2}{W_S^2}\right] \ldots\ldots\ldots\ldots\ldots\ldots\ldots\ldots\ldots\ldots\ldots \quad (3.5)$$

HR is the hardness of the reference material, WR and WS are the scratch widths on the reference and specimen, respectively. The scratching loads for the specimen (FS) and the reference (FR) should be such that the scratch widths should be similar.

In this thesis, the indentation, scratch, and imaging techniques were employed for evaluation of mechanical and tribological properties of numerous film specimens using a scratch test of the coated film was performed using a scratch tester (HEIDON-22, Shinto Scirntific) equipped with a Rockwell diamond C stylus of 200 Am radius and friction force measurement. The photograph of the instrument employed in this thesis and its schematic representation are presented in figure 3.14.

The measurements were made at progressive loads from 0 to 30 N. The stage speed was 0.40 mm/s and the stylus was pressed on a sample at the rate of 0.26 mm/s. All scratch traces were observed by laser microscope. Its software allows for image analysis to obtain scratch depth profile along any direction of the image. The hardness values were obtained from equation (3.5) above. Three samples were selected for each condition and tests were performed twice for each sample.

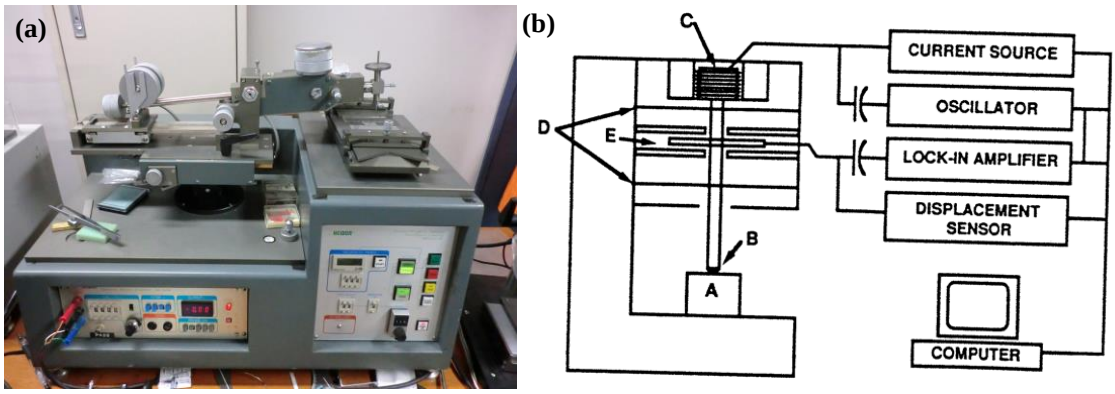

Fig. 3.14 (a) Scratch tester (HEIDON-22, Shinto Scirntific), (b) a schematic representation of the experimental apparatus used to perform the indentation experimement: (A) sample; (B) indenter; (C) load application coil; (D) indentation column guide springs; (E) capacitive displacement sensor.

The method is based on the notation that, at peak load, the material conforms to the shape of the indenter to some depth; if this depth can established from the load-displacement data, the projected area of contact can be estimated directly from the shape fuction.

Figure 3.15 shows the representative load-displacement plots, the unloading portions of which were analyzed using the Oliver-Pharr methodology **[12]**. Two obvious choices for the depth, though not the only one, are the depth at peak load, h_{max} (i.e., the residual depth of the hardness impression after loading cycle), and the final depth, h_f (i.e, the residual depth of the heardness impression after final unloading), both of which are easily determined from indentation load-displacement data as illustrated in figure 3.15. Figures 3.16 shows load-displacement curves obtained from indentation tests on a quartz glass substrate and pure TiO_2 thin film fabricated quartz glass.

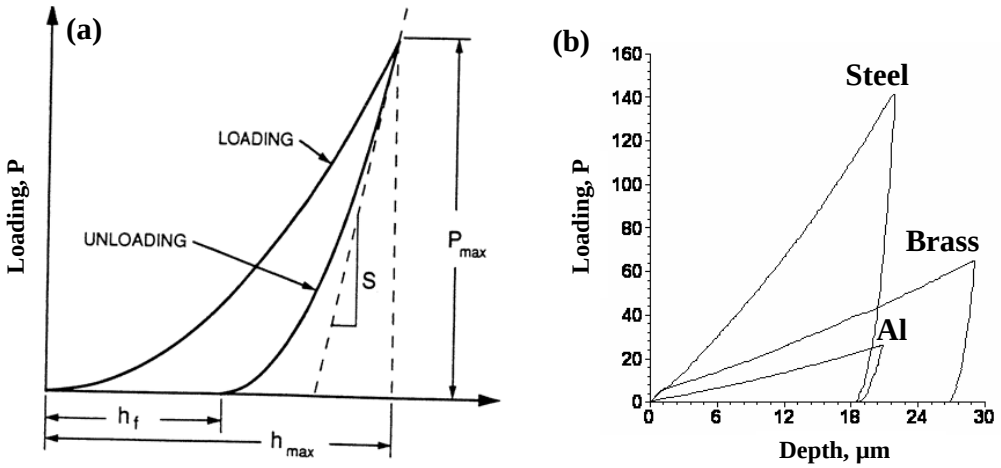

Fig 3.15 (a) A schematic representation of load versus indenter displacement data **[12]** (b) load-displacement plots for metals **[15]**.

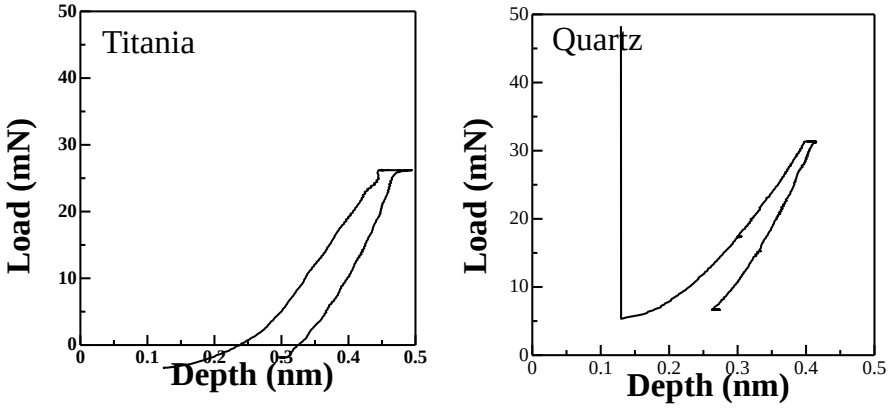

Fig. 3.16 Indent test curves of the pure titania and quartz glass.

3-2.5 TG-DTA technique

Thermal gravimetry (TG) is method of thermal analysis in which changes in physical and chemical properties of materials are measured as a function of increasing temperature (with constant heating rate), or as a function of time (with constant temperature and/or constant mass loss) **[16]**. TG is commonly used to determine selected characteristics of materials that exhibit either mass loss or gain due to

decomposition, oxidation, or loss of volatiles (such as moisture). On the other hand differential thermal analysis (DTA) is a thermoanalytic technique, similar to differential scanning calorimetry. In DTA, the material under study and an inert reference are made to undergo identical thermal cycles, while recording any temperature difference between sample and reference. This differential temperature is then plotted against time, or against temperature (DTA curve or thermogram). Changes in the sample, either exothermic or endothermic, can be detected relative to the inert reference. Thus, a DTA curve provides data on the transformations that have occurred, such as glass transitions, crystallization, melting and sublimation.The combination of the two instruments refer as TG-DTA can provide the temperature and heat flow of the sample, simultaneously with mass loss. It can be used to study the crystallization behavior of a precursor solution under thermal condition.

In this thesis, TG-DTA machine, (Model TAS-100, Rigaku, Japan) is employed. A DTA consists of a sample holder comprising thermocouples, sample containers and a ceramic or metallic block; a furnace; a temperature programmer; and a recording system. The key feature is the existence of two thermocouples connected to a voltmeter. One thermocouple is placed in an inert material such as Al_2O_3, while the other is placed in a sample of the material under study. As the temperature is increased, there will be a brief deflection of the voltmeter if the sample is undergoing a phase transition. This occurs because the input of heat will raise the temperature of the inert substance, but be incorporated as latent heat in the material changing phase.

The assessment of DTA data must be done with care since the curves and their interpretation can be influenced significantly by experimental conditions that can cause

to lower temperatures: (1) a slow heating rate results in peak broadening, which lowers the onset temperature; (2) a slow heating rate also causes the entire peak to shift; (3) fine particle size shifts and narrows the entire peak; and (4) the static enclosed atmosphere induces a slightly reducing atmosphere, which enhances oxygen vacancy formation in oxides.

3-2.6 Preparation of KCl gel for salt bridge.

In this thesis, a salt bridge consists of a U-shaped glass tube filled with a relatively inert electrolyte; potassium chloride is used. The electrolyte is jellified with agar to help prevent the intermixing of fluids which might otherwise occur. The conductivity of a glass tube bridge depends mostly on the concentration of the electrolyte solution. An increase in concentration below saturation increases conductivity. Beyond-saturation electrolyte content and narrow tube diameter may both lower conductivity **[17]**.

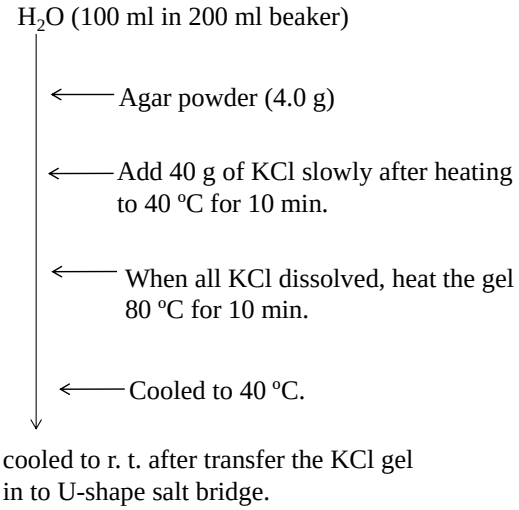

Scheme 3.II. Preparation procedure of the KCl salt bridge used in photocurrent measurement.

3-3 REFERENCES

1. Wanga L., Liu R., Teng Y. (**2011**). *Journal of Luminescence* **131**, 705–709.

2. Sato M., Hara H., Nishide T., Sawada Y. (1996). *J Mater. Chem.* **6**, 1767-1770.

3. Nagai H., Sato M. (2012). *InTech, Winchester*, Chapter **13**, 297-322.

4. Lee PC., Meisel DJ. (1982). *Phys. Chem.* **86**, 3391–3395.

5. Turkevich J., Stevenson PC., Hillier J. (1951). *Discuss. Faraday Soc*. **11**, 55.

6. Kang J-G., Sohn Y. (2012). *J. Mater. Sci.*, 47:**2**, 824-832.

7. Seery MK., George R., Floris P., Pillai SP. (2007). *J. Photochem. Photobiol A: Chem*., 189: **2-3**, 258–263.

8. Holzwarth U. and Gibson N. (2011). *Nat. Nanotech.* **6**, 534.

9. Schopf G. and Koßmehl G. (1997). *Berlin: Springer*.

10. Špaková J., Dusza J., and Juhász A. (2008). *Powder Metallurgy Progress*, 8:**1**, 29-34.

11. Marshall DB., Noma T., Evans AG. (1982). *Am. Ceram. Soc*., **65**, C175-176.

12. Oliver WC., Pharr GM. (1992). *J. Mater. Res.*, **76**, 1564-1583.

13. Sneddon IN. (1963). *Int. J. Eng. Sci.*, **3**, 47.

14. ASTM E. 1876-99, (1999). *ASTM Philadelphia,* 1-7.

15. Gitis N., Vinogradov M., Hermann I., Kuiry S. (2007). *Res. Soc. Symp. Proc*. 1049

16. Coats AW., Redfern JP. (1963). *Analyst* **88**, 906–924.

17. Lee EK., Pearson EP. (1945). *Electrochem. Soc.* 88:**1**, 171-183

CHAPTER 4: DETERMINATION OF OPTIMAL HEAT TREATMENT TEMPERATURE FOR THE FABRICATION OF Ag/TiO_2 COMPOSITE THIN FILMS USING MPM.

4−1 INTRODUCTION

Specific heat treatment temperature causes the changes in material structure, nature of distribution of the nanoparticles/crystallites in the film, material density, desorption of volatile impurities from the film surface depending on the method, dopants, temperature, time etc **[1]**. The effects of heat treatment temperature are expected to be reflected in the crystal phase of the films. TiO_2 has three crystal phases: anatase (tetragonal), rutile (tetragonal) and brookite (orthorhombic). Among them, the anatase is a meta-stable phase and has a band gap (3.2 eV) higher than the other ones. In the synthesis of TiO_2 films by various methods, the initial crystalline TiO_2 phase formed is generally anatase. However, anatase and brookite phases may be transformed to rutile phase with heat treatment **[2]**. The latter is difficult to synthesize and so is seldom studied **[3]**. The production of high photoactivity material with high temperature anatase phase stability is one of the key challenges in smart coating technology. Increase in temperature allows the structural transformation of TiO_2 from anatase to rutile irreversibly at elevated temperatures **[4]**. This transformation does not have a unique temperature and the processes that are involved in the transformation. Recently, Behforooz *et al.,* **[5]** review the differences between the two main polymorphs of titanium dioxide, the nature of the anatase to rutile transformation, and the principles of controlling phase composition through the inhibition or promotion of the transformation of anatase to rutile.

The rutile structure has a band gap of 3.0 eV and is the most common white pigment in paint products due to its extremely high refractive index (n = 2.8) **[6]**. It should be noted that it is possible to form rutile under near room temperature conditions **[7, 8]**. Hydrothermal methods of synthesis, which can facilitate the precipitation of crystalline

TiO_2 directly from a liquid phase, can be controlled to precipitate rutile. Aside from this method, rutile is obtained only through high-temperature treatment. It is well known that temperatures that promote the anatase to rutile transformation, which can take place anywhere between 650 and 1,000 ºC, depending on the coating solution characteristics **[9−11]**. The temperature difference between the phase transformation from anatase to rutile in the sol–gel method and the MPM is reported by Nagai *et al.*, **[12]**. Using both MPM and conventional sol-gel method, the anatase phase appears during the heat-treatment of both precursor films at a temperature between 400 and 500°C **[13]**. By using MPM, anatase can be transformed to the rutile one between 500 and 700°C **[12]**, while a sol–gel process reprted by other authors **[14−16]** showed that anatase could not transformed to the rutile one, even when heat-treated at 900°C. Moreover, research has shown that the addition of a foreign agent to the initial solution controls phase transition, particles size and morphology of TiO_2 **[17]**. The applications of titania depend on its crystal phase, particle size, surface area and thermal stability. Hence, it is important to have full comprehension of the influence of the processing parameters in a particular technique.

Although numerous techniques have been applied, the majority of these efforts are through doping of the TiO_2 with; noble metals, transition metal ions, or anions **[18−22]**. Of particular interest here is the doping of TiO_2 with silver (Ag/TiO_2). In term of doping titania with silver as a foreign agent, it has been shown that the introduction of Ag, even in small amounts, can greatly affect TiO_2-based thin film properties including; crystallinity, morphology, and chemistry **[23]**. Therefore, the effects of Ag to TiO_2 thin film properties must being understood completely include introduction of large amount of Ag into TiO_2-based thin film. Various processing parameters, including heat

treatment temperature and time can be used to control material properties including crystal phase, crystal size, density, and surface structure of titania **[2, 5, 23, 24]**. The generation of the phases of TiO_2 depends significantly on the synthesis parameters, which in turn affect the product. The kinetics of these processes typically is considered in this chapter in terms of temperature while keeping heat treatment time and the atmospheric environment constant. In terms of the former, It is known that anatase is considered widely to begin to transform irreversibly to rutile in air at 600ºC **[25]**; however, the reported transition temperatures vary in the range 400–1200ºC owing to the use of different methods of determining the transition temperatures, raw materials, and processing methods **[14−16, 26, 27]**. In the absence of a foreign agent or precursor modification, anatase to rutile transformation in synthetic TiO_2 usually occurs at a temperature of 600 to 700 ºC **[14−16]**. Using MPM, Nishide *et al.,* **[27]** prepared titania gel and films from Ti-edta complex solutions. Anatase appeared in the gel at firing temperatures between 450 and 500ºC, and was transformed to rutile at temperatures between 550 and 600ºC. They concluded that this low transformation temperature is presumed to be due to the small crystalline size and micro pores in the film.

Moreover, as stated in the introduction chapter (Chapter 2), the MPM has many advantages with respect to the other fabrication techniques in terms of crystallinity, purity, homogeneity and stability. Sato and his group **[12, 13]** compared the crystallite sizes of the TiO_2 thin films fabricated by MPM and those fabricated my sol-gel method. The crystallite size of the oxide particles in the resultant thin films fabricated by the MPM is generally smaller than those prepared by the conventional sol–gel method. Compared to a conventional sol–gel solution, the stability of the molecular precursor solution for Ti complex of EDTA and a SrO precursor solution containing a Sr complex

of EDTA is extremely high, and therefore, the molecular precursor method has practical advantages **[13]**. Based on the excellent miscibility of the molecular precursors in the $SrTiO_3$ thin film fabrication, heat-treatment was shown to be an essential step. Moreover, using MPM, the metal complex ions dissolve independently in each precursor solution and the homogeneity of the mixed solution can be kept at the molecular level. On the basis of this excellent miscibility in the MPM, Ag-nanoparticle/titania (Ag- NP/TiO_2) composite thin films with a wide range of volumetric fractions of Ag in the titania matrix can be developed using the titania precursor $\boldsymbol{S_{Ti}}$.

In this chapter, using the two precursor solutions of titania and silver prepared using MPM, the resultant composite solution with a 1:1 mixed molar ratio was used to fabricate Ag/TiO_2 composite thin films and heat treated at different temperatures (250–800ºC). The structural and optical properties of silver/titania nanoparticles were studied using X-ray diffraction (XRD), X-ray photoelectron spectroscopy (XPS), field-emission scanning electron microscope (FE-SEM), Thermal gravimetry/ differential thermal analysis TG/DTA) and UV–Vis absorption spectroscopy. Mixed-phase photocatalysts with rutile–anatase compositions have been reported to exhibit enhanced photoactivity relative to single-phase titania**[14−16, 26, 27]**. The aim of this chapter is to find the optimal heat treatment temperature that will allow me to fabricate pure, homogeneous, stable and mixed-phase Ag-NP/TiO_2 composite thin films with rutile–anatase compositions. Alternatively, as discussed subsequently through chapter 2 and 3, doping also may act advantageously through reduction in the band gap and improvement in the charge carrier separation, associated extended exciton lifetime **[28]** and enhance electrical conductivity of the thin film. With those properties, electrical conductivities

and photoelectrochemical properties of the synthesized Ag/TiO_2 composite thin films fabricated at different heat treatment temperature will be also reported in this chapter.

4−2. EXPERIMENTAL

4-2.1 Materials

All the materials employed in this chapter are tabulated in Chapter 3, Table 3.1.

4-2.2 Fabrication Process of Ag/TiO_2 composite thin films at different heat treatment temperature.

After substrate cleaned by chemicals as illustrated in the Chapter 3, section 3-1.2.1, Ag /TiO_2 composite film were fabricated by a spin coating system. Spin coating is one of the coating processes used to deposit ultra-thin films on substrates. The preparation of silver ($\boldsymbol{S_{Ag}}$) with titania ($\boldsymbol{S_{Ti}}$) precursor solutions are reported in the previous chapter (Chapter 3). The composite precursor solution ($\boldsymbol{S_{composite}}$), with a 1:1 mixed molar ratio were achieved by mixing $\boldsymbol{S_{Ag}}$ with $\boldsymbol{S_{Ti}}$, respectively. Then, the $\boldsymbol{S_{composite}}$ were sonicated with stirring for 5 min to increase the homogeneity. The Ag-NP/TiO_2 composite thin films were deposited by spin coating of the $\boldsymbol{S_{composite}}$ onto the substrates with a double step mode: first at 500 rpm—5 s and then at 2000 rpm—30 s in all the cases. Figure 4.1a–g shows the photographs of the resultant composite thin films. Thin films were fabricated by heat-treatment at different temperatures (70–800ºC) for 0.5h in order to find the optimal heat treatment temperature. Thin films of pure TiO_2 were also fabricated for comparison purpose by heat treating the spin-coated $\boldsymbol{S_{Ti}}$ precursor films at different temperatures.

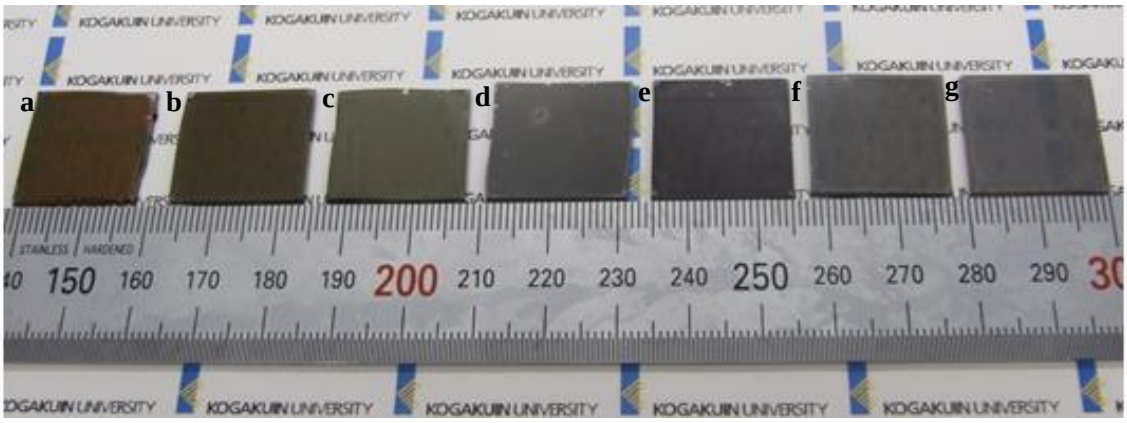

Fig. 4.1 Photographs a–h, of the Ag-NP/TiO_2 composite thin films fabricated by heat-treatment at different temperatures: a 250, b 300, c 400, d 500, e 600, f 700, and g 800ºC, respectively for 0.5h in air.

Crystal structural, surface morphology and nanostructures of the fabricated thin films were performed using XRD, and FE-SEM, as described in chapter 3, respectively. A Phi Quantum 2000 Scanning ESCA Microprobe (Shimadzu) with a focused monochromatic Al-Kα X-ray (1486.6 eV) source was employed in order to evaluate the elemental states and quantities—Ti, O, C and Ag— in the thin films. No critical surface charging during the XPS measurements was observed; thereby, no correction of binding energy was performed. The depth profiles were obtained with the identical instrument. The stepwise etching was performed by bombarding the Ar^+ ions with 2 kV for 3 min before measuring each layer.

The absorption spectra for these composite thin films fabricated on quartz glass substrates were measured in the range 200–800 nm using the double-beam mode. The measurement was performed using a spectrophotometer (U-2800, Hitachi) and air was used as a reference. Respective electrical resistivity and photoelectrochemical properties were examined by employing four-probe and three-electrode methods.

4–3 RESULTS AND DISCUSSION

4-3.1. Crystal structure of the thin films

Figure 4.2 shows the XRD patterns for pure TiO_2 films and Ag/TiO_2 composite thin films heat treated at different temperatures. The peaks found at 2θ = 27.5, 36.2, 39.3, 41.4, 44.3, 54.5, 56.7, 64.2, and 69.2º, corresponding to the (110), (101), (200), (111), (210), (211), (220), (310), and (301) phases of rutile [JCPDS card 21-1276]. The peaks observed at 2θ = 25.6, 38.1, 48.4, 54.2, 55.5, 62.9, 69.1, 70.7, and 75.3º, corresponding to the (101), (004), (200), (105), (211), (204), (116), (220), and (215) phases of anatase [JCPDS card 21-1272]. The peaks at 38.18, 44.39, 64.58, and 77.54° are assigned as the (111), (200), (220), and (311) reflection lines of fcc Ag particles (JCPDS file, No. 04-0783), respectively [JCPDS card 4-783]. Weak and broadened peaks in the spectra might be due to the small grains of the composites.

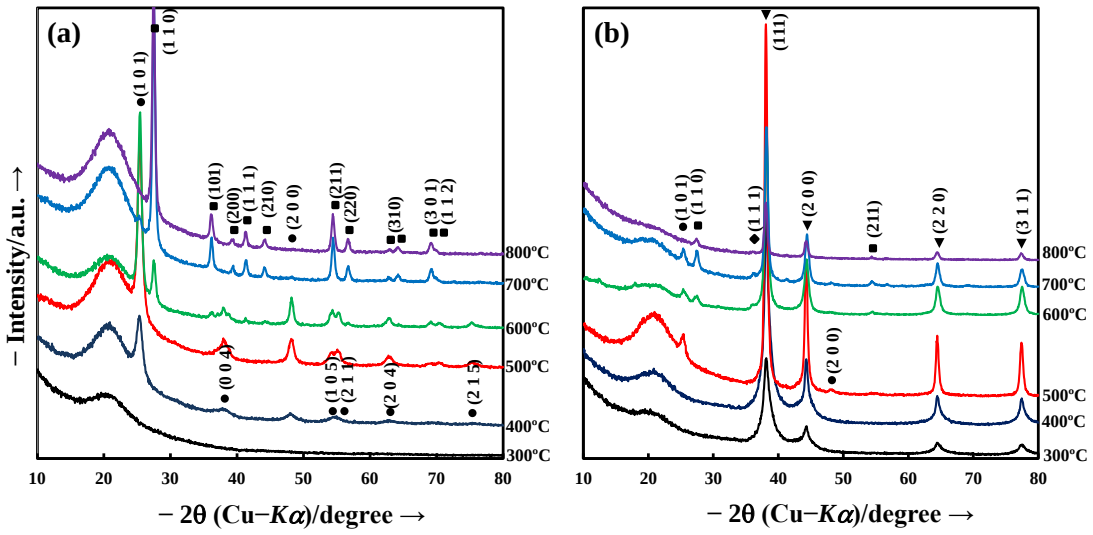

Fig. 4.2 XRD of (a) Pure TiO_2, (b) Ag/TiO_2 composite thin films heat treated at different temperatures fabricated by MPM. The peaks of each phase are denoted as follows: filled inverted triangle silver, filled circle anatase, and filled square rutile.

Pure TiO_2 thin films heat treated at 300ºC and below are amorphous. For Ag/TiO_2 composite thin film sample heat treatment at 400ºC and below, no diffraction peaks at 25.4º corresponding to anatase were observed, indicating that TiO_2 was amorphous or well dispersed inside the silver/organic matrix, with a crystal size smaller than those of silver particles **[29]**. The intensity of the (111) and (200) diffraction peaks of Ag phases found to be increased as the heat treatment is increasing up to 500ºC. Sharp diffraction peaks indicated the formation of pure silver of high crystalline **[30]**. Anatase and rutile mixed phases in composite thin films obtained at 600 and 700 ºC consists of about 63 wt% anatase phase and 37 wt% rutile phase. After heat treatment temperature above 700ºC for 0.5 h, the peak intensity of anatase greatly decreased and the samples mainly consisted of rutile.

Usually, anatase transforms to rutile at high temperature such as 700C in air from Ti-edta complex solutions **[27]**. This is exactly what happens for my pure TiO_2 thin film as illustrated in figure 4.2. However in the case of the Ag/TiO_2 composite thin films, 100% rutile phase could be only obtained at round 800ºC. No extraneous peaks appeared under the heat treatment, only peaks for Ag metallic and TiO_2 were detected with the exception of the peak observed at 36.5º in the XRD pattern of the composite thin films fabricated at high temperature (600, 700 and 800ºC); indicates the presence of silver oxide [JCPDS card 40-909]. Thermodynamics studies have suggested that silver is more stable than Ag_2O/AgO at temperature of > 189.8 °C in air **[31]**. Therefore, any of Ag_2O/AgO that is present decomposed to metallic silver during heat treatment stage. The small amount of Ag_2O that appear in the XRD may be formed during the cooling stage. These results indicated that low mechanical energy associated with silver oxide

decelerated the phase transformation of anatase to rutile, thus delay the transformation of anatase to 100 % rutile until round 800ºC.

4-3.2. Chemical identity of the Ag/TiO_2 composite thin films

I performed depth profiling XPS to further clarify changes in chemical states and electronic structures with change in heat treatment temperature. Figure 4.3 shows the XPS high resolution wide scans for Ag/TiO_2 composite thin film heat treated at 600ºC. The major XPS peaks include C1s Ag 3d, Ti 2p and O1s (Figure 4.3 insets). The carbon might come from two sources: adventitious element carbon from the impurity of equipment chamber, and carbon residues from the impregnation of alcoholic precursor.

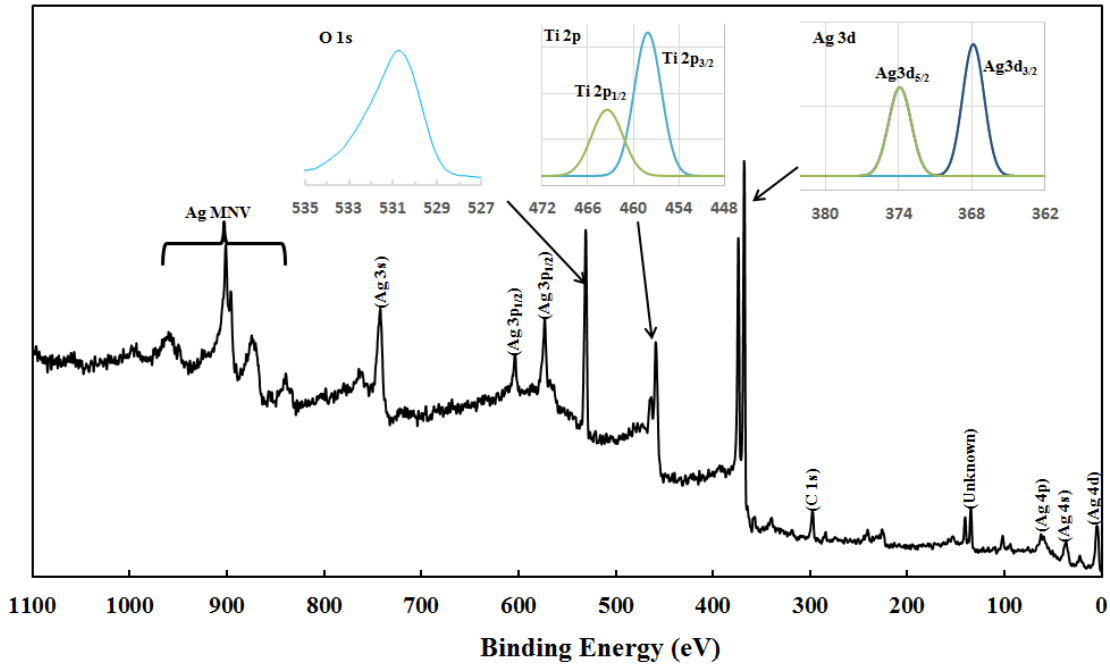

Fig. 4.3 Representative wide-scan XPS survey spectrum taken from the surface of Ag/TiO_2 composite thin films heat treated at 600ºC.

For narrow scan, the depth profile for Ag/TiO_2 composite thin films at different heat treatment temperatures were also performed and are tabulated in Table 4.1. The high

resolution Ag 3d peaks for all thin films are located at 370.6 eV ($3d_{5/2}$) and 376.7 eV ($3d_{3/2}$) on average. The interpretation of Ag 3d peaks is rather delicate because the chemical shifts between metallic and oxide phases are very weak. However, it is now admitted that oxide contributions generate negative shift **[32]**. The shift is usually smaller for Ag_2O (0.3−0.4 eV) and larger for AgO (0.8−1.0 eV) **[33]**. The best way to evaluate this is to consider the spin-orbital splitting. The metallic Ag is known to exhibit a spin–orbit splitting of 6.0 eV **[34]**. All the Ag/TiO_2 composite thin films exhibit such spin-orbital splitting of 6.0 eV, hence this is attributed to mainly metallic Ag **[34, 35]**, consistent with the XRD result reported above.

Table 4.1 XPS peak value for Ag/TiO_2 composite thin films at different heat treatment temperatures.

Heat treatment temperature (°C)	**$Ag3d_{5/2}$**	**$Ag3d_{3/2}$**	**$Ti2p_{3/2}$**	**O1s**
70	372.6	378.5	459.5	536.4
250	372.3	378.2	459.3	537.9
300	372.4	378.3	459.1	535.3
400	372.0	378.2	459.6	534.6
500	368.1	374.3	458.1	531.1
600	367.8	373.9	458.5	530.9
700	370.1	376.4	458.7	533.0
800	369.3	375.8	459.8	532.5

The Ti $2p_{3/2}$ peak (Table 4.1) is found in the range of 458.1–459.69 eV eV (within experimental uncertainty), attributed to Ti^{4+} for pure crystalline TiO_2 **[33, 36]**. The Ti $2p_{3/2}$ binding energy band at lower heat treatment temperature (70 to 400ºC) shifts to a higher position than that fabricated at higher heat treatment temperature (500−800ºC), indicating a decrease in electron density of the Ti atoms in the Ag/TiO_2 composite thin film samples with heat treatment temperature.

Spectral changes in the O 1s region of XPS spectra provided more quantitative information on the kinetics of Ag oxide and TiO_2 formation. Peak values od high-resolution spectra of O1s obtained from the samples heat treated at different temperature are presented in Table 4.1. The O1s spectra are broad and complex (figure 4.3, insets), suggesting contributions of several oxygen species. A peak at 530.6 eV is attributed to Ag_2CO_3 and adsorbed CO_2 (530.5-531.0 eV) **[34]**. A broad peak at 531.9-532.0 eV is associated with dissolved oxygen (530.5-531.5 eV) **[36]**. Therefore, the O 1s peaks (Fig. 4.3) found at 530.9-537.9 eV wide range region is decomposed into several contributions. The main contribution is attributed to Ti-O in TiO_2 **[37]**. The other kinds of oxygen contributions can be counted by Ti-O bond of hydroxyl groups from alcohol precursor, the C-O bonds and the adsorbed H_2O, respectively

4-3.3. TG/DTA of the Ag/TiO_2 composite thin films

The presence of unintentional impurities or intentional dopants has a strong effect on the kinetics of the anatase to rutile transition **[38]**. TG-DTA peak apices can be considered to be applicable for comparative analysis of the phase transformation considering the impurities. TG-DTA analysis shown in figure 4.4 indicates that residual organic substances have exotherm maximum at 343.2ºC and then at 463.7ºC and

completely burned out at about 513.4ºC. Therefore all the prepared samples heat treated at around 463.7ºC will result in the transformation of titania amorphous to crystalline anatase phase. High crystalline anatase is only expected to be formed at around 513.4ºC when complete combustion took place thus a very sharp exothermic peak is observed due to the formation of anatase phase.

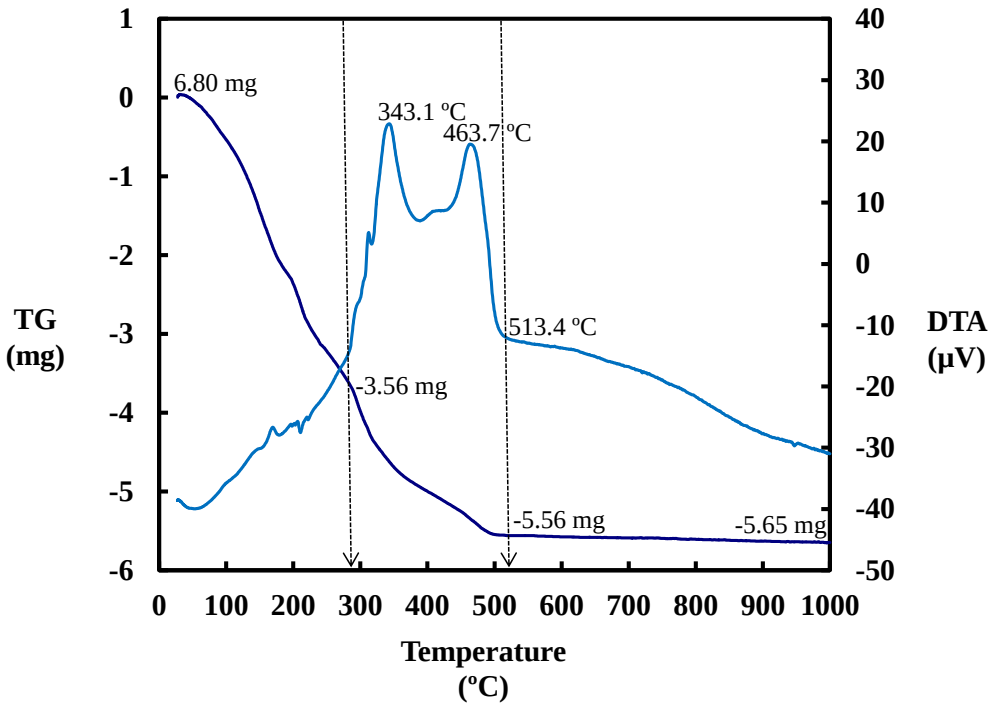

Fig.4.4 TG/DTA curves of Ag/TiO_2 composite precursor solution ($S_{composite.}$)

From these results, DTA analysis results seem to yields higher transformation temperatures than XRD analysis. This probably is a result of the sigmoidal form of the kinetics curve, as shown subsequently. That is, the phase transformation commences slowly at an onset temperature of 463.7ºC and so it is more likely that the exotherm maximum (viz., the apex) is observed later in the phase transformation process, when the transformation rate is greatest; the rate of transformation subsequently decreases along with the corresponding latent heat as anatase converts to rutile. Usually, heat treatment at

450°C afforded an anatase phase, while treatment at 700 °C yielded a rutile phase using sol-gel method **[39]**. Hu *et al.,* **[40]** have reported that TiO_2 normally undergone an anatase-to-rutile phase transition at around 600–700°C. While using MPM, Nishide *et al.*, **[27]** reported that anatase appeared in the gel at firing temperatures between 450 and 500ºC, and was transformed to rutile at temperatures between 550 and 600ºC.

For thermal gravimetry analysis, a TG curve in figure 4.4, can be divided into three stages. The first stage is from room temperature to around 285ºC. The rate of weight loss is the greatest, up to approximately 53%, which is caused by dehydration and evaporation of alcohol contained in the composite precursor. The second stage is from 285 to 513ºC. The rate of weight loss is approximately 34%, which is assigned to the combustion and carbonization of organic materials. However, some carbon element still exists in the films, which can be seen from the results of XPS studies above. The third stage is from 513 to 1000ºC. The rate of weight loss is approximately 7%, which is attributed to oxidation of residue carbon and evaporation of chemisorbed water.

4-3.4. FESEM images of the Ag/TiO_2 composite thin films heat treated at different temperatures.

The effects of heat treatment are expected to be reflected in the surface morphology of the films. To study the dependence of the surface morphology of the Ag/TiO_2 composite thin films upon heat treated at different temperature, the FE-SEM images were taken for the Ag/TiO_2 composite thin films heat treated at different temperatures and such FE-SEM images are shown in figure 4.5. White dots represent Ag grains confirmed by EDX mapping (results not shown for sake of brevity). The dense structures of silver nanoparticles seem to be increasing with the increase in heat treatment

temperature. The SEM image of films annealed at 300ºC and 400ºC has a lower contrast compared to that of films annealed at higher temperature, indicating the possible presence of organic block coverage on the films. Their surface is relatively smooth, and very few pores are observed. Thin films heat treated at higher temperatures had a highly porous network structure, with continuous porosity. This tells us that heat treatment temperature changed the morphology characteristics and structure of the thin films, allowing the thin films to develop higher porosity.

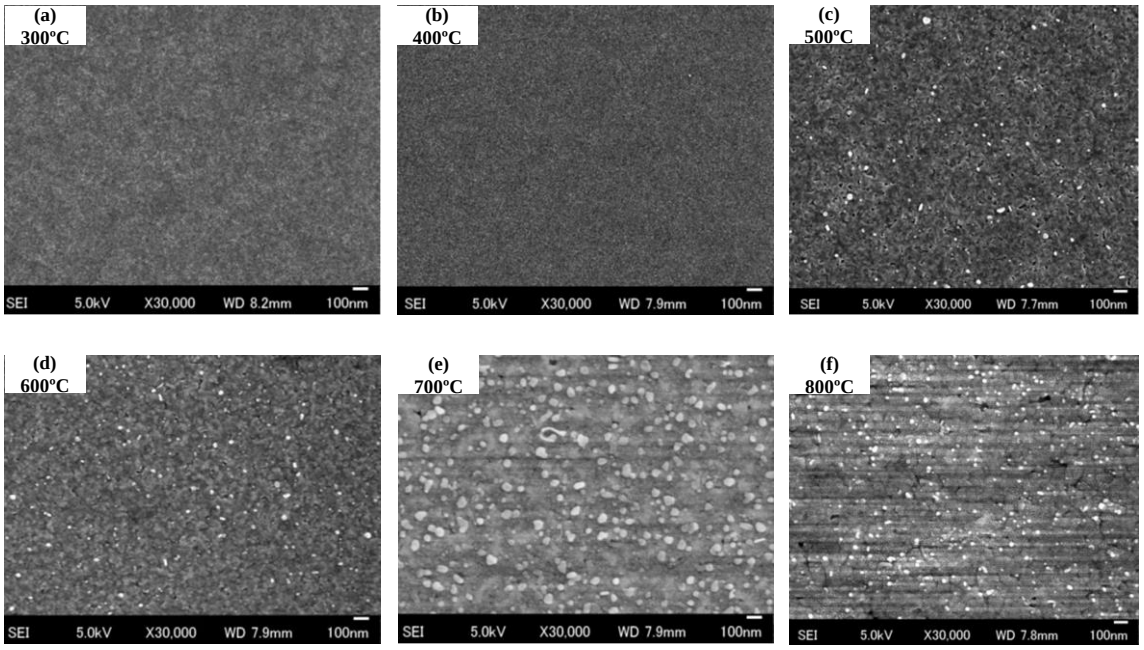

Fig. 4.5 FE-SEM images of the Ag-NP/TiO_2 composite thin films (a–f) fabricated at differet heat treatment temperature of 300, 400, 500, 600, 700, and 800ºC respectively.

Moreover, the Ag nanoparticles are being increasing on the surface of the thin film with increase of heat treatment temperature. The lack of agglomerated Ag NPs on the surface of the thin film for lower temperature thin films could be that the Ag particles are too small, hence are trapped inside the organic structure of the incomplete combustion of $S_{\mathbf{composite}}$ **[29]**. At the highest heat treatment temperature (800ºC), the surface became

cracked and irregular (Figure 4.4f), which was in agreement with the results reported by Ishizawa *et al*., **[41]**.

4-3.5. Optical properties of Ag/TiO_2 composite thin films heat treated at different temperatures.

It is where known that the changes in the profiles of absorption spectra at different heat treatment temperatures can be attributed to the changes in the surface morphology of the thin films **[42]**. This can be characterized by study absorbance using UV-visible spectroscopy. Figure 4.6 (a) and (b) represent the UV-Vis absorption spectra for Ag/TiO_2 composites thin films heat treated at different temperatures.

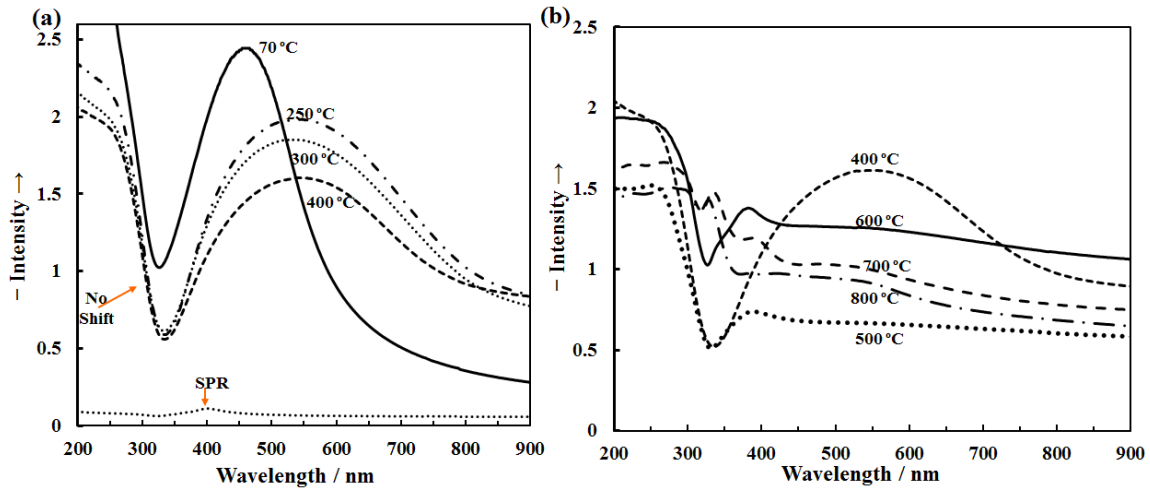

Fig. 4.6 Absorption spectra of Ag-NP/TiO_2 composite thin films: (a) low heat treatment temperature (b) high heat treatment temperature at 70, 250, 300, 400, 500, 600, 700, and 800ºC respectively.

The absorbance spectra of the synthesized Ag-NP/TiO_2 composite thin films are decreasing, and then increase with heat treatment temperature, indicating that the heat treatment temperatures are capable of sensitizing Ag/TiO_2 thin film. Therefore, the

Ag-NP/TiO_2 composite thin films can be activated by visible light to generate electrons and holes, which is favorable to the improvement of the visible light photocatalytic activity of TiO_2. For Ag/TiO_2 composite thin film heat treated at 70ºC, an absorption band is obtained at around 410 nm and it corresponds to the surface plasmon resonance absorption band of silver nanoparticles indicating that the nanoparticles are existed in the composite. UV-visible spectroscopy is a valuable tool for structural characterization of silver nanoparticles. It is well recognized that the absorbance of silver nanoparticles depends mainly upon size and shape **[43]**. Zhou *et al.*, **[44]** reported that metal nanoparticles exhibit the absorption bands at 410nm because of surface plasmon resonance (SPR). In the case of Ag/TiO_2 composite thin film heat treated at 250ºC to 500ºC curves, it can be observed that SPR shift to longer wavelength with peak position around 540 nm and it is decreasing with increase of heat treatment temperature, probably due to the fact that the lack of agglomeration of Ag particles as illustrated in the FE-SEM images.

However, an absorption band at 395 nm starts appearing in absorption spectra of the prepared Ag-NP/TiO_2 composite films heat treated at temperature greater than or equal to 500ºC, which show clearly that the presence of increased amounts of silver on the surface of the thin films due to agglomeration facilitates SPR, which shifting to shorter wavelength with heat treatment temperature. The absorption spectra of these thin films are then increasing in intensity with the increase in temperature upto 600ºC and then decrease again for the 800ºC sample. The enhancement in intensity of the absorption spectra is related to the increase in the number of Ag nanoparticles/crystallites in/on the film. The optical signature of this sample can be better understood in terms of the distribution of sizes and shapes observed in my SEM images above.

Composite thin film heat treated at 600ºC exhibit the highest absorption spectrum and well define SPR/LSPR signatures compare to other higher temperature heat treated composite thin films as shown in figure 4.6b. The role of heat treating is therefore found to be responsible for the gradual enhancement in the surface states which changes the optical properties. Thus, the optical properties of the films depend strongly on the heat treatment temperature conditions. One must note that, there was no shift in band edge of the absorption spectra of Ag/TiO_2 composite thin films. Hence, no big change in band gap of the TiO_2.

4-3.6 Electrical conductivity of Ag/TiO_2 composite thin films heat treated at different temperatures.

A systematic study of size effect on the electrical properties of semiconducting nanocrystallites is essential for understanding their technological applications **[45]**. Electrical conductivity is the ability of a material to conduct an electric current. When there is an electrical potential difference placed across a conductor, its movable charges flow, giving rise to an electric current **[46]**. Figure 4.7 shows the impedance spectrum for various temperature regions of prepared Ag/TiO_2 composite thin film samples obtained used a 4-point probe measuring system.

At low temperature region, that is 70–400ºC, the resistance varies from 9.6×10^{00} to 1.7×10^{00} Ω cm. In this temperature region, Ag particles are too small as observed in SEM images in figure 4.5, hence are trapped inside the organic structure of the incomplete combustion of $S_{composite}$. Hence, in this region, a low conductivity is observed in the sample. As the temperature is further increased, from 400 to 600ºC, the resistance values of thin films are found to be decreased from 1.7×10^{00} to 1.1×10^{-4} Ω cm.

This observation indicates that the Ag NP growth enhancing the grain–grain interaction as temperature increases.

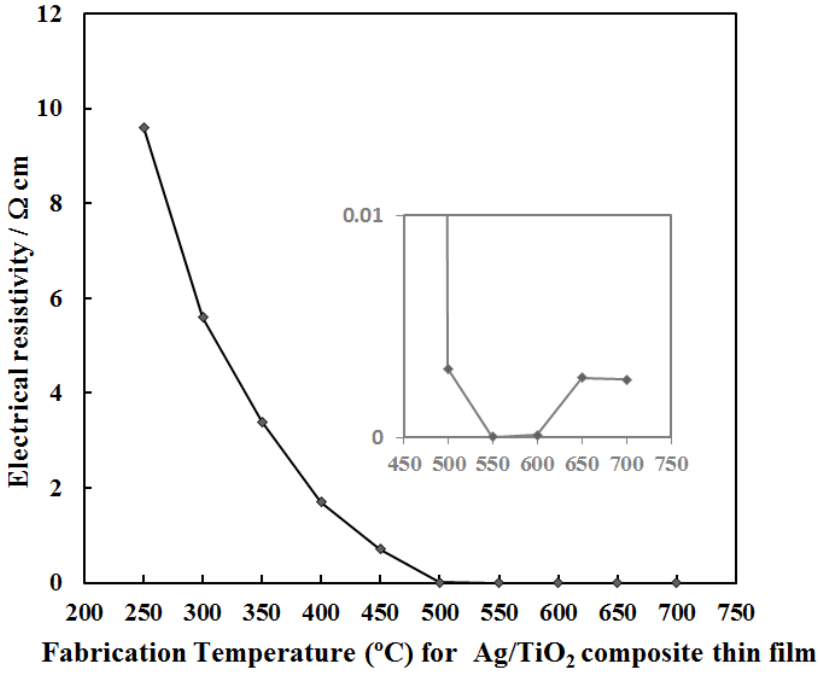

Fig.4.7 Resistivity of Ag/TiO_2 composite thin film heat treated at different temperatures

At the higher temperature region, 800ºC, the resistance values have decreased considerably, from 1.1×10^{-4} Ω cm to undetectable conductivity. Figure 4.5f of SEM image shows that there exists cracks on the thin films attributing to the effect of grain boundary. In general, the decrease in resistivity with heat treatment temperatures can be explained as follow: the Ag grains size increases with increase heat treatment temperature (See SEM images above) which lead to a decrease in Ag grain boundaries and hence resistivity. Larger silver grans size will provide higher surface contact between each other, improving electron migration. But, in thin film heat treated at 800°C case, it can be seen that the thin film is full of crack which affect the formation of the connecting network.

4-3.7. Photoelectrochemical property of Ag/TiO_2 composite thin films heat treated at different temperatures.

The enhanced near-field amplitude of localized surface plasmon resonance in the proximity of metal nanoparticles can boost the photoactivity of the neighboring semiconductor, which has been proven and has attracted wide interest recently **[47]**. One best way to prove this is simple by study the photoelectrochemical properties of the doped semiconductor. In this chapter, the photocurrent measurement was conducted using the measurement set up described in chapter 3. Anodic photocurrent could be observed in the composite thin films under dark, visible and UV-light irradiation as shown in figure 4.8.

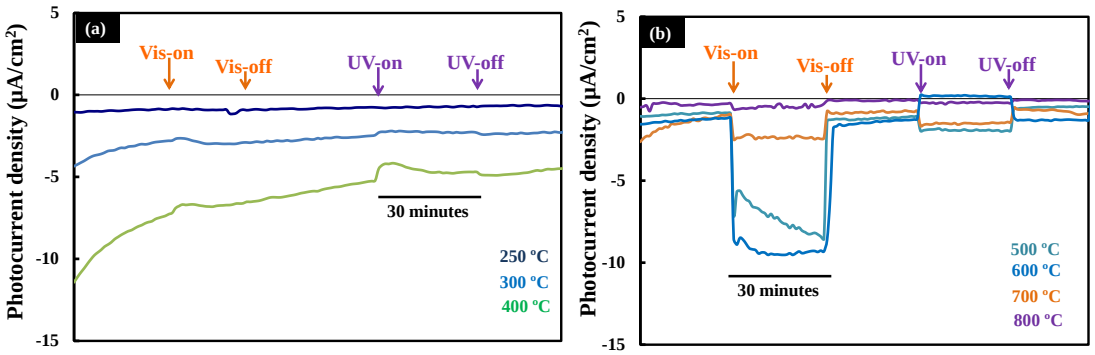

Fig. 4.8 Photocurrent densities of Ag-NP/TiO_2 composite thin films: (a) low heat treatment temperature (b) high heat treatment temperature at 70, 250, 300, 400, 500, 600, 700, and 800ºC respectively.

Dark currents were observed in all composite thin films heat treated at different temperature. This indicates that there is a redox potential between the counter Ag electrode and working electrode (composite thin films), hence chemical redox reactions occurred to the system. The anodic photocurrent for this TiO_2 thin film under

UV-irradiation is due to the wide band gap of anatase/rutile that allowed it to absorb only UV light and to produce electron/hole pairs. Under vis-light irradiation, the cathodic photocurrent density of these films increased with an increase in the Ag content. The large cathodic photocurrent density observed could be mainly due to LSPR **[48]**.

4-3.8 Mechanical strength of the thin films

The mechanically strength of quartz glass, and Ag-NP/TiO_2 thin films whose heat treated at higher temperature (500, 600, and 700ºC) were examined in order to check their potential use in practical systems. The mechanical strength of pure TiO_2 fabricated at 600ºC was also investigated for comparison purpose. Figures 4.9 shows load-displacement curves obtained from indentation tests on the composite thin films.

Young`s modulus has been calculated from an equation (4.1), which is dominated by the accuracy of the bar`s width (w) and length (l), but especially by its thickness (t):

$$E = 0.9465 \times \left[\frac{m \times {f_r}^2}{b}\right] \times \left[\frac{L^3}{t^3}\right] \quad \text{.....(4.1)}$$

where f_r represents the resonance frequency and m the mass of the sample. L, b, and t are the dimensional units (length, width, and thickness).

The scratch hardness (HS) can be obtained using equation (4.2) **[49]**:

$$HS = \mathrm{H}_R \times \left[\frac{{f_S}^2}{f_R}\right] \times \left[\frac{W_R^2}{W_S^2}\right] \quad \text{.....(4.2)}$$

HR is the hardness of the reference material, WR and WS are the scratch widths on the reference and specimen, respectively. The FS and FR are the scratching loads for the specimen and the reference, respectively.

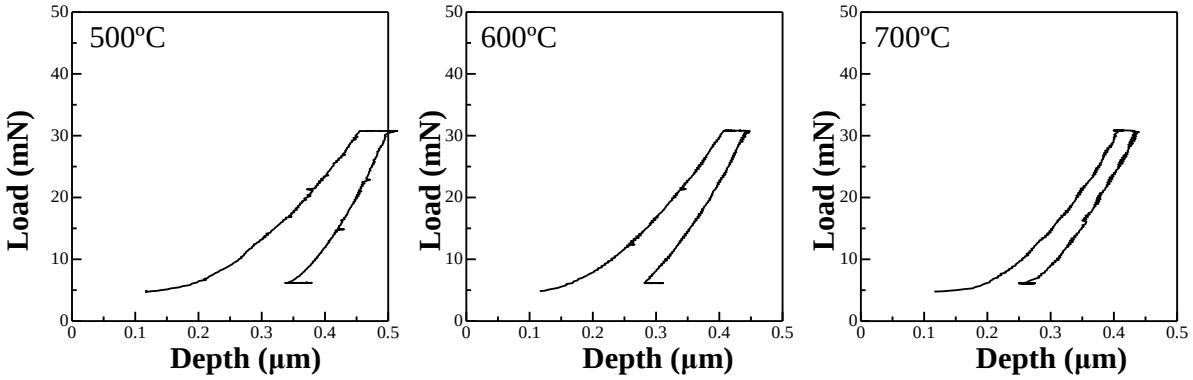

Fig. 4.9 Indent test curves of of Ag-NP/TiO_2 composite thin films: high heat treatment temperature at 500, 600, and 700ºC respectively.

Table 4.2 tabulated the Young`s modulus and knoop hardness results obtained during the measurement of mechanical strength of the samples. The results illustrated that there is a distinct decrease of Young`s modulus values with an increasing of heat treatment temperature. Values of Young`s modulus obtained by indentation methods are load dependent and highly sensitive to local defects (porosity, matrix grain pull-out, micro cracks, etc.) or structural in homogenities **[50]**. Therefore, the decrease of the Young`s modulus values with an increasing of heat treatment temperature can be probably explained mostly by change in microstructure of the thin film. Never the rest, indentation of all the thin films heat treated at different temperature showed good mechanical results since their mechanical strength are between pure TiO_2 thin film and those of naked quartz glass substrate. Such good mechanical properties are necessary for their wide– spread application in different areas of industry.

Table 4.2 Young`s modulus and knoop hardness results obtained during the measurement of mechanical strength of the Ag-NP/TiO_2 composite thin films fabricated on a quartz glass.

Notation	**Young`s Modulus**	**Knoop Hardness**
ºC	**Pa**	**Gpa**
Quartz glass	1.10×10^{11}	8.41
TiO_2	7.47×10^{10}	2.44
500	6.70×10^{10}	2.70
600	8.49×10^{10}	2.99
700	9.87×10^{10}	5.36

4−5 SUMMARY

In this chapter, the structural, optical, electrical resistance and electrochemical properties of Ag/TiO_2 composite thin films were studied. The Ag/TiO_2 composite thin films were synthesized by MPM and the effects of different heat treatment temperatures on transition of the anatase phase to rutile phase in air have been investigated. An understanding of the transformation of anatase to rutile is of great importance to those studying TiO_2 for photocatalysis or other applications. The phase composition of the material has significant consequences on its properties and performance and therefore it

may be desirable to enhance or inhibit the transformation to give a particular phase or phase mixture subsequent to thermal treatment. In this chapter, rutile is thermodynamically formed after calcination over 600°C with dense structure which according to literature makes rutile to have low photocatalytic efficiency. On the other hand, anatase is recognized as the most suitable phase for photocatalysis; however, anatase is not stable enough to exist alone. Therefore, the Ag/TiO_2 composite thin films that have a mixed-phase of anatase-rutile are interesting for further investigation.

Unlike, other Ag/TiO_2 composite thin films investigated in this chapter, the XRD patterns of the Ag/TiO_2 composite thin fabricated at 600ºC shows sharp peaks for both Ag, Anatase and rutile, reflecting high crystalline phases with anatase to rutile ratio, *f*, to be 0.63. Its Ag 3d peaks are located at 368.0 eV ($3d_{5/2}$) and 374.0 eV ($3d_{3/2}$), exactly where the bonding energy of metallic Ag that are reported in literature. SEM shows well define Ag NP scattering in/onto surface of titania, a necessity for localize plasmon resonance (SPR). Its plasmonic property was further supported by its UV-Vis spectrum which shows the highest absorption band intensity with a wide wavelength range in the visible light compare to other Ag/TiO_2 composite thin films investigated in this chapter.

From all these observations, I can conclude that heat treatment temperature at 600ºC is an optimal temperature for obtaining a mixed-phase with anatase-rutile with appropriate composition that deserves a further investigation. Moreover the study of electrical resistance of the thin films shows the crack-free composite thin fabricated at 600ºC exhibit lowest electrical resistance, of $1.1\times10^{-4}\,\Omega$ cm. Furthermore the electrochemical property of the composite thin film heat treated at 600ºC shows the highest cathodic photocurrent under visible light irradiation. The mechanically strength showed an

excellent degree of adhesion of the coated film on the quartz glass substrate. Therefore, Ag/TiO_2 composite thin films fabricated at 600ºC proved that, it is the best thin films that deserve further investigation. The following chapters will therefore concentrate of further investigations on the Ag/TiO_2 composite thin films fabricated at 600ºC only.

4−5 REFERENCES

1. Ma Q., Qin TP., Liu SJ., Weng LQ., Dong WY. (2010). *Applied Physics A*, 104:**1**, 365–373.

2. Stamate M., Lazar G., Lazar I. (2008). *Journ. Phys.*, **53**, 217-221.

3. Landmann M., Rauls E., Schmidt WG. (2012). *J. Phys.: Condens. Matter* **24**, 195503-195510.

4. Shchipunov Y., Postnova I. (2009). *Colloid Surf B* **74**,172-177.

5. Behforooz MR., Toujali S., Haji S. (2012). *Australian J. Basic and Appl. Sci.* 6:**8**, 316-319.

6. Toda K., Kawakami M., Uematsu K., Sato M. (2003). *Key Eng Mater* **248**,107–110.

7. Shin H., Jung HS., Hong KS., Lee JK. (2005). *J Solid State Chem* 178:**15**, 324-249.

8. Li G., Boerio-Goates J., Woodfield BF., Li L. (2004). *Appl Phys Lett* **85**, 2059.

9. Kim DJ., Hahn SH., Oh SH., Kim EJ. (2002). *Mater Lett* **57**, 355–360.

10. Hou YQ., Zhuang DM., Zhang G., Zhao M., Wu MS. (2003). *App Surf Sci* **218**, 98–106.

11. Yu J-G., Yu H-G., Cheng B., Zhao X-J., Yu JC., Ho W-K. (2003). *J Phys Chem B* **107**,13871–13879.

12. Nagai H., Mochizuki C., Hara H., Takano I., Sato M. (2008). *Sol Energ Mat Sol Cell* **92**, 1136– 1144.

13. Nagai H., Sato M. (2012). *InTech*, Chapter **5**, 103−128.

14. Czanderna A. W., Rao CNR., Honig JM. (1958). *Trans. Faraday Soc.*, **54**, 1069.

15. Kumar SR., Pillai SC., Hareesh US., Mukundan P., Warrier KGK. (2000). *Mater. Lett*., 43:**5–6**, 286–290

16. Yoganarasimhan SR., Rao CNR. (1962). *Trans. Faraday Soc.* **58**, 1579.

17. Uekawa N., Suzuki M., Ohmiya T., Mori F., Wu YJ., Kakegawa K. (2003). *J Mater Res* **18**, 797–803

18. Reddy KR., Nakata K., Ochiai T., Murakami T., Tryk DA., Fujishima A. (2011). J. *Nanoscience and Nanotechnology*, 11:**4**, 3692-3695.

19. Tian-hua X., Chen-lu S., Yong L., Gao-rong H. (2006). *J Zhejiang Univ Science B* 7:**4**, 299-303.

20. Akpan UG., Hameed BH. (2010). *Applied Catalysis A: General* **375**, 1–11.

21. Meng Q., Li X., Liu L., Cao B. (2012). *J Mater Sci.* **47**, 5926–5932;

22. Guana H., Wang X., Guo Y., Shao C., Zhang X., Liu Y., Louh R-F. (2013). *App. Surf. Sci.* **280**, 720– 725.

23. Akgun BA., Durucan C., Mellott PN. (2011). *J Sol-Gel Sci Technol* **58**, 277–289.

24. Azizi F., Bagheri-Mohagheghi M.-M. (2013). *J Sol-Gel Sci Technol* **65**, 329–335.

25. Hirano M., Nakahara N., Ota K., Tanaike O., Inagaki N. (2003). *J Solid State Chem* **170**, 39.

26. Jing Z., Qian X., Zhaochi F., Meijun L., Can L. (2008). *Angew Chem Int Ed* **47**,1766.

27. Nishide T, Sato M., and Hara H. (2000). *J. Mater. Sci.* **35**, 465– 469.

28. Wu T-S., Wang K-X., Li G-D., Sun S-Y., Sun J., Chen J-S. (2010). *ACS App. Mater. Interfaces*, l. 2: **2**, 544–550.

29. Maldonado-Ho ´dar FJ, Moreno-Castilla C, Rivera-Utrilla J (2000). *Appl Catal A* 203:**151**, 235-243.

30. Zhang F-J., Oh W-C. (2010). *Bull. Korean Chem. Soc.*, 31:**7**, 1981–1987.

31. Zhang H., Banfield JF. (1999). *Am Mineral,* **84**, 528−535.

32. Grabowska E., Zaleska A., Sorgues S., Kunst M., Etcheberry A., Colbeau-Justin C., Remita H. (2013). *J. Phys. Chem. C*, **117**.

33. Han S., Zhang X., Yu Q., Lei L. (2012). *Sci. China Chem.*, 55:**11**, 2462–2470.

34. Kang J-G., Sohn Y. (2011). *J. Mater. Sci.*, 47:**2**, 824–832.

35. Zhang WF., He YL., Zhang MS., Yin Z., Chen Q. (2000). *J Phys D* **33**, 912.

36. Huang C-H., Lin Y-M,, Wang I-K., Lu C-M. (2012). *Int. J. Photoenergy* **2012**, Article ID 548647, 1-13.

37. Nasser SA. (2000). *App. Surf. Sci*., 14–22.

38. Hanaor AHD., Sorrell CC. (2011). *J Mater Sci.* **46**, 855–874.

39. Ji X., Lou W., Wang Q., Ma J., Xu H., Bai Q., Liu C., Liu J. (2012). *Int. J. Mol. Sci.* **13**, 5242-5253.

40. Hu Y., Tsai HL., Huang CL. (2003). *Mater. Sci. Eng. A,* **344**, 209–214.

41. Ishizawa H., Ogino M. (1999). *J. Mater. Sci.* **34**, 5893–5898.

42. Hasan MM., Haseeb ASMA., Saidur R., Masjuki HH. (2008). *Engineering **2008***, 92–96.

43. Elechiguerra J., Burt L., Morones JR., Camacho-Bragado A., Gao X., Lara HH., Yacaman MJ. (2005). *J. Nanobiotechno*., **3**, 6.

44. Zhou X., Liu G., Yu J., Fan W. (2012). *J. Mater. Chem.*, **22**, 21337–21354.

45. Chellammal S., Sankar S., Murugaraj R., Selvakumar S., Viswanathan E., Sivaji K. (2010). *J. Mater. Sci* 45:**24**, 6701–6706.

46. Sarah MSP., Musa MZ., Asiah MN., Rusop M. (2010). *2010 International Conference on Electronic Devices, Systems and Applications*, 361–364.

47. Wang H., You T., Shi W., J. Li, and L. Guo, (2012). *J. Phys. Chem. C*, **116**.

48. Warren S., Walker D., Grzybowski B. (2012). *Langmuir : the ACS J. surfaces and colloids*, 28: **24**, 9093–9102.

49. Gitis N., Vinogradov M., Hermann I., Kuiry S. (2007). *Mater. Res. Soc. Symp. Proc.* 1049.

50. Špaková J., Dusza J., and Juhász A. (2008), *Powder Metallurgy Progress*, 8:**1**, 29-34.

CHAPTER 5: PERCOLATION THRESHOLD FOR ELECTRICAL RESISTIVITY OF SILVER NANOPARTICLE/TITANIA (Ag NP/TiO_2) COMPOSITE THIN FILMS FABRICATED USING MOLECULAR PRECURSOR METHOD

5−1 INTRODUCTION

Enhancement of the conductivity of semiconductor materials is desirable from a technological perspective. In order to accomplish this goal, the incorporation of metal nanoparticles into semiconductor materials has been extensively studied **[1-3]**. The semiconductor titania (TiO_2) has been the focus of various research efforts, and it is well established that the relatively high resistivity of titania films (10^{12} Ω·cm at 25°C) can be reduced by incorporating metal nanoparticles into the titania matrix based on the fact that the electrically conductive particles can be randomly distributed within the semiconductor matrix to form a composite **[1, 4]**. The composite sample is non-conducting, until the volume fraction of the conducting phase reaches the so-called percolation threshold **[5]**. However, it is noteworthy that the classical percolation theory applied to conductive-insulator systems must meet some definite conditions: the particles must be spherical, mono-disperse, and have an isotropic conductivity. If one or all of these conditions are not fulfilled, the theoretical value will deviate substantially from the realistic one **[6]**. In some cases, however, it is unclear which condition is not met. Moreover, it has been known that the conductivity of a metal nanoparticle/insulator composite close to the percolation threshold is very sensitive to any change in the metal nanoparticle distances.

In recent years, significant progress has been made in the manufacture and application of conductive polymer composites by blending conductive components such as gold nanoparticles, carbon nanotubes, copper fillers, and carbon powders with polymer matrices in semiconductor matrices **[7−10]**. Macwan and co-workers, **[11]** wrote a review where they described the synthesis and applications of nano-TiO_2 using the

sol-gel method and reported that metals such as Nb, Cr, Sn, Pt, Zn, and Y were found to increase the conductivity of titania. The inclusion of nanoparticles into various materials and methods may offer unique advantages in terms of electrical characteristics **[12]**. Therefore, any literature review on the metal incorporation/doping into an insulating matrix must inevitably deal with the fact that the use of numerous different preparation methods for obtaining these materials may have given rise to their different properties.

Various metallic phases have been used in metal-semiconductor composites, including Pt, Pd, Al, Cu, Ni, and Ag. Nonetheless, the use of Pt and Pd is limited by the associated expense, whereas Al, Cu, and Ni are undesirably oxidized during sintering at higher temperatures **[13]**; silver is possibly the most commonly used metallic substrate due to its excellent conductivity and chemical durability **[4]**. Fabrication of metal/TiO_2 composite thin films is performed using various techniques, each of which offers a unique set of advantages and disadvantages; currently, it remains unclear which of these will eventually prove to be the most effective. The most widely applied technique for the preparation of metal/TiO_2 composite materials is the sol–gel process **[1, 14−17]**, which has been applied to the fabrication of the Ag-nanoparticle/titania (Ag-NP/TiO_2) system by Li and co-workers **[1]**. They prepared a solution for fabricating the Ag-NP/TiO_2 composite thin films by mixing a sol–gel solution of titania for thin film fabrication with a silver nitrate solution having a concentration of up to 18 mol%; a 6 mol% ethanol solution of silver nitrate was also employed. The electrical resistivity of the resultant composite thin film with the highest concentration (18 mol%) of Ag nanoparticles was of the order of 10^3 Ω·cm, even though titania is a typical dielectric. Because the sol–gel method used in these studies involves the process of metalloxane polymer formation in the medium and because the poor miscibility of each component

is inevitable, Li *et al.*, **[1]** reported that it was difficult to obtain a homogeneous solution for silver concentrations above 18 mol%. Therefore, it is envisioned that lower electrical resistivity in the composite thin film may be attained in the event that a solution with an even higher volumetric fraction of Ag nanoparticles can be homogeneously dispersed in the dielectric titania matrix because the electrical conductivity is largely dependent on the volumetric fraction, size, and connectivity of the Ag nanoparticles and the homogeneity of dispersed silver in the dielectric titania matrix **[1, 5, 13, 18, 19]**. It has been experimentally and theoretically verified that in the conductor/semiconductor composite with a conductor ratio at or above a given volume fraction ($\varphi_{conductor}$), a network of conducting particles is established, and thus, the resistivity of the composite suddenly decreases **[1−3, 19]**.

The volumetric fraction, φ_i, is generally defined according to equation (5.1), where V_i and V represent the volumes of a constituent, i, and of all constituents of the mixture prior to mixing, respectively **[20]**:

$$\varphi_i = V_i/V \qquad (5.1)$$

Based on this general formula, the volumetric fraction of silver particles in a composite, namely, φ_{Ag}, which is strongly related to the percolation threshold, can be defined by equation (5.2), where d_{Ag} and $d_{titania}$ represent the density of silver and titania ($3.8 \leq d_{titania} \leq 4.2$), respectively; Fw_{Ag} and $Fw_{titania}$ represent the formula weight of silver and titania, respectively; and N_{Ag} and $N_{titania}$ represent the amount of substance of silver and titania, respectively, under the assumption of cubic silver and tetragonal titania.

$$\varphi_{Ag} = \left(\frac{Fw_{Ag} \bullet N_{Ag}}{d_{Ag}}\right) / \left(\frac{Fw_{Ag} \bullet N_{Ag}}{d_{Ag}} + \frac{Fw_{Titania} \bullet N_{Titania}}{d_{Titania}}\right) \qquad (5.2)$$

Based on equation (2), the silver concentration of 18 mol% used in the abovementioned Ag-NP/TiO_2 composite prepared by Li *et al*., **[1]** corresponds to a significantly small φ_{Ag} value of 0.1. Unprecedentedly high conductivity would thus be expected in the case of an Ag-NP/TiO_2 composite thin film having a larger φ_{Ag} value, exceeding 0.1.

Recently, the molecular precursor method has been demonstrated to offer excellent miscibility of the solutions, which has also been observed in several precursor solutions during the fabrication of ceramic films by the method developed by our laboratory **[21−25]**. Unlike, other Ag/TiO_2 composite thin films investigated in chapter 4, where I concluded that heat treatment temperature at 600ºC is an optimal temperature for obtaining a mixed-phase with anatase-rutile with appropriate composition that deserves a further investigation. On the basis of these considerations, Ag-NP/TiO_2 composite thin films were fabricated at 600ºC by employing various Ag volumetric fraction values. In this chapter I am reporting, for the first time, the percolation threshold found for the electrical resistivity of Ag-NP/TiO_2 composite thin films. Crystal structural, surface morphology and nanostructural evaluations of the fabricated thin films were performed using X-ray diffraction (XRD), field-emission scanning electron microscope (SEM) and transmission electron microscopy (TEM), respectively. The film thickness and electrical resistivity of the thin films were examined using a profilometer and by the four-probe method, respectively. The relationships between the mechanical properties of the composite thin films with different Ag concentrations were also investigated. The mechanically strength showed an excellent degree of adhesion of the coated film on the quartz glass substrate− pose no problem for clinical applications.

5−2. EXPERIMENTAL

5-2.1 Materials

All the materials employed in this chapter are tabulated in Chapter 3, Table 3.1.

5-2.2 Synthesis of precursor solution (S_{Ag}) for fabrication of Ag nanoparticles

Silver acetate (0.24 g, 1.4 mmol) and dibutylamine (0.56 g, 4.3 mmol) were added to 1 g of ethanol. The solution was sonicated with stirring for 5 min. The concentration of silver was 0.8 mmol g^{-1}.

5-2.3 Preparation of precursor solution ($S_{titania}$) for fabrication of titania thin films

The precursor solution containing the Ti^{4+} complex of EDTA was obtained by a method that reported by our laboratory and is illustrated in Chapter 3, scheme 3.I **[21]**. Dibutylamine (3.58 g, 27.7 mmol) and EDTA (3.56 g, 12.2 mmol) were added to a mixture of 10 g of ethanol and methanol. The solution was refluxed for 2 h with stirring and then cooled to room temperature. After adding 3.47 g (12.2 mmol) of $Ti(O^{i}Pr)_4$, the solution was refluxed for 4.5 h. The reaction mixture was cooled to room temperature, and 1.56 g (13.8 mmol) of 30% H_2O_2 was carefully added. The solution was then refluxed for 0.5 h. The concentration of titanium was 0.4 mmol g^{-1}.

5-2.4 Preparation of the composite precursor solution ($S_{composite}$)

The precursor solution for fabricating Ag-NP/TiO_2 composite thin films ($S_{composite}$) was prepared by mixing the solutions S_{Ag} and $S_{titania}$ of various concentrations to adjust the silver concentration in the range 10–80 mol%.

5-2.5 Film fabrication by coating and heat treatment

Precursor films were deposited on the quartz glass substrate at ambient temperature using the spin-coating method, in a double-step mode: the first step was carried out at 500 rpm for 5 s and the second, at 2000 rpm for 30 s, for all preparations.

Two thin films of Ag nanoparticles and titania were formed by heat treating the spin-coated precursor films and applying the solutions $\mathbf{S_{Ag}}$ and $\mathbf{S_{titania}}$, respectively as illustrated in Chapter 3, Fig. 3.1 The Ag-nanoparticle/titania composite (COMP-Ag*n*) films were fabricated by heat treating the spin-coated precursor films, while applying the solution $\mathbf{S_{composite}}$, at 600°C for 30 min in air. The number *n* in the notation of the composite films indicates the silver molar percentage (Ag mol%) to TiO_2; for example, the name COMP-Ag40 indicates that the silver molar percentage in the $S_{\mathbf{composite}}$ solution was 40 mol%.

For TEM observations, $S_{\mathbf{composite}}$ at S_{Ag} concentrations of 40, 45 and 70 mol% were spin-coated and heat treated on NaCl single crystals at 600°C for 30 min. After dissolving the NaCl crystals in water, the ultra–thin films were then carefully transferred onto Cu grid plates.

5-2.6 Observation of surface morphology, nanostructure and mechanical strength

The surface morphology of the resultant films was observed using a field-emission scanning electron microscope (S-4200, Hitachi) at an accelerating voltage of 5.0 kV. The elemental mapping of COMP-Ag70 films was observed with an EDX equipment (S-4200, Hitachi). The nanostructure images were observed with a transmission electron microscope (TEM H8100, Hitachi) at an accelerating voltage of 120 kV. The

mechanical strength of the thin films on the quartz glass substrates were investigated by scratch tester (HEIDON-22, Shinto Scientific) by applying a load of 30N and a scratch speed of 0.40mm/s.

5-2.7 Crystal structure and particle size

The X-ray diffraction (XRD) patterns of Ag particles, titania, and COMP-Ag*n* films were measured using an X-ray diffractometer (MXP-18 AHF22, Bruker AXS) with Cu–*K*α rays generated at 45 kV and 300 mA. Parallel beam optics were employed with an incident angle of 0.3°. The anatase to rutile ratio, *f*, for titania and the COMP-Ag*n* films was calculated with the empirical equation (5.3), using the peak ratio I/I_o: rutile (1 1 0) and I/I_0: anatase (1 0 1), according to the literature [Spurr and Myers, 1957]. The *f* values were then used to determine the volumetric fraction of silver particles in Ag-NP/TiO_2 composite thin films, namely, φ_{Ag}, using equation (5.4):

$$f = \frac{1}{1 + 1.26\left(\frac{(I/I_o)_{rutile}}{(I/I_o)_{anatase}}\right)} \qquad (5.3)$$

$$\varphi_{Ag} = \left(\frac{Fw_{Ag} \bullet N_{Ag}}{d_{Ag}}\right) / \left(\frac{Fw_{Ag} \bullet N_{Ag}}{d_{Ag}} + \frac{Fw_{Titania} \bullet N_{Titania}}{(d_{anatase} \bullet f + d_{rutile} \bullet (1 - f))}\right) \qquad (5.4)$$

where $d_{anatase}$ and d_{rutile} represent the density of anatase (3.8 gcm^{-3}) and rutile (4.2 gcm^{-3}), respectively, under the assumption of tetragonal titania.

5-2.8 Measurement of thickness and electrical properties of films

The film thicknesses of titania and COMP-Ag*n* films were measured using a stylus profilometer (DEKTAK3, Sloan). The electrical resistance at 25°C was measured using the four probe method involving two multimeters (VOAC7512, Iwatsu and Model 2010

Multimeter, Keithley) and a regulated DC power supply (Model PAB 32-1.2, Kikusui Electronics Corp.). Four gold-plated tungsten probes (FELL type, K&S) were placed at intervals of 1 mm, and an added load of 0.2 kg was applied. The electrical resistivity, ρ, of the films was calculated using equation (5.5):

$$\rho = cRt \qquad (5.5)$$

where c, R, and t represent the correction value (4.45), electrical resistance, and film thickness, respectively.

5−3 RESULTS AND DISCUSSION

The precursor solution, $\mathbf{S_{Ag}}$, for fabricating silver films could be obtained by dissolving an appropriate amount of silver acetate in ethanol in the presence of dibutylamine. Furthermore, the titania precursor solution, $\mathbf{S_{titania}}$, involving the Ti–EDTA complex was also successfully prepared. Fifteen precursor solutions, $\mathbf{S_{composite}}$, with various molar percentages of Ag, could be facilely obtained by mixing the two solutions.

5-3.1 Structural and electrical properties of silver and titania films

Figure 5.1 shows the surface morphology of the silver and titania films. The surface of the silver film comprises a number of discretely deposited particles, whereas the surface of the titania thin film is continuous, i.e., completely uninterrupted. The titania film was 130 nm thick; however, the thickness of the silver film could not be determined because the particles were discontinuously deposited, as revealed by the FE-SEM observation (Fig. 5.1). The electrical resistance of both the silver and titania film exceeded 10^8 Ω

and the values were too high to be determined using the conventional apparatus employed in the present study.

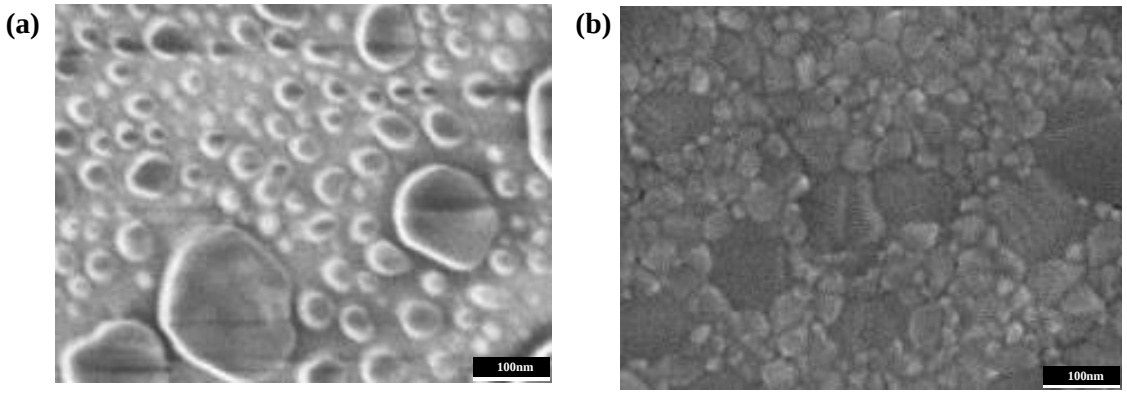

Fig. 5.1 Surface morphology of (a) silver and (b) titania thin films

5-3.2 Structural properties of Ag-NP/TiO_2 composite thin films

Figure 5.2 (a) shows XRD patterns of Ag-NP/TiO_2 composite thin films, with various volumetric fractions of silver particles, deposited on quartz glass substrates and heat treated at 600°C for 30 min. Except for the extremely small amount of silver oxide that appeared in COMP-Ag80 (φ_{Ag} = 0.68), the XRD analysis indicates that no phases other than titania and metallic silver were present in the composite thin films. This indicates that no reaction took place between titania and silver during heat treatment. The silver oxide appeared exceptionally in the XRD patterns of the Ag-NP/TiO_2 composite thin films at the highest Ag content 80 mol% may have formed during the cooling stage. It is well known that the crystalline phase adopted by titania is mainly dependent on the heat treatment temperature **[24, 26]** and method **[27]**, hence, under the current conditions, anatase and rutile mixed phases are obtained at 600°C. The peaks at 38.2°, 44.4°, 64.6°, and 77.5° are assignable to the (111), (200), (220), and (311) reflection lines of fcc Ag particles, respectively [JCPDS card 4-783, 1978]. The intensity of the (111) and (200)

diffraction peaks of the Ag phases increased with increasing content of Ag in the titania matrix whereas a decrease in the intensity of the (101) and (111) diffraction peaks of titania was observed with increasing Ag content.

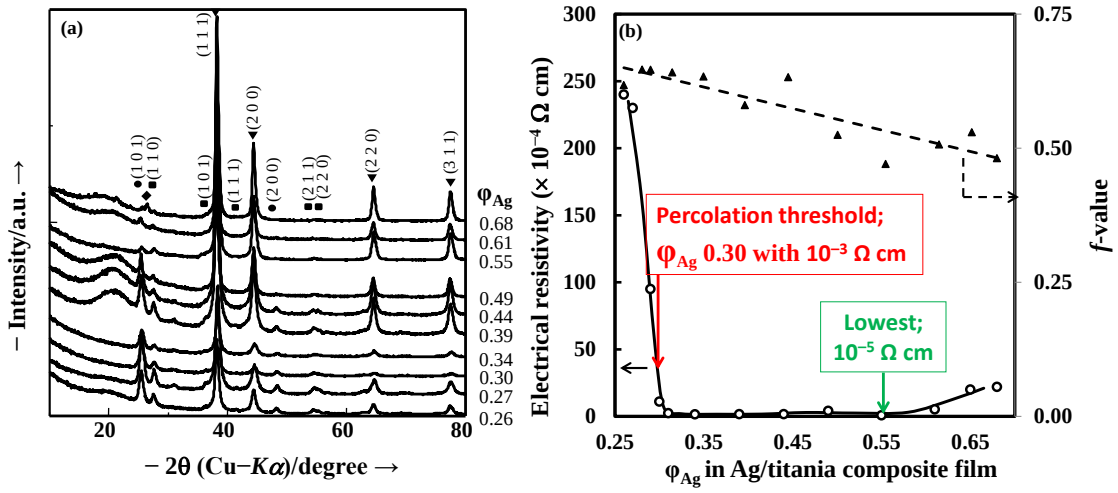

Fig. 5.2 (a) XRD patterns of the Ag-NP/TiO_2 composite thin films with various φ_{Ag}. The peaks are denoted as follows: filled inverted triangle silver, filled circle anatase, filled square rutile, and filled diamond silver oxide. **(b)** Electrical resistivity and anatase/rutile content (*f*) as a function of Ag volumetric fraction φ_{Ag} in the Ag/TiO_2 composite thin films. The lines indicate as follows: open circle Resistivity, filled triangle *f*-value.

On the basis of the XRD results in Figure 5.2(a), and equations (5.3) and (5.4), the anatase/rutile ratio (*f*) and volumetric fraction of Ag (φ_{Ag}) in the composite thin films, COMP-Ag*n*, were calculated and the *f* values are plotted as a function of φ_{Ag} in figure 5.2(b). The decreasing trend of the *f* value clearly shows that the rutile content increases at the expense of anatase as φ_{Ag} increases. The identification of the various Ag-NP/TiO_2 composite thin films used in this report is based on the calculated volumetric fraction of silver, φ_{Ag}, listed in Table 5.1.

Table 5.1 The anatase/rutile ratio, *f*, film thickness, and electrical resistance of the Ag-NP/TiO_2 composite thin films fabricated on a quartz glass using the mixed precursor solution $S_{composite}$.

Notation	*Volumetric fraction of Ag*	*f*	*Film thickness*	*Electrical Resistance*[1)]
	φ_{Ag}		**nm**	**Ω**
TiO_2	0.00	0.71	130	$>10^8$
COMP-Ag40	0.26	0.62	100	$>10^8$
COMP-Ag42	0.27	0.65	100	$5.0\ (2) \times 10^2$
COMP-Ag45	0.30	0.65	100	25 (2)
COMP-Ag46	0.31	0.64	100	12 (1)
COMP-Ag50	0.34	0.63	100	5.0 (0.1)
COMP-Ag55	0.39	0.58	100	3.0 (0.3)
COMP-Ag60	0.44	0.63	100	4.0 (0.3)
COMP-Ag65	0.49	0.53	110	8.0 (0.7)
COMP-Ag70	0.55	0.47	110	2.0 (0.4)
COMP-Ag75	0.61	0.51	110	7.0 (3)
COMP-Ag78	0.65	0.53	170	26 (15)
COMP-Ag80	0.68	0.48	260	19 (12)

1) Estimated standard deviations are presented in parentheses.

5-3.3 Determination of percolation threshold for the electrical resistivity of the Ag-NP/TiO_2 composite thin films

Table 5.1 above also lists the film thickness and electrical resistance of composite thin films with φ_{Ag} ranging from 0.26 to 0.68. The percolation threshold value for the influence of Ag addition on electrical resistivity of Ag-NP/TiO_2 composite thin films on quartz glass can be extracted from Figure 6.2(b) by a differentiation method. The percolation threshold was found at $\varphi_{Ag} = 0.30$.

The percolation theory is useful for understanding the properties of composite materials based on the distribution and continuity of the components in composite materials. A drastic change in the properties of the composite occurs in the vicinity of the percolation threshold **[28]**. In the present study, it was elucidated that the high electrical resistivity of the thin films changes to a low resistivity value of 10^{-3} Ω·cm at $\varphi_{Ag} = 0.30$. The change in anatase/rutile content within the thin films does not have an effect on the electrical resistivity of the thin films at 600°C, as shown in Figure 5.2(b).

5-3.4 Morphological changes and resistivity recovery of high Ag loaded composite films

FE-SEM images of Ag-NP/TiO_2 composite thin films with φ_{Ag} values of 0.26, 0.30, 0.34, 0.44, 0.55, and 0.68 are shown in Figs. 5.3(a)–(f), respectively. The white particles that appear in the FE-SEM images represent the Ag particles on the film surfaces, because an EDX in figure 5.4(f) analysis elucidated that these particles correspond to the Ag element. Thus, the presence and distribution of Ag particles on the surface of the Ag-NP/TiO_2 composite films can be observed in the FE-SEM images.

At the lower Ag load ($\varphi_{Ag} = 0.26$) shown in Fig. 5.3(a), there are few Ag particles, and these are dispersed far from each other on the film surface. However, for silver loads

where $0.30 < \varphi_{Ag} \leq 0.55$, many Ag particles are uniformly distributed across the films, although this caused partial agglomeration with an increase in the silver load. Moreover, for the SEM image with the highest silver load ($\varphi_{Ag} = 0.68$), it appears that the Ag particles became aggregated and formed a large cluster, as shown in Fig. 5.3(f). Therefore, the morphology of composite thin films with large amounts of loaded silver was found to have a tendency that was identical to that of a silver film without a titania matrix, as has been shown in Fig. 5.1. Additionally, the morphological change caused by the agglomeration of Ag nanoparticles may increase the film thickness from 110 nm for $\varphi_{Ag} \leq 0.55$ to 260 nm for $\varphi_{Ag} = 0.68$, resulting in an increase in the electrical resistivity because of the inevitable increase in contact resistance between the grown particles. Thus, the resistivity recovery of composite films (Fig. 5.4) with φ_{Ag} values larger than 0.60 can be attributed to this morphological change.

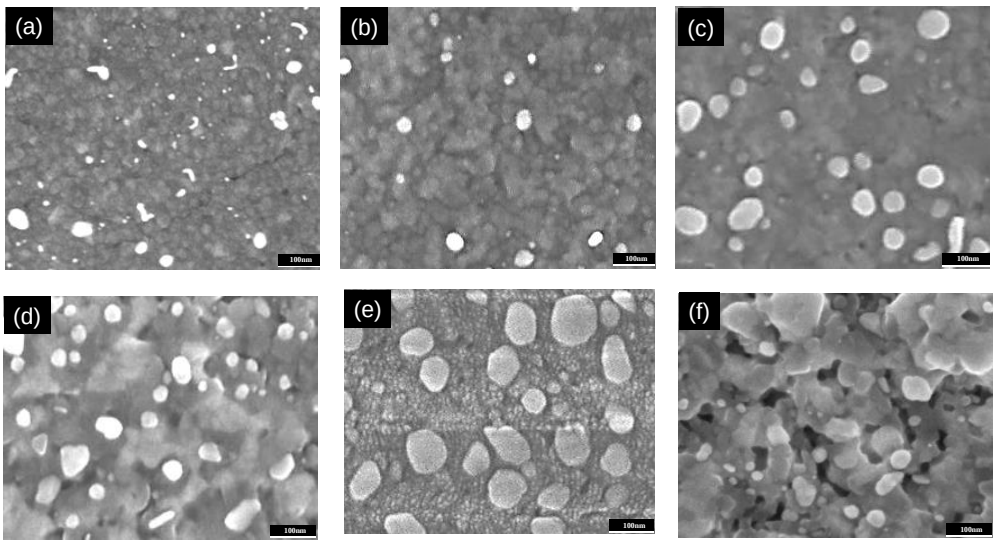

Fig. 5.3 FE-SEM images of the Ag-NP/TiO_2 composite thin films (a–f) at Ag volumetric fractions, φ_{Ag}, of 0.26, 0.30, 0.34, 0.44, 0.55, and 0.68, respectively.

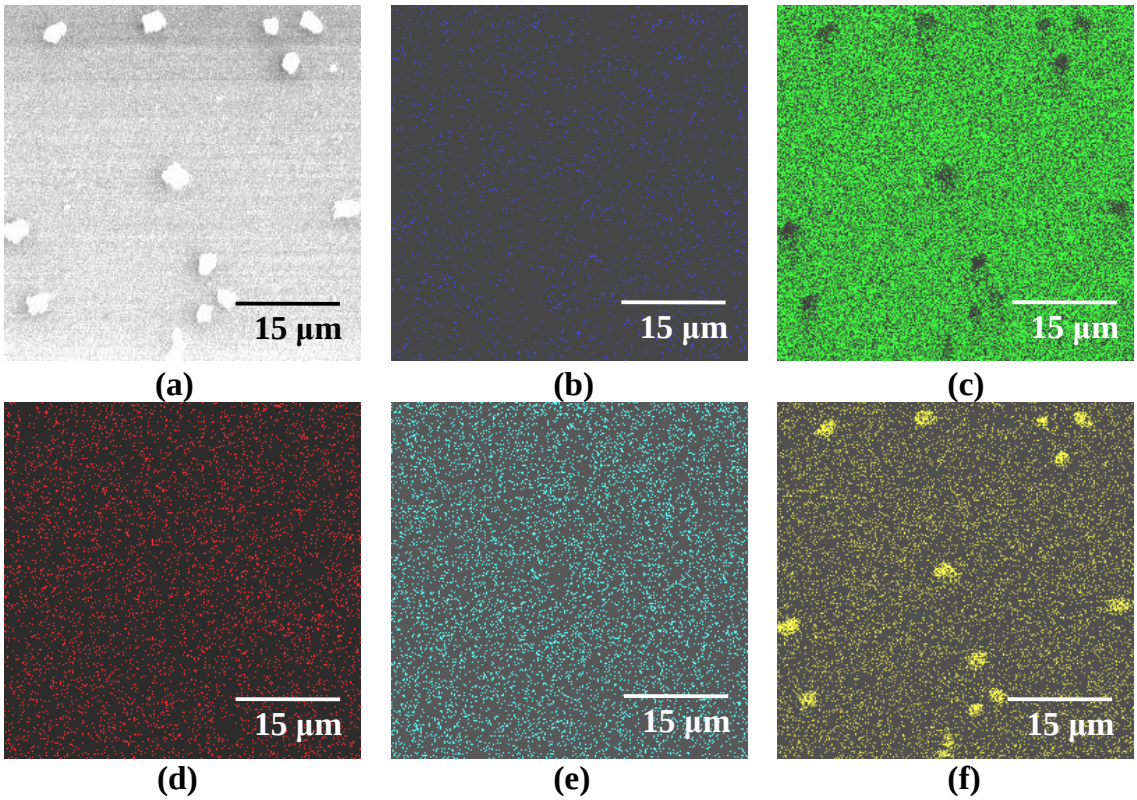

Fig. 5.4 Elemental mapping of Ag-NP/TiO_2 composite thin films at Ag volumetric fractions, φ_{Ag} value 0.34, observed by using energy-dispersive X-ray spectroscopy at an accelerating voltage of 20 kV. (a), (b), (c), (d), (e), and (f) were indicated surface appearance, C Kα, Si Kα, Ti Kα, Ti Lα1, and Ag Lα1 map, respectively.

It is proposed that the electrical resistivity change is strongly dependent on the shape and size of the particles, and the quality of the particle boundary, which determines the percolation effects **[6, 29]**. From these points of view, the influences of Ag nanoparticles on the electrical resistivity of the present composite thin films are discussed in the following sections based on TEM observations, which provide quantitative information about the Ag nanoparticles in the composite thin films. TEM images of Ag-NP/TiO_2 composite thin films with φ_{Ag} values of 0.26, 0.30, and 0.55 are shown in Figure 5.5, along with histograms of the particle size distributions. The

presence and distribution of the Ag nanoparticles (dark particles) within the composite films can also be observed clearly.

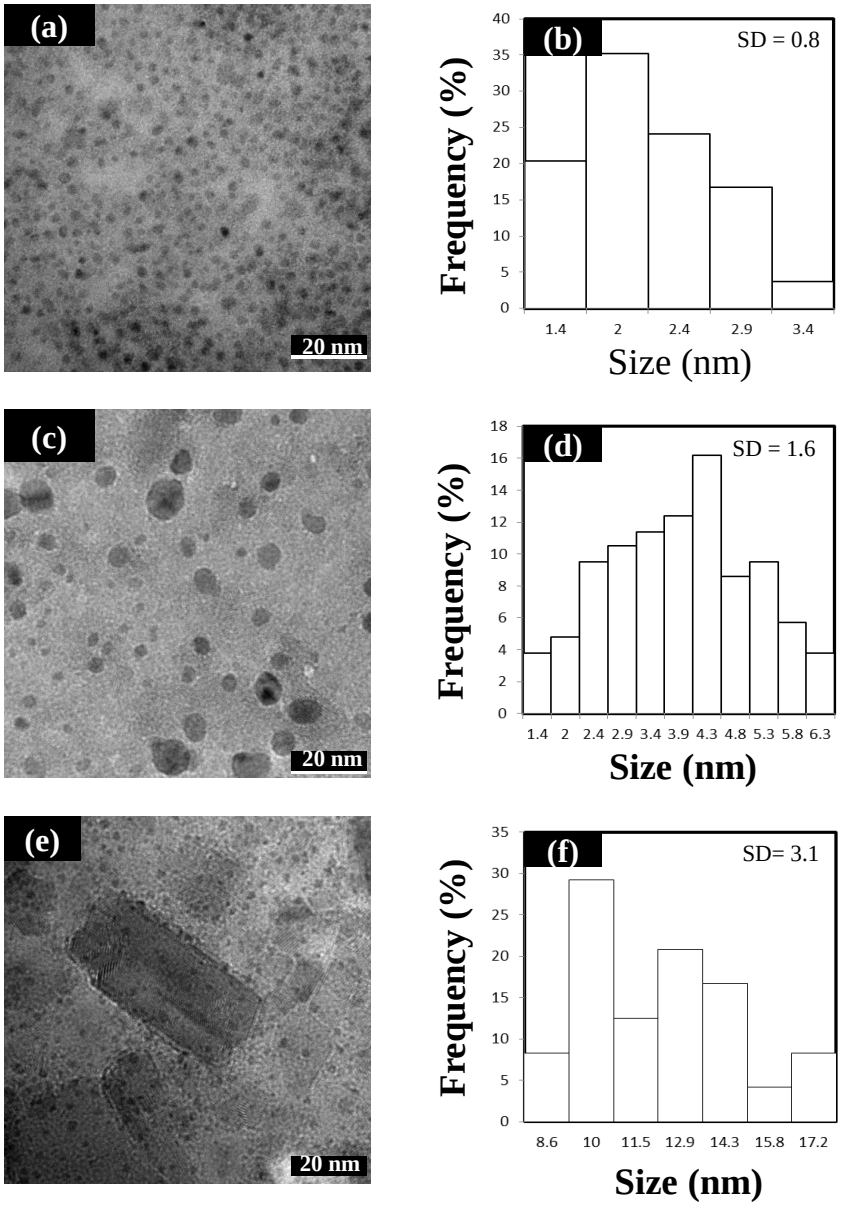

Fig. 5.5 TEM images a, c, and e and size distribution of silver nanoparticles b, d, and f of the Ag-NP/TiO_2 composite thin films at Ag volumetric fractions, φ_{Ag}, of 0.26, 0.30, and 0.55, respectively

5-3.5 Influence of silver nanoparticles` shape and distribution on electrical resistivity of composite thin films

The shape of the conductive material in an insulator plays a significant role with respect to reducing the critical limit for making a conductive composite **[6, 9]**. In the case of the present Ag-NP/TiO_2 thin films, the TEM observations demonstrated that all of the films exhibited spherical Ag nanoparticles in the titania matrix, with the exception of the composite thin film with an Ag volumetric fraction of 0.55 (Fig.5.5(e)), which showed a mixture of small spherical, rod-like, and agglomerated Ag nanoparticles. The small spherical Ag nanoparticles associated with rod-like and agglomerated Ag nanoparticles observed for $\varphi_{Ag} = 0.55$ may have been released into the TiO_2 matrix from the agglomerated Ag particles by the energy provided from the ultrasonic stirring during the preparation procedure **[29]**. These small spherical Ag-NPs also lead to the formation of more conducting paths per unit volume. The smaller particles coalesce to form small aggregates, but their greater number results in a smaller gap between the aggregates, which aids the electron flow by electron hopping or tunneling **[6]**. This may explain why a significantly lower electrical resistivity was observed for the thin films with $\varphi_{Ag} = 0.55$ compared to the other thin films.

5-3.6 Influence of silver nanoparticles` size on electrical resistivity of composite thin films

The TEM histograms (Figs. 5.5(b), (d), (f)) with the standard deviations illustrate that the mean diameter of the Ag nanoparticles was in the range of 1.4−3.4 nm for φ_{Ag} = 0.26, 1.4−6.3 nm for φ_{Ag} = 0.30, and 8.6−17.2 nm for φ_{Ag} = 0.55. In the TEM histograms, it is noteworthy that raising the Ag concentration not only increases the

average Ag nanoparticle size, but also, more importantly, facilitates the construction of interconnected nanoparticles to establish effective conducting paths. Therefore, it is expected that the thin film with the highest φ_{Ag} value should have the lowest resistivity. Hence, the concept of using nano-sized silver particles instead of micro-sized particles is important for electrical conductivity given that the use of nanoparticles should offer the conceivable advantage of preventing the settling problem encountered in some micro-sized Ag particle systems **[30]**, which may prevent the homogeneous distribution of Ag particles within the titania matrix resulting in the agglomeration of the Ag nanoparticles.

Moreover, apart from the particle size range for φ_{Ag} = 0.55 in the TEM histogram presented in Fig. 5.5(f), there are also many smaller spherical Ag-NPs with a particle size of about 1.4 nm associated with the rod-like Ag-nanoparticles. The frequency of these small particles is not included in the histogram because they are heavily distributed all over the thin film with a φ_{Ag} value of 0.55. The presence of these small Ag-nanoparticles associated with the rod-like Ag-particles in the titania matrix may form part of the explanation of why the composite film at φ_{Ag} = 0.55 registered the lowest electrical resistivity.

5-3.7 Influence of distance between silver nanoparticles on percolation threshold and electrical resistivity of composite thin films

From the TEM image, the spacing range between neighboring particles was determined to be 4−30 nm for the film with φ_{Ag} = 0.26. In the Ag-NP/TiO_2 thin film with φ_{Ag} = 0.30, the Ag nanoparticles were less densely packed than those in the composite film with φ_{Ag} = 0.55, with an average distance of 8 nm from each other. Although contact between

metallic particles appears to be necessary to achieve electrical conductivity, it has been observed that a certain level of conductivity could be obtained in systems where the particles were not necessarily in contact **[31]**. This may account for the occurrence of the percolation threshold of the electrical resistivity at φ_{Ag} = 0.30, where the particles are not yet in contact with each other, and also explains why a significantly higher electrical resistance was observed at φ_{Ag} = 0.26. Jeonga *et al*., **[32]** proposed a carrier tunneling mechanism for this phenomenon. By this mechanism, the distance between particles had to be less than 10 nm for tunneling to work. It is therefore acceptable that the percolation threshold appeared at φ_{Ag} = 0.30 in the present study, on the basis of the carrier tunneling mechanism, because an average distance of 8 nm between Ag nanoparticles was attained at the stated Ag volumetric fraction.

In the case of the Ag-NP/TiO_2 thin film with φ_{Ag} = 0.55, the TEM observations shown in Fig. 5.5(e) demonstrated that some of the Ag nanoparticles make contact with each other to form agglomerated Ag particles. Because the resistivity change is strongly dependent on the nature of the particle boundary, which determines the percolation effects, better conduction properties should be expected from films with larger particles and shorter distances between the particles **[33]**. This may further explain why the sample with φ_{Ag} = 0.55 exhibited a lower electrical resistivity.

5-3.8 Mechanical strength of the thin films

The mechanically strength of quartz glass, TiO_2 and Ag-NP/TiO_2 composite thin films were performed to determine the degree of adherence of the coated films onto the quartz glass substrate. The Young`s modulus values measured by Knoop indentation as a function of the indentation load are illustrated in figure 5.6. Table 2 presents the mean

hardness and Young's modulus values, obtained from three tests on each specimen. The adhering strength of the thin films on quartz substrate are 2.44, 2.56, 2.99, 2.97 and 8.41 GPa corresponding to TiO_2, φ_{Ag} 0.26, φ_{Ag} 0.30, φ_{Ag} 0.55 and naked quartz glass respectively. Adhering strength of all thin films is 2 times less adhesive than uncoated quartz glass. The stress of the thin films on quartz glass are almost identical where the φ_{Ag} 0.30 thin film show the lowest stress of 48.93 MPa. This is probably that titanium ions of TiO_2 links covalently to the O atoms belong to quartz molecules to form a robust interface between glass and TiO_2 as reported by Nagai *et al.* **[34]**.

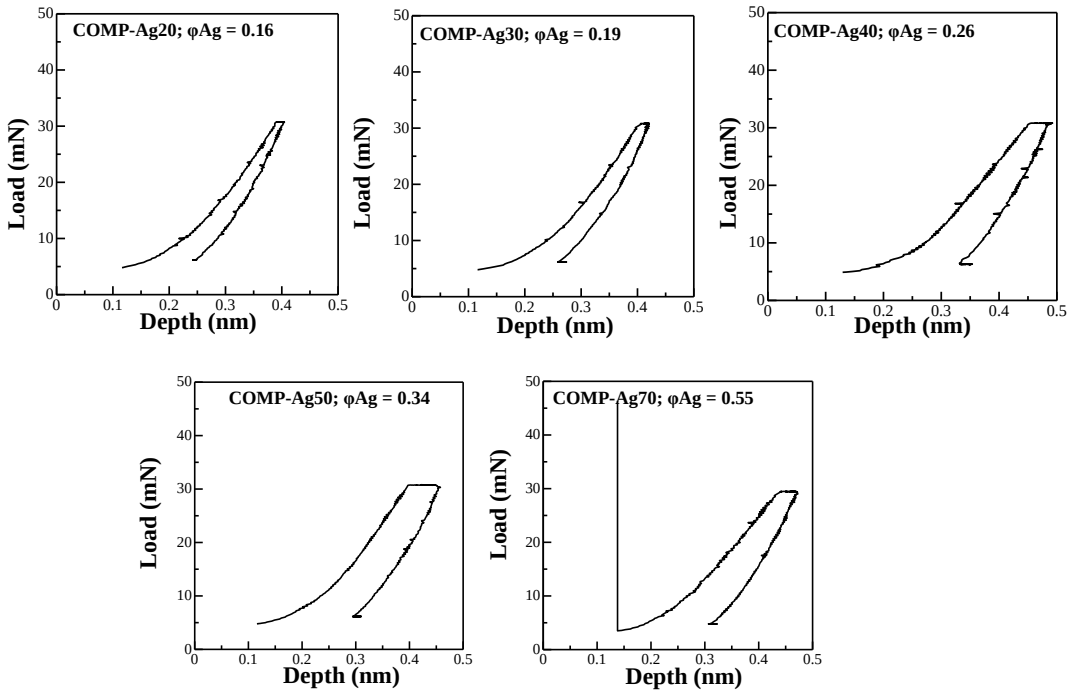

Fig. 5.6 Indent test curves of Ag-NP/TiO_2 composite thin films with various φ_{Ag}.

The presence of silver makes the Ag-NP/TiO_2 composite thin films even stronger as compare to naked TiO_2 thin film. Generally, incorporation of particles to a matrix may increase or decrease the tensile strength of the composites. For example, Fiber type fillers normally result in improved the tensile strength, as the fibers are able to support

the stresses transferred from the matrix. However, other researchers reported the decrease in tensile strength may be attributed to restriction of matrix chain movements due to agglomeration of the filler particles to form a domain that acts like a foreign body as well as weak interfacial region **[35]**. From SEM images, the poor Ag dispersion will reduce the Ag/TiO_2 interaction and consequently reduce the physical properties. This shows why the decrease in mechanical strength for the high silver concentration composites was larger than thin films with lower silver concentration composites.

Table 5.1 Young`s modulus, knoop hardness and Stress results obtained during the measurement of mechanical strength of the Ag-NP/TiO_2 composite thin films fabricated on a quartz glass.

Notation	**Volumetric fraction of Ag**	**Young`s Modulus**	**Knoop Hardness**	**Stress**
	φ_{Ag}	**Pa**	**GPa**	**MPa**
Quartz glass	-	1.10×10^{11}	8.41	-
TiO_2	0.00	7.47×10^{10}	2.44	51.56
COMP-Ag20	0.16	1.09×10^{11}	3.90	50.46
COMP-Ag30	0.19	1.10×10^{11}	3.82	51.87
COMP-Ag40	0.26	7.84×10^{10}	2.56	52.19
COMP-Ag50	0.34	8.32×10^{10}	2.99	48.92
COMP-Ag70	0.55	8.40×10^{10}	2.97	51.35

5−4 SUMMARY

Ag-nanoparticle/titania thin films, with various volumetric fractions of silver (φ_{Ag}) in a titania matrix, were successfully fabricated using the molecular precursor method, and their structural and electrical properties were clarified. This study shows that the molecular precursor method, which offers excellent miscibility of the silver and titania precursor solutions is effective for overcoming the limitations in miscibility of the conventional sol–gel method and is necessary for fabricating composite thin films having a large φ_{Ag} value.

Increasing the Ag volumetric fraction from 0.27 to 0.55 decreases the electrical resistivity from in excess of 10^{-2} Ω·cm to 10^{-5} Ω·cm. It was elucidated from both FE-SEM and TEM observations that the decrease in electrical resistivity was attributed to a change in the shape and size of the Ag nanoparticles and the distance between the nanoparticles. Based on the relationship between the volumetric fraction of Ag and the electrical resistivity of the thin films, the percolation threshold of the Ag-NP/titania composite thin film was found at a silver volumetric fraction of 0.30. A drastic reduction in the electrical resistivity of the composite thin film was observed near the percolation threshold upon addition of a small amount of Ag nanoparticles, in order to build the conductive network, even though the total connection of the Ag nanoparticles was still not accomplished. The electrical resistivity recovered, moving from 10^{-5} to 10^{-3} Ω·cm, with further increase in the φ_{Ag} values from 0.61 to 0.68, due to an inevitable increase of the separation distance between the grown particles caused by the agglomeration of Ag nanoparticles.

The relationships between the mechanical properties of the composite thin films with different Ag concentrations were also investigated. The mechanical strength test revealed the stable attachment of the coated film to quartz glass substrate. It revealed that the coated film on quartz glass produced by the molecular precursor method showed excellent adhesion to the glass. It is assumed that the adhesive characteristic of the Ag/TiO_2 composite thin films pose no problem for clinical applications.

5−5 REFERENCES

1. Li H, Zhao G., Song B., Han G. (2008). *J Cluster Sci.*, **19**, 667-673.

2. Cattin L., Morsli M., Dahou F., Yapi S., Khelil A., Bernède JC. (2010). *Thin Solid Films* **518**, 4560–4563.

3. Kumpika T., Thongsuwan W., Singjai P. (2008). *Thin Solid Films* **516**, 5640–5644.

4. Lee H., Chou K., Shih Z. (2005). *Int J Adhes. Adhes.* **25**, 437–441.

5. Ambrozic M., Dakskobler A., Valant M., Kosmac T. (2005). *Mater. Sci-Pol.* **23**:2, 535-539.

6. Zhang W., Dehghani-Sanij AA., Blackburn RS. (2007). *J. Mater. Sci.* **42**:3408–3418.

7. Hanisch C., Ni N., Kulkarni A., Zaporojtchenko V., Strunskus T., Faupel F. (2011). *J. Mater. Sci.* **46**: 438-445.

8. Gupta A. and Choudhary V. (2011). *J Mater. Sci.* **46**: 6416–6423.

9. Ho L., Nishikawa H. and Takemoto T. (2011). *J Mater. Sci.: Mater. Electron* **22**:538–544.

10. Shin S. (2010). *Electronic Materials Letters*, **6**:2. 65-70.

11. Macwan DP., Dave PN. and Chaturvedi S. (2011). *J Mater. Sci.*, **46**:3669–3686. DOI 10.1007/s10853-011-5378-y.

12. Hong C., Park H., Moon J, Park H. (2006). *Thin solid film* 515:**3**, 957–960.

13. Lo CT., Chou K. and Chin W. (2001). *J Adhes Sci Technol.*, 15:**7**, 783–792

14. Wang Z., Helmersson U., Kall P. (2002). *Thin Solid Films* **405**, 50–54

15. Addamo M., Augugliaro V., Di Paola A., García-López E., Loddo V., Marcì G., Palmisano L. (2008). *Thin Solid Films* **516**, 3802–3807.

16. Traversa E., Di Vona M., Nunziante P., Licoccia V. (2000). *J Sol-Gel Sci. Technol.* **19**, 733–736.

17. Miao L., Jin P., Kaneko K., Terai A., Nabatova-Gabain N., Tanemura S. (2003). *Appl. Surf. Sci.* **212**, 255–263.

18. Ren P., Fan H., Wang X., Shi J. (2011). *J Alloy Compd* **509**, 6423–6426.

19. Sancaktar E. and Bai L. (2011). *Polymers*, **3**, 427-466.

20. McNaught AD. and Wilkinson A. (1997). *Blackwell Science, 2nd ed.* **267**. [ISBN 0-86542-6848].

21. Sato M., Hara H., Nishide T., Sawada Y. (1996). *J Mater. Chem*. **6**, 1767-1770.

22. Sato M., Hara H., Kuritani H., Nishide T. (1997). *Sol Energ Mat Sol C* **45**, 43-49.

23. Sato M., Tanji T., Hara H., Nishide T., and Sakashita Y. (1999). *J Mater. Chem*., **9**, 1539-1542.

24. Nishide T., Sato M., Hara H. (2000). *J Mater. Chem*. **34**: 465-469

25. Takahashia K., Hayakawa T., Yoshinari M., Hara H., Mochizuki C., Sato M., Nemoto K. (2005). *Thin Solid Films*, **484**, 1-9.

26. Nagai H, Aoyama S, Hara H, Mochizuki C, Takano I, Baba N, Sato M (2009). *J Mater Sci* **44**:861-868.

27. Zhang H. and Banfield JF. (2009). *Am. Mineral.*, **84**, 528–535.

28. Deepa KS., Nisha SK., Parameswaran P., Sebastian MT., and James J. (2009). *Appl phys lett*, **94**, 142902-142903.

29. Elechiguerra JL., Burt JL., Morones JR., Camacho-Bragado A., Gao X., Lara HH.,

Yacaman MJ. (2005). *J Nanobiotechnology*, **3**:6, 1-10.

30. Standridge SD., Schatz GC., Hupp JT. (2009). *Langmuir* **25**, 2596-2600

31. Ye L, Lai Z, Liu J, Tholen A (1999). *IEEE T Electron Pa M* **22**: 299-302.

32. Jeonga SH., Lim DC., Boo J-H., Lee SB., Hwang HN., Hwang CC., Kim YD. (2007). *Appl Catal A-Gen*, **320**, 152–158.

33. Kim WJ., Taya M., Nguyen MN. (2009). *Mech Mater* **41**, 1116–1124.

34. Nagai H., Mochizuki C., Hara H., Takano I., Sato M. (2008). *Sol Energ Mat Sol Cell* **92**, 1136– 1144.

35. Deshmukh S.P., Rao A.C., Gaval V.R., Joseph S., Mahanwar P.A. (2010). *J. Min. Mater. Charact. Eng.* 9:**9**, 831-844

CHAPTER 6: FURTHER INVESTIGATION OF PERCOLATION THRESHOLD FOR ELECTRICAL RESISTIVITY OF SILVER NANOPARTICLE INCORPORATED IN ZIRCONIA MATRIX; AN INSULATOR.

6−1 INTRODUCTION

When electrically conducting particles are randomly distributed within an insulating matrix such as metal-ceramic matrix composites, the sample is non-conducting, until the volume fraction of the conducting phase reaches the so-called percolation threshold **[1]**. In chapter 5, I found the percolation threshold for the electrical resistivity of metallic Ag-nanoparticle/titania (Ag-NP/TiO_2) composite thin films, with different volumetric fractions of silver ($0.26 \leq \varphi_{Ag} \leq 0.68$) to titania, fabricated on a quartz glass substrate at 600°C using the molecular precursor method. The percolation threshold was identified at a φ_{Ag} value of 0.30. The lowest electrical resistivity of 10^{-5} Ω·cm at 25°C was recorded for the composite with the Ag volumetric fraction, φ_{Ag}, of 0.55. X-ray diffraction (XRD), field-emission scanning electron microscope (FE-SEM), and transmission electron microscopic (TEM) evaluation of the effect of the morphology and the nanostructures of the Ag nanoparticles in the composite thin films on the electrical resistivity of the film revealed that the films consist of rutile, anatase, and metallic Ag nanoparticles homogeneously distributed in the titania matrix. It could be deduced that the electrical resistivity of the thin films formed at 600°C was unaffected by the anatase/rutile content within the thin film, whereas the shape, size, and separation distance of the Ag nanoparticles strongly influenced the electrical resistivity of the Ag-nanoparticle/titania composite thin films. In this chapter, the objective is to investigate if the percolation threshold found for electrical resistivity of Ag NP incorporated in titania matrix, a metal oxide semiconductor can be the identical to those of Ag NP incorporated in zirconia matrix, a metal oxide insulator.

Zirconia (Zirconium dioxide or ZrO_2) is considered as a potential replacement of SiO_2 due to its high dielectric constant (~25), wide band gap (4.6–7.8 eV), low leakage current level, and superior thermal stability **[2]**. The equilibrium phase of undoped ZrO_2 (baddeleyite) is monoclinic (α) under normal conditions and tetragonal (β) up to ~ 1170ºC, and the high-temperature cubic (γ) phase is stable above 2370ºC up to the melting point at ~2710ºC **[3]**. Figure 6.1 shows schematic representation of crystal structures of zirconia, and a continuous heating phase transition of ZrS_2 in oxygen **[4]**. A spread in the transition temperatures of the Zr‑O phase diagram is encountered due to the variety of metastable states arising from sluggish kinetics of phase transformations even at 1000ºC **[4−6]**.

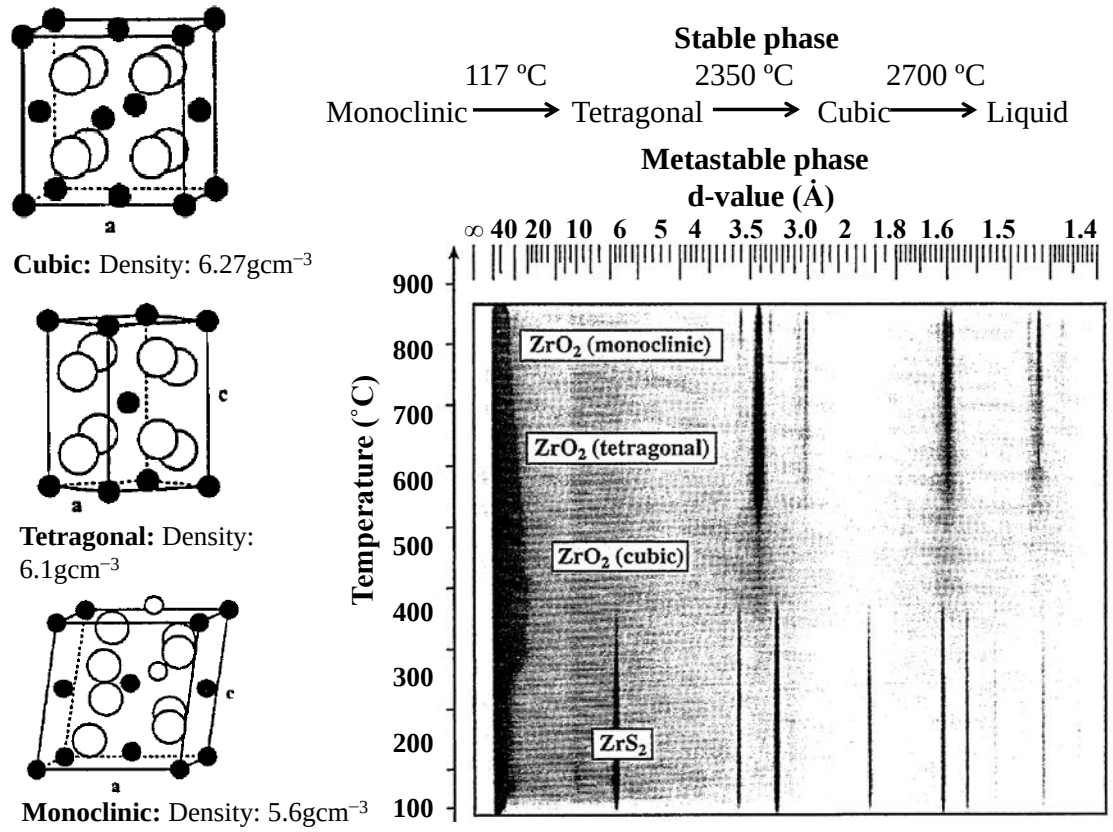

Fig. 6.1 Schematic representation of crystal structures of zirconia, and a continuous heating X-ray powder diffraction pattern of ZrS_2 in oxygen **[4]**.

On the other hand, silver (Ag) is a good conductor and it is facile and fairly low cost. Like Ag NP in TiO_2 matrix, incorporating Ag nanoparticles with ZrO_2 matrix can be expected that Ag nanoparticles to form stable conducting paths inside of ZrO_2 matrix. Therefore, the resistance of ZrO_2 film can be lowered. In application, the particles need to be well connected to form the conduction path, while the ZrO_2 help to adhere these particles to the glass substrates. In order to control the electrical characteristics of such systems, it is very important to have exact knowledge of the percolation threshold, whereby conductor/semiconductor composite with a conductor ratio at or above a given volume fraction ($\varphi_{conductor}$), established a network of conducting particles, and thus, the resistivity of the composite suddenly decreases **[7]**.

As we reported in previous chapter, the volumetric fraction, φ_i, is generally defined according to equation (6.1), where V_i and V represent the volumes of a constituent, i, and of all constituents of the mixture prior to mixing, respectively **[8]**:

$$\varphi_i = V_i/V \qquad (6.1)$$

Based on this general formula, the volumetric fraction of silver particles in a composite, namely, φ_{Ag}, which is strongly related to the percolation threshold, can be defined by equation (7.2), where d_{Ag} and $d_{zirconia}$ represent the density of cubic silver and zirconia respectively. The density of cubic silver is 3.8 g/cm^3 whereas the density of zirconia depend on the crystal phase of the thin film at a given moment (6.27, 6.1 and 5.6 g/cm^3 for cubic, tetragonal and monoclinic zirconia respectively) and N_{Ag} and $N_{zirconia}$ represent the amount of substance of silver and zirconia, respectively, under the assumption of cubic silver and crystal phase of zirconia of a given thin film.

$$\varphi_{Ag} = \left(\frac{Fw_{Ag} \bullet N_{Ag}}{d_{Ag}}\right) / \left(\frac{Fw_{Ag} \bullet N_{Ag}}{d_{Ag}} + \frac{Fw_{Zirconia} \bullet N_{Zirconia}}{d_{Zirconia}}\right) \qquad (6.2)$$

Since metal incorporation into an insulating matrix must inevitably deal with the fact that the use of numerous different preparation methods for obtaining these materials may have given rise to their different properties. The inclusion of nanoparticles into various materials and methods may offer unique advantages in terms of electrical characteristics **[9]**. In order to validate that, I tried to fabricate Ag NP/ZrO_2 composite thin films with different volumetric fractions of silver using the identical method; molecular precursor method (MPM), identical heat-treatment temperature; on the basis of these considerations, Ag-NP/ZrO_2 composite thin films were fabricated at 600ºC by employing various Ag volumetric fraction values. The percolation volume φ for Ag (φ_{Ag}) particles in zirconia was also calculated to test the reliability of the percolation threshold found in chapter 6. Crystal structural evaluations of the fabricated thin films were performed using X-ray diffraction (XRD). The film thickness and electrical resistivity of the thin films were examined using a profilometer and by the four-probe method, respectively. It is known that the exhibition of high absorption spectrum in the visible region of the Ag containing thin film is an idication that the Ag particles are metallic due to the plasmonic properties **[10]**. Therefore, the optical properties of the new fabricated Ag NP/ZiO_2 composite thin films were also investigated using UV/Vis spectrometer in order to prove that main constitute of silver species in the composite thin films are mettallic.

6−2 EXPERIMENTAL

6-2.1 Materials

All the materials employed in this chapter are tabulated in Chapter 3, Table 3.1.

6-2.2 Preparation of silver (SAg) and zirconia ($S_{Zirconia}$) precursor solutions ($S_{titania}$) by molecular precursor method (MPM).

The preparation of Ag precursor solution is reported in both chapter 4 and 5 and the schematic outline is again illustrated in Scheme 6.I (a). The precursor solution containing the Zr^{4+} complex of NTA was obtained by a MPM and is also illustrated in Scheme 6.I(b):

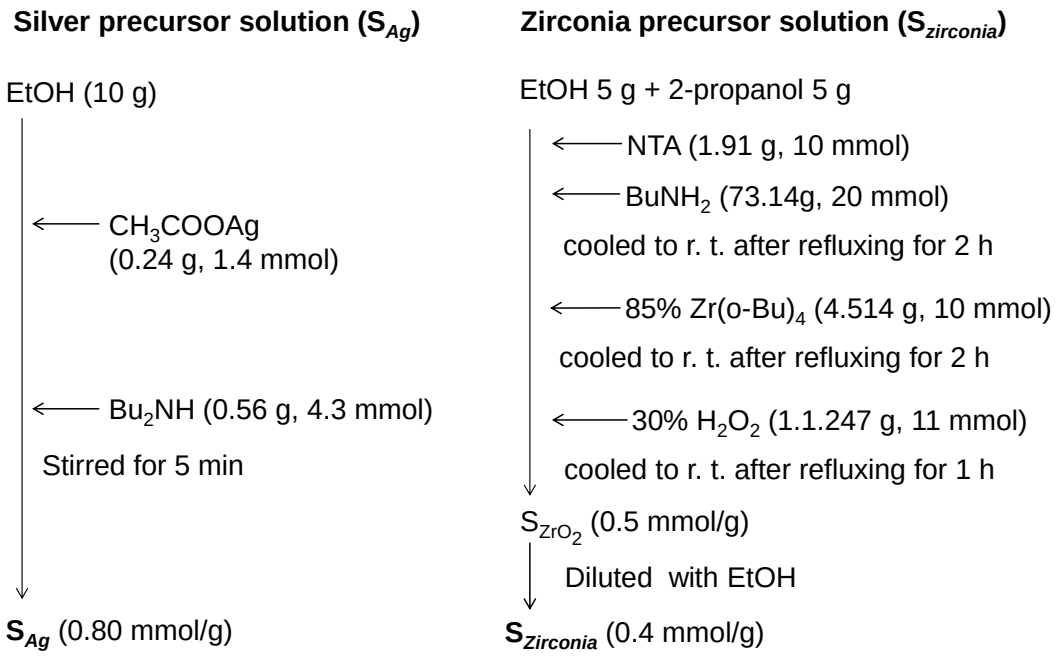

Scheme 6.I Preparation procedure of the (**a**) precursor solution, S_{Ag} containing silver acetate and (**b**) precursor solution S_{Ti} contains a Zr^{4+} complex of NTA precursor solution.

Dibutylamine (73.14 g, 20 mmol) and NTA (1.91 g, 10 mmol) were added to a mixture of 5 g of ethanol and 5 g of 2-propanol. The solution was refluxed for 2 h with stirring and then cooled to room temperature. After adding 4.514 g (10 mmol) of $Zr(o\text{-}Bu)_4$, the

solution was refluxed for 2 h. The reaction mixture was cooled to room temperature, and 1.247 g (11 mmol) of 30% H_2O_2 was carefully added. The solution was then refluxed for 1 h. The concentration of titanium was 0.5 mmol g^{-1} and diluted with ethanol to 0.4 mmol/g, equivalent to titania precursor solution ($\mathbf{S}_{\boldsymbol{Tatania}}$)`s molar concentration.

6-2.3 Preparation of the composite precursor solution ($S_{composite}$)

The precursor solution for fabricating Ag-NP/ZrO_2 composite thin films ($S_{composite}$) was prepared by mixing the solutions $\mathbf{S_{Ag}}$ and $\mathbf{S_{Zirconia}}$ of various concentrations to adjust the silver concentration in the range 10–80 mol%.

6-2.4 Film fabrication by coating and heat treatment

Precursor films were deposited on the quartz glass substrate at ambient temperature of 600ºC using the spin-coating method, in a double-step mode: the first step was carried out at 500 rpm for 5 s and the second, at 2000 rpm for 30 s, for all preparations.

Two thin films of Ag nanoparticles and pure zirconia were formed by heat treating the spin-coated precursor films and applying the solutions $\mathbf{S_{Ag}}$ and $\mathbf{S_{zirconia}}$, respectively. The Ag-nanoparticle/zirconia composite (COMP-Ag*n/*ZrO_2) films were fabricated by heat treating the spin-coated precursor films, while applying the solution $\mathbf{S_{composite}}$, at 600°C for 30 min in air. The number *n* in the notation of the composite films indicates the silver molar percentage (Ag mol%) to TiO_2; for example, the name COMP-Ag40 indicates that the silver molar percentage in the $S_{composite}$ solution was 40 mol%.

6-2.5 Crystal structure and particle size

The X-ray diffraction (XRD) patterns of Ag particles, pure zirconia, and COMP-Ag*nZrO*$_2$ films were measured using an X-ray diffractometer (MXP-18 AHF22, Bruker AXS) with Cu–*K*α rays generated at 45 kV and 300 mA. Parallel beam optics were employed with an incident angle of 0.3°. The monoclinic content ratio, C_m, to zirconia crystals phases for zirconia and the COMP-Ag*nZrO*$_2$ films was calculated with the empirical equation (6.3), using the peak ratio I_m: monoclinic (1 1 1), I_t: tetragonal (101) and I_c: cubic (1 1 1), according to the literature **[11]**. The C_m values can be then use to determine the volumetric fraction of silver particles in Ag-NP/TiO_2 composite thin films, namely, φ_{Ag}, using equation (6.4):

$$C_m = \frac{I_{m\ onoclinic}(111) + I_{m\ onoclinic}(-111)}{I_{tetragona}(101) + I_{cubic}(111) + I_{m\ onoclinic}(111) + I_{m\ onoclinic}(-111)} \qquad (6.3)$$

$$\varphi_{Ag} = \left(\frac{Fw_{Ag} \bullet N_{Ag}}{d_{Ag}}\right) / \left(\frac{Fw_{Ag} \bullet N_{Ag}}{d_{Ag}} + \frac{Fw_{Zirconia} \bullet N_{Zirconia}}{d_{tetragona}(1-C_m) + d_{cubic} \bullet (1-C_m) + d_{monocrinic} \bullet C_m}\right) \qquad (6.4)$$

where $d_{monoclinic}$, $d_{tetragonal}$ and d_{cubic} represent the density of monoclinic (5.6 gcm^{-3}), tetragonal (6.1 gcm^{-3}) and cubic (6.27 gcm^{-3}), respectively.

6-2.6 Measurement of thickness and electrical properties of films

The film thicknesses of zirconia and COMP-Ag*nZrO*$_2$ films were measured using a stylus profilometer (DEKTAK3, Sloan). The electrical resistance at 25°C was measured using the four probe method reported in chapter 3. The electrical resistivity, ρ, of the films was calculated using equation (5.5) reported in Chapter 5.

6–3 RESULTS AND DISCUSSION

The precursor solution, $\mathbf{S_{Ag}}$, for fabricating silver films could be obtained by dissolving an appropriate amount of silver acetate in ethanol in the presence of dibutylamine. The zirconia precursor solution, $\mathbf{S_{zirconia}}$, involving the Zr–NTA complex was successfully prepared. Twelve composite precursor solutions, $\mathbf{S_{composite}}$, with10, 20, 30, 40, 42, 45, 46, 50, 55, 60, 70 and 80 molar percentages of Ag, could be facilely obtained by mixing the two solutions. Figure 6.2a–g shows the photographs of some of the resultant thin films. Figure 6.2 shows the photograph images of the Ag NP, Pure ZrO_2 and Ag-NP/ZrO_2 composite thin films.

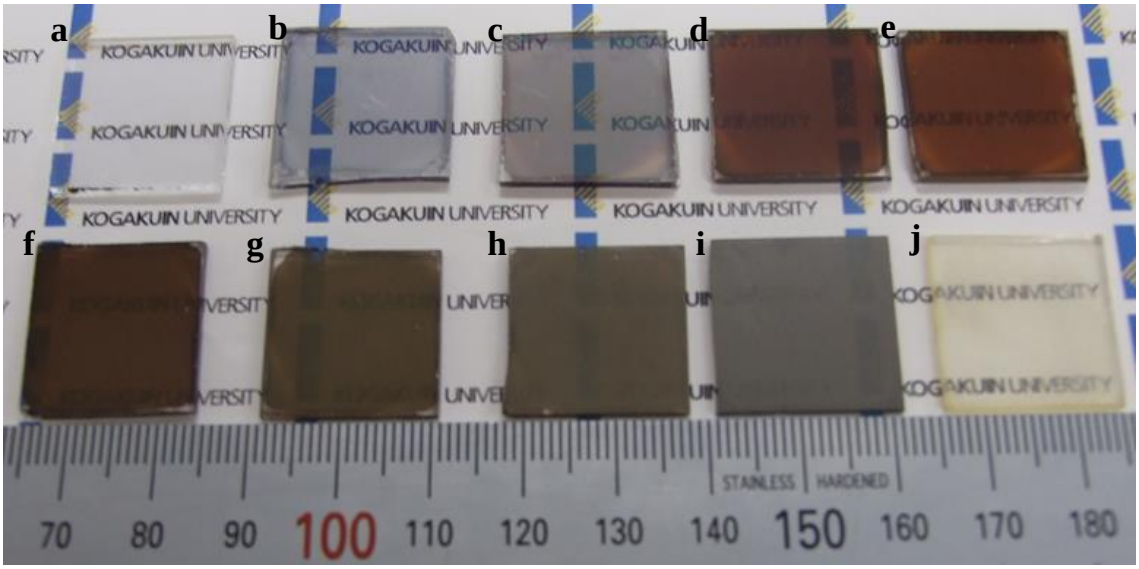

Fig. 6.2 Photographs a–h, of the resultant thin films fabricated: (a) Ag NP, (j) pure ZrO_2, COMP-Ag*n*ZrO_2 thin films where *n*=(b) 10, (c) 20, (d) 30, (e) 40, (f) 50, (g) 60, (h) 70 and (i) 80 respectively.

6-3.1 Structural, optical and electrical properties of silver, ZrO_2 thin film and Ag-NP/ZrO_2 composite thin films

The ZrO_2 thin film was 90 nm thick; however, the thickness of the silver film could not be determined because the particles were discontinuously deposited, as revealed by the FE-SEM observation chapter 3, (Fig.3.7). The electrical resistance of both the silver and ZrO_2 thin film exceeded 10^8 Ω and the values were too high to be determined using the conventional apparatus employed in the present study.

Figure 6.3 (a) shows XRD patterns of pure ZrO_2 and COMP-Ag50ZrO_2 deposited on quartz glass substrates and heat treated at 600°C for 30 min.

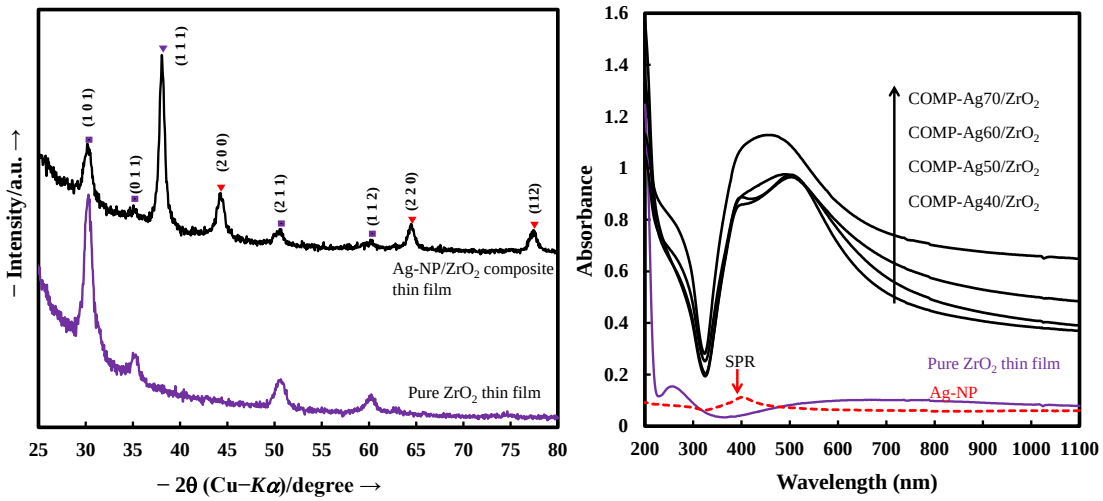

Fig. 6.3 (a) XRD patterns of the ZrO_2 and Ag-NP/ZrO_2 composite thin films with various φ_{Ag}. The peaks are denoted as follows: filled inverted triangle silver, filled circle anatase, filled square rutile, and filled diamond silver oxide. **(b)** UV/Vis Absorption spectra of the synthesized thin films.

The XRD analysis indicates that no phases other than tetragonal zirconia and metallic silver were present in the composite thin films. This indicates that no reaction took place between zirconia and silver during heat treatment. It is well known that the crystalline phase adopted by zirconia is mainly dependent on the heat treatment temperature **[4−6]**, hence, under the current conditions, single phase of tetragonal

zirconia are obtained at 600°C, corresponding to the same phase reported in literature at an identical heat treatment temperature **[4]**. The presence of Ag NP in the composite does not have any influence on the crystal phase of zirconia.

The peaks at 38.2º, 44.4º, 64.6º, and 77.5º are assignable to the (111), (200), (220), and (311) reflection lines of fcc Ag particles, respectively [JCPDS card 4-783, 1978]. The peaks at 30.4º, 35.2º, 50.4º, and 60.1º are assignable to the (101), (011), (211), and (112) reflection lines of tetragonal zirconia, respectively [JCPDS card 83-0810, **12**]. On the basis of these XRD result, the composite thin films are only consist of a single phase, tetragonal zirconia, hence equations (6.3) was omitted since C_m=1 for the calculation of Ag volumetric fraction φ_{Ag} values in Ag/ZrO_2 composite thin films. The calculated volumetric fractions of silver, φAg, listed in Table 6.1 were obtained using equation 6.4 modified to equation 6.5:

$$\varphi_{Ag} = \left(\frac{Fw_{Ag} \bullet N_{Ag}}{d_{Ag}}\right) / \left(\frac{Fw_{Ag} \bullet N_{Ag}}{d_{Ag}} + \frac{Fw_{\text{tetragonal}} \bullet N_{\text{tetragonal}}}{d_{\text{tetragonal}}}\right) \qquad (7.5)$$

Figure 6.3 (b) shows UV-Vis absorption spectra of Ag-NP, pure ZrO_2 thin films and Ag-NP/ZrO_2 composite thin films. The ZrO_2 thin film showed a low-intensity absorption band in the Vis-region; however, its absorption intensity increased steeply at shorter wavelengths. In contrast, the Ag NP film showed a weak and broad absorption band at around 410 nm. This absorption band can be also observed for the Ag-NP/ZrO_2 composite thin films, though the peak become width and some exhibit overlapping peaks upon increasing the Ag content. Theoretical when Ag-NP film is irradiated with vis-light, a large oscillating electric field is observed around the metal particles **[10, 13, 14]**. The absorption band in this region corresponds to the characteristic SPR of metallic

Ag NPs. Hence prove that the metallic Ag NP with different size and shapes due to overlapping peaks were synthesized.

Table 6.1 The Ag volumetric fraction, φ_{Ag}, values, film thickness, and electrical resistance of the ZrO_2, TiO_2, Ag-NP/ZrO_2 and Ag-NP/TiO_2 composite thin films fabricated on a quartz glass.

Notation	***Volumetric fraction of Ag in ZiO_2***	***Volumetric fraction of Ag in TiO_2***[1)]	***Film thickness (Ag-NP/ZrO_2)***	***Electrical Resistance***[2)] **(Ag-NP/ZrO_2)**	***Electrical Resistance***[1,2)] ***(Ag-NP/ZrO_2)***
	φ_{Ag}	**φ_{Ag}**	**nm**	**Ω**	**Ω**
ZrO_2	0.00	-	90	$>10^8$	$>10^8$
TiO_2	-	0.00	130	$>10^8$	$>10^8$
COMP-Ag40	0.25	0.26	110	$>10^8$	$>10^8$
COMP-Ag42	0.27	0.27	120	$>10^8$	$5.0\ (2) \times 10^2$
COMP-Ag45	0.29	0.30	120	$>10^8$	25 (2)
COMP-Ag46	0.30	0.31	110	$>10^8$	12 (1)
COMP-Ag50	0.34	0.34	120	$>10^8$	5.0 (1)
COMP-Ag55	0.38	0.39	140	$>10^8$	3.0 (3)
COMP-Ag60	0.43	0.44	130	96.7 (5)	4.0 (3)
COMP-Ag70	0.54	0.55	170	68.0 (7)	2.0 (4)
COMP-Ag80	0.67	0.68	270	$>10^8$	19 (12)

1) Data extracted from Table 5.1 from Chapter 5.

2) Estimated standard deviations are presented in parentheses.

Table 6.1 also lists the film thickness and electrical resistance of Ag-NP/ZrO_2 composite thin films with φ_{Ag} ranging from 0.26 to 0.68. Ag/ZrO_2 composite thin films with φ_{Ag} values of 0.43 and 0.54 exhibit the lowest electrical resistance of 96.7Ω and 68.0Ω corresponding to electrical resistivity of 4.4×10^{-3} and 3.0×10^{-3} Ωcm, respectively. The percolation threshold value for the influence of Ag addition on electrical resistivity of Ag-NP/ZrO_2 composite thin films on quartz glass must be found therefore, between $0.43 \leq \varphi_{Ag} \leq 0.54$. For comparison purpose, the Ag volumetric fraction φ_{Ag} values of Ag-NP/TiO_2 composite thin films extracted from the previous chapter are also tabulate in the same table. In this case, for Ag-NP/TiO_2 composite thin films, the percolation threshold was identified at a φ_{Ag} value of 0.30 with the magnitude of 10^{-3} Ω·cm while the lowest electrical resistivity of 10^{-5} Ω·cm was recorded for the composite with the Ag fraction, φ_{Ag}, of 0.55. It is proposed that the electrical resistivity change is strongly dependent on the shape and size of the particles, and the quality of the particle boundary, which determines the percolation effects **[15, 16]** as well as the types of matrix accommodating the fillers and in addition the film thickness.

From these points of view, the influences of Ag nanoparticles on the electrical resistivity of the present composite thin films are mainly due to the insulation nature of zirconium oxide compare to the semiconductor nature of titanium oxide.

Additionally, the morphological change caused by the agglomeration of Ag nanoparticles may increase the film thickness from 110 nm for $\varphi_{Ag} \leq 0.55$ to 170 nm for $\varphi_{Ag} = 0.68$, resulting in an increase in the electrical resistivity because of the inevitable increase in contact resistance between the grown particles. Thus, the resistivity recovery

of composite films (Table 6.1) with φ_{Ag} values larger than 0.54 can be attributed to this morphological change.

6−4 SUMMARY

Ag-nanoparticle/zirconia thin films, with various volumetric fractions of silver (φ_{Ag}) in a zirconia matrix, were successfully fabricated using the molecular precursor method, and their structural and electrical properties were clarified. This study shows that the molecular precursor method, does not only able to fabricate metallic Ag NPs in titania as discussed in thesis but also offers excellent miscibility of the silver and zirconia precursor solutions is effective for overcoming the limitations in miscibility of the conventional sol–gel method and is necessary for fabricating composite thin films having a large φ_{Ag} value. However, the percolation of the electrical conductivity of depends on the nature of the specific matric where Ag NP as fillers are incorporated. Thus increasing the Ag volumetric fraction from 0.27 to 0.55 decreases the electrical resistivity for Ag NP/TiO_2 composite thin film from in excess of 10^{-2} Ω·cm to 10^{-5} Ω·cm while the lower and detectable electrical resistivity of Ag-NP/ZrO_2 thin films could be only observed between Ag volumetric fraction, $0.26 \leq \varphi_{Ag} \leq 0.68$. The electrical resistivity recovered, moving from 10^{-5} to $>10^{8}$ Ω·cm after 0.61 to 0.68, due to an inevitable increase of the separation distance between the grown particles caused by the agglomeration of Ag nanoparticles. I can assumed that the incorporation of Ag NP in any medium using MPM is applicable but electrical conductivity will depend on the property of the matrix and these observation pose no problem for clinical applications.

6−5 REFERENCES

1. Ambrozic M., Dakskobler A., Valant M., Kosmac T. (2005). *Mater. Sci-Pol.* 23:**2**, 535-539.

2. Wilk G. D., Wallace R. M., and Anthony J. M. (2001). *J. Appl. Phys.* **89**, 5243.

3. Garvie RC. (1970). A.M. Alper (Ed.), High Temperature Oxides Part II, *Academic, New York*, 117.

4. Amberg M., Giinter RJ. (1996). *Solid State Ionics* 84, 313-321.

5. Qi W., Nieh R., Lee B., Kang L., Jeon Y., and Lee JC. (2000). *Appl. Phys. Lett.* **77**, 3269.

6. Yashima Y., Kakihana M., Yoshimura M. (1996). *Solid State Ionics*, **86–88**, 1131.

7. Sancaktar E. and Bai L. (2011). *Polymers 2011*, **3**, 427-466.

8. McNaught AD., Wilkinson A (1997) IUPAC compendium of chemical terminology, 2nd edn. *Blackwell Science, Oxford*, 267. ISBN 0-86542-6848

9. Hong C., Park H., Moon J, Park H. (2006). *Thin solid film* 515:**3**, 957–960.

10. Awazu K., Fujimaki M., Rockstuhl C., Tominaga J., Murakami H., Ohki Y., Yoshida N., and Watanabe T. (2008). *J. Ameri. Chem. Soc.,* 130:**5**, 1676–80.

11. Hirano M., Watanabe S., Kato E., Mizutani Y., Kawai M., Nakamura Y. (1998). *Solid State Ionics* **111**, 161–169.

12. Kazemi F., Saberi A., Malek-Ahmadi S., Sohrabi S., Rezaie H.R., Tahriri M (2011). *Ceramics – Silikáty* 55:**1**, 26-30.

13. Kang J-G, Sohn Y (2011). *J Mater Sci* **47**:824-832.

14. Elechiguerra J. L., Burt J. L., Morones J. R., Camacho-Bragado A., Gao X., Lara H. H., Yacaman M. J. (2005). *J Nanobiotechnology*, 3:**6**, 1-10.

14. Petryayeva E, Krull UJ (2011). *Anal Chim Acta* **706**:8–24.

16. Ho L., Nishikawa H. and Takemoto T. (2011). *J Mater. Sci*.: *Mater. Electron* **22**:538–544.

CHAPTER 7: PLASMONIC PROPERTY OF Ag-NP/TiO_2 COMPOSITE THIN FILMS.

7−1 INTRODUCTION

On silver nanoparticles (Ag NP), light can excite the collective oscillations of the free electron density, also known as plasmon resonances **[1]**. The excitation of plasmon resonances is a unique property of Ag NP and represents the most efficient mechanism by which light interacts with matter. It has been demonstrated in previous chapter, Chapter 4, that the absorption spectra of metallic Ag nanoparticle/titania (Ag NP)/TiO_2 composite thin films, COMP-Ag*n*, with Ag 50 mol% fabricated on a quartz glass substrate at different heat treatment temperature, *T*, 70º ≤ *T*≤ 800°C exhibit plasmonic property. The main absorption peaks for all composites thin films were around 400 nm and wide-range absorption in the visible region at wavelengths greater than 400 nm. This illustrate that the metallic Ag NP must be large enough (c.a. 10 or more atoms) to have free electron density, but be small enough (less than the wavelength of visible light) that the optical properties change with particle size, shape, and local environment **[2, 3]**. Theoretically, the excitation of plasmon resonances on a NP can be named either as surface plasmon resonance (SPR) or localized surface Plasmon resonance (LSPR) **[4]**. When particles are small as compared to the wavelength of incident radiation, the entire particle experiences the same phase of the incident radiation. For Ag NP, this mainly occurs around the 400 nm wavelength, a phenomenon known as SPR. The excitation of plasmon resonances in NPs produces a local electromagnetic field that extends from the particle surface and into the surrounding environment **[5, 6]**. This field is 'enhanced' as compared to the incident field and is a concentration of the incident field around the particle. As the particle dimensions become larger, the different areas experience different phases resulting in the formation of multiple plasmon modes. The increase in bandwidth is also a result of radiative damping of the

plasmon oscillations in the nanoparticle. The efficient emission (scattering) of photons reduces the lifetime of the plasmon oscillations and broadens the plasmon band, a phenomenon known as LSPR **[4, 5]**. However, the overall plasmon coupled peak depends on the particle size and shape, distance between, nature of the supporting substrate, and local dielectric environment **[2, 7]**.

In this chapter, a study related to the effects of the amount, size, shape, and the separation distance between Ag-NP on the coherent plasmon in Ag NP/TiO_2 composite thin films is under investigation. The absorption spectra of Ag-NP/TiO_2 composite thin films were analyzed, in order to study the plasmonic effect of Ag-nanoparticles (Ag NP) in dielectric TiO_2 matrix. It was found that there is a correlation between the amount, size, shape and separation distance between Ag in the composite with both the absorption peak positions and intensities. The work presented in this chapter will be used to investigate the photocurrent and photocatalytic properties of Ag NP/TiO_2 composite thin films in the following two chapters, Chapter 9 and Chapter 10, respectively. The findings may further open up other further investigation on photo responsive studies.

7−2 EXPERIMENTAL

7-2.1 Materials

All the materials employed in this chapter are tabulated in Chapter 3, Table 3.1.

7-2.2 Synthesis of coating solutions and fabrication of COMP-Agn

A precursor solution containing a Ti^{4+} complex of EDTA, $\boldsymbol{S_{TiO2}}$, was prepared in accordance with MPM outlined in Chapter 3, Scheme 3.I. A silver acetate ethanol solution, $\boldsymbol{S_{Ag}}$, for the fabrication of Ag NPs used in the composite thin films was prepared according to a new method also illustrated in Sceme3.I. Respective TiO_2 and Ag NP thin films on quartz glass substrates were fabricated at 600°C in air by using the $\boldsymbol{S_{TiO2}}$ and $\boldsymbol{S_{Ag}}$ precursor solutions. The $\boldsymbol{S_{TiO2}}$ and $\boldsymbol{S_{Ag}}$ solutions were then mixed at different Ag molar concentrations (*n*) to prepare coating solutions for COMP-Ag*n*, $\boldsymbol{S_{composite}}$. Ten COMP-Ag*n* films were fabricated at 600°C in air on quartz glass substrates. Figure 3.3 (a) through (h) of Chapter 3 shows the photographs of the resultant composite thin films and their thicknesses of these films are listed in Table 5.1 of Chapter 5. Ag-NP/TiO_2 composite ultra-thin films used to measure the TEM images of the composite was also prepared using the same procedure, except that the thin film was fabricated on NaCl single crystals as a supportive substrate and the ultra-thin films were transfer on Cu grid upon.

7-2.3 Absorption spectra for TiO_2, Ag NP, and COMP-Agn thin films fabricated on quartz glass substrates

The absorption spectra for the TiO_2, Ag NP, and COMP-Ag*n* thin films fabricated on quartz glass substrates were measured in the range 200–800 nm using the double-beam mode. The measurement was performed using a UV/Vis spectrophotometer (U-2800, Hitachi) shown in figure 7.1 and air was used as a reference. The reflectance spectra of pure TiO_2 as well as for those of the Ag-NP/TiO_2 composite thin film samples were performed with a Perkin-Elmer Lambda 900 spectrometer provided with a diffuse reflectance accessory

Fig. 8.1 Photo for UV/Vis/NIR spectrometer (Lambda 900, PerkinElmer).

7-2.4. Surface morphology of Ag-NP/TiO_2 composite thin films

The surface morphology of the all resulting composite thin films was observed with a field-emission scanning electron microscope (FE-SEM S-4200, Hitachi, Tokyo, Japan) at an accelerating voltage of 0.5 kV. The nanostructure images for Ag-NP/TiO_2 composite thin films were observed with a transmission electron microscope (TEM H8100, Hitachi, Tokyo, Japan) at an accelerating voltage of 120 kV using the ultra-thin films applied on Cu grid.

7−3 RESULTS AND DISCUSION

Ag NP and eight Ag NP/TiO_2 composite thin films (COMP-Ag*n*; *n* = 10, 20, 30, 40, 50, 60, 70, and 80) were fabricated. The XRD spectra patterns of these Ag NP/TiO_2 composite thin films are presented in Chapter 5 and may be referred to for more details.

X-ray diffraction (XRD) revealed that the films consist of rutile, anatase, and metallic Ag nanoparticles distributed in the titania matrix.

7-3.1 Absorption spectra of TiO_2, Ag NP, and COMP-Agn thin films

Figure 7.2 represents the UV-vis absorption spectra for TiO_2, Ag NP, and COMP-Ag*n* ($10 \leq n \leq 60$) thin films. The TiO_2 thin film showed a low-intensity absorption band in the vis-region; however, its absorption intensity increased steeply at shorter wavelengths.

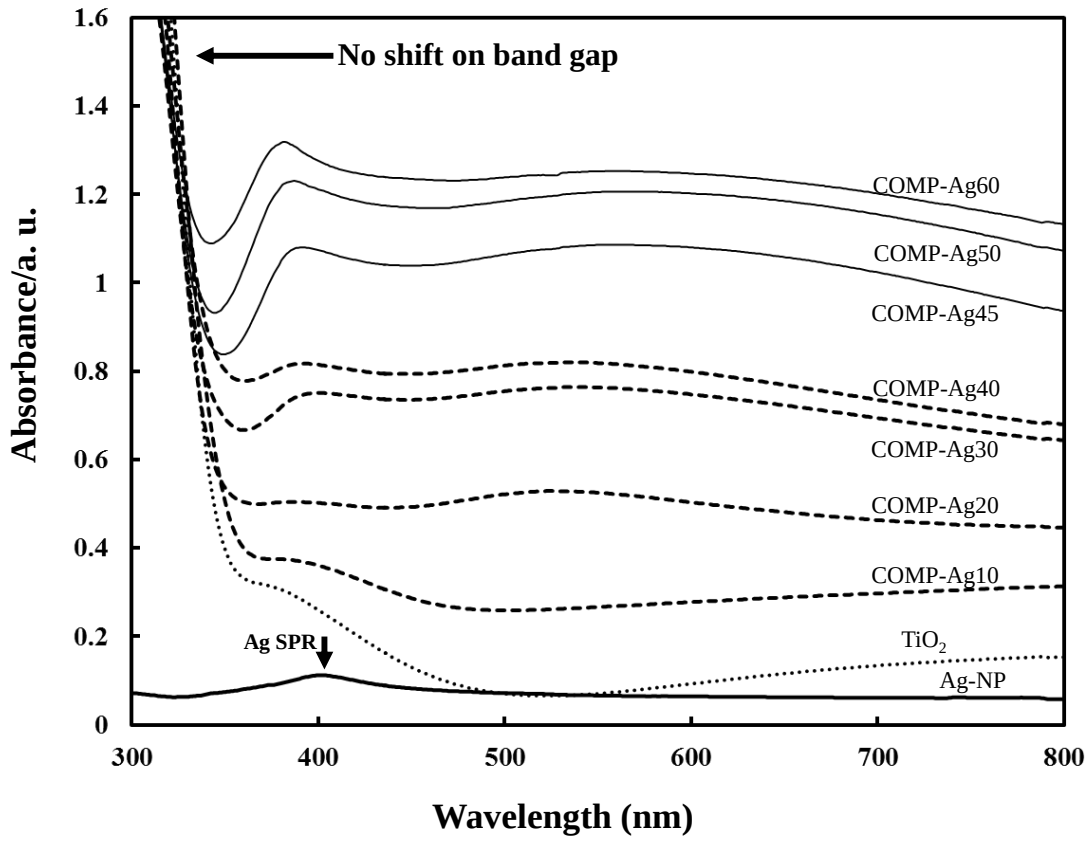

Fig. 7.2 UV–Vis absorption spectra for Ag NP (thick solid line), TiO_2 thin film (dotted line), COMP-Ag10–40 thin film (dashed line), and COMP-Ag50–60 composite thin film (thin solid line).

In contrast, the Ag NP film showed a weak and broad absorption band at around 410 nm. This absorption band are observed for the COMP-Ag*n* thin films, though the peak position in this region gradually shifted to shorter wavelengths upon increasing the Ag content. When a Ag NP film is irradiated with vis-light, a large oscillating electric field is observed around the metal particles **[5, 8−11]**. The absorption band in this region corresponds to the characteristic SPR of Ag NPs. Just like in previous chapters, for COMP-Ag*n*, apart from an SPR peak around 400 nm, additional wide-range absorption spread in the wide vis-region at wavelengths greater than 400 nm was observed.

Theoretically, when samples are irradiated by vis-light, large oscillating electric fields are produced around and between the metal nanoparticles because of LSPR **[1, 12, 13]**. According to several studies, wide-range absorption corresponds to a tip-to-tip plasmon mode and intraparticle plasmonic coupling of tip and cavity resonances **[1, 14−16]** and scattering of the incident light **[6, 17]**. Therefore, the wide-range absorption observed in the vis-region can be due to the characteristic LSPR for the Ag NPs incorporated in the TiO_2 matrix. Moreover, the absorption spectra for COMP-Ag*n* indicate an increase in the absorption intensity in the vis-region with an increase in the Ag content. It is well known that an increase in the Ag content in composite thin films leads to an increase in absorption intensity **[18−20]**.

The UV-vis absorption spectra for COMP-Ag*n* (*n* = 70, 75, and 80) are shown in figure 7.3. The intense absorption band at approximately 390 nm has a shoulder component in the shorter wavelength region. They are assignable to the SPR peaks due to Ag NPs with different sizes. For composite thin films with Ag content more than 70 mol%, the intensity of wide-range absorption in the vis-region decreased with an increase in the

Ag content. This decrease in the wide-range absorption intensity can be attributed to the decrease in the amount of TiO_2.

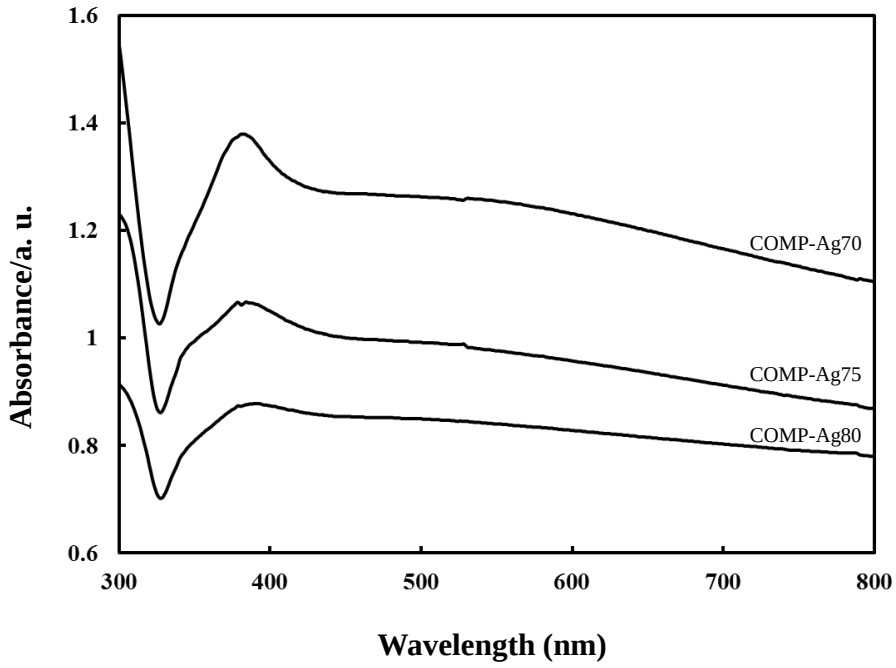

Fig.7.3 UV–Vis absorption spectra for COMP-Ag70–80 composite thin films fabricated on quartz glass.

From these absorption spectra, COMP-Ag*n* can be categorized into three types depending on the Ag content—COMP-Ag10-40 ($10 \leq$ Ag mol% ≤ 40), COMP-Ag50-60 ($40 <$ Ag mol% < 70), and COMP-Ag70-80 ($70 \leq$ Ag mol%) thin films. The COMP-Ag10-40 thin films show one weak or non-detectable SPR peak at around 400 nm, which can be observed at around 410 nm for the Ag NP film. The COMP-Ag50-60 thin films show one well-defined and intense absorption band due to SPR at approximately 400 nm, with intense and wide-range absorption assignable to LSPR in the vis-light region. This wide-range absorption by the COMP-Ag50-60 thin films increases with an increase in the Ag content. The COMP-Ag70-80 thin films show two

overlapping SPR peaks at approximately 390 nm, with intense absorptions across the wide vis-light region. This wide-range absorption by the COMP-Ag70-80 thin films decreased with an increase in the Ag content, which is in contrast to the absorption behaviors of the COMP-Ag10-40 and COMP-Ag50-60 thin films.

For additional observation and for your information, it seems important to note that these three levels of Ag content in COMP-Ag*n* are strongly correlated to their electrical resistivity, as we reported in a previous chapter, Chapter 6. The COMP-Ag10-40 thin films show resistivity higher than 10^6 Ω cm. On the other hand, the COMP-Ag50-60 thin films show low electrical resistivity in the range 10^{-1}–10^{-5} Ω cm, which gradually decreases with an increase in the Ag content. The electrical resistivity of the COMP-Ag70 to 80 thin films increases again from 10^{-5} Ω cm to 10^{-2} Ω cm with an increase in the Ag content from 70 mol% to 80 mol%, respectively.

7-3.2. The effect of the amount of Ag NP in the Ag-NP/TiO_2 composite thin films on plasmon.

To investigate the distribution and consecutive growth of metallic Ag-NP in the COMP-Agn, all the composite thin film samples plus Ag NP film were examined with TEM, and the micrographs are shown in figure 8.4. As presented in Figure 7.4(a), the presence and distribution of the Ag NP can be observed clearly as dark spots. Hence, the dark spots within the composite films micrographs (figure 7.4 (b)–(j)) represent the Ag NP. The high-resolution TEM image (figure 7.4 (b)) confirmed that the composite samples was comprised of crystalline titania and silver nanoparticles with the lattice spacing of a-axis agreeing well with the anatase phase (0.352 nm) and metallic silver (0.240 nm), respectively.

All the TEM micrographs (figure 8.5(a)–(j)) exhibited small Ag-nanoparticles: 5 ± 2 nm. Three other populations of Ag NP are obtained; small spherical nanoparticles: 11 ± 7 nm, larger spherical: 29 ± 8 nm, and rod-like: 45 ± 25 nm, or agglomerated ones depending on the amount of silver in a given thin film. Therefore, COMP-Ag*n* can be categorized into three types depending on the Ag content—COMP-Ag10–40 (10 ≤ Ag mol% ≤ 40), COMP-Ag50–60 (40 <Ag mol% <70), and COMP-Ag70–80 (70 ≤ Ag mol%) thin films. The COMP-Ag10–40 thin films show spherical Ag NP homogeneously distributed in the titania with diameter 11 ± 7 nm. Most of Ag NP by the COMP-Ag70–80 thin films is more agglomerated, which is in contrast to the behaviors of the other two thin films categories.

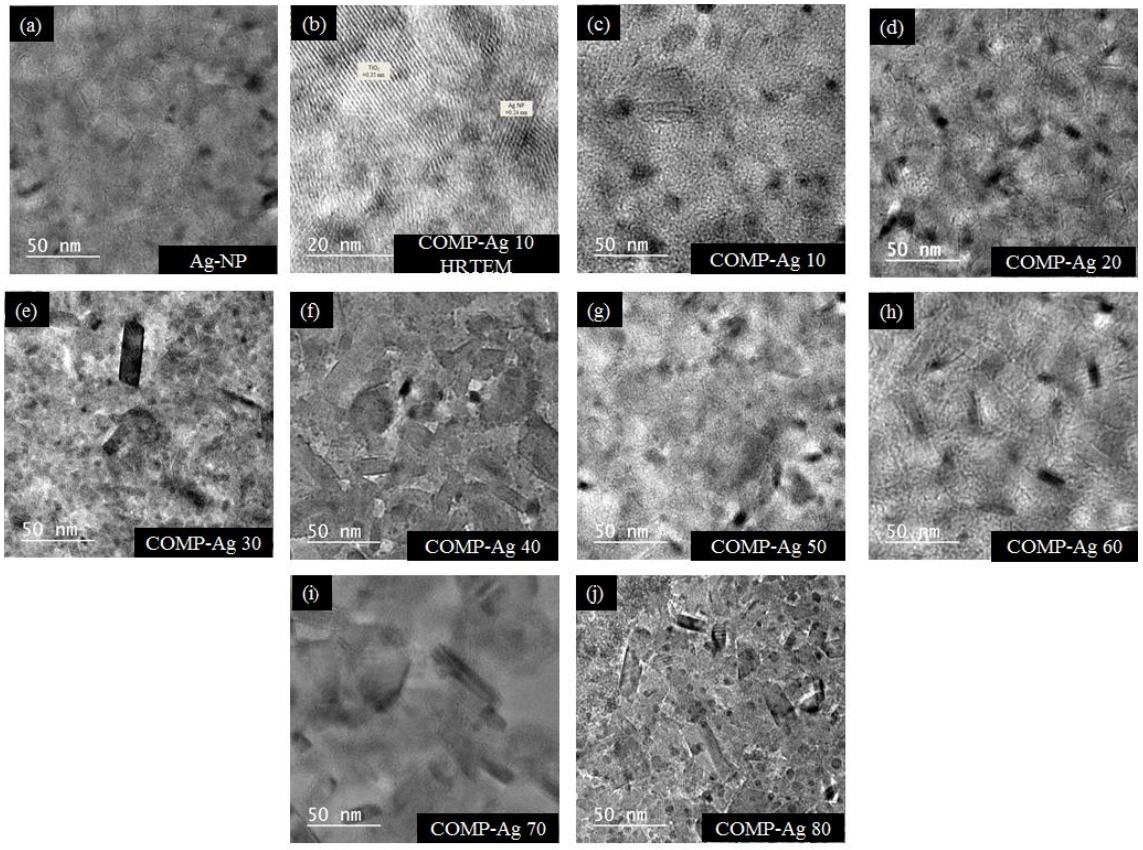

Fig. 7.4 (**a**) TEM image of Ag NP; (**b**) HRTEM image of COMP-Ag10, and (**c**)–(**j**) TEM images of Ag-NP/TiO_2 composite thin films at various amounts of Ag molar

concentrations: (**c**) 10; (**d**) 20; (**e**) 30; (**f**) 40; (**g**) 50; (**h**) 60; (**i**) 70 and (**j**) 80, respectively.

An important observation in the UV/Vis absorption spectra of composites is that the plasmon bands broaden and peak intensities decreasing as the amount of Ag in the composite increases. As the amount of Ag in the composite is increasing, the surface area available for the incident radiation is also increasing, hence the particles will respond to more frequencies of the incident light leading to a broader plasmon band.

7-3.3. The effect of the Ag NP size in the Ag-NP/TiO_2 composite thin films on plasmon.

All the TEM micrographs (figure 7.4(a)–(j)) exhibited small Ag-nanoparticles: 5 ± 2 nm. Three other populations of Ag NP are obtained; small spherical nanoparticles: 11 ± 7 nm, larger spherical: 29 ± 8 nm, and rod-like: 45 ± 25 nm, or agglomerated ones depending on the amount of silver in a given thin film. Therefore, using TEM information, COMP-Ag*n* can be categorized into three types that are identical to the UV/Vis absorption spectra categories done in above section—COMP-Ag10–40 (10 ≤ Ag mol% ≤ 40), COMP-Ag50–60 (40 <Ag mol% <70), and COMP-Ag70–80 (70 ≤ Ag mol%) thin films. The COMP-Ag10–40 thin films show spherical Ag NP homogeneously distributed in the titania with diameter 11 ± 7 nm. Most of Ag NP by the COMP-Ag70–80 thin films is more agglomerated, which is in contrast to the behaviors of the other two thin films categories. An important observation in the UV/Vis absorption spectra of composites is that the plasmon bands broaden and peak intensities increasing as the size of Ag in the composite increases. And then decrease as the Ag NP starts to agglomerate. This is probably due to the phase retardation of the

incident radiation that occurs as the dimensions of Ag NPs increase **[21]**. When particles are small as compared to the wavelength of incident radiation, the entire particle experiences the same phase of the incident radiation.

7-3.4. The effect of the shape of Ag NP in the Ag-NP/TiO_2 composite thin films on plasmon.

From TEM images of the seven COMP-Agn (Fig. 7.4a-g), two populations of Ag NP are obtained; small spherical nanoparticles (0.5−1.5 nm) and larger ones (mean diameter 4 to 45 nm depending on the amount of Ag in the composite thin film). The small spherical Ag nanoparticles associated with larger spherical, rod-like or agglomerated Ag nanoparticles observed in each thin film may have been released into the TiO_2 matrix from the agglomerated Ag clusters by the energy provided from the ultrasonic stirring during the preparation procedure **[22]**. An important observation in the spectra is that the numbers of the plasmon bands are increasing or overlapping as the Ag NP shape is changing from spherical to rod-like and then to agglomerated. As the particle dimensions become larger, the different areas of the particles experience different phases resulting in the formation of several numbers of the plasmon bands **[23]**. Moreover, larger particles interact with more wavelengths of the incident light and result in the excitation of multiples Ag NP with different geometry in the thin film. This translates into more wavelengths for excitation and, consequently, multiple plasmon overlapped peaks **[24]**.

7-3.5. The effect of the separation distance between large Ag NP in the Ag-NP/TiO_2 composite thin films on plasmon.

A decrease in UV/Vis absorption spectra peaks intensity at both short wavelength and long wavelength regions can be observed in figure 7.3. This observation could be due to the increase in distance between the large Ag NP caused by the change in the geometry of Ag NP from spherical for COMP-Ag10 to rod-like and partially agglomerated Ag NPs in COMP-Ag70. The plasmon resonances (wave) must travel between the particles, however, large distance between the particles results in a lower resonant frequency to maintain an excited state, hence lower intensity. The increase in distance between particles may occur because of the agglomeration of Ag NP associated with the increase in the amount of Ag in the composite thin film.

In order to validate the changes in separation distance of the Ag NP on the surface of the composite thin film, electron microscope images were acquired to illustrate the appearance of the surface of Ag NP/TiO_2 composite thin films on the glass substrate and determine the separation distance between the larger Ag NP on the surface. The representative plain view SEM images of the composite thin films obtained at various Ag molar concentration (mol%) are shown in figure 7.5a-g.

The SEM images show three different shapes of (spherical, rod-like, and agglomerated) Ag NPs. For COMP-Ag10—40, Ag-NP (white dots confirmed by EDX mappings) of size 20—40nm are observed to be separated by typical separation distance in the range of 20—50nm (figure 8.6a-d, respectively). COMP-Ag50—70, the particles sizes are 40-100nm (figure 8.6e-g, respectively), with separation distance of <20nm. From DRS plasmon spectra, the peaks intensities are seem to be decreasing with the increasing of separation distance. COMP-Ag80 is highly agglomerated and it is difficult to observe the separation distance.

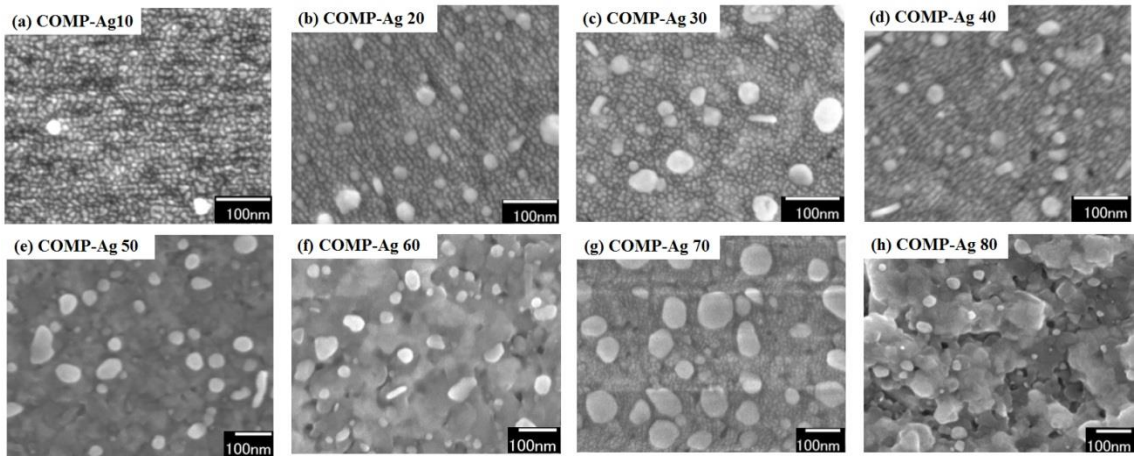

Fig. 7.4. SEM images a-h, of the Ag-NP/TiO_2 composite thin films at various amounts of Ag molar concentrations: (**a**) 10; (**b**) 20; (**c**) 30; (b) 40; (**e**) 50; (**f**) 60, (**g**) 70 and (**h**) 80, respectively.

7−4 SUMMARY

The increase in the amount (*n*) of Ag in the Ag-nanoparticles/TiO_2 composite thin films (COMP-Ag*n*, where *n* is Ag-mol%, $10 \leq n \leq 80$) resulted in the exhibition of plasmon peak at 400 nm for all thin films followed by the exhibitions of extra peaks at blue and red spectral side of the this peak, 400 nm depend on the amount, size and the geometry of the Ag NP in the composite and is consistent with other literature reports. Apart from an SPR peak around 400 nm, additional wide-range absorption spread in the wide vis-region at wavelengths greater than 400 nm was observed. The wide-range absorption is due to a tip–tip plasmon mode, intraparticle plasmonic coupling of tip and cavity resonances (LSPR). The spectral peak positions followed a linear correlation against the amount of Ag in the composite. This correlation provides the ability to obtain a specific lambda maximum by selecting the corresponding amount of Ag mol % to be doped in titania. The decrease in the spectral peak intensities followed a linear correlation against the increase in agglomeration associated with the increase in the

amount of Ag in the composite thin films. It was further observed that the composites with Ag NP of different amount, size and shape were large enough to experience the excitation of multiple plasmon sharp bands at different specific lambda maximum at blue spectra regions 310 nm—400 nm. This reflects that my composite thin films are more suitable candidates achieving better photo-responce efficiency under visible and this may further open up a variety of optical and further development of their photonic/plasmonic/spectroscopic applications. These optical properties of my Ag-NP/TiO_2 composite thin films already make themselves attractive for optical study such as photocurrent (Chapter 8) and photocatalytic (Chapter 9), the final chapter before the conclusion and recommendations] and this may further open up a variety of optical and photonic applications such photovoltaic, biosensors, optical filters, plasmonic waveguides, and substrates for surface-enhanced Raman spectroscopy.

7−5 REFERENCES

1. Zhu J., Ren Y. (2012). *J Nanopart Res*, **14**, 1326−1334.

2. Haes AJ., Van Duyne RP. (2002). *J. Amer. Chem. Soc*., 124:**35**, 10596−10604.

3. Awazu K., Fujimaki M., Rockstuhl C., Tominaga J., Murakami H., Ohki Y., Yoshida N., Watanabe T. (2008). *J. Amer. Chem. Soc.*, 130:**5**, 1676–80.

4. Mortazavi D., Kouzani A., Vernon K. (2012). *Researchg* **130**, 429–446.

5. Kang J-G, Sohn Y. (2011). *J Mater Sci* **47**, 824−832.

6. Petryayeva E., Krull UJ. (2011). *Anal Chim Acta* **706**,8–24.

7. Sung J., Hicks ME., Van Duyne PR., Spears GK. (2007). *J. Phys. Chem. C*, 11:**28**, 10368-10376.

8. Zhao G., Kozuka H., Yoko T. (1997). *Sol. Energ. Mat. Sol. C*. **46**, 219−223.

9. Rochholz H., Bocchio N., Kreiter M. (2007). *New J Phys* **9**, 053.

10. Behnajady MA., Modirshahla N., Shokri M., Rad B. (2008). *Global Nest J* 10:**1**, 1−7.

11. Bocchio N.L., Unger A., lvarez M. A, Kreiter M. (2008). *J Phys Chem C* **112**,14355–14359.

12. Tian Y., Tatsuma T. (2004). *Chem. Commun.* 1810−1811.

13. Takahashi Y., Tatsuma T. (2010). *Nanoscale*, **2**, 1494−1499.

14. Ross BM., Lee LP. (2008). *Nanotechnology* **19**, 275201−275207.

15. Kim J., Liu GL., Lu Y., Lee LP. (2005). *Opt Express* **13**, 8332–8338.

16. Liu GL., Lu Y., Kim J., Doll JC., Lee LP. (2005). *Adv Mater* **17**, 2683–2688.

17. Tanabe I., Tatsuma T. (2012). *Nano let.,* 12:**10**, 5418–5421.

18. Ochoo L., Migwi C., Okumu J. (2012). *J Nanopart Res* **14**,1261.

19. Velmurugan R., Sreedhar B., Swaminathan M. (2011). *Chem. Cent. J*. 5:**1**, 46.

20. Xing Y., Li R., Li Q. and Yang J. (2012). *J Nanopart Res* **14**, 1284−1292.

21. Kumbhar AS., Kinnan MK., Chumanov G. (2005). *J. Amer. Chem. Soc*, 127:**36**, 12444−12445.

22. Elechiguerra JL., Burt JL., Morones JR., Camacho-Bragado A., Gao X., Lara HH., Yacaman MJ. (2005). *J Nanobiotechnology*, 3:**6**, 1−10.

23. Su KH., Wei Q-H., Zhang X. (2003). *Nano Lett.*, 3:**8**, 1087−1090.

24. Jain PK., El-Sayed MA. (2008). *J. Phys. Chem. C*, 112:**13**, 4954−4960.

CHAPTER 8: PHOTOCURRENT DENSITY OF Ag NANOPARTICLES/TiO_2 COMPOSITE THIN FILMS WITH VARIOUS AMOUNT OF Ag.

8−1 INTRODUCTION

In 1996, the molecular precursor method (MPM), which is a wet chemical process, was developed in our laboratory **[1]**. Since then, MPM has been used for fabricating phosphate and metal oxide thin films **[2−10]**. This method requires heat treatment to eliminate organic ligands from metal complexes present in spin-coated precursor films and to fabricate thin films of crystallized metal oxides or phosphates **[11]**. In Chapter 6, I have demonstrated that MPM can be used to fabricate Ag nanoparticles (Ag NPs)/TiO_2 composite thin films (COMP-Ag*n*) with various and unprecedentedly high amounts of Ag (up to 80 mol%) homogeneously distributed in a TiO_2 matrix by heat-treating precursor films at 600°C. Thus, MPM is now necessary for fabricating composite thin films having high Ag content and high electrical conductivity.

Most studies on the photoelectrochemical mechanism of noble metal/TiO_2 composites have been focused on the details of photoinduced electron transfer, which can be used to determine the vis-light response of the composites, though the Ag content in these composites is quite low (3−6 mol%) **[12, 13]**. Zhao *et al.*, **[13]** fabricated TiO_2 film electrodes with a TiO_2 overlayer containing dispersed Ag particles by a sol-gel method, and reported the effect of Ag particles on the photoelectrochemical properties of the TiO_2 electrodes. The photoelectrochemical properties reported in literatures obtained mainly through sol-gel method by doping Ag into TiO_2 showed photosensitivity in the visible–light region, where anodic photocurrent can be observed in aqueous solution. Naturally occurring TiO_2 displays anodic photocurrent (*n*- type conductivity) due to its native defects such as titanium interstitials and oxygen vacancies. An anoding photocurrent could be observed in Ag/TiO_2 systems where by anodic photocurrent is

increasing with the increase in heat treatment temperature and Ag molar concentration in titania as illustrated in figure 8.1:

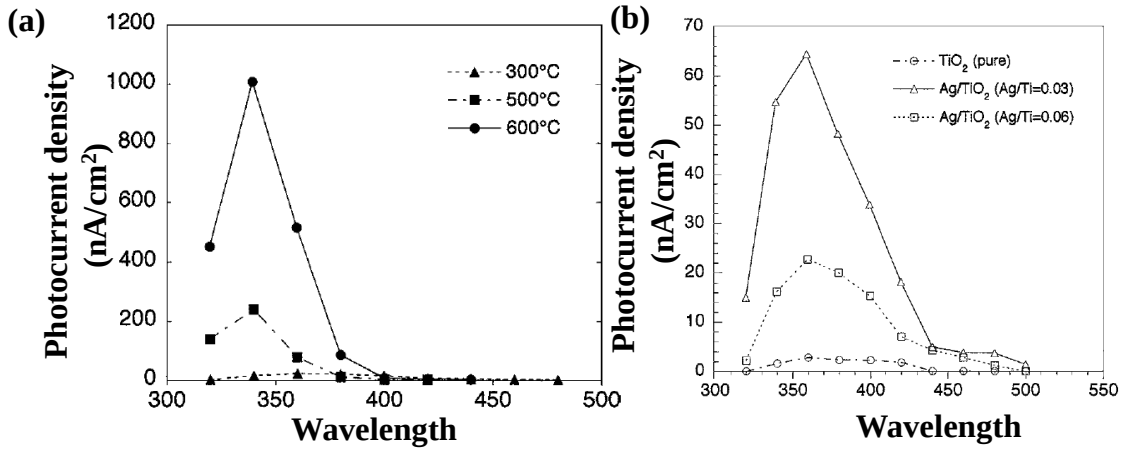

Fig. 8.1 Photocurrent density of 0.06 mol% Ag-TiO_2 thin films heat-treated at different temperature, (b) pure TiO_2, 0.03 and 0.06 mol% Ag-TiO_2 thin films, deposited on ITO substrates at 600ºC, as a function of irradiating light at +1.0 V vs. Ag/AgCl in 0.1mol/L Na_2SO_4 aqueous solution**[12]**.

An increase in the anodic photocurrent under visible (vis-) light irradiation, which might have resulted from the surface plasmon resonance (SPR) of the metal particles, was observed. The anodic photocurrent increased under ultraviolet (UV-) light irradiation and then decreased for an excess amount of Ag particles. These effects of the dispersed Ag particles on the photoelectrochemical properties of the TiO_2 electrodes were explained on the basis of band models by taking into account Schottky barriers formed at the TiO_2-metal and TiO_2-solution interfaces **[12, 13]**.

The cathodic photocurrents of TiO_2 electrodes with noble metals and fabricated by the electrodeposition method have also been reported **[14−16]**. Tian and Tatsuma **[14]**,

reported on the photoelectrochemical properties of TiO_2 electrodes electrodeposited on Au NP (ITO/TiO_2/Au NP) and TiO_2-coated Au NP (ITO/Au NP/TiO_2) electrodes for which anodic and cathodic photocurrents, respectively, were observed under vis-light irradiation. They indicated that the electron transfer from Au NPs to TiO_2 generates a cathodic photocurrent because of the localized surface plasmon resonance (LSPR) of photoexcited Au NPs. In another study, Takahashi and Tatsuma **[16]**, replaced Au NPs with cheaper Ag NPs, simply because Ag NPs are more effective for preparing a photoelectrode with wide-wavelength-range absorption. However, their ITO/TiO_2/Ag NP electrodes were short-lived because Ag NPs on TiO_2 are easily oxidized and dissolved in an electrolytic solution under vis-light irradiation. They then fabricated electrodeposited Ag NPs on an ITO/TiO_2 electrode through an Al_2O_3 nanomask and examined their photoelectrochemical responses at various potentials between −0.5 and −2.0 V vs. Figure 8.2 illustrated the importance of masking done by Tatsuma and his group. Ag/Ag^+. The ITO/Ag NP/TiO_2 electrode generated a cathodic photocurrent by photoexcited electron transfer from Ag according to the LSPR process.

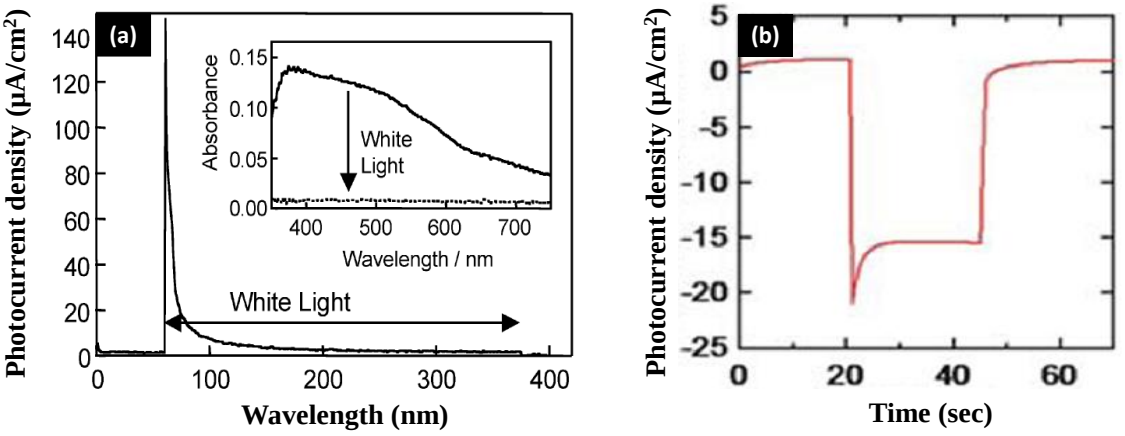

Fig. 8.2 Photocurrent (a) ITO/TIO_2/Ag-NP without masking **[18]** (b) ITO/AgNP/TiO_2 with Al_2O_3 nanomask **[17]**.

Thus, the photoelectrochemical property of COMP-Ag*n* with various amounts of Ag are of interest, although Li *et al*. reported that it is difficult to obtain a homogeneous solution for Ag concentrations above 18 mol% by using a sol-gel method because of the poor miscibility resulting from metalloxane polymerization in the medium **[17]**.

In this chapter, I am reporting on the photoelectrochemical properties of COMP-Ag*n* prepared by MPM; a cathodic photocurrent was generated by the prepared thin films. To the best of my knowledge, this is the first report reporting a cathodic photocurrent generated by Ag NP/TiO_2 composite thin films prepared using a wet chemical process. Furthermore, the mechanism of vis-light-excited electron transfer in a noble metal/TiO_2 composite system has not been fully clarified and detailed investigations into the effects of such transfer on the optical properties of Ag NP/TiO_2 composite thin films are still needed. The purpose of this study is therefore to elucidate the mechanism of vis-light-excited electron transfer occurring in a Ag NP/TiO_2 composite system by examining the absorption spectra.

8−2 EXPERIMENTAL

8-2.1 Materials

All the materials employed in this chapter are tabulated in Chapter 3, Table 3.1.

8-2.2 Synthesis of coating solutions and fabrication of COMP-Agn

Ten COMP-Ag*n* films were fabricated at 600°C in air on quartz glass substrates based on the preparation method reported in previous chapters. The $\boldsymbol{S_{TiO2}}$ and $\boldsymbol{S_{Ag}}$ solutions were then mixed at different Ag molar concentrations (*n*) to prepare coating solutions

for COMP-Ag*n*, $\boldsymbol{S_{composite}}$. Respective TiO_2 and Ag NP thin films on quartz glass substrates were also fabricated at 600°C in air by using the $\boldsymbol{S_{TiO2}}$ and $\boldsymbol{S_{Ag}}$ precursor solutions.

8-2.3 Calculation of band gap using absorption spectra for TiO_2, and COMP-Agn thin films fabricated on quartz glass substrates

The absorption spectra for the TiO_2, and COMP-Ag*n* thin films fabricated on quartz glass substrates were measured in the range 200–800 nm using the double-beam mode. The measurement was performed using a spectrophotometer (U-2800, Hitachi) and air was used as a reference. The absorption spectra results obtained are presented in Chapter 7.

The optical band edge, E_g, of the TiO_2 and composite thin films were calculated using the following Tauc expression:

$$\alpha = \frac{A(E_{phot} - E_g)^{\,n}}{E_{phot}} \quad \ldots\ldots\ldots\ldots\ldots\ldots\ldots\ldots (8.1)$$

where E_{phot} ($h\nu$) is photon energy equal to 1239/λ (eV), A is a constant, and α is the absorption coefficient at wavelength λ (nm), and n is equal to 0.5 by considering values for the direct mode of transition. A value of E_{phot} extrapolated to $\alpha = 0$ gives a value for absorption energy that corresponds to the band gap energy E_g **[18, 19]**.

8-2.4 Photocurrent density measurement for TiO_2 and COMP-Agn thin film electrodes

Scheme 8.I shows a conventional three-electrode system used for photocurrent density measurements.

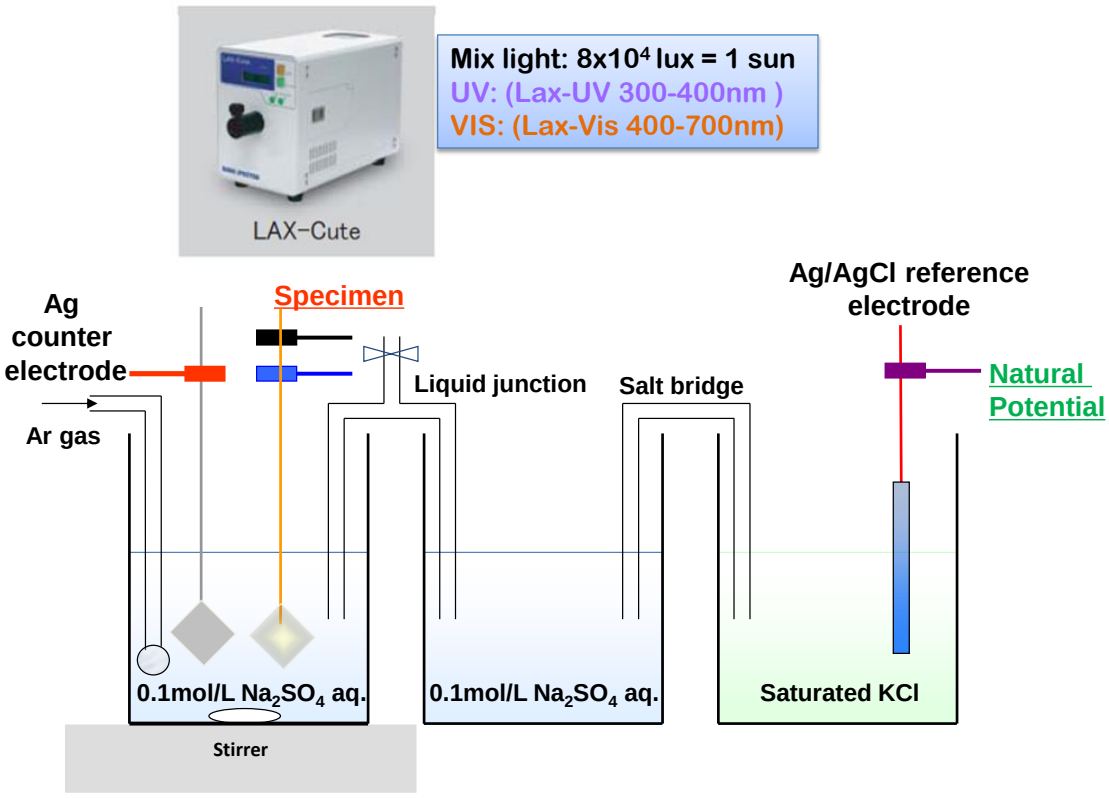

Scheme 8.I Three-electrode method for photocurrent density measurement employed in this study.

TiO_2 and COMP-Ag*n* thin films with different amounts of Ag were used as the working electrode. A Cu wire was attached to the sample surface by a C foil. For all cases, a Ag metal plate, with a size equal to that of the working electrode, and a Ag/AgCl electrode were used as the counter and reference electrodes, respectively. The photocurrent density of the sample electrodes was measured under Xe light irradiation (passed through spectra filters) from a lamp (Lax-Cute); under UV light irradiation in the wavelength range 300–400 nm from Lax-UV(300–400); and under vis-light in the wavelength range 400–700 nm from Lax-Vis(400–700). The light intensity for the latter

two irradiations was 8.0×10^4 lux. All the measurements were performed in a 0.1 mol/L Na_2SO_4 solution after bubbling Ar gas at 50 mL/min for 10 min. The flow rate for the Ar gas bubbling was equal for all measurements. The photocurrent densities were obtained at 10 s intervals by irradiating the samples with the chosen light for 30 min. The photocurrent density was recorded using a Toho Technical Research galvanostat/potentiostat (model: 2090) under natural potential. The photocurrent for the same COMP-Ag70 film was repeated again after 2 weeks and after 3 months to study the stability of the thin film. Furthermore, the photocurrent of a newly prepared COMP-Ag70 film was measured using the same conditions and procedure but now changing the counter electrodes, namely: Al, Cu, Zn, Pb, Pt, Ag, Fe and Ni.

The average photocurrent density (APD) was calculated from three independent measurements using different films, according to the following equation:

$$\mathrm{APD} = \frac{\sum \mathrm{PD}}{\mathrm{No.\,of\ data}} \quad \text{.....(8.2)}$$

where PD is the photocurrent density measured every 10 s for 30 min after switching on the light. Dark current—current without light irradiation—was also recorded during the measurements and the average dark current density (ADD) was calculated according to the following equation:

$$\mathrm{ADD} = \frac{\sum \mathrm{DD}}{\mathrm{No.\,of\ data}} \quad \text{.....(8.3)}$$

where DD is the current density measured every 10 s for 30 min between switching off and on the light.

The Film thickness, averaged photocurrent density (APD), averaged dark current density (ADD) of the TiO_2 and Ag-NP thin films are tabulated in Table 8.1.

Table 8.1 Film thickness, averaged photocurrent density (APD), averaged dark current density (ADD) of the TiO_2 and Ag-NP films fabricated at 600°C on the quartz glass substrate.

Notation	Film thickness	APD[a, b]		ADD[a, b]
		Vis-light	UV-light	Dark
	nm	μA/cm^2		
TiO_2	130	ND	1.0(3)	ND
Ag-NP	rough	ND	ND	ND

[a] The standard deviations are presented in parentheses.

[b] ND; Current generated is smaller than 10 nA.

8-3 RESULTS AND DISCUSSION

TiO_2, Ag NP thin films, and ten Ag NP/TiO_2 composite thin films (COMP-Ag*n*; *n* = 10, 20, 30, 40, 45, 50, 60, 70, 75, and 80) were fabricated. The XRD, FE-SEM, TEM and absorption spectra results for, as well as the electrical conductivities of these Ag NP/TiO_2 composite thin films are presented in chapter 5 and 7, and may be referred to for more details.

8-3.1 Dark current densities of COMP-Agn

Dark currents were observed for the COMP-Ag50-60 and COMP-Ag70-80 thin films, as shown in figure 8.3, and the average values of dark current are tabulated in Table 8.2.

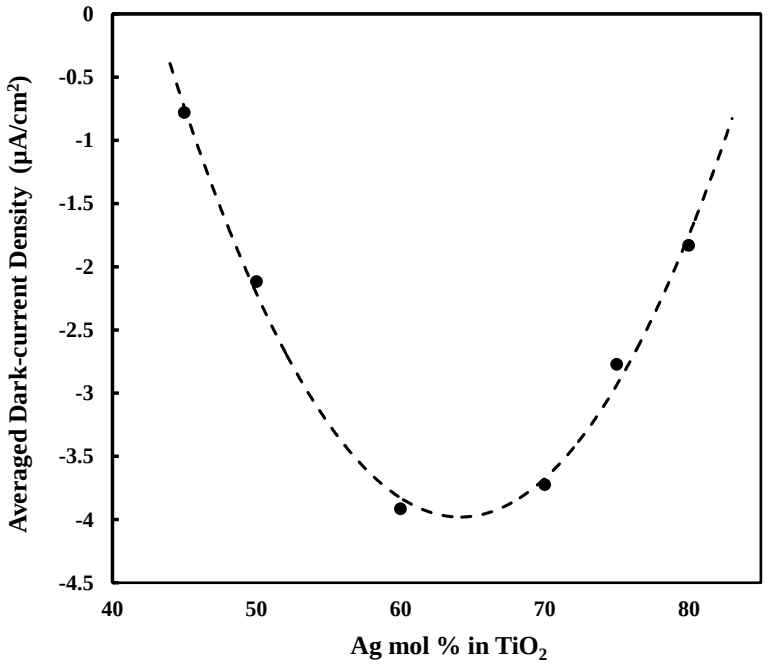

Fig. 8.3 Average dark current density of Ag NP/TiO_2 composite thin films fabricated on quartz glass as function of Ag mol% in Ag NP/TiO_2 composite thin films.

This indicates that there is a redox potential between the counter Ag electrode and working electrode (composite thin films), hence chemical redox reactions occurred to the system. These results suggest that a new composite with a different electrical potential could be produced by Ag species in the TiO_2 matrix of Ag NP/TiO_2 composite thin films. Their densities were smaller at 1/5–1/20 of those observed under vis-light irradiation, as shown in Table 8.2:

It has been reported that dark current can be generated in an electrochemical cell because of the recombination of charges by the reduction of species in the electrolyte or counter electrode, with species on the working electrode **[20, 21]**. Cathodic dark current can be generated in composite thin films, given that the potential originating at the

counter electrode is high enough to drive electrons flowing from the conductive composite thin film into the electrolyte.

Table 8.2 Film thickness, averaged photocurrent density(APD) under vis- and UV-light, and averaged dark current density (ADD) of the COMP-Ag*n* films fabricated at 600°C on the quartz glass substrate, where *n* = 10, 20, 30, 40, 45, 50, 60, 70, 75, and 80 mol%.

Notation	Film thickness	APD[a, b]		ADD[a, b]
		Vis-light	UV-light	Dark
	nm	μA/cm^2		
COMP-Ag10	120	ND	ND	ND
COMP-Ag20	150	ND	ND	ND
COMP-Ag30	110	ND	ND	ND
COMP-Ag40	100	ND	ND	ND
COMP-Ag45	100	−6.0(5)	−0.1(1)	−0.8(2)
COMP-Ag50	100	−10(1)	−1(1)	−2(1)
COMP-Ag60	100	−11(3)	−1(1)	−4(1)
COMP-Ag70	110	−19(2)	−2(2)	−4(1)
COMP-Ag75	110	−10(2)	−1.2(3)	−2.8(4)
COMP-Ag80	rough	−1.6(3)	−0.5(3)	−1.8(2)

[a] The standard deviations are presented in parentheses.

[b] ND; Current generated is smaller than 10 nA.

8-3. 2 Photocurrent densities of TiO_2 thin film and COMP-Ag10-40 (10 ≤ Ag mol% ≤ 40) thin films

The APD for the TiO_2 thin film on a quartz glass substrate was 1.02 µA cm^{-2} (Figure 8.4). As expected, an anodic photocurrent could be observed in the TiO_2 thin film under UV-light irradiation.

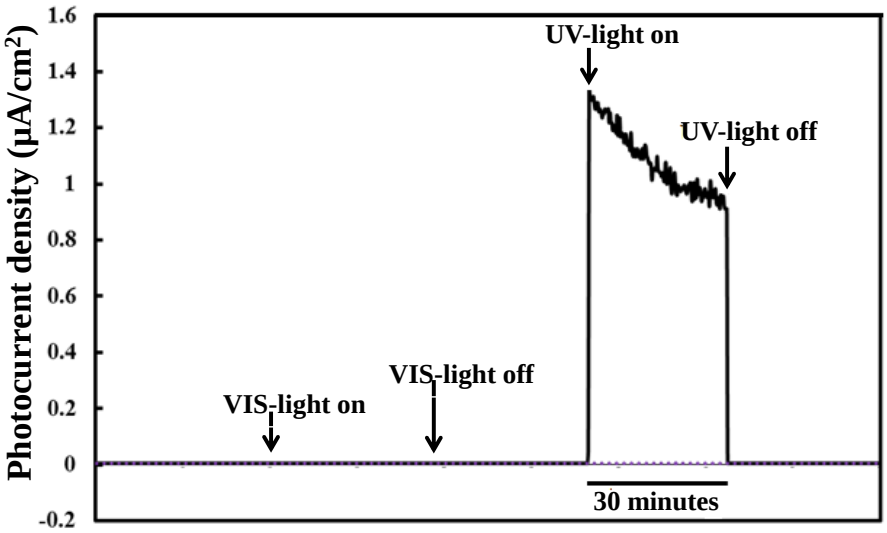

Fig. 8.4 Photocurrent density of TiO_2 thin film fabricated on quartz glass.

Extrapolating the optical band gap of the TiO_2 thin film, an E_g value of 3.61 eV was obtained, which is in fact equal to the band gap of pure anatase **[5]** (assuming direct transition). Thus, the incorporation of Ag NPs into the TiO_2 matrix did not affect the band gap of TiO_2 because the band edge of all COMP-Ag*n* films was comparable to that of a pure TiO_2 thin film, as shown in Figure 8.5.

The extrapolating optical band gap of the COMP-Ag*n* films which is equal to that of pure TiO_2 corroborate that the anatase band gab did not change with incorporating silver into titania matrix. The anodic photocurrent for this TiO_2 thin film under UV-irradiation

is due to the wide band gap of anatase that allowed it to absorb only UV light and to produce electron/hole pairs.

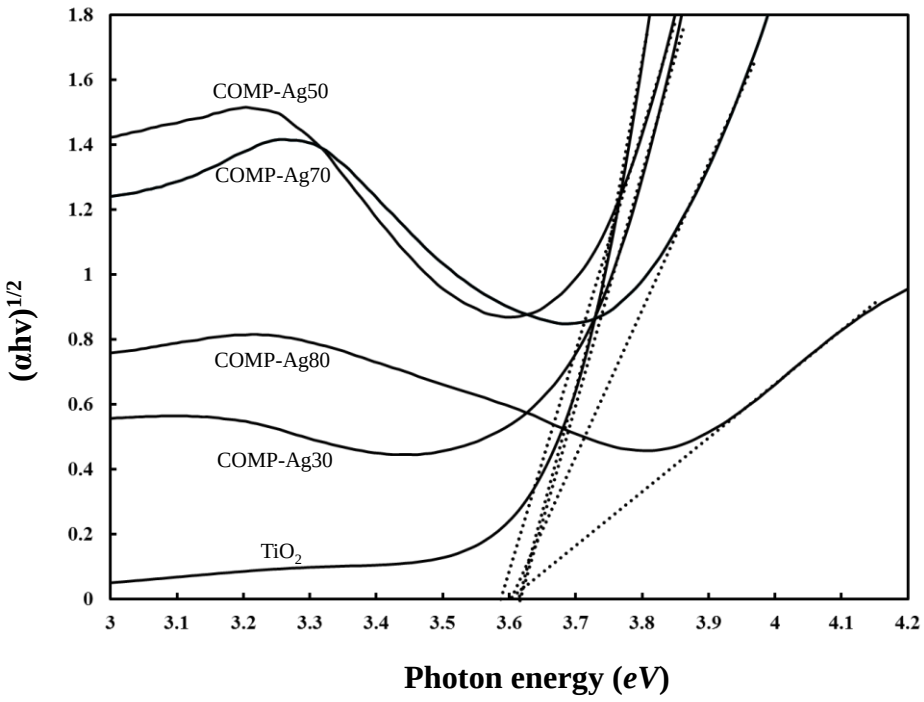

Fig. 8.5 UV‑Vis absorption spectrum of the TiO_2 and COMP-Ag 30, 50, 70, and 80 composite thin films for determining the value of the optical band gap. The plots have linear regions and the depicted extrapolation of the straight line to a = 0 gives the indirect band gaps to be 3.61, 3.62, 3.59, 3.60, and 3.60 eV, respectively. The band gap of COMP-Ag 10, 20, 30, and 60 have an identical range with composite thin films plotted here and were omitted for brevity.

COMP-Ag10-40 thin films did not show any detectable response either to vis- or to UV light. These films could still easily absorb photons to produce photoexcited electrons under both UV and vis-light because they had a band gap corresponding to that of pure TiO_2. Owing to this band gap, they could respond to UV light and show characteristic

absorptions due to SPR and LSPR caused by vis-light. However, the injection of these photoexcited electrons into the conducting band of TiO_2 is difficult because of very high electrical resistivity associated with COMP-Ag10-40 thin films **[16]**. Hence, it was difficult for the photoexcited electrons to reach the TiO_2 surface, leading to an increase in extinction probability, which was unfavorable to the photoresponsive activity of the COMP-Ag10-40 thin films.

8-3.3 Photocurrent densities of COMP-Ag50-60 (40 < Ag mol% < 70) thin films

The results of photocurrent density measurements for the COMP-Ag50-60 thin films are shown in Fig. 8.6. Under vis-light irradiation, the cathodic photocurrent density of these films increased with an increase in the Ag content. The large cathodic photocurrent density observed could be mainly due to LSPR. Moreover, the photocurrent density of COMP-Ag50 was measured under different visible light specific range, namely blue light, red light and green light range. The resultant cathodic photocurrent spectra are shown in figure 8.7. These results proved that apart from SPR plasmon around 410 nm, the wide range LSPR plasmon is also responsible for the photo responsive of my composite thin films in the visible region.

On the other hand, the APD values under UV-light irradiation were extremely small and comparable to those for the dark currents (Table 8.2), as well as those for the abovementioned COMP-Ag10-40 thin films. The high electron transportability of the electrode facilitated the easy flow of electrons from the external circuit into the Ag NPs, which released the photoexcited electrons by LSPR. Therefore, with an increase in the amount of Ag NPs, the COMP-Ag50-60 thin films absorbed larger numbers of photons and the photoexcited electrons then transferred from Ag NPs to the TiO_2 matrix.

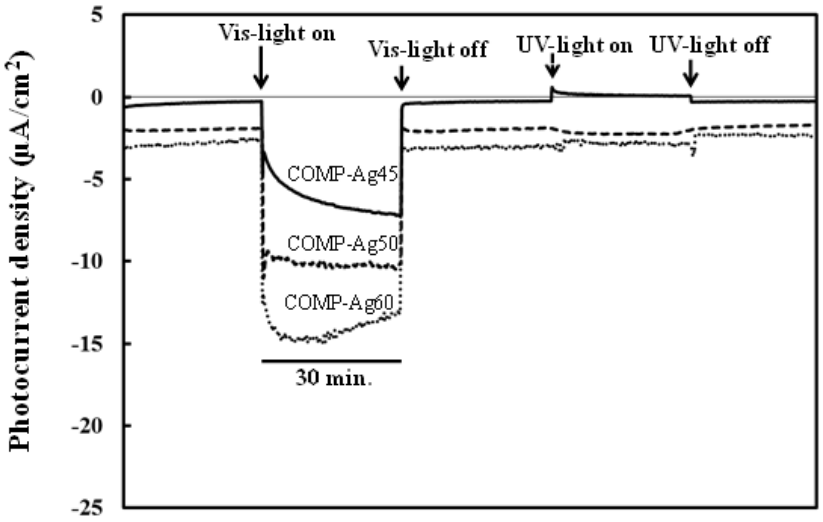

Fig. 8.6 Photocurrent densities of a COMP-Ag45 (solid line), COMPAg50 (dashed line), COMP-Ag60 (dotted line).

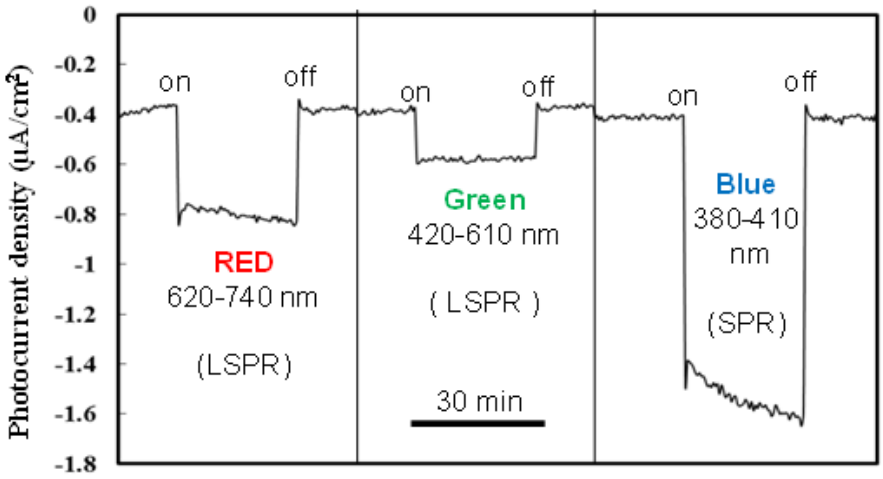

Fig. 8.7 Photocurrent density of COMP-Ag50 composite thin film using blue, green and red optical filters.

Consequently, owing to the higher electrical conductivity associated with middle-Ag-level composite thin films (Fig. 8.8), the photoresponse of these composite

thin films increased under vis-light irradiation as the photoexcited electrons were injected easily into the conduction band of TiO_2.

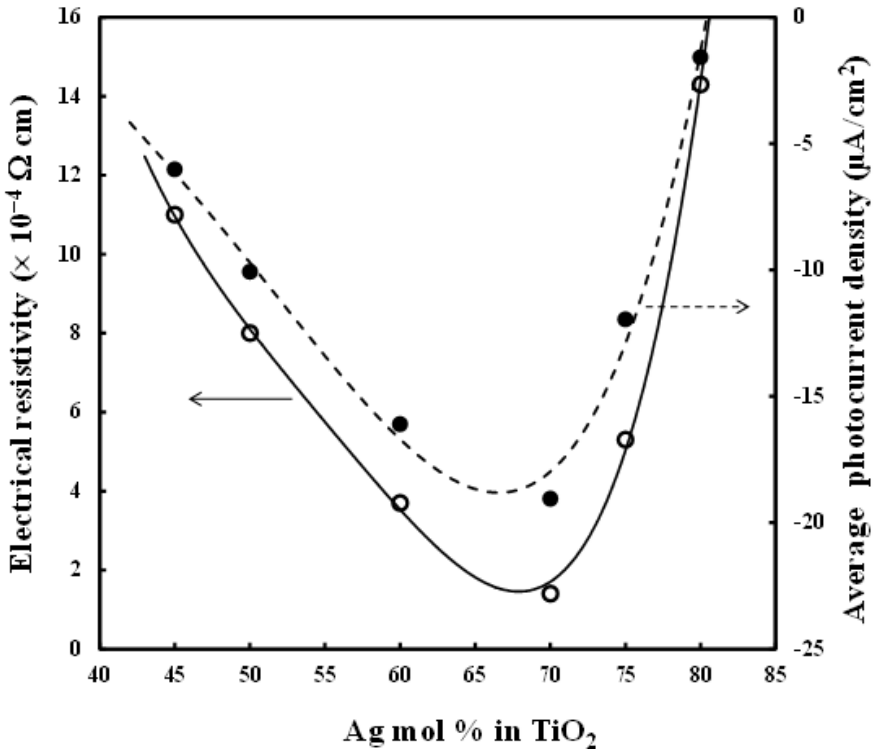

Fig. 8.8 Electrical resistivity and average photocurrent density generated under vis-light irradiation as function of Ag mol% in Ag/TiO_2 composite thin films. Lines indicate as follows: open circle, Resistivity; filled circle.

8-3.4 Photocurrent densities of COMP-Ag70-80 (70 ≤ Ag mol%) thin films

The increased content of Ag NPs in COMP-Ag70-80 thin films resulted in a decrease in the cathodic photocurrent density under vis-light, as shown in Fig. 8.9 above. The lower photocurrents for the COMP-Ag70-80 thin films corresponded to the weaker absorption intensities of the thin films, as reported in chapter 7. This may be consistent with the decrease in the electrical resistivity of the composite thin films, as reported chapter 5

and illustrated in Fig. 8.8, coupled with the decrease in the intensity of LSPR peaks, which can produce photoexcited electrons in Ag NPs, Chapter 7.

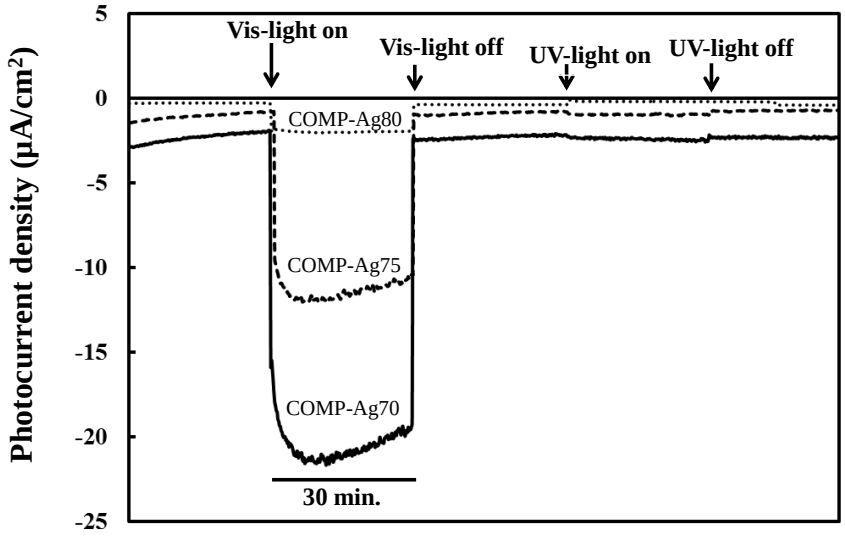

Fig. 8.9 Photocurrent densities of COMP-Ag70 (solid line), COMP-Ag75 (dashed line), COMP-Ag80 (dotted line) thin films fabricated on quartz glass.

8-3.5 Repeatability, perspectives and mechanical strength of the thin films

The stability, and reproducibility of plasmonic Ag-TiO_2 thin films were examined in order to check their potential use in practical systems. The TiO_2 doped with non-metal such as nitrogen and sulfide sometimes suffer from instability in practical application **[23]**. So, the stability of plasmonic Ag-TiO_2 composite thin film is further investigated by the recycle experiments of photocurrent as shown in figure 8.10. After four recycles for the photocurrent measurements for Ag-NP/TiO_2 thin film COMP-Ag70, photocurrent response does not exhibit any significant loss of activity, indicating that the thin films are stabile during the photocurrent measurements. Further observation shows that after the first cycle, the activity slightly decreases probably due to a drop of a

small amount of Ag-NPs from the surface of the thin film, and then the activity almost keeps stable. The XRD pattern of same sample at the end of the repeated photocurrent experiments is almost identical to that of the initial sample, although small peak peak observed at 26.5º in the XRD pattern (not shown) indicates the presence of silver oxide [JCPDS card 40-909]. The presence of silver oxide before and after photocurrent measurement indicates that depositing Ag on the surface of TiO_2 promotes the stability of Ag/TiO_2 composite thin film due to the chemical adsorption between O− anions in TiO_2 and Ag^+ cations in composite **[24]**.

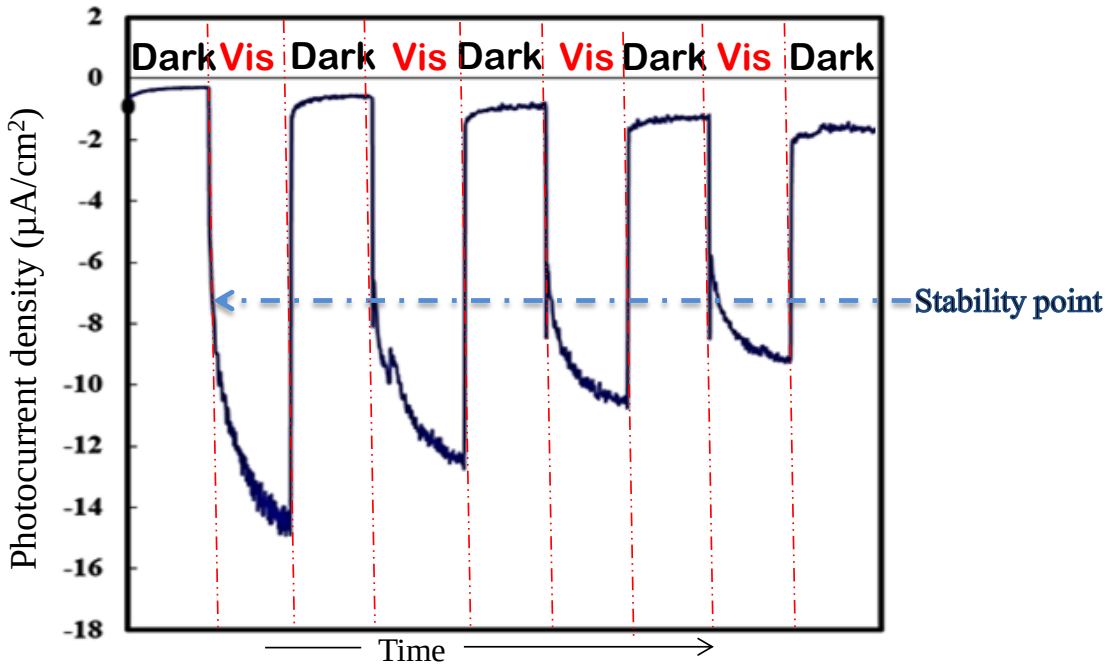

Fig. 8.10 Change in photocurrent density for COMP-Ag70 under dark and Vis light switched for every 20 minutes non-stop using Ag plate as a counter electrode.

8-3.6 The influence of counter electrode type on photocurrent density of Ag-NP/TiO_2 thin films

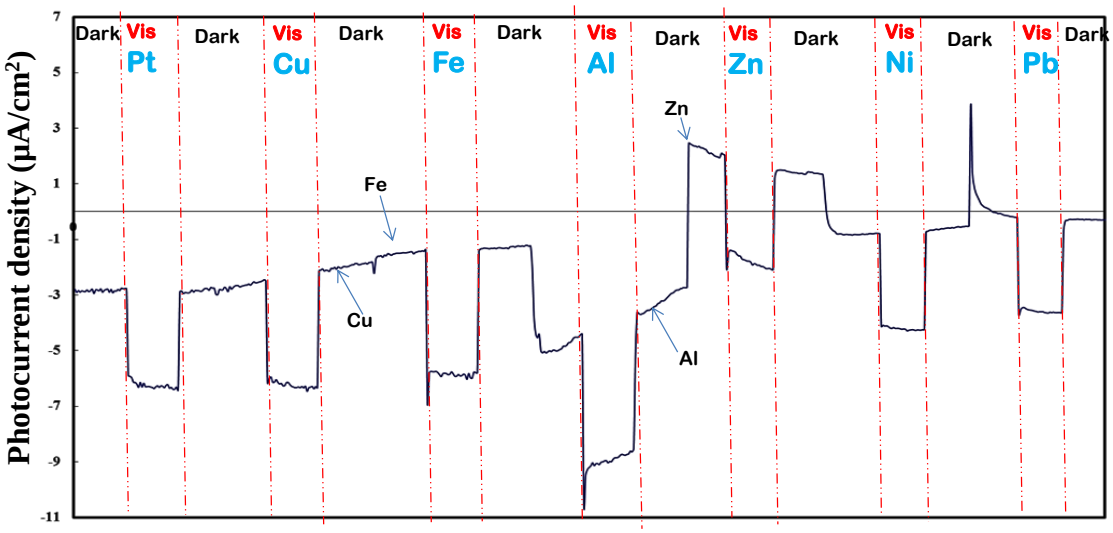

Fig. 9.12 Change in photocurrent density for COMP-Ag70 under dark and Vis light switched for every 20 minutes non-stop using different counter electrodes

Table 8.3 Net photocurrent density for COMP-Ag70 obtained using different counter electrodes.

Counter	**Dark 1**	**Visible Light**	**UV Light**
Electrode	μA/cm^2	μA/cm^2	μA/cm^2
Al	-0.9	-6.0	2.5
Zn	1.4	-5.2	0.1
Ni	-4.1	-6.4	-1.3
Pb	-1.6	-7.4	0.01
Fe	-0.4	-4.7	-0.5
Cu	-2.8	-3.8	0.1
Ag	-1.9	-8.2	0.3
Pt	-6.2	-6.8	-1.5

The idea of fabricating a UV/Vis light/electrode-controlled optielectronic switch by simply change the counter electrode while using a single device, Ag-NP/TiO_2 composite thin film, COMP-Ag 70 could be attained as shown in figure 8.11. Dark

current was subtracted from the visible light photocurrents and the net current is tabulated in Table 8.3.

All counter electrodes give a negative photocurrent under visible light. Al, Cu, Zn, and Pb as counter electrodes give a positive photocurrent while Fe, Ni, Ag and Pt give a negative photocurrent density under UV light. Different metals have different standard-state reduction potentials, E^{o}_{red}. From this information one can tell that the potential different between the metallic Ag/TiO_2 composite thin film and the metallic counter electrode have the influence on the polarity of the photocurrent. For instead, the counter electrode with the most negative E^{o}_{red} value is the strongest reduction agent (donate electrons eg Zn electrode in equation 8.4 electrode) while the electrode with the most positive E^{o}_{red} value is the strongest oxidizing agent (accept electrons eg Ag electrode).

$$Zn_{(s)} + Ag^{+}_{(aq)} \rightarrow Zn^{2+}_{(aq)} + Ag_{(s)} \quad \text{.....(8.4)}$$

stronger reducing agent	stronger oxidizing agent	weaker oxidizing agent	weaker reducing agent

The porality of photocurrent will depend on the overall potential different between the two electrodes, equation 8.5;

$$E^{o}_{overall} = E^{o}_{ox} + E^{o}_{red} \quad \text{.....(8.5)}$$

Hence, electrode at which reduction takes place in electrochemical cell is the cathode, equation 8. 6. The electrode at which oxidation occurs is the anode, equestion 8.7. Therefore the polarity will depend on the $E^{o}_{overall}$, whereby positive will give an anodic photocurrent whereas the negative value will give the cathodic photocurrent.

$2Ag^{+} + 2e^{-} \rightarrow 2Ag$ $E^{o}_{red} = 0.7996$ V (cathode)……..…(8.6)

$+ Zn \rightarrow Zn^{2+} + 2\ e^{-}$ $E^{o}_{ox} = 0.76$ V (anode)…….(8.7)

$Zn + 2Ag^{+} \rightarrow Zn^{2+} + 2Ag$ $E^{o} = E^{o}_{red} + E^{o}_{ox} =$ **1.5596 V** ……..…….(8.8)

$2Ag^{+} + 2e- \rightarrow 2Ag$ $E^{o}_{red} = 0.7996$ V……..(8.6)

$+ Pt \rightarrow Pt^{2+} + 2\ e^{-}$ $E^{o}_{ox} = -1.2$ V……(8.9)

$Pt + 2Ag^{+} \rightarrow Pt^{2+} + 2Ag$ $E^{o} = E^{o}_{red} + E^{o}_{ox} =$ **-0.4004 V**……...…..(8.10)

From this results and calculation, one can change the control the polarity of photocurrent by simply just changing the types of counter electrode while keeping other conditions constant. At present the phenomena behind is not clear. In addition, this work opens the possibility to develop light/electrode-controlled switch and work is currently in progress to study the phenomenon in more details.

8-3.7 Proposed mechanism for photoelectrochemical properties of plasmonic Ag NP/TiO_2 composite thin films

The absence of wavelength shift near the absorption edges of the pure TiO_2 thin film in the spectra for the present Ag NP/TiO_2 composite thin films shown in Figure 8.6, demonstrates that there was no change in the band gap of TiO_2 by the addition of Ag NPs. Furthermore, the UV-vis absorption spectra showed that the well-defined SPR peaks and wide-range LSPR bands due to Ag NPs are capable of efficiently sensitizing the Ag/TiO_2 composite thin films. Therefore, these plasmonic properties of the Ag NP/TiO_2 composite thin films can help us in elucidating the mechanism behind photocurrent generation by Ag NP/TiO_2 composite thin films.

Herein, we propose a plasmonic photoelectrochemical mechanism for the vis-light absorbance by Ag NP/TiO_2 composite thin films prepared by MPM. This mechanism is illustrated by three steps in Scheme 8.II. (1) Due to LSPR, electrons from Ag NPs are promoted to higher states in the band. (2) These electrons are then injected into the conduction band of TiO_2 if they have sufficient energy **[25]**. (3) The photoexcited electrons then travel faster through the electrolyte to counter electrode, producing a cathodic photocurrent. Depending on the redox potential difference between the composite thin films and counter electrode, if the potential originating at the counter electrode is high enough to drive electrons flowing from the conduction band of TiO_2 to the conductive substrate instead of electrons moving into the electrolyte, an anodic photocurrent can be generated **[14, 19, 23, 26]**.

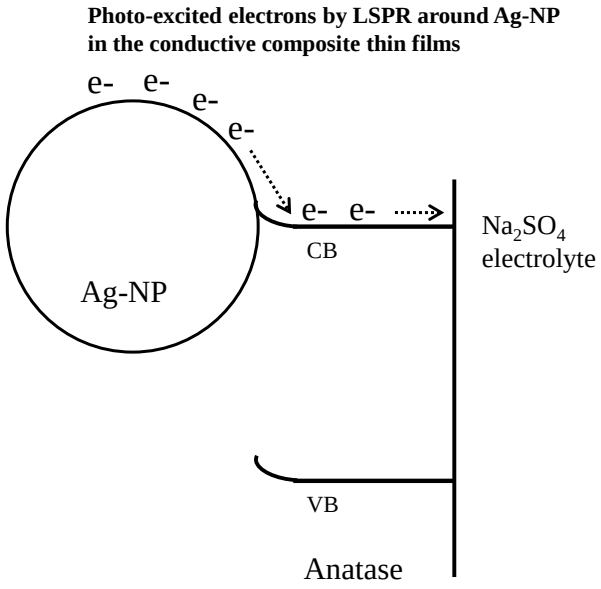

Scheme 8.II Proposed mechanism model for cathodic photocurrent generated by Ag NP/TiO_2 composite thin films.

Although the general conclusions that can be drawn from this proposed mechanism are entirely consistent with the findings reported earlier **[14, 19, 23, 26]**, Scheme 8.II shown here provides a simple explanation as to why the composite thin films exhibit a cathodic photocurrent. This explanation cannot be currently found in the literature.

8−4 SUMARRY

In short, the photoelectrochemical properties and absorption spectra of Ag NP/TiO_2 composite thin films (COMP-Ag_n) with various amounts of Ag (10 mol% $\leq n \leq$ 80 mol%) in a TiO_2 matrix were investigated. It was shown that MPM, which results in excellent miscibility of Ag NP and TiO_2 precursor solutions, is necessary for fabricating composite thin films capable of generating a cathodic photocurrent rather than an anodic one reported in many papers. The metallic property of Ag NPs and their UV-vis absorption spectra indicate that well-defined and intense absorption bands at approximately 410 nm, which correspond to their SPR peaks and the wide-range LSPR band in the visible region, are capable of efficiently sensitizing Ag NP/TiO_2 composite thin films. Therefore, the plasmonic property of Ag NPs can facilitate the elucidation of the mechanism behind the cathodic photocurrent generation from the Ag NP/TiO_2 composite thin films. Thus, the excellent vis-light response of the COMP-Ag*n* and the major factors affecting their photoresponsive nature are discussed from the viewpoints of a particle-plasmon band of Ag NPs. The absorption spectra reveal that the LSPR of Ag NPs can enhance the photoresponse of CONP-Ag*n* electrodes in the vis-region. Moreover, the high electrical conductivity of the COMP-Agn is important for affording a photoresponsive activity by enhancing the high separation efficiency of charge carriers.

8−5 REFERENCES

1. Sato M., Hara H., Nishide T., Sawada Y. (1996). *J. Mater. Chem.*, **6**, 1767−1770.

2. Sato M, Hara H, Kuritani M, Nishide T (1997). *Sol. Energy Mater. Sol. Cells* **45**, 43-49.

3. Nishide T, Sato M, Hara H (2000). *J. Mater. Sci.* **35**, 465-469.

4. Sato M, Tanji T, Hara H, Nishide T, Sakashita Y (1999). *J. Mater. Chem*. **9**, 1539-1542.

5. Nagai H, Hasegawa M, Hara H, Mochizuki C, Takano I, Sato M (2008). *J. Mater. Sci.* **43**, 6902-6911.

6. Nagai H, Mochizuki C, Hara H, Takano I, Sato M (2008). *Sol. Energy Mater. Sol. Cells* **92**, 1136-1144.

7. Nagai H, Aoyama S, Hara H, Mochizuki C, Takano I, Honda T, Sato M (2010). *J. Mater. Sci.* **45**, 5704-5710.

8. Nagai H, Aoyama S, Hara H, Mochizuki C, Takano I, Baba N, Sato M (2009). *J. Mater. Sci.* **44**,861-868.

9. Mochizuki C, Sasaki Y, Hara H, Sato M, Hayakawa T, Yang F, Hu X, Shen H, Wang S (2009). *J. Biomed. Mater. Res. Part B* **90**, 290-301.

10. Honda T, Oda T, Mashiyama Y, Hara H, Sato M (2010). *Phys. Status. Solidi*. **7**, 2471-2473.

11. Nagai H. and Sato M. (2012). Heat Treatment−Conventional and Novel Applications, edited by Frank Czerwinski, *InTech, Chapter **5***, 103-128.

12. Transversa E., Di Vona M. L., Nunziante P., Licoccia S. (2001). *J. Sol-Gel Sci Technol* 115-123.

13. Zhao G., Kozuka H., Yoko T. (1996). *Thin Solid Films*, 277:**1-2**, 147-154.

14. Tian Y. Tatsuma T. (2004). *Chem. Commun.* 1810-1811.

15. Ito S., Takeuchi T., Katayama T., Sugiyama M., Matsuda M., Kitamura T., Wada Y.,

Yanagida S., (2003). *Solar Cells Chem Mate.* **15**, 2824-2828.

16. Takahashi Y., Tatsuma, T. (2010). *Nanoscale* **2**, 1494–1499.

17. Kawahara K., Suzuki K., Ohkowab Y., Tatsuma T. (2005). *Phys . Chem. Chem*., **7**, 3851-3855.

18. Li H, Zhao G., Song B., Han G. (2008). *J Cluster Sci.*, **19**, 667-673.

19. Gupta K., Jana P.C., Meikap A.K. (2010). *Synt. Met.* **160**,1566–1573.

20. Reddy K. M., Manorama S. V., Reddy A. R. (2002). *Mater. Chem. Phys*. **78**,239-245.

21. Kavan L., O'Regan B., Kay A., Gratzel M. (1993). J. Electroanal. Chem., 346:**1-2**, 291-307.

22. Lee S., Jun Y., Kim K., Kim D. (2001). *Sol. Energ. Mat. Sol.,* **65**, 193-200.

23. Wei D., Amaratunga G. (2007). *Int. J. Electrochem. Sci.,* **2**, 897 – 912.

24. Yao W., Zhang B, Huang C, Ma C, Song X., Xu Q. (2012). *J. Mater. Chem.*, **22**, 4050-4055.

25. Linsebigler A. L., Lu G., Yates J. T. (1995). *Chem. Rev.*, 95:**3**, 735–758.

26. Zhao G. Kozuka H., Yoko T. (1997). *Sol. Energ. Mat. Sol. C*. **46**, 219-223.

CHAPTER 9: PHOTOCATALYTIC ACTIVITY OF VIS-RESPONSIVE Ag-NANOPARTICLES/TiO_2 COMPOSITE THIN FILMS.

9−1 INTRODUCTION

Metal oxide photocatalytic degradation of organic pollutants has attracted significant attention by researchers because of its usefulness in tackling environmental contaminants **[1]**. Whereas titanium dioxide as a metal oxide seems to be one of the most promising semiconductors for many photocatalytic applications due to its low cost, chemical stability and non-toxicity. Its utilization remains typically confined to UV light because of its wide band gap (3.2 eV for anatase and 3.0 eV for rutile) **[2]**. This limits the efficient utilization of solar energy for TiO_2 because TiO_2 cannot efficiently utilize solar light since UV light accounts for only 4–6% of solar radiation. Therefore, many attempts have been undertaken in recent decades to shift the threshold of the photo-response of TiO_2 into the visible region, which would enhance its potential for chemical solar energy conversion and open possibilities for further applications **[3−6]**. One of the alternative approaches for achieving the threshold of the photo-response of TiO_2 into the visible region is to make a composite semiconductor by modifying TiO_2 with noble metals. These noble metals act separately or simultaneously depending on the photoreaction conditions, experimental methods used and they may (i) enhance the electron-hole separation by acting as electron traps **[7−10]**, (ii) extend the light absorption into the visible range and enhance surface electron excitation by size- and shape-dependent plasmon resonances excited by visible light **[6, 11−13]** and/or (iii) modify the surface properties of TiO_2 **[14, 15]**. The early methods **[16−18]**, to produce noble-metal nanoparticles are still used today **[19−21]** and continue to be the standard by which other synthesis methods are compared. In particular, silver as a noble metal has attracted considerable attention, as a result of its remarkable role in the improvement of the photo-activity of semiconductors **[8, 12, 22]**. They could be reused,

and handled more easily and economically if impregnated on substrates. Therefore, many researchers have focused on modifying TiO_2 with Ag by synthesis Ag/TiO_2 heterostructures **[6−13, 22, 23]**.

Although the synthesis of Ag/TiO_2 heterostructures was intensively reported in large quantities **[6−13, 22, 23]**, there are few reports about Ag/TiO_2 composite thin films with amounts of Ag > 18 mol%, prepared by chemical methods such as sol-gel, so far in the literatures. It is well reported that incorporating larger amount of Ag particles was limited by the sol-gel dip-coating method of up to 18 mol% due to Ag particles coalescing with each other into huge particles during sintering **[24]**. Moreover, Ag/TiO_2 electrodes were short-lived because Ag NPs on TiO_2 are easily oxidized and dissolved in an electrolytic solution under vis-light irradiation **[25, 26]**. Ag NPs must be coated with a SiO_2 shell or Al_2O_3 mask to prevent foremost their oxidation by TiO_2 **[25, 26]**. By incorporating silver ions and Cu ions into clay minerals/TiO_2 mixtures with different ratio, it obtained composites capable of degrading ethanol in the visible wavelength range about twice as fast as the reference photocatalyst type P25 **[27, 28]**. Using molecular precursor method (MPM), a coating precursor solution can be prepared by a reaction of $Ti(O^iPr)_4$ with ethylenediamine-*N*,*N*,*N*′,*N*′-tetraacetic acid (EDTA) under the presence of dibutylamine and hydrogen peroxide **[29, 30]**. Consecutively, the Ag acetate ethanol solution can be easily prepared, simply by dissolving the silver salt in ethanol. The two precursor solutions can be then mixed at different molar concentration to form a composite solution. By spin coating the composite precursor solution on quartz glass substrates, the potential of producing metallic Ag-nanoparticles/titania (Ag NP/TiO_2) composite thin films with various and unprecedentedly high Ag particles, up to 80 mol% of Ag homogeneously distributed in a titania matrix can be fabricated by heat

treated at 600 °C as reported in previous chapters where, I concluded that the MPM offers excellent miscibility of the silver and titania precursor solutions, and is effective for overcoming the limitations in miscibility of the conventional sol-gel method and is necessary for fabricating Ag/TiO_2 composite thin films with amounts of Ag ≤ 80 mol%.

In this chapter, I am reporting the photocatalytic activity of Ag-NP/TiO_2 composite thin films with various amounts of Ag (10≤ Ag mol% ≤ 80) in titania and compare them with pure TiO_2 thin film, both fabricated by the MPM. The relationship between the unprecedentedly high amounts of metallic silver in TiO_2 and photocatalytic decoloration rate of methylene blue was examined. Homogeneous distribution and growth of Ag-NP in the composite thin films were clarified by the FE-SEM and TEM observations. The absorption spectra of Ag-NP/TiO_2 composite thin films were analyzed by using Kubelk-Munk equation for diffuse reflectance spectra (DRS), in order to study the plasmonic effect of Ag-nanoparticles (Ag NP) in dielectric TiO_2 matrix. The findings demonstrated that a positive relationship exists between Ag NP surface plasmon absorption and the rate enhancements of decoloration and prove the hypothesis that the metallic plasmonic enhances rates of photocatalytic reactions **[20]**.

9−2 EXPERIMENTAL

9-2.1 Materials

All the materials employed in this chapter are tabulated in Chapter 3, Table 3.1.

9-2.2 Preparation of Coating Precursor Solutions, S_{Ti}, S_{Ag}, $S_{composite}$ and the fabrication of Ag-NP/TiO_2 composite thin films

The precursor solution S_{Ti} contains a Ti^{4+} complex of EDTA and the ethanol solution of Ag-nanoparticle, S_{Ag} for fabrication of Ag-nanoparticles titania thin film was prepared in accordance with the molecular precursor method (MPM) reported in chapter 4, 5 and 7. The $S_{composite,}$ with different compositions, was achieved by mixing a certain amount of S_{Ag} with S_{Ti}. Then, the $S_{composite}$ was sonicated with stirring for 5 min to increase the homogeneity. Ag-NP/TiO_2 composite thin films were deposited by spin coating of the $S_{composite}$ onto the substrates with a double step mode: first at 500 rpm for 5 s and then at 2000 rpm for 30 s in all the cases. Thin films were fabricated by heat-treatment at 600 °C for 0.5 h to remove residual organic compounds.

9-2.3. Characterization of Ag-NP/TiO_2 Composite Thin Films

A Phi Quantum 2000 Scanning ESCA Microprobe (Shimadzu, Tokyo, Japan) with a focused monochromatic Al-Kα X-ray (1486.6 eV) source was employed in order to evaluate the elemental states and quantities—Ti, O, C and Ag—in the thin films. No critical surface charging during the XPS measurements was observed; thereby, no correction of binding energy was performed. The depth profiles were obtained with the identical instrument. The stepwise etching was performed by bombarding the Ar^+ ions with 2 kV for 3 min before measuring each layer.

9-2.4. Photocatalytic Measurement of TiO_2 Thin Film and Various Ag-NP/TiO_2 Composite Thin Films

The study of the decoration of methylene blue aqueous solution was done using the method adapted in our laboratory **[31, 32]**. Here, the photocatalytic activity of pure TiO_2 and composite thin films was estimated by measuring the decoloration rate of

methylene blue (0.01 mM) in an aqueous solution (10 mL) containing 20 × 20 mm^2 thin film photocatalyst. Various Ag-NP/TiO_2 composite thin films with different Ag molar concentration or pure TiO_2 thin film was used as the photocatalyst. The photocatalysts were immersed in the 0.02 mM MB aqueous solutions overnight in the dark to allow equilibrate adsorption on the film surfaces.

For UV measurements, the suspension was irradiated using a black light, National FL10BL-B, which emits UV light. The distances of the black light sources from sample surfaces were adjusted to maintain UV intensities at 365 nm of 1.2 mW cm^{-2} which was measured by an UV meter, UVR-400, Iuchi Co., Ltd. (Tokyo, Japan). Vis-light was obtained from a fluorescent light, Duro-Test Vita-Lite, by removing light of wavelengths shorter than 400 nm using a cut-off filter, Ishihara Window Paint. The vis-light intensity after removing UV components from the fluorescent light, which was estimated by an illuminometer, LX-105, CUSTOM Co., Ltd. (Tokyo, Japan) was 0.8 m W cm^{-2}. In order to examine the degree of adsorption on the glass substrate and self-decomposition of MB, same measurement was performed on the same samples without irradiation (dark) as a reference.

The MB concentration was determined by measuring the absorption spectra of the aqueous solution with the U-2800 spectrophotometer. For the decoloration test, *ca.* 3 mL of the 0.01 mM MB aqueous solution was transferred into a quartz cell of dimensions 1 W × 1 L × 4.5 H cm^3 at 20-min intervals. After spectral measurement in the range of 600–700 nm, the solution was immediately returned to the vessel and mixed with the aliquot. The mixed solution continued to be used until the test for each film was completed. The mixed solution was further used until the test for each film

was done again after 18 h. The absorption peak value at 664 nm were used in order to determine the concentration of MB after *t* minutes, C(*t*), using Equation 9.1:

$$C(t) = 10 \times \frac{abs(t)}{\mathrm{abs}(0)} = \mu M \tag{9.1}$$

where Abs(*0*) and Abs(*t*) represent the absorption values of the solution just before the light irradiation and after *t* minutes during irradiation, respectively.

The decoloration rate of MB was examined three times for each film, and the initial decoloration rate (*k*) values of concentration after *t* minutes of 0.01 μM MB aqueous solution by photoreaction with each potential photocatalytic thin film and a blank were measured by an approximate line for the function of C(*t*) *versus t* obtained in the range from $0 \leq t \leq 180$ min by a least-square method. The index of photocatalytic activity (IPCA) of the film was estimated from the averaged value of *k*, using equation 9.2 adapted from **[31, 33]**.

$$IPCA = 10^3 \times \frac{|k_n|}{3} = nM\ min^{-1} \tag{9.2}$$

where k_n indicates each initial decoloration rate obtained thrice (n = a, b, c), independently, thus determined by a standardized method.

9−3 RESULTS

The TiO_2 thin film and eight Ag-NP/TiO_2 composite thin films (COMP-Ag*n*; *n* = 10, 20, 30, 40, 50, 60, 70, and 80) were fabricated. The XRD, TEM, SEM, absorption spectra and electrical conductivity results of these Ag-NP/TiO_2 composite thin films are presented in the previous chapters.

9-3.1. Chemical Characterization of Thin Films by XPS

The depth profile for COMP-Ag40, 50 and 70 were scanned as shown in Figure 9.1; including the spectra obtained after performing Gaussian curve-fitting.

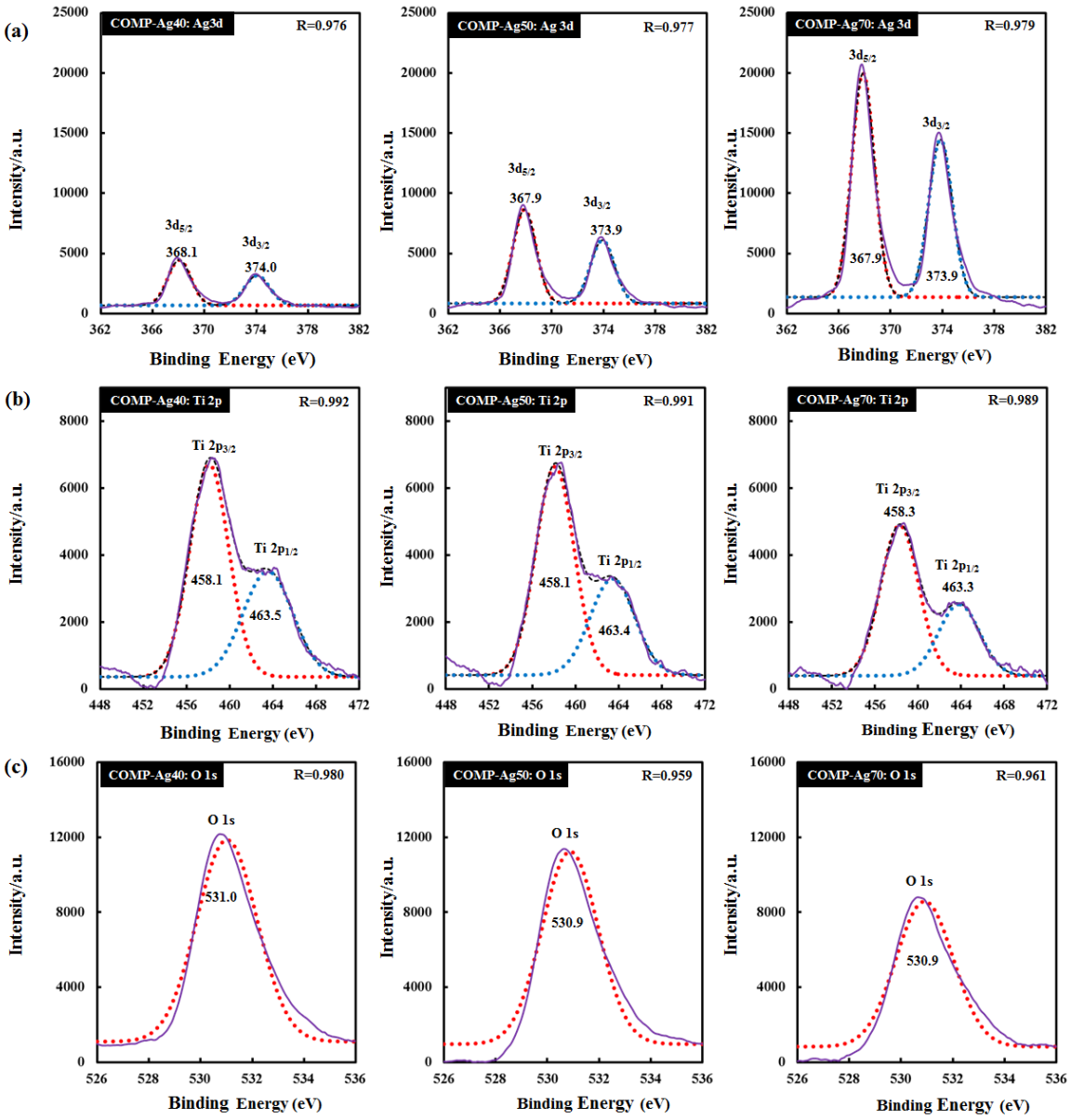

Fig. 9.1 High resolution regional (**a**) Ag3d; (**b**) Ti 2p and (**c**) O 1s XPS spectra. The thin solid lines indicate the original data of XPS. The dashed curves show theoretically fitted curves by assuming Gaussian distribution.

The Ag 3d peaks (Figure 9.1a) for all thin films are located at 368.0 eV ($3d_{5/2}$) and 374.0 eV ($3d_{3/2}$), with a spin-orbit splitting of 6.0 eV. This is attributed to metallic Ag **[34]**, consistent with the XRD result reported previously **[29]**. By increasing the amount of Ag in the composite thin films, the Ag 3d peak shifts slightly to a lower binding energy position by only 0.1 eV (within experimental uncertainty).

The Ti $2p_{3/2}$ and $2p_{1/2}$ peaks (Figure 9.1b) are found at 458.1 and 463.5 eV, respectively, attributed to Ti^{4+} for pure crystalline TiO_2 **[34, 35]**. The peak position shows no critical change compared to that of pure TiO_2. This indicates that there is no significant interfacial interaction between Ag and TiO_2. The O 1s peaks (Figure 9.1c) found at 531.0 eV is due to O^{2-} of TiO_2 **[34, 36]**. The Ti 2p and O 1s peaks are reduced in intensity. The O:Ti ratio obtained from XPS for TiO_2, COMP-Ag*n* (*n* =40, 50 and 70) are 2.003, 1.997, 2.007 and 2.130, respectively. Further, any peak around 457.4 eV attributable to the Ti^{3+} ion could not be observed **[36]**.

9-3.2. Optical Properties of TiO_2 Thin Film, Ag-NPs and Ag-NP/TiO_2 Composite Thin Films

Figure 9.2 represents the UV-vis absorption spectra for TiO_2 and Ag NP extracted from the absorption spectra reported in Chapter 7. The TiO_2 thin film showed a low-intensity absorption band in the vis-region; however, its absorption intensity increased steeply at shorter wavelengths with the band edge at around 355. In contrast, the Ag NP film showed a weak and broad absorption band at around 410 nm. The absorption band in this region corresponds to the characteristic SPR of Ag NPs. This absorption band was also observed for the COMP-Ag*n* thin films reported in Chapter 8, though the peak position in this region gradually increased in intensity upon increasing the Ag content.

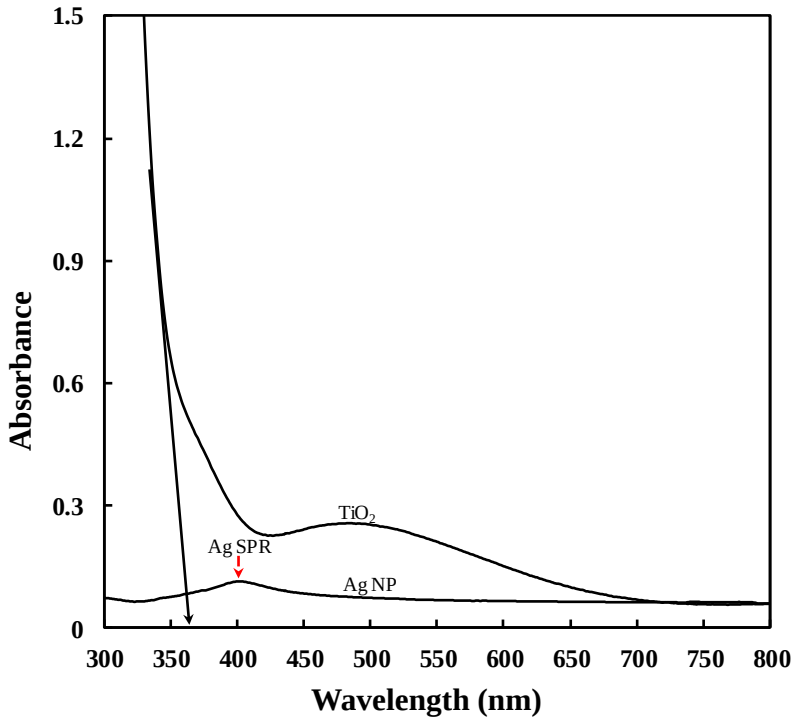

Fig. 9.2. UV-vis absorption spectra for TiO_2 thin film and Ag NP fabricated on quartz glass.

The DRS of the composite thin films are presented in Figure 9.3 (a−g). The DRS measured in the range of 200–800 nm were converted to the absorbance spectra using Kubelka-Munk equation (Equations 9.3 and 9.4) **[37, 38]**.

$$F(R_\infty(\lambda)) = \frac{(1 - R_\infty)^2}{2R_\infty} \tag{9.3}$$

$$R_\infty = \frac{\mathrm{R}}{R_{TiO2}} \tag{9.4}$$

Where R is the reflectance recorded and R_{TiO2} is the reference recorded for a reference (titania in this case). The Origin9 software (OriginLaB Co., Northampton, MA, USA) was used to obtained individual Gaussian peaks, which are theoretically fitted peaks by assuming Gaussian distribution.

The peak positions and peak areas obtained by analysis with curve-fitting procedure are listed in Table 10.2. All the composites show two main peaks, labeled peak 2 and 3. Peak 2, which is at 365 nm on average, may represent a typical semiconductor optical absorption since the lambda maximum of pure TiO_2 is at around 365 nm, corresponding to a band gap of around 3.4 eV.

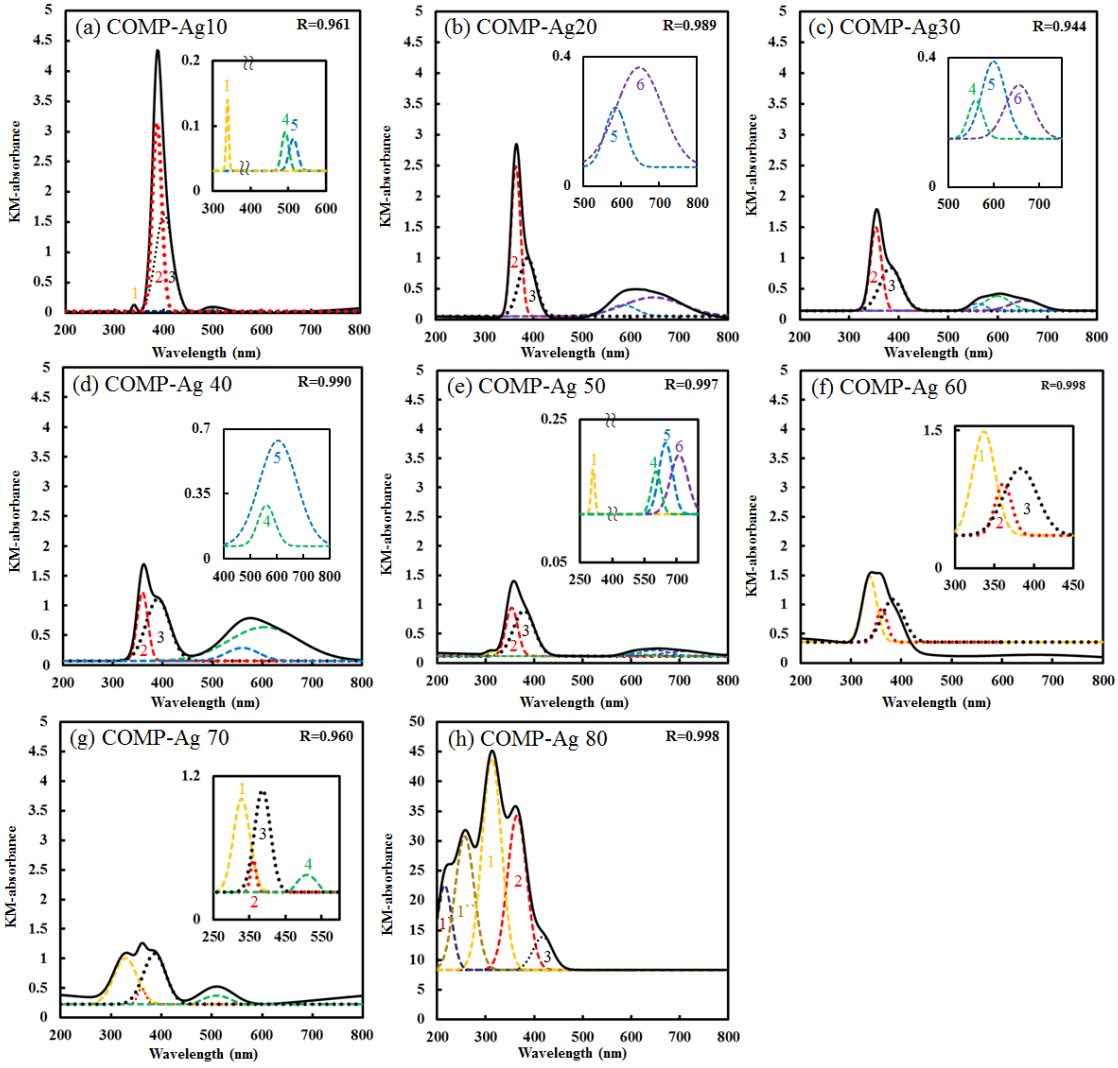

Fig. 9.3 UV–Vis diffuse reflectance spectra (DRS) of Ag-NP/TiO_2 composite thin films at various amounts of Ag molar concentrations: (**a**) 10; (**b**) 20; (**c**) 30; (**d**) 40; (**e**) 50; (**f**) 60; (**g**) 70 and (**h**) 80, respectively.

As shown in Figure 9.2, the band edge of TiO_2 is around 365 nm and according to absorption spectra in chapter 7 and the band gap calculation done in chapter 8, there was no band gap shift observed for TiO_2 in all the composite thin films; therefore, we assign peak 2 in all the composites to be related to the TiO_2 absorption spectrum. Peak 3, which is located at around 390 nm, can be regarded as the main Gaussian peak since it has the largest peak area ratio per volume compared to the other peaks.

Table 9.1. The DRS peak positions and peak area ratios of Ag-NP/TiO_2 composite thin films. These data were obtained by Gaussian curve-fitting using ORIGIN9 software (OriginLaB Co., Northampton, USA).

Notation	Peak position (λ nm)						Peak area ratio (%)					
	1	2	3	4	5	6	1	2	3	4	5	6
COMP-Ag10	340	386	400	492	520	-	1	49	46	2	2	-
COMP-Ag20	-	365	390	−	584	640	-	44	31	-	10	15
COMP-Ag30	-	351	385	559	598	655	-	35	35	5	13	12
COMP-Ag40	-	359	390	560	600	-	-	15	30	9	46	-
COMP-Ag50	310	354	379	603	649	710	2	29	46	4	9	10
COMP-Ag60	336	361	383	-	-	-	44	15	41	-	-	-
COMP-Ag70	329	360	386	510	-	-	41	5	43	11	-	−
COMP-Ag80	312	364	417	-	-	-	53	39	8	-	-	−

Although the average lambda maximum peak position for peak 3 is at 390 nm, as shown in Figure 9.3 a–h, more than one-third of its area is covering the visible region ≥400 nm. In addition, peak 1 is also exhibited in COMP-Ag10 as well as in the middle- and high-Ag-level composite thin films. Moreover, with exception to COMPAg60, overlapped Gaussians peaks with smaller peak areas than those of peak 2 and 3 are appearing in the visible light regions. These peaks 4, 5 and 6 have lambda maximum at around 500 nm, 600 nm and 550 nm, respectively.

9-3.3. Photo-Responsive Activity of Ag-NP/TiO_2 Composite Thin Films

The photocatalytic activity of MB decoloration was investigated quantitatively by monitoring the changes between the initial MB absorption spectra and the final MB absorption spectra intensity positions, as well as qualitatively by determining the decoloration rate of MB (nM min^{-1}). The absorption spectra of decoloration of 1×10^{-2} mM of MB aqueous solution tested under dark, UV light and vis-light irradiation for 18 h are shown in Figure 10.4a–c, respectively, by employing the pure TiO_2 thin film, pure Ag NP, COMP-Ag*n* thin films, where $10 \leq n \leq 80$ and the blank.

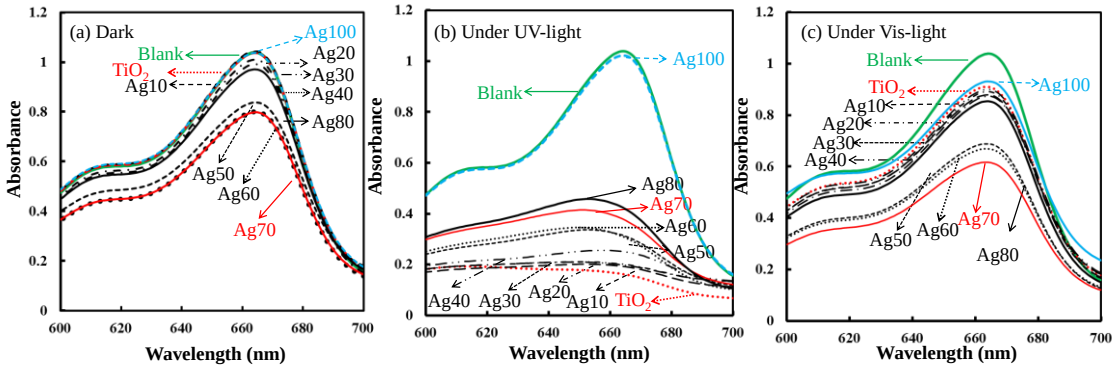

Fig. 9.4 Absorption spectra of decomposition of 0.001 mmol of MB aqueous solution in the presence of different Ag-NP/TiO_2 thin films after kept under (**a**) dark; (**b**) UV and (**c**) vis-light irradiation for 18 h.

Under dark (Figure 9.4a), the MB absorption spectra change for pure TiO_2, pure Ag (Ag100) and COMP-Ag10 are at the identical intensity position to that of the blank. This illustrated that there was no catalytic activity taking place in these two samples under dark condition. The absorption spectra for COMP-Ag20, 30 and 40 show small changes compared to those of COMP-Ag50, 60 and 70.

COMP-Ag80's absorption spectral change is smaller than those of COMP-Ag 50, 60 and 70 composite thin films but larger than for low-Ag-level composite thin films. The

influence of the amount of the Ag in titatia on self-decoloration of MB could be thus evaluated.

In Figure 9.4b, the absorption spectral changes is getting smaller with the increase in the Ag amount in COMP-Ag*n*; whereby COMP-Ag80 and pure Ag NP (high-Ag-level) show the smallest changes and TiO_2 shows the biggest change under UV-light irradiation. The pure Ag NP exhibited a very poor photocatalytic activity under UV and dark almost equal to that of the blank, which reflected that Ag did not act as catalytic on itself. Almost 100% decoloration of MB solution has been attained when UV-light was irradiated for 18 hours on pure TiO_2 and on low-Ag-level composite thin films.

Middle-Ag-level shows the moderated change between the initial MB absorption spectra and the final MB absorption spectra intensity positions. In Figure 9.4c, the absorption spectral change was larger with an increase in the amount of Ag in COMP-Ag*n* thin film under visible-light irradiation. Pure TiO_2 shows the smallest change, while COMP-Ag70 shows the largest change. Kőrösi *et al.*, **[5]** showed that the rate of photooxidation of organic compounds was significantly enhanced by silver-modification of titania.

In order to obtain qualitative data, an index of photocatalytic activity (IPCA, nM min^{-1}) of decoloration rate of 1×10^{-2} mM MB solution permitted us to directly compare the performance of pure TiO_2 and composite thin films under light irradiation to the dark condition. Each experimental set was repeated three times. The results were reproduced within narrow limits and the mean value was selected. The IPCA values extracted from a decoloration rate of 1×10^{-2} mM MB solution by photoreaction with each thin film and a blank are shown in Table 9.2.

Table 9.2. The index of photocatalytic activity (IPCA) of decoloration rate of 1.0×10^{-2} mM MB solution by photoreaction with each thin film and a blank.

Notation	IPCA/nM min^{-1}		
	Vis-light	**UV-light**	**Dark**
Blank	3.2(5)	2.8(6)	4(1)
TiO_2	5.1(9)	22(5)	4.5(1)
COMP-Ag10	5.6(6)	23(6)	5.5(4)
COMP-Ag20	4.1(1)	21(2)	4(2)
COMP−Ag30	5.4(8)	20(2)	5.1(3)
COMP-Ag40	7.5(9)	14(1)	7(1)
COMP-Ag50	10(4)	18(3)	6.9(5)
COMP-Ag60	9.4(4)	18(3)	5(1)
COMP-Ag70	13(3)	19(8)	8(1)
COMP-Ag80	9.6(8)	9(4)	8(1)
Pure Ag NP	4.6(5)	3.3(3)	4.2(1)

[a] The standard deviations are presented in parentheses.

Under UV-light irradiation, none of the composite samples exhibit more photoactivity than pure TiO_2, while all of the composite samples are more photoactive than pure TiO_2 under both dark and visible-light irradiation. The different results reveal that the photoactive enhancement mechanisms under UV and visible-light irradiation are different.

9-3.4 Influence of Electrical Resistivity on Photocatalytic Decoloration Rate of the Composite Thin Films

In Figure 9.5, electrical resistivity and dependency of net photocatalytic decoloration rate (ΔIPCA) of each thin film as a function of Ag mol% in the Ag-NP/TiO_2 composite thin films are presented. The electrical resistivity values are extracted from the Table 5.1 of Chapter 5. The ΔIPCA value of each thin film is calculated as the difference

between the IPCA under UV- or vis-light irradiation and the corresponding value measured for each thin film under dark conditions.

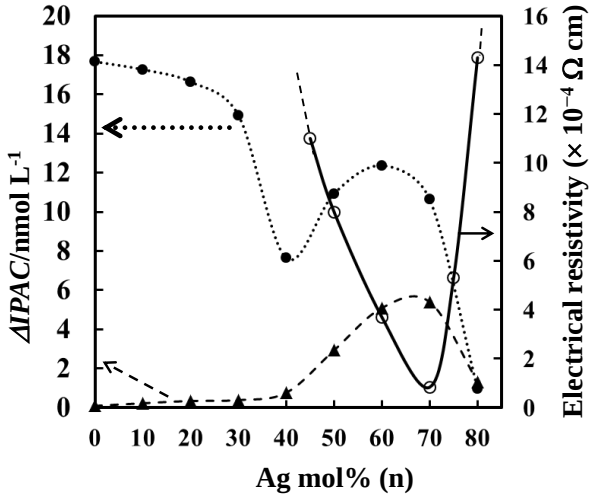

Fig. 9.5 Electrical resistivity and dependency of net photoreactivity (ΔIPAC) of each thin film as a function of Ag mol% in the Ag/TiO_2 composite thin films. The lines indicate as follows: open circle, resistivity; close circle ΔIPAC under UV; filled triangle ΔIPAC under Vis. These values (ΔIPAC) were obtained to measure the differences between the IPAC of the decomposition of MB aqueous solution under UV and Vis-light irradiation with those under dark conditions.

The low-Ag-level thin films show electrical resistivity higher than 10^6 Ω cm, the ΔIPCA values show a decrease trend under UV-light irradiation, and very lower ΔIPCA values slightly increasing under vis-light irradiation with the increase of Ag mol % in the composites. Middle-Ag-level composite thin films show low electrical resistivity in the range 10^{-1}–10^{-4} Ω cm and their ΔIPCA values increases again toward the two-third level of the original TiO_2 ΔIPCA value under UV-light irradiation. In contrary, the middle-Ag-level composite under vis-light irradiation shows the vis-response, whose

level is slightly lower than the decreased UV-sensitivity of the identical thin film samples. A net photocatalytic activity local maximum appears between 60 and 70 mol% for vis-sensitivity. The electrical resistivity of high-Ag-level thin films is increasing from 10^{-5} Ω cm for COMP-Ag70 to higher than 10^{6} Ω cm for COMP-Ag80, hence the acute decrease of the ΔIPCA value under both UV- and vis-light irradiation can be observed between 70 and 80 mol% of the Ag amount

9−4 DISCUSSION

The photocatalytic activity of the Ag-NP/TiO_2 composite thin films including those of unprecedentedly high Ag amounts was quantitatively examined by the decoloration reaction of MB in an aqueous solution. In Figure 9.5, the dependency of net photoreactivity (ΔIPCA) of each thin film as a function of Ag mol% in the Ag NP/TiO_2 composite thin films are presented, along with that of electrical resistivity. Each ΔIPCA value was calculated as the difference between the IPCA under UV- and vis-light irradiations and the corresponding value measured for each thin film under dark conditions (Table 9.1) **[31]**. The IPCA under dark condition can be representing both adsorption and self-decoloration of MB **[39, 40]**, and they are dependent on the Ag amount in the thin films. The IPCA of pure Ag NP is slightly high under visible light compare to those under UV-light and dark; this could be due to the plasmonic photocatalyst associated with Ag nanoparticles **[41]**.

9-4.1. Photocatalytic Activity under UV-Light Irradiation

As shown in Figure 9.5, the ΔIPCA of the composites under UV irradiation has two points of inflection depending on the Ag amount in the composites. One appears at 40

mol% as a local minimum and another at 60 mol% as a local maximum. The high ΔIPCA values of the composites whose Ag amounts to up to 30 mol% indicates UV-sensitivity almost identical to anatase thin films **[31]**. The decreasing tendency of the activity in this region is due to both the decreases of anatase in TiO_2 and the TiO_2 amount in the composites by increasing the Ag amount in the composites. The photocatalytic activity of TiO_2 under UV-light irradiation should be due to the anatase form of TiO_2 in the thin films and not to the rutile form **[31]**, because it was indicated that the photocatalytic activity of these composite thin films is not owing to the oxygen deficiency by the present XPS analysis (Figure 9.1).

The acute decrease of the activity occurs between 30 and 40 mol% of the Ag amount which critically corresponds to the percolation threshold of electrical conductivity of the composites. The ΔIPCA decrease of the composite thin films due to TiO_2 components under UV-light irradiation is thus inevitable by the decrease of anatase with the increase of Ag NP. This tendency should be accelerated by increasing the Ag amount in the composites, because the covering of the TiO_2 surfaces by the deposited Ag particles occurs significantly even if the Ag NP distribute homogeneously as observed in TEM and FE-SEM images reported in previous chapters.

It can be therefore accepted that the decrease of the photocatalytic activity by anatase under UV-irradiation should be consecutive with the increasing amount of Ag NP. However, the ΔIPCA value increases again toward the local maximum whose position deviates slightly from that of the lowest electrically resistivity of the composite thin films, at 60 mol% of Ag amount in the composite. Consequently, the activity recovery to a two-third level of the original TiO_2 may be assisted by the enhanced electrical

conductivity of the composite. The slight difference between the local-minimum position of the photocatalytic activity and that of the electrical resistivity suggests that the anatase amount in the composites is more effective than the electrical resistivity.

9-4.2 Photocatalytic Activity under Vis-Light Irradiation

We have shown in Figure 10.4c that the increase in the amount of Ag in the composite consistently increased the vis-sensitivity of the composite thin films. This increase in vis-sensitivity of the composite was not only significant, but relatively large in magnitude (Figure 9.4). The synergistic effect can be interpreted as the result of the excellent adsorption capabilities of the Ag NP combined with the advantageous effect of silver nanoparticles on light absorption in the visible range **[27, 28]**. While there were general positive effects on photocatalytic activity with the increase in the amount of Ag in the composite of up to 70 mol% of Ag amount in the composite, an acute decrease of the ΔIPCA value can be observed between 70 and 80 mol% of the Ag amount. Collectively, these results suggest that the ultimate impact of Ag NP on composite thin films' photocatalytic activity may be quite predictable. However, the mechanistic basis for vis-sensitivity could be difficult to understand and predict without a good deal of optical absorption spectra **[25, 26]**. Therefore, the optical absorption of AgNP/TiO_2 composite thin films were characterized by UV/vis DRS (Figure 10.3) in order to study the apparition of different resonant absorption peaks caused by the difference in amounts of Ag in the composite.

9-4.2.1. Contribution of SPR and LSPR in Photocatalytic Activity under Vis-Light Irradiation

In Figure 9.3, when the composite has less than or equal to 70 Ag mol% it is possible to appreciate only a DRS peak 3 (black dotted line). This first well-defined DRS peak was found centered at around *ca.* 390 nm (peak 3), and it is attributed to the natural optical resonance of spherical Ag NP **[11, 13]**. Although this peak is centered around 390 nm, about one-third of its area in all the composite thin films belongs to visible light region (≥400 nm). The lamp used to study the decoloration of MB aqueous solution employed in this study doe emit 0.8 $mWcm^{-2}$ at a wide range of 400 nm–800 nm, which is sufficient to stimulate visible light photocatalytic activity even for the area that cover by the SPR peak 3. All the composites exhibit this SPR peak 3, and are therefore reflecting their capability to respond to visible light. Whereby, peak 3 takes the potential advantage of being present in the same visible spectra widow of the natural optical SPR of spherical Ag NP.

In addition, all the composite thin films showed a typical semiconductor optical absorption band with a lambda maximum peak at around ca. 365 nm (peak 2), which corresponded to the band gap of pure TiO_2, and that is only responsible for UV-sensitivity **[31]** and hence not important for vis-sensitivity. Titanium dioxide displays photocatalytic behavior under UV illumination. However, other DRS peaks (peak 1, 4, 5 and 6) are assignable to localized surface plasmon resonance (LSPR). Size-shape-dependent LSPR occur when metallic Ag NP with a different size, shape and separation distance are irradiated by light, whereby large oscillating electric fields are produced between the metal nanoparticles [Yu *et al.*, 2009]. Therefore, these plasmonic properties of the Ag NP/TiO_2 composite thin films can help us in elucidating the mechanism behind photocurrent generation by Ag NP/TiO_2 composite thin films. (1) Due to LSPR, electrons from Ag NPs are promoted to higher states in the band. (2)

These electrons are then injected into the conduction band of TiO_2 and defuse to catalytically active sites at the semiconductor/liguid interface where they drive chemical transformations **[8, 41]**. The proposed mechanism is already confirmed by the experiments of transient photocurrent response we reported in Chapter 8 and supported by Yu and his group, 2009.

TEM and SEM micrographs we reported in chapter 8 corroborate that the composites have Ag NPs with different size and shapes. XPS results show that Ag NPs are metallic. The metallic property of the Ag NP in our composite thin film is consistent with the XRD we reported in Chapter 6. Usually, Ag/TiO_2 thin films are short-lived because Ag NPs on TiO_2 are easily oxidized under vis-light irradiation; therefore, no plasmonic photocatalyst was observed unless the Ag core is covered with a silica (SiO_2) shell **[26]** or masked with an Al_2O_3 nanomask **[25]** to prevent oxidation of Ag by direct contact with TiO_2. Molecular precursor method enables plasmonic photocatalysis without covering the metallic Ag core in the composite.

9-4.2.2. Contribution of Electrical Conductivity on the Photocatalytic Activity

Something to be noted is that the dependency of net photocatalytic decoloration rate ΔIPCA of middle-Ag-level composite thin films was significantly higher than that for low- and high-Ag-level composite thin films (Figure 9.5). It is interesting that the net photocatalytic decoloration rates of the composite thin films are strongly correlated to their electrical resistivity rather than to the number of LSPR peaks that appeared in the visible region. The low-Ag-level thin films show resistivity higher than 10^6 Ω cm and exhibit the poorest photocatalytic activity under visible light irradiation. These films could still easily absorb photons to produce photoexcited electrons under vis light due to

SPR and LSPR DRS peaks in visible light region. However, the movement of these photoexcited electrons is difficult because of very high electrical resistivity associated with low-Ag-level composite thin films. Hence, this is leading to an increase in extinction probability, which is unfavorable to the photoresponsive activity of the thin film.

On the other hand, the middle-Ag-level thin films show low electrical resistivity in the range 10^{-1}–10^{-5} Ω cm and high photocatalytic activity, which gradually increases with an increase in the amount of Ag NP on the surface of titania. The increase of Ag NP on the surface of titania may result in a lower electron density of the Ti atoms in the Ag/TiO_2 samples. However, it is widely accepted that the Ag NPs in TiO_2 will benefit the separation of photogenerated electron-hole pairs due to electrical conductivity, thus enhancing the photocatalytic activity **[8]**.

The electrical resistivity of the high-Ag-level thin films increases again from 10^{-5} Ω cm–10^{-2} Ω cm with an increase in the amount of Ag in titania from 70 mol%–80 mol%, respectively. At the same time, the photocatalytic activity of the high-Ag-level thin films has acute decreases with an increase in the amount of Ag from 70 mol%–80 mol%, respectively. This reveals that the electrical conductivity of Ag-NP/TiO_2 composite thin film is important for the higher photocatalytic decoloration rate observed under both UV and vis-light irradiation. Thus, the electrical conductivity property of the thin film facilitates the transportation of extra electrons to the conduction band, which in turn are able to produce more reactive species at the titania surface, blocking electron–hole recombination which stops the production of radicals at the surface **[42]**.

9−5 SUMMARY

In this work, the photocatalytic activity of the Ag-NP/TiO_2 composite thin films including those of unprecedentedly high Ag amounts (10–80 molar%) was quantitatively examined by the decoloration reaction of methylene blue (MB) in an aqueous solution. Different attenuation DRS absorption sharp peaks have been obtained in the 310 nm−710 nm spectra range. Two of these peaks is inherent to the natural optical SPR of spherical Ag NP (the peak around 390 nm) and to the typical pure TiO_2 optical absorption (the peak around 365 nm), respectively. All the composites exhibit these two peaks, reflecting the capability to respond to both UV and visible light.

On the other hand, the size- and shape-dependent LSPR peaks appear at different lambda maximum was also observed. An analysis of DRS spectra of the obtained composites proved that Ag NP absorb visible light, facilitated by surface plasmon absorption of the composite thin films. Hence, the findings demonstrated that a positive relationship exists between Ag NP surface plasmon absorption and the rate enhancements, and proves the hypothesis that the metallic plasmon enhances rates of photocatalytic reaction, as enhanced by the electrical conductivity of the thin film.

9−6 REFERENCES

1. Fujishima A., Rao T.N., Truk D.A. (2000). *J. Photochem. Photobiol. C*, **1**, 1–21.

2. Fujishima, A.; Honda, K. (1972). *Nature*, **238**, 37–38.

3. Rehman, S.; Ullah, R.; Butt, A.M.; Gohar, N.D. (2009). *J. Hazard. Mater.*, **170**, 560–569.

4. Hamal, D.B.; Klabunde, K.J. 2007, *J. Colloid Interface Sci*., **311**, 514–522.

5. Kőrösi, L.; Papp, S.; Ménesi, J.; Illés, E.; Zöllmer, V.; Richardt, A.; Dékány, I. (2008). *Colloids Surfaces A*, **319**, 136–142.

6. Janovák, L.; Veres, Á.; Bujdosó, T.; Rica, T.; Fodor, E.; Tallósy, S.; Buzás, N.; Nagy, E.; Dékány, I. (2011). *J. Adv. Oxid. Technol.*, **15**, 205–216.

7. Loganathan, K.; Bommusamy, P.; Muthaiahpillai, P.; Velayutham, M. (2012). *Environ. Eng. Res.* **16**, 81–90.

8. Liu, S.X.; Qu, Z.P.; Han, X.W.; Sun, C.L. (2004). *Catal. Today*, **93–95**, 877–884.

9. Jakob, M.; Levanon, H.; Dame, N. (2003). *Nano Lett.*, **3**, 353–358.

10. Hirakawa, T.; Kamat, P.V. (2005). *J. Am. Chem. Soc.*, **127**, 3928–3934.

11. Yu, J.; Dai, G.; Huang, B. (2009). *J. Phys. Chem. C* , **113**, 16394–16401.

12. Dahmen, C.; Sprafke, A.N.; Dieker, H.; Wuttig, M.; von Plessen, G. (2006). *Appl. Phys. Lett.*, **88**, 11923.

13. Standridge, S.D.; Schatz, G.C.; Hupp, J.T. (2009). *Langmuir*, **25**, 2596–600.

14. Wodka, D.; Bielańska, E.; Socha, R.P.; Elzbieciak-Wodka, M.; Gurgul, J.; Nowak, P.; Warszyński, P. (2010). *ACS Appl. Mater. Interfaces*, **2**, 1945–1953.

15. Rad, B. (2008). *Global NEST J.*, **10**, 1–7.

16. Turkevich, J.; Stevenson, P.C.; Hillier, J. (1951). *Discuss. Faraday Soc.*, **11**, 55.

17. Enustun, B.V.; Turkevich, J. (1963). *J. Am. Chem. Soc.*, **85**, 3317.

18. Frens, G. (1973). *Nat. Phys. Sci.*, **20**, 241.

19. Kumar, K.P.; Paul, W.; Sharma, C.P. (2012). *BioNanoScience*, (2), 144–152.

20. Kuntyi, O.; Okhremchuk, Y.; Bilan', O.; Hapke, J.; Saldan, I. (2013). *Central Eur. J. Chem.*, **11**, 514–518.

21. Patakfalvi, R.; Papp, S.; Dékány, I. (2007). *J. Nanopart. Res.*, **9**, 353–364.

22. Seery, M.K.; George, R.; Floris, P.; Pillai, S.C. (2007). *J. Photochem. Photobiol.*, **189**, 258–263.

23. Grabowska, E.; Zaleska, A.; Sorgues, S.; Kunst, M.; Etcheberry, A.; Colbeau-Justin, C.; Remita, H. (2013). *J. Phys. Chem. C*, **117**, 2013.

24. Li H.; Zhao, G.; Song, B.; Han, G. J. (2008). *Cluster Sci.*, **19**, 667–673.

25. Takahashi, Y.; Tatsuma, T. (2010). *Nanoscale*, **2**, 1494–1499.

26. Awazu, K.; Fujimaki, M.; Rockstuhl, C.; Tominaga, J.; Murakami, H.; Ohki, Y.; Yoshida, N.; Watanabe, T. (2008). *J. Am. Chem. Soc.*, **130**, 1676–1680.

27. Ménesi, J.; Kékesi, R.; Oszkó, A.; Zöllmer, V.; Seemann, T.; Richardt, A.; Dékány, I.(2009).*Catal. Today*, **144**, 160–165.

28. Ménesi, J.; Kékesi, R.; Zöllmer, V.; Seemann, T.; Richardt, A.; Dékány, I. (2009) *React. Kinet. Calal. Lett.* **96**, 367–377.

29. Sato, M.; Hara, H.; Niside, T.; Sawada, Y. (2006). *J. Mater. Chem.*, **6**, 1767–1770.

30. Nagai, H.; Aoyama, S.; Hara, H.; Mochizuki, C.; Takano, I.; Honda, T.; Sato, M. (2010). *J. Mater. Sci.*, **45**, 5704–5710.

31. Nagai, H.; Hasegawa, M.; Hara, H.; Mochizuki, C.; Takano, I.; Sato, M. (2008). *J. Mater. Sci.*, **43**, 6902–6911.

32. Nagai, H.; Mochizuki, C.; Hara, H.; Takano, I.; Sato, M. (2008). *Solar Energy Mater. Solar Cell.*, **92**, 1136–1144.

33. Nagai, H.; Aoyama, S.; Hara, H.; Mochizuki, C.; Takano, I.; Baba, N.; Sato, M. (2009). *J. Mater. Sci.*, **44**, 861–868.

34. Kang, J.-G.; Sohn, Y. (2012). *J. Mater. Sci*., **47**, 824–832.

35. Wan, L.; Li, J.F.; Feng, J.Y.; Sun, W.; Mao, Z.Q. (2007). *Appl. Surface Sci*., **253**, 4764–4767.

36. He, W.F.Z.Y.L.; Zhang, M.S.; Yin, Z.; Chen, Q. (2000). *J. Phys. D*, **33**, 912.

37. Li, J.; Xu, J.; Dai, W.; Fan, K. (2009). *J. Phys. Chem. C*, **113**, 8343–8349.

38. Kortum, G. 1969. Reflectance Spectroscopy; Springer-Verlag: *Berlin, Germany*, 180.

39. Li H.; Bian, Z.; Zhu, J.; Huo, Y.; Li, H.; Lu, Y. (2007). *J. Am. Chem. Soc*., **129**, 4538.

40. Kosanic, M.M.(1998). *J. Photochem. Photobiol. A*, **119**, 119–122.

41. Christopher, P.; Xin, H.; Linic, S. (2011). *Nat. Chem.*, **3**, 467–472

42. Kiyonaga, T.; Mitsui, T.; Torikoshi, T.M.; Takekawa, M.; Soejima, T.; Tada, H. (2006), *J. Phys. Chem. B*, **110**, 10771.

CHAPTER 10: CONCLUTION AND RECOMMEDATIONS

10−1 CONCLUDING REMARKS

The preceding chapters mainly investigated Ag-nanoparticle/titania thin films, with various volumetric fractions of silver (φ_{Ag}) in a titania matrix, successfully fabricated by a wet chemical method, the molecular precursor method (MPM). Respective precursor solutions for Ag nanoparticles and titania were prepared from Ag salt and a titanium complex and their structural, electrical and photo-responsive properties were clarified. X-ray diffraction (XRD) patterns, X-ray photoelectron spectroscope (XPS) spectra and transmission electron microscopy (TEM) images indicated that the Ag-NP/TiO_2 composite thin films consist of rutile, anatase and metallic Ag nanoparticles homogeneously distributed in the titania matrix. This study shows that the molecular precursor method, which offers excellent miscibility of the silver and titania precursor solutions is effective for overcoming the limitations in miscibility of the conventional sol–gel method and is necessary for fabricating composite thin films having a large φ_{Ag} value. Regarding the research topics, new discoveries presented in the thesis include:

1. To find the percolation threshold for the electrical resistivity of Ag-nanoparticle/titania composite thin films, metallic Ag-nanoparticle/titania composite thin films, with different volumetric fractions of silver ($0.26 \leq \varphi_{Ag} \leq 0.68$) to titania, were fabricated on a quartz glass substrate at 600°C using the molecular precursor method. The resistivity of the films was of the order of 10–2 to 10–5 Ω·cm with film thicknesses in the range 100–260 nm. The percolation threshold was identified at a φ_{Ag} value of 0.30. The lowest electrical resistivity of 10−5 Ω·cm at 25°C was recorded for the composite with the Ag fraction, φ_{Ag}, of 0.55. It could be deduced that the electrical

resistivity of the thin films formed at 600°C was unaffected by the anatase/rutile content within the thin film, whereas the shape, size, and separation distance of the Ag nanoparticles strongly influenced the electrical resistivity of the Ag-nanoparticle/titania composite thin films.

2. To study the absorption spectra and photocurrent densities of metallic Ag nanoparticle/titania (Ag NP/TiO_2) composite thin films, COMP-Agn, with various amounts of Ag (10 mol% ≤ n ≤ 80 mol%) were fabricated on a quartz glass substrate at 600°C using the molecular precursor method. It was shown that MPM, which results in excellent miscibility of Ag NP and TiO_2 precursor solutions, is necessary for fabricating composite thin films capable of generating a cathodic photocurrent rather than an anodic one reported in many papers. The metallic property of Ag NPs and their UV-vis absorption spectra indicate that well-defined and intense absorption bands at approximately 410 nm, which correspond to their SPR peaks and the wide-range LSPR band in the visible region, are capable of efficiently sensitizing Ag NP/TiO_2 composite thin films. Therefore, the plasmonic property of Ag NPs can facilitate the elucidation of the mechanism behind the cathodic photocurrent generation from the Ag NP/TiO_2 composite thin films. Thus, the excellent vis-light response of the COMP-Agn and the major factors affecting their photoresponsive nature are discussed from the viewpoints of a particle-plasmon band of Ag NPs. The absorption spectra reveal that the LSPR of Ag NPs can enhance the photoresponse of CONP-Agn electrodes in the vis-region. Moreover, the high electrical conductivity of the COMP-Agn is important for affording a photoresponsive activity by enhancing the high separation efficiency of charge

carriers.

3. The relationship between the unprecedentedly high amounts of metallic silver in TiO_2 and photocatalytic decoloration rate of methylene blue (MB) in an aqueous solution was also examined. The decoloration rates monitored by the absorption intensity of the MB solution indicated that the composite thin films of Ag amount less than 40 mol% are not effective under Vis-irradiation, though they can work as a photocatalyst under UV-irradiation. Further, the UV-sensitivity of the composite thin films gradually decreased to almost half level of that of the TiO_2 thin film fabricated under the identical conditions, when the Ag amount increased from 10 to 40 mol%. Contrarily, the composite thin films of Ag content larger than 50 mol% showed the Vis-responsive activity, whose level was slightly lower than the decreased UV-sensitivity. Diffuse reflectance spectra suggested that the Vis-responsive activity of the composite thin films is due to the localized surface plasmon resonance (LSPR) and surface plasmon resonance (SPR) of Ag-NP. Hence, the findings demonstrated that a positive relationship exists between Ag NP surface plasmon absorption and the rate enhancements, and proves the hypothesis that the metallic plasmon enhances rates of photocatalytic reaction, as enhanced by the electrical conductivity of the thin film.

10−2 RECOMMENDATIONS

As the most widely investigated metal oxide, TiO_2 has unique physicochemical properties, and thus it has a wide range of applications. Based on our research, future work is suggested in the following area:

1. Enhancement of the conductivity of semiconductor materials is desirable from a technological perspective. Moreover, it is well established that the relatively high resistivity of materials such as metal oxide and polymers, can be reduced by incorporating metal nanoparticles into their matrix based on the fact that the electrically conductive particles can be randomly distributed within the matrix to form a composite. The inclusion of Ag nanoparticles into various materials and methods may offer unique advantages in terms of electrical characteristics. Therefore, the reduction of electrical resistivity observed in Chapter 5 and 6 for titania and zirconia matrix respectively, can be further investigated in other materials such as silicon oxide thin films and polymers, considering the percolation threshold found for the electrical resistivity of Ag-NP/TiO_2 composite thin films.
2. Recently, renewable energies have gained much more attention because of their dominant advantages comparing with the previously used conventional energies such as fossil fuels. Conventional energies' limited resources along with their relevant environmental pollutions which threaten the public health are the most important issues regarding with these kinds of energies. The recent crisis happened here in Japan's nuclear power plants due to the earthquake in 2011 is just an example of these threats that usually occur and cause the human beings experience some terrible tragedies. Currently, a unique photo electrochemical solar cell based on a TiO_2 nanoparticle photoelectrode sensitized with a light-harvesting, is on the verge of commercialization offering an interesting alternative for the existing silicon based solar cells as well as for the thin film solar cells. However, there is an essential problem concerning the stability of the device. These types of solar cell hydrolyzed by the electrolyte, so the equipments do not last longer. Using the

Ag/TiO_2 system may provides better possibility for the long-lasting electron transmission in the electrode for DSSC solar cell and enhances photocurrent in the cells. Moreover, the study of p-n junction solar cell involved Ag/TiO_2 composite thin films is highly that responsive to visible light is highly recommedate. The use of evacuated tube for water heating system involved Ag/TiO_2 composite thin film is under investigation.

3. Pollution is a very serious problem for many countries at present. TiO_2 have been investigated to decompose organic compounds by photocatalysis. However, due to its high reflective index and band gap (3.2 eV), the light can not reach a distance longer than only the photons in UV region can be absorbed to produce highly active species, which are the main reactants to decompose the organic compounds. Incorporation of plasmonic Ag NP in to TiO_2 can be one of the ways to overcome these drawbacks. Morover, the study of antibacterial, hydrogen production and hydrophilics of the composite thin films is encouraged.

As a summary for this chapter, for this research topic, so much is known now about structures, preparation, and properties; yet, so much is still to be learned.

研 究 業 績 書

審査付論文

PUBLICATIONS:

1) Daniel S.L., Nagai H., Sato M..

   Photocatalytic activity of Vis-responsive Ag-nanoparticles/TiO_2 composite thin films fabricated by molecular precursor method (MPM). *Catalysts* **3**, 625-645 (2013).

2) Daniel S.L., Nagai H., Sato M..

   Photoelectrochemical Property and the mechanism of plasmonic Ag-NP/TiO_2 composite thin films with high silver content fabricated using molecular precursor method. *J. Mater. Sci.*, **48**, 7162–7170 (2013).

3) Daniel S.L., Nagai H., Aoyama S., Mochizuki C., Hara H., Baba N., and Sato M..

   Percolation threshold for electrical resistivity of Ag nanoparticle/titania composite thin films fabricated using molecular precursor method, *J. of Mater. Sci.*, **47**, 3890–389947 82012).

4) Daniel S.L., Kiremire EMR, Chibale K., Rosenthal P.J., Kiratu T. M., Guto P. M., Kamau G. N..

   The FT-IR and malarial biological studies of copper(II) complexes containing thiosemicarbazone and semicarbazone ligands derived from ferrocene and pyridyl fragments. *Inter. J. of BioChemiPhysics*, **18**, 1-18 (2010).

5) Kiremire E.M.R., Daniel S.L., Chibale K., Kambafwile H. and Rosenthal P.J..

   Inducement of antimalarial biologicasl activity in some S-based ligands by Zn(II) ions. *Biosci., Biotechnol. Res. Asia*, **5(1)**, 121-123 (2008)

6) Kiremire E.M.R., Daniel S.L., Muashekele H., Chibale K. and Kambafwile H..

   Further investigation into phenomental paramagnetic shift influence of Cu(II) ion on ferrocene-thiosemicarbazone-based bimetallic complexes. *Mater. Sci. Res.*, **4**, 263-267 (2007).

7) Kiremire E.M.R., Daniel S.L., Muashekele H., Chibale K. and Kambafwile H..

   Phenomenal paramagnetic shifts in certain ferrocene thio-based copper(II) metal complexes. *Orient. J. Chem.*, **23(3)**, 785-791 (2007)

8) Kiremire E.M.R., Daniel S.L., Muashekele H., Chibale K. and Kambafwile H..

   The crystal structure of a new anti-malarial bis{3-[1-(2-pyidyl)ethylidene] hydrazinecarbodithioato}Cadmium(II) complex, *Orient. J. Chem.*, **23(2)**, 415-422 (2007).

9) Kiremire E.M.R., Daniel S.L., Chibale K., Rosenthal P. J..

   Metal Complexes with High Biological Activity against Chloroquine Resistant strain of *plasmodium falciparum* parasite. *Biosci., Biotechnol. Res. Asia*, **4(2)**, 401-404 (2007).

口頭研究発表

ORAL PRESENTATIONS:

International conferences presentations:

1) Daniel S.L., Nagai H., Hara H., Sato M.. *The 12th International Symposium on Advanced Technology* (ISAT-12). Southern Taiwan University of Technology, Tainan, Taiwan. (13-15 November 2013).

2) Daniel S.L., Nagai H., Sato M.. *20th International SPACC-20 Symposium*, Changxhu-China. (11-15 September 2013).

3) Daniel S.L., Nagai H., Aoyama S., Mochizuki C., Hara H., Baba N., and Sato M.. *Intl' symposium on nano-science and technology*, Southern Taiwan University of Technology, Tainan, Taiwan. (18-19 November 2011).

4) Daniel, S.L. and Kiremire E.M.R.. *Kenya Chemical Society and East And Southern Africa Environmental/Theoretical Chemistry Conference*. Mobasa, Kenya. (5-9 October 2009).

5) Daniel S.L., Chibale K., Rosenthal P.J., Negonga A.M., Munyolo F.M. and Kiremire E.M.R.. *35th Annual Congress of the Parasitological Society of Southern Africa* (PARSA), Ministry of Mines and Energy, Windhoek, Namibia. (24–26 September 2006).

6) Kiremire E.M.R., Chibale K., Rosenthal P.J., Daniel S.L., Negonga A.M.N., and Munyolo F.M.. *35th Annual Congress of the Parasitological Society of Southern Africa* (PARSA) conference, Windhoek, Namibia. (24-26 September 2006).

Domestic conferences presentations:

1) Daniel S.L., Nagai H., Sato M.. *Conference on LED and Its Industrial Application* (LEDIA-`13) Yokohama-Pacifico, Japan. (21-22 April 2013).

2) Daniel S.L., Nagai H., Sato M.. *The 11th International Symposium on Advanced Technology*. Kogakuin University, Tokyo, Japan. (30 October 2012).

3) Daniel S.L., Nagai H., Sato M.. *19th International SPACC-CSJ Symposium*. Hokkaido University, Sapporo, Japan. (2-4 August 2012).

4) Daniel S.L., Nagai H., Aoyama S., Mochizuki C., Hara H., Baba N., and Sato M.. *Ceramic society of Japan 2012 annual meeting.* Kyoto University, Kyoto, Japan. (19-21 March 2012).

5) Daniel S.L., Nagai H., Aoyama S., Mochizuki C., Hara H., and Sato M.. *18th The Society of Pure and Applied Coordination Chemistry-CSJ Symposium*. Yokohama-Pacifico, Japan. (26th-28th March 2011).

6) Daniel S.L., Kiremire EMR, Kambafwile K., Chibale K.. *The 9th International Symposium on Advanced Technology* (9th ISAT), Kogakuin University, Shinjuku, Japan. (3-6 November 2010).

POSTER PRESENTATIONS:

1) Daniel S.L., Nagai H., Sato M.. *20th International SPACC-20 Symposium*, Changxhu-China. (11-15 September 2013).

2) Daniel S.L., Nagai H., Sato M.. *Conference on LED and Its Industrial Application* (LEDIA-`13), Yokohama-Pacifico, Japan. (21-22 April 2013).

学会（委員会関係も含む）および社会における活動状況等

MEMBERSHIP:

1) The Ceramics Society of Japan (from 2012- present)
2) The Japan Chemistry Society (form 2011- present)

その他の業績（特許・資格・賞罰も含む）

ACADEMIC AWARDS:

1) Best Conference Presentation Award (19 November 2011). Intl' symposium on nano-science and technology; Southern Taiwan University of Technology, Tainan, Taiwan.
2) Researcher Student Certificate (April 2010- March 2011). Coordination Chemistry Laboratory. Kogakuin University, Tokyo, Japan.
3) Invited Lecturer certificate (6 November 2010) The 9th International Symposium on Advanced Technology., Kogakuin University, Shinjuku, Japan.
4) Japanese Language Intensive Certificate (April 2010-October 2010). University of Electrocommunication (UEC), Chofu, Japan.
5) Ministry of Education, Culture, Sports, Science, and Technology (Monbukagakusho:MEXT) Scholarship. (March 2010-March 2014). Kogakuin University, Tokyo, Japan.
6) The Petroleum Training and Education Fund (PETROFUND) Scholarship and Research Grants. (February 2006-December 2008). Windhoek, Namibia.

履　歴　書

2014 年 02 月 20 日

ふりがなだにえる，しっぴーしょ　りきうす

氏 名 Daniel, Shipwiisho LIKIUS 印 男　本籍地 Namibia （都道府県）

生年月日　1981 年 04 月 06 日生（32 才）　現住所 101 Dani-Itsukumino Corp. 584 Inumemachi, Hachioji, Tokyo, 193-0802 (〒193-0802)℡ 080-3552-7255

学 歴

1996 年 02 月 01 日 OTjikoto Junior Secondary School grade 8-10

2000 年 11 月 30 日 OTjikoto Senior Secondary School grade 11-12

2001 年 02 月 01 日 University of Namibia B. Sc. (Chemistry and Biology)

2006 年 11 月 31 日 University of Namibia, **B. Sc.** (completed)

2007 年 02 月 01 日 University of Namibia, M. Sc. (Inorganic chemistry)

2009 年 04 月 01 日 University of Namibia, **M. Sc.** (completed)

2010 年 04 月 01 日 Graduate school of Kogakuin University, Research student

2011 年 04 月 01 日 Graduate school of Kogakuin University, Doctorate student

2014 年 03 月 31 日 Graduate school of Kogakuin University, **PhD** (Engineering) –(completed) 修了予定

学位（学士・修士）、称号

（学士）2006 年 04 月 16 日 University of Namibia 大学より Bachelor of Science (Chemistry and Biology) の学位を授与される。

（主論文題目）「Determinations of iodine content in table salts (NaCl) found in Windhoek Supermarkets, Namibia」

（修士）2008 年 04 月 16 日 University Of Namibia 大学より Master of Science (Inorganic Chemistry)の学位を授与される。　（主論文題目）「The synthesis, characterization and biological studies against malaria parasites of sulphur-based metal complexes of Cu(II), Cd(II), Co(II), Mn(II), Al(III) and Ag(I).」

職 歴　（教歴の場合は担当科目を記入）

2012 年 04 月 01 日 Research Assistant . Kogakuin University

2008 年 07 月 01 日 Laboratory Technologist. University of Namibia

2008 年 01 月 01 日 Applied Physics and Chemistry Lecturer, Faculty of engineering, Polytechnic of Namibia

2007 年 01 月 01 日 Physical science teacher, Jahn Mohr high School, Windhoek

2005 年 01 月 01 日 Mathematic and Physical Science Teacher, Concordia college

2005 年 01 月 01 日 Hostel Supervisor, Concordia College

2004 年 02 月 01 日 Inorganic chemistry Demonstrator, University of Namibia

1997 年 02 月 01 日 Volunteer, Cancer Association of Namibia (CAN).